Field-cycling NMR investigations of nuclear spin relaxation and proton tunnelling

Weimin Wu, B.Sc.

2005.12

Thesis submitted to the University of Nottingham for the degree of

Doctor of Philosophy.

Contents

Chapter 4. The dynamics of proton transfer in the hydrogen bonds of benzoic acid

List of Figures

Fig 4.13 The inverse temperature dependence of the inverse correlation times, τ_c^{-1}, for proton transfer in BA. At low temperature the proton transfer rate is independent of temperature but smoothly evolves towards Arrhenius behaviour at higher temperatures. The blue filled circles are the data transferred directly from T_1 vs 1/T curve, the red filled rectangles were extracted from the fits shown in Fig 4.4a and Fig 4.4b, the black triangles were earlier field-cycling data from [11]. It is evident that all these data are in good agreement with each other and with the ST model. The solid line has been calculated from the ST model and parameters reported in [11] and listed in Table 4.2, determined before field-cycling

Abstract

A current-switched superconducting field-cycling NMR spectrometer has been designed and built for studying the role of quantum tunnelling in molecular dynamics. The instrument is designed for work in the solid state with sample temperatures extending from 4K up to 300K. The maximum field-switching rate is $10Ts^{-1}$. Among the samples studied in this thesis is the nuclear spin-relaxation and proton tunnelling.

Concerted double proton transfer in the hydrogen bonds of carboxylic acid dimers is well established as the model system for translational quantum tunnelling. The model system has been chosen to illustrate the smooth quantum-to-classical transition and at all temperatures the proton transfer is characterised by a single correlation time.

Quadrupolar interactions introduce an additional relaxation to the proton spin polarisation. The enhanced relaxation of the proton spin appears as a dip in the proton magnetisation curve. This technique is employed to measure the quadrupolar transition frequency of ^{14}N and ^{35}Cl and determine the structure of heroin hydrochloride.

The introduction of a second spin species has a significant effect on the spin-lattice relaxation. Compared with homonuclear systems, the spectral density acquires additional components characterised by the sum and difference Larmor frequencies of the two nuclei. Further, instead of a single relaxation time, there are four elements of a relaxation matrix. Therefore, the magnetisation recovery becomes bi-exponential and the initial polarisation state of the second nucleus strongly affects the magnetisation recovery of the nucleus which is being observed. We shall report on the results of spin-lattice relaxation investigations on ^{1}H-^{13}C, ^{1}H-^{19}F systems. The role of heteronuclear interactions in spin-lattice relaxation and the newly developed methodology of field-cycling relaxometry will be discussed. This represents the first ^{13}C field-cycling NMR experiment and the first to measure the field dependence of the off-diagonal element of the relaxation matrix.

Acknowledgements

Sincere thanks go to my supervisor A. J. Horsewill for all his guidance and encouragement during these two years and to J. R. Owers-Bradley for his help in our ^{13}C experiments and examining of my first and second year reports.

In the Physics department here at Nottingham many thanks go to M. Carter, Chris Pallender and Bob Chettle for help with helium supply and probe trouble-shooting.

Thanks also go to Daniel Noble for probe designing and question discussing. Thanks also go to the University for EPSRC scholarship support.

Best wishes to my father for recovering from the cancer treatment and thanks must go to him for his optimism and encouragement during the treatment of cancer.

Last but not least I thank my wife for all her love and support.

Chapter 1 Introduction

The transfer of protons involved in hydrogen bonding is fundamental to many chemical and biological processes. It has been widely studied [1-16]. The sample BA (benzoic acid) has been established as a model system to illustrate the dynamics of the proton transfer process in hydrogen bonds. At low temperature, the proton dynamics are dominated by quantum tunnelling process, while at high temperature, the dynamics more closely approximates to Arrhenius behaviour. A theoretical study has been successfully set up by Skinner and Trommsdorff (ST) [5] to model the proton transfer dynamics. Later Brougham *et al* [11] modified the theory to account for tunnelling pathways via excited states which become important at higher temperature.

As a unique and powerful tool to investigate the quantum molecular dynamics, FCNMR (field-cycling NMR) has an advantage over many other NMR techniques which permits one to cover several decades of frequency with the same instrument. Therefore the field dependence curve of the inverse spin-lattice relaxation time maps out the spectral density directly, enabling the correlation rate for molecular dynamics to be determined very accurately. This advantage has been utilised in the investigation of the molecular quantum dynamics on the samples studied here. Both homonuclear and heteronuclear systems have been modelled and investigated here using FCNMR.

FCNMR could be employed in many application fields [17-22]. The application fields in my work cover some of those listed in these reference papers such as quadropolar dips and polymers (not related to the publication and no results and discussion in this thesis), and a new explored application field, the dynamics of heteronuclear system, which was a challenging problem not only in FCNMR experiments but also in the analysis of the experimental data.

This thesis is configured to focus on the topics related to my published papers. There are five main chapters from Chapter 2 to Chapter 7.

The background of NMR and theories for understanding and analysing the experimental data are described in Chapter 2. The structure of our FCNMR

spectrometer and function of each component are presented in Chapter 3, as well as the pulse sequences which were designed for different experimental purposes. From Chapter 4 to Chapter 7, the experimental results and discussion are presented in detail in order of complexity and difficulty of experiments and data analysis.

The model system BA was chosen to investigate the spectral densities (the field dependence of the spin-lattice relaxation time) with FCNMR at a set of temperature in Chapter 4. Each spectral density curve which was characterised by only one correlation rate was the best proof for confirming the theory of ST and arguing against a non-physical theory proposed by Latanowicz and Reynhardt [23] (LR). The smooth transition between quantum and classical mechanics was obtained in perfect agreement with the ST model and with many quantum phenomena in which there should be no distinguished difference between quantum behaviour and classical behaviour, because classical behaviour is the extreme of quantum behaviour. Only with FCNMR could the inadequacy of LR theory be completely revealed.

In Chapter 5, quadrupolar dips of ^{14}N and ^{35}Cl were observed in the spectrum of ^{1}H magnetisation recorded at the liquid helium temperature and at zero magnetic field with FCNMR in heroin hydrochloride supplied by Prof. Smith, King's College London. These dips were due to the enhanced relaxation of ^{1}H spins which was affected by the quadrupolar interaction. The measured spectra were employed to assist in the determination of the structure of the sample. It indicated that FCNMR/NQR could be a potential tool of identifying the particular drug in the presence of other closely related compounds.

In Chapter 6 and Chapter 7, the heteronuclear interactions between two spin ½ nuclei were studied on two samples sample ^{13}C-BA (Benzoic acid, 99% ^{13}C substitution of the carboxy carbon) and TFTA (tetrafluoroterephthalic acid: $C_6F_4(COOH)_2$) respectively. Although both the systems obey the same theory as discussed in Chapter 2, the difference in the relative magnitude of the off-diagonal elements of the relaxation matrix meant that different experimental techniques and data analysis methods had to be employed for the two different samples. For the sample ^{13}C-BA studied in Chapter 6, the first ^{13}C FCNMR investigation to be reported, the off-diagonal element was so small that the magnetisation recovery curve could be fitted

with a single exponential function and the effective relaxation time was employed to record the experimental data; however since the effective relaxation time was the weighted average of the two time constants characterising the underlying bi-exponential magnetisation recovery curve, the initial conditions which determined the coefficients of the two spin species became a dominant problem to deal with. For TFTA by contrast, the sample studied in Chapter 7, the off-diagonal elements were comparable with the diagonal elements. The magnetisation recovery curves were bi-exponential and two relaxation rates were determined. The problem is that no function is known *a priori* for fitting the spectral density curve; an alternative approach was designed to measure the off-diagonal elements directly by setting up appropriate initial conditions. Using this novel experiment, the correlation rate was determined directly from the field dependence of the off-diagonal elements. This method could in principle be applied on most of heteronuclear samples which exhibit bi-exponential relaxation.

In this thesis, a key concept is the fluctuation of local magnetic field which arises from the motion of the moment-carrying molecule. The relaxation processes, both in homonuclear system and in heteronuclear system, are driven by this random motion.

Chapter 2 Theory

The theories related to my work will be summarised here. The relevant background knowledge of the nuclear magnetic resonance (NMR) [24-28] will be introduced in section 2.1 giving emphasis to the spin-lattice relaxation process which underpins most of the experimental work in this thesis. Proton transfer dynamics and the model developed by Skinner and Trommsdorff will be presented in section 2.2 to describe the proton tunnelling process in hydrogen bonds. We study both single spin and two spin systems so the theory of the homonuclear and heteronuclear spin-lattice relaxation will be studied in section 2.3 and section 2.4 respectively in the context of the proton transfer dynamics in hydrogen bonds. Finally in section 2.5, the nuclear quadrupolar interaction, leading to completely different heteronuclear interaction, will be introduced to deal with the samples where quadrupolar nuclei are present.

2.1 NMR

2.1.1. Larmor Precession

When a nucleus is placed in a magnetic field $\boldsymbol{B}$, the Hamiltonian operator for the interaction is given by

$$\hat{H} = -\boldsymbol{\mu}\boldsymbol{\cdot}\boldsymbol{B} \tag{2.1}$$

where $\boldsymbol{\mu}$ is the magnetic moment of the nucleus with magnetogyric ratio γ,

$$\boldsymbol{\mu} = \gamma\boldsymbol{L} \tag{2.2}$$

where $\boldsymbol{L}$ is spin angular momentum, so associating this with the dimensionless spin angular momentum operator $\hat{I}$, we can write $\boldsymbol{L} \rightarrow \hbar\hat{I}$ and take the applied magnetic field to be B_0 along z-direction, finally

$$\hat{H} = -\hbar\gamma B_0\hat{I}_z \tag{2.3}$$

The eigenvalues of this Hamiltonian are simple, proportional to the eigenvalues of $\hat{I}_z$. Therefore the allowed energies are

$$E_m = -\gamma \hbar B_0 m \tag{2.4}$$

where $m = I, I-1, ..., -I$. These energies are illustrated in Fig 2.1 for the case $I = 3/2$.

The levels are equally spaced, the energy gap Δ between adjacent levels being $\gamma \hbar B_0$.
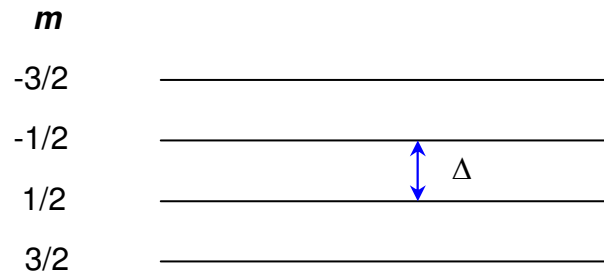
Fig 2.1 Energy levels of equation (2.4)

When μ is interacting with the magnetic field, there is a tendency for it to align parallel with field B to lower the total energy of system; it experiences a torque $\mu \times B$. We can gain useful insight by viewing the system classically. Equating the rate of changing of angular momentum with the torque, the equation of motion for μ can be obtained as follows

$$\frac{d\mu}{dt} = \gamma \mu \times B \tag{2.5}$$

The solutions are illustrated in Fig 2.2, describing a precession of the magnetic moment about the axis of the applied field at the frequency $\omega_L = \gamma B_z$, which is known as the Larmor frequency. The magnetic moment goes around and around on the same precession cone, always keeping the same angle between the spin axis and the magnetic field.
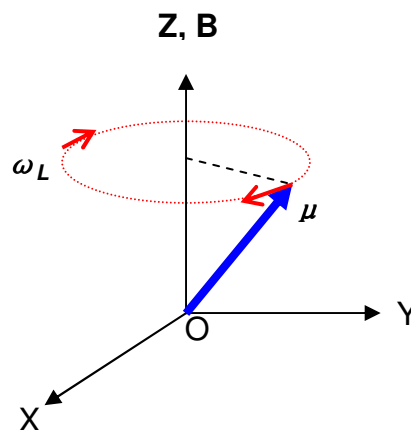
Fig 2.2 Larmor precession of the magnetic moment

2.1.2 Bulk magnetisation

We have discussed a single nucleus in the magnet field B_z, however real systems consist of many nuclear spins. A sample containing a large number of spin moments in an applied magnet DC field $B_z = B_0$ for an extended period will reach a state of equilibrium, where the populations are described by Boltzmann's law. Under the assumption of isolated spins, the populations P_m are proportional to $\exp(-E_m / k_B T)$, where E_m is the magnetic energy corresponding to the quantum number m of the spin, as illustrated in Fig 2.1. The net magnetisation of a sample containing N spins will be

$$M = N\gamma\hbar \frac{\sum_{m=-I}^{I} m\exp(\gamma\hbar m B_0 / k_B T)}{\sum_{m=-I}^{I} \exp(\gamma\hbar m B_0 / k_B T)} \tag{2.6}$$

The energy difference between the neighbouring levels, $\gamma\hbar B_0$, is extremely small in comparison with $k_B T$, it is permissible to make a linear expansion of the Boltzmann exponential, thus obtaining

$$M = \frac{N\gamma^2\hbar^2 B_0}{k_B T} \frac{\sum_{m=-I}^{I} m^2}{2I+1} = \frac{N\gamma^2\hbar^2 I(I+1)}{3k_B T} \mu_0 H_0 = \chi_0 H_0 \tag{2.7}$$

where χ_0 is the static nuclear susceptibility. The proportionality of χ_0 to $1/T$ is the well-known Curie law.

The assumption is in fact a good deal more general, as can be demonstrated easily using the formalism of the density matrix method.

Suppose that the Hamiltonian of a system of N nuclear spins contains, besides their Zeeman energy $\hat{H}_0 = -\gamma\hbar B_0 \sum_j I_z^j = -\gamma\hbar B_0 J_z$, where $J_z = \sum I_z^j$, other terms such as dipolar couplings between the spins or quadrupolar couplings with local gradients, which we describe as an extra term, $\hat{H}_1$, in the Hamiltonian. The assumption of thermal equilibrium between the spin system and the lattice is expressed by a statistical spin operator

$$\hat{\rho} = \exp\left(-\frac{\hat{H}_0 + \hat{H}_1}{k_B T}\right) \bigg/ \mathrm{tr}\left[\exp\left(-\frac{\hat{H}_0 + \hat{H}_1}{k_B T}\right)\right] \tag{2.8}$$

the macroscopic nuclear magnetic moment of the sample will be $M = \mathrm{tr}\{\gamma\hbar J_z \hat{\rho}\}$ or, if

we assume that the ratio $\left(\hat{H}_0 + \hat{H}_1\right)/k_B T$ is small,

$$M \cong \frac{-\mathrm{tr}\left\{\gamma\hbar J_z \left(\hat{H}_0 + \hat{H}_1\right)\right\}}{\mathrm{tr}\{1\}} \frac{1}{k_B T} \tag{2.9}$$

if $\hat{H}_1$ is such that $\mathrm{tr}\{\hat{H}_1 J_z\} = 0$, which happens to be the case for both spin-spin

couplings and quadrupolar couplings, it will be seen that

$$M \cong \frac{-\mathrm{tr}\left\{\gamma\hbar J_z \hat{H}_0\right\}}{\mathrm{tr}\{1\}} \frac{1}{k_B T} = \frac{-\mathrm{tr}\left\{\gamma^2\hbar^2 B_0 J_z^2\right\}}{\mathrm{tr}\{1\}} \frac{1}{k_B T} = \frac{N\gamma^2\hbar^2 I(I+1)B_0}{3k_B T} \tag{2.10}$$

in accordance with (2.7) and irrespective of the relative magnitude of $\hat{H}_0$ and $\hat{H}_1$,

provided that both are much smaller than $k_B T$.

In order to measure the energy separation Δ between two energy levels of a system, or other parameters corresponding to the bulk magnetisation or the change of the bulk magnetisation, which is the fundamental spectroscopic problem, a resonant method was introduced. The system under consideration is irradiated by an r.f. pulse, the frequency of which can be changed continuously. As long as the resonance condition $\Delta = h\nu$ is not fulfilled, the probability for a transition of the system to be induced by the field is very weak, but it increases considerably when the value $\nu = h/\Delta$ is reached. If the increase of the rate of transitions causes a detectable change in the system, a resonance has occurred and the measurement of Δ is reduced to the measurement of a frequency.

2.1.3 Rotating Frame; the interaction with EM radiation

When the nuclear spins interact with EM photons to introduce flips in the spin state, the interaction is driven by the oscillating magnetic field associated with the EM radiation. Let us treat the system classically and apply linearly polarised r.f. radiation

$B_1(t)$ to a single nuclear spin in the presence of a static field B , commonly

$$\begin{cases} B = B_0 k \\ B_1(t) = i2B_1 \cos \omega t \end{cases}$$

(2.11)

and $B_1(t)$ can be resolved into two rotating components as Fig 2.3

$$\begin{cases} B_a(t) = B_1(i \cos \omega t + j \sin \omega t) \\ B_c(t) = B_1(i \cos \omega t - j \sin \omega t) \end{cases}$$

(2.12)
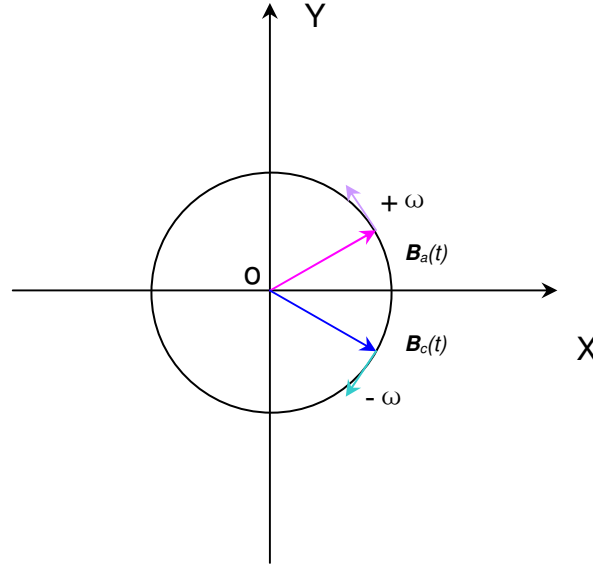
Fig 2.3 Two rotating components of $B_a(t)$

Both B_a and B_c will introduce a torque on μ . In Fig 2.4, the torque of B_c on μ is

$$torque = \mu \times B_c$$

(2.13)

Its direction is perpendicular to both μ and B_c . If $\omega = \omega_L$, which means B_c rotates at the same frequency as μ is precessing, then the torque due to the r.f. field is consistently in the same direction. The effect is to change the direction of μ , that is, to introduce transitions amongst spin states. We can see when $\omega = \omega_L$, the effect of B_c is the strongest. As one moves away from this resonance condition then the torque no longer acts consistently in the same direction and the ability of a non-resonant r.f. field to introduce transitions is rapidly diminished as ω moves further from ω_L.
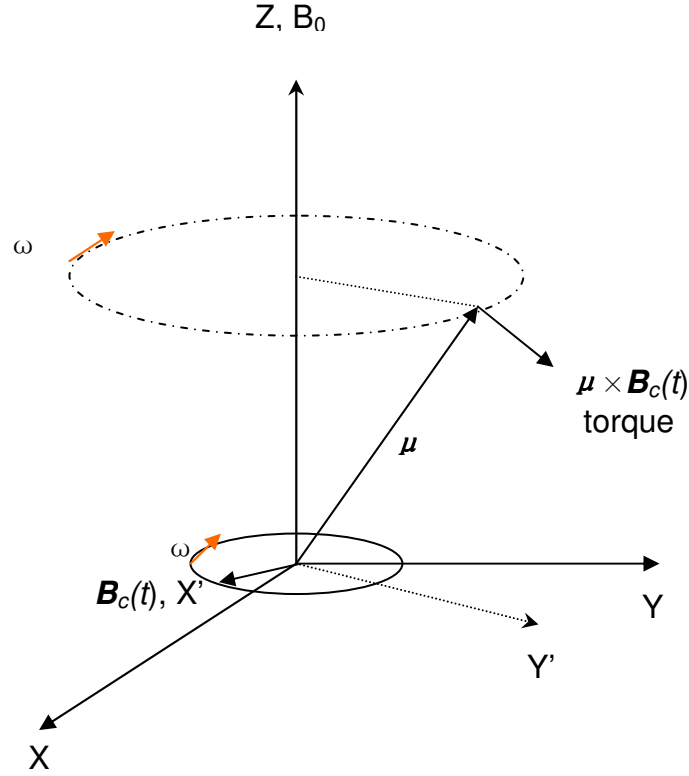
Fig 2.4 Torque introduced by time dependent field

We will find it easy to discuss the interaction between nuclear spins and EM photons when we move into a frame of reference which rotates clockwise about the z-axis at the r.f. frequency $-\omega$. It is a frame of reference called '**The Rotating Frame**' where B_1 is stationary, as shown in Fig 2.5a.

$$\boldsymbol{B}_1(t) = B_1 \boldsymbol{i}' \tag{2.14}$$

In this rotating frame, the magnetic moment will precess about the axis of $\boldsymbol{B}_{eff}$ (an effective magnetic field, equation (2.15)). $\boldsymbol{B}_{eff}$ and the motion are illustrated in Fig 2.5b and Fig 2.5c.

$$\boldsymbol{B}_{eff} = B_1 \boldsymbol{i}' + \left(B_0 - \frac{\omega}{\gamma} \right) \boldsymbol{k} \tag{2.15}$$

When $\omega = \omega_L$, that is when the r.f. field is on resonance with the Larmor precession, then $\boldsymbol{B}_{eff} = B_1 \boldsymbol{i}'$, and while the r.f. field is present, $\boldsymbol{\mu}$ precesses about the X' axis ($\boldsymbol{B}_c$ direction) in the $Y' - Z$ plane at the angular frequency $\omega = -\gamma B_1$.
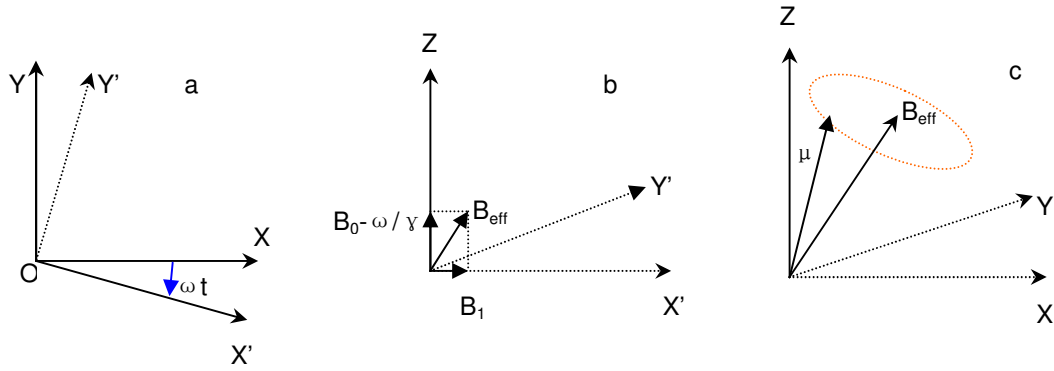
Fig 2.5 The rotating frame (a), effective magnetic field (b) and the precess motion in rotating frame (c).

In a time t_ω, $\boldsymbol{\mu}$ rotates through the angle

$$\theta = \gamma B_1 t_\omega \tag{2.16}$$

So it appears that applying a pulse of resonant r.f. radiation enables us to change the orientation of the magnetic moment. After the r.f. pulse is turned off, the magnetic moment will precess about $\boldsymbol{B}_0$. In the laboratory a coil is fixed to measure the emf which will be induced by the alternating flux in the coil. It is a typical experimental arrangement to observe the magnetisation by studying the emf. This process is illustrated in Fig 2.6.
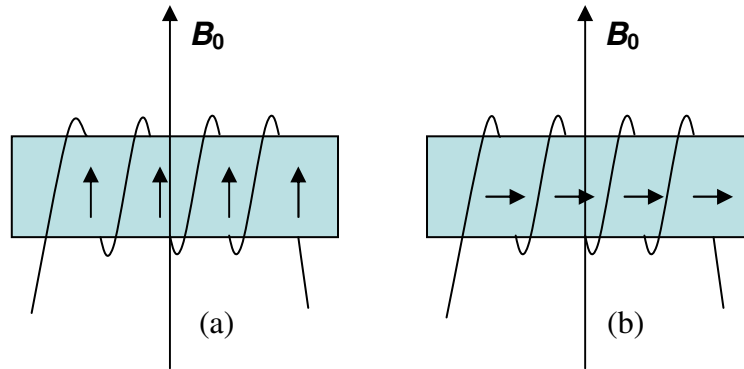
Fig 2.6 (a) coil containing sample. In thermal equilibrium the moments are parallel to magnetic field $\boldsymbol{B}_0$. (b) following a 90-degree pulse, the moments precess at angular frequency γB_0 perpendicular to $\boldsymbol{B}_0$. The moments produce a flux through the coil which is alternating as the spins precess. The induced emf may be observed.

The induced emf would persist indefinitely if there were no interactions of the spins with their surroundings. But in practice, these interactions cause a decay which means the moments along z-axis are getting bigger and the moments in x-y plane are getting

smaller. Therefore the emf is getting smaller during the decay. The decay may last in liquids for many milliseconds, but in solids it is more typically less than $100\,\mu s$. This is called the "free induction decay" (FID). It has the great virtue of enabling one to study the resonance signal in the absence of the voltages needed to produce $\boldsymbol{B}_1$. It is illustrated in Fig 2.7.
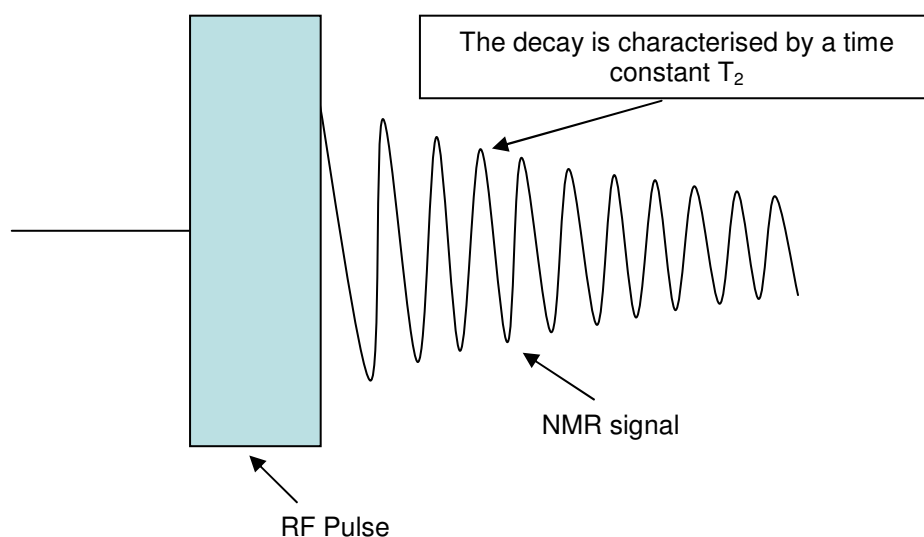
Fig 2.7 r.f. pulse and the induced NMR signal(FID).

2.1.4 Relaxation

Now let us inquire what will happen to the real samples which contain an ensemble of nuclei if we apply r.f. radiation to them. After the r.f. pulse, we create a non-equilibrium $\boldsymbol{M}$ (total magnetisation vector). When the r.f. field is removed, $\boldsymbol{M}$ will come back to its initial thermal equilibrium value by two relaxation mechanisms. One is the recovery of the longitudinal magnetisation M_z, and the other is the decay to zero of the transverse magnetisation M_x and M_y.

The Bloch equations [29] provide an exceedingly successful description of the magnetic properties of ensembles of nuclei in an external magnetic field. Let us obtain these equations following these steps:

First, in an arbitrary homogeneous field by analogy with the earlier treatment for an isolated magnetic moment, the equation of motion of the nuclear magnetisation for an ensemble of free spins can be written as

$$\frac{d\boldsymbol{M}}{dt} = \gamma \boldsymbol{M} \times \boldsymbol{B} \ .$$

(2.17)

Second, in a static field $B_z = B_0$, the trend of the magnetisation towards its equilibrium value $M_z = M_0 = \chi_0 B_0 / \mu_0$ can often be described with good accuracy by the equation $\frac{dM_z}{dt} = -\frac{M_z - M_0}{T_1}$. T_1 is the relaxation time characterising the longitudinal magnetisation.

Third, if by any means such as an r.f. pulse, the nuclear magnetisation is given a component at right angles to the applied field, the various local fields, owing to the fact that the spins are actually not free but interact with each other and with their surroundings, cause the transverse magnetisation to decay at a rate which can often be represented by the equations $\frac{dM_x}{dt} = -\frac{M_x}{T_2}, \frac{dM_y}{dt} = -\frac{M_y}{T_2}$, where T_2 is called the transverse relaxation time.

All these lead to the Bloch equation

$$\frac{d\boldsymbol{M}}{dt} = \gamma \boldsymbol{M} \times \boldsymbol{B} - \frac{M_x \boldsymbol{i} + M_y \boldsymbol{j}}{T_2} - \frac{M_z - M_0}{T_1} \boldsymbol{k}$$

(2.18)

where $\boldsymbol{i}$, $\boldsymbol{j}$ and $\boldsymbol{k}$ are the unit vectors of the laboratory frame of reference.

If the system is initially at equilibrium, $M_z = M_0$, $M_x = M_y = 0$, then after a $\frac{\pi}{2}$-pulse, the magnetisation is tipped into the transverse plane and we can write the Bloch equations as

$$\begin{cases} \dfrac{dM_x}{dt} = \gamma M_y B_z - \dfrac{M_x}{T_2} \\[2mm] \dfrac{dM_y}{dt} = -\gamma M_x B_z - \dfrac{M_y}{T_2} \\[2mm] \dfrac{dM_z}{dt} = 0 - \dfrac{M_z - M_0}{T_1} \end{cases} \qquad (2.19)$$

where T_1 and T_2 are two kinds of relaxation time :

- T_1 is the spin-lattice relaxation time. It governs the recovery of the longitudinal magnetisation M_z. This process involves an exchange of energy with the lattice to flip the nuclear spins.

- T_2 is the spin-spin relaxation time. It governs the recovery of the transverse magnetisation M_x and M_y. This process involves a dephasing process amongst the spins.

Both the relaxation of longitudinal magnetisation and the relaxation of transverse magnetisation are driven by the randomly fluctuating field which is a crucial concept in this thesis.

The electrons and nuclei that comprise molecule are all sources of magnetic fields, and undergo constant vigorous motion. Therefore, the local field on each molecule fluctuates rapidly both in space and in time. It has a slightly fluctuating magnitude and a slightly fluctuating direction, therefore a gradual breakdown of the constant-angle 'cone precession' of the nuclear spins arises. However the spin reorientation is towards an energy favourable orientation with the magnetic moment parallel to the magnetic field. This leads to an anisotropic distribution of nuclear spin polarisations, at thermal equilibrium in an applied magnetic field. Therefore a small net magnetic moment along the applied magnetic field, named the *longitudinal magnetisation*, is obtained. The process of returning this component to thermal equilibrium is conventionally called spin-lattice *relaxation*.

As we discussed in *2.1.3*, by applying an r.f. pulse of appropriate frequency and duration, the net spin polarization along the z-axis (longitudinal magnetisation) can be

transferred into a net spin polarization along the y-axis (or any axis in the xy plane perpendicular to the magnetic field). The net magnetic moment perpendicular to the magnetic field is called the *transverse magnetisation*.

After the pulse is turned off, the spins will resume their precessional motion. The bulk magnetic moment rotates in the xy-plane, perpendicular to the applied magnetic field. Due to slightly fluctuating microscopic magnetic fields, different spins experience different magnetic fields and therefore precess at slightly different frequencies. The precessing nuclear spins gradually get out of phase with each other and lose the transverse magnetisation. The time constant T_2, characterising the decay as illustrated in Fig 2.7, is sometimes called the spin-spin relaxation time constant.

2.1.5 NMR spectrum

As illustrated in Fig 2.7 and expressed in equation (2.19), the transverse magnetisation components after the r.f. pulse have the following form:

$$\begin{cases} M_y(t) = -M_0 \cos(\omega_0 t) \exp(-t/T_2) \\ M_x(t) = M_0 \sin(\omega_0 t) \exp(-t/T_2) \end{cases}, \qquad (2.20)$$

or combining them to form a complex signal $s(t)$:

$$s(t) \sim \exp(i\omega_0 t) \exp(-t/T_2) \qquad (2.21)$$

where $M_y(t) = \mathrm{Re}\big[s(t)\big]$ and $M_x(t) = \mathrm{Im}\big[s(t)\big]$ are the real and imaginary parts of the complex FID signal respectively.

Both components oscillate at the nuclear Larmor frequency ω_0, and decay with the time constant T_2. The signals represented by equation (2.20) contain enough information to determine both the magnitude of the Larmor frequency ω_0 and the decay time constant T_2. In practice, the determination of both the magnitude of the Larmor frequency ω_0 and the decay time constant T_2 is performed by *Fourier transformation*.

The NMR spectrum, defined in the frequency domain, is the Fourier transform of the FID,

$$s(\omega) = \int_0^\infty s(t)\exp(-i\omega t)\,dt \qquad (2.22)$$

A simple example of an NMR spectrum is plotted in Fig 2.8, which is the real part of the *Fourier transform* of the NMR FID illustrated in Fig 2.7 and the input function shown in equation (2.20). It has the following mathematical form:

$$\mathrm{Re}\big[s(\omega)\big] = \frac{\lambda}{(\omega - \omega_0)^2 + \lambda^2} \qquad (2.23)$$

where $\lambda = 1/T_2$.
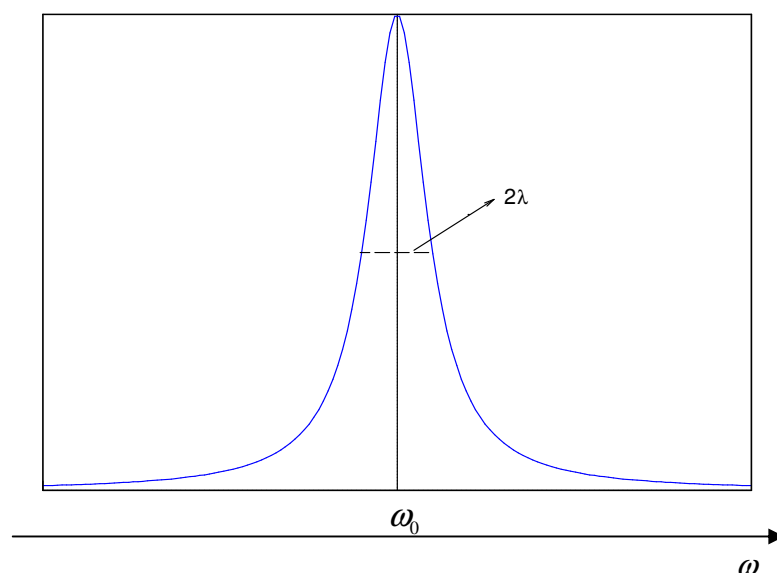
Fig 2.8 A simple NMR spectrum centred at ω_0 and with width 2λ.

This is a Lorentzian peak (Fig 2.8) with full width at half-height, equal to $2\lambda = 2/T_2$.

Both FID and NMR spectrum are complex quantities. $\mathrm{Re}\big[s(\omega)\big]$ is the absorption component whereas $\mathrm{Im}\big[s(\omega)\big]$ is called the dispersion. The latter is illustrated in Fig 2.9. Both absorption and dispersion are relevant to NMR experiments and will be discussed again in Chapter 3.

$$\text{Im}\big[s(\omega)\big] = -\frac{\omega - \omega_0}{\lambda^2 + (\omega - \omega_0)^2}$$

$(\omega_0, 0)$

ω
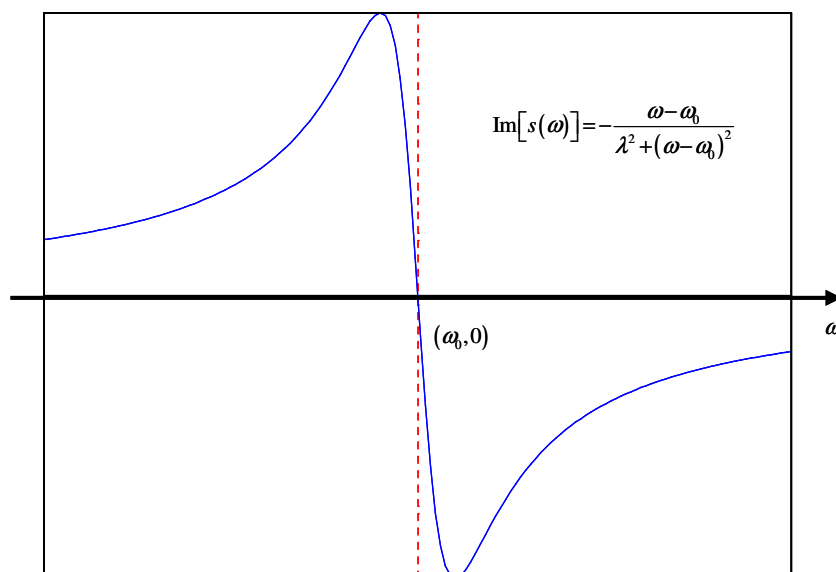
Fig 2.9 Dispersion Lorentzian line in a simple NMR spectrum.

2.2 Proton transfer dynamics and ST model

Proton transfer in the hydrogen bond is one of the fundamental chemical reactions. It is a process that is relevant to many biological processes important to life. It is the main theme of the work presented in this thesis where we have explored the use of heteronuclear interactions to measure the proton transfer rate. As illustrated in Fig 2.10, the hydrogen is exchanging its position between the two oxygen atoms in the hydrogen bond. This process is called proton transfer and the interchange between the two equilibrium states is hindered by an interceding potential barrier [1, 5, 11-14, 30-51]. At high temperature, classical hopping dominates the process; but in low temperature and intermediate temperature regimes, quantum mechanics must be employed to explain the proton transfer process since tunnelling plays an important role. In this section, the dynamics of this process will be discussed along with the theoretical models used to describe it.

O-H---O ⇌ O---H-O
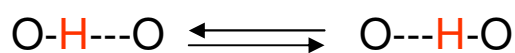
Fig 2.10 Proton transfer in hydrogen bonds.

We will discuss the proton transfer dynamics in detail based on the model system, Benzoic Acid (in Chapter 4). Here we introduce the background to proton transfer dynamics.

2.2.1 Coherent and incoherent quantum tunnelling

Particles are confined to certain regions of space because they do not have enough energy to 'escape' from that region. These regions are defined by potential energy wells on a potential energy surface comprising wells and barriers.

Quantum tunnelling is where a particle is found outside a confining potential despite it having insufficient energy to cross the barrier classically. For example, as illustrated in Fig 2.11, a particle whose kinetic energy K_E is smaller than the barrier potential P_E, according to the classical theory, should be localized in the left well; but as a matter of fact, it can be found and detected in the right well, which seems that the particle undergoes a tunnelling process. This is due to the wave nature of particles at the quantum level: there will always be a finite probability of finding the particle on the other side of the barrier unless this is infinitely high or wide. The wavefunctions of the two sides of the barrier are therefore coherent. This is *coherent quantum tunnelling*. The coherent wavefunctions will overlap in both wells. One kind of parameter is introduced in quantum theory to characterise the overlap, called *tunnelling matrix elements*,

$$\Delta_{ij} = \left\langle L,i \mid \hat{H} \mid R,j \right\rangle \tag{2.24}$$

which is the energy for tunnelling between two energy states $\left| L,i \right\rangle$ and $\left| R,j \right\rangle$. Δ^i is often used in this thesis representing the energy for tunnelling between the $\left| i \right\rangle$ states of the left and the right wells,

$$\Delta^i = \left\langle L,i \left| \hat{H} \right| R,i \right\rangle \tag{2.25}$$

It can be shown mathematically that the probability of tunnelling decreases exponentially with the height of the barrier, the width of the barrier and the square root of the mass of the particle, as in equation (2.26),

$$\Delta \propto \exp\left(-\frac{\sqrt{2mV}}{\hbar}d\right) \tag{2.26}$$

where V is the height of the barrier, and d is the barrier width.
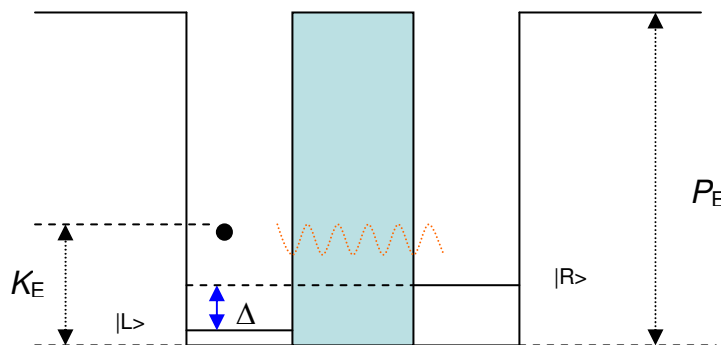
Fig 2.11 Particle tunnelling process in double wells when the kinetic energy is smaller than barrier potential energy. The particle will be found in both wells with a finite possibility. |L> and |R> are the wavefunctions in both wells which are coherent due to the quantum tunnelling. The overlap of these two wavefunctions is characterised by a parameters Δ which is called *tunnelling matrix element*. Δ is insignificant in the samples we studied. Here it is enlarged to make a clear show.

Thus tunnelling is very important for light particles such as electrons but is insignificant for heavier entities such as diatomic molecules because the probabilities involved are negligibly small. In the case of nuclear spin system, the proton atom is the lightest one rendering a significant tunnelling effect which may be observed in NMR experiments.

When the barrier is large, which applies to all the samples we studied, it turns out that coherent tunnelling is insignificant, especially in comparison with the energy asymmetry of the DMP (Double Minimum Potential). In practice, asymmetry in the environment leads to an energy asymmetry in the depths of the potential wells, Fig 2.12.

Despite the fact that coherent quantum tunnelling is suppressed and negligible in our samples, tunnelling still plays an important role especially in low temperature. So long as the system can interact with a thermal bath, the tunnelling matrix element provides a pathway for through barrier crossing; this is phonon assisted tunnelling

because the phonons provides the energy mismatch between the wells. It is an incoherent process because information on the phase of wavefunction is lost in the interaction with the environment.
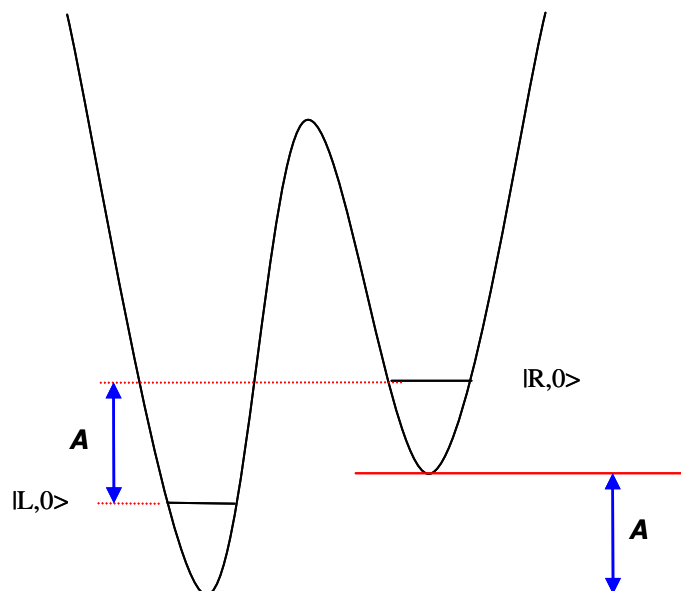
Fig 2.12 Phonon assisted tunnelling process in asymmetric DMP. *A* is the energy asymmetry. The coherent tunnelling process is suppressed and the tunnelling matrix element Δ^0 is too small in comparison with the energy asymmetry *A* to be illustrated in the figure.

For phonons to be available to mediate the process, the energy asymmetry must be generally be smaller than the Debye frequency ω_D.

2.2.2 Proton transfer rate and ST model in small energy asymmetry

As discussed above, the tunnelling in the asymmetric DMP is dominated by incoherent process. At low temperature, an assumption was made by Skinner and Trommsdorff [5] that only the two ground states of the DMP are populated (It's also implicit that the energy asymmetry *A* is smaller that the Debye cut-off energy), then the low temperature tunnelling rate Γ^{LT} can be calculated as the sum of the upward and downward rates which are shown in Fig 2.13.
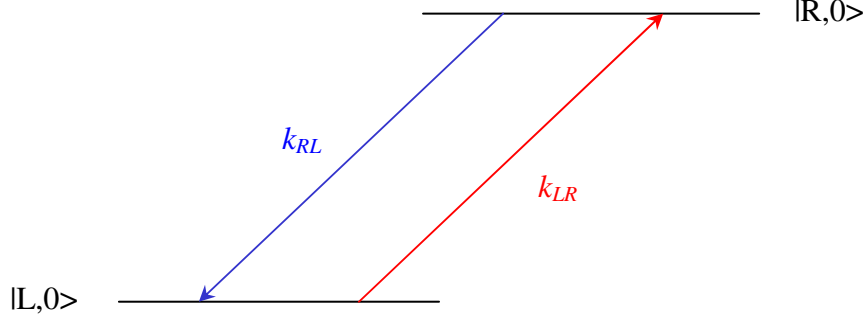
Fig 2.13 Random hopping between two ground states. k_{RL} and k_{LR} are the 'downward' tunnelling rate and the 'upward' tunnelling rate respectively.

At thermal equilibrium, detailed balance applies so we have

$$k_{RL} / k_{LR} = \exp\left(A / k_B T\right) \tag{2.27}$$

together with

$$\Gamma^{LT} = k_{RL} + k_{LR} \tag{2.28}$$

It can be shown that

$$\Gamma^{LT} = k_0 \coth\left(\frac{A}{2k_B T}\right) \tag{2.29}$$

where $k_{RL} = \dfrac{k_0 \exp\left(A / k_B T\right)}{\exp\left(A / k_B T\right) - 1}$, $k_{LR} = \dfrac{k_0}{\exp\left(A / k_B T\right) - 1}$. The 'downward' tunnelling rate

k_{RL} has contributions from both simulated and spontaneous one-phonon emissions and therefore has a finite value at $T = 0$K, while the 'upward' tunnelling rate k_{LR} vanishes as the temperature approaches zero. k_0 is the incoherent tunnelling rate constant, which can be written as:

$$k_0 = c_p^2 \frac{3\pi}{2} \left(\frac{\Delta}{\hbar \omega_D}\right)^2 \frac{A}{\hbar} \tag{2.30}$$

where Δ is the tunnelling matrix element as described in equation (2.25), and c_p is the phonon coupling constant. The incoherent tunnelling rate constant k_0 is therefore proportional to the square of the tunnelling matrix element.

As the temperature rises, the excited states of the DMP become occupied, and the measured tunnelling rate will be faster since new tunnelling pathways become

available, Fig 2.14. If the first excited states are taken into account, that is to say, if the two ground states and two excited states are considered, the low temperature tunnelling rate can be written as follows [34]:

$$\Gamma^{LT} = \frac{k_0 + k_1 \exp(-V_{exc} / k_B T)}{1 + \exp(-V_{exc} / k_B T)} \coth\left(\frac{A}{2k_B T}\right) \tag{2.31}$$

where k_1 is the incoherent tunnelling rate constant for the first excited states, V_{exc} is the mean energy difference between levels $|L,0\rangle, |L,1\rangle$ and $|R,0\rangle, |R,1\rangle$. The equation (2.31) will reveal the importance of excited state tunnelling in describing the intermediate temperature range.
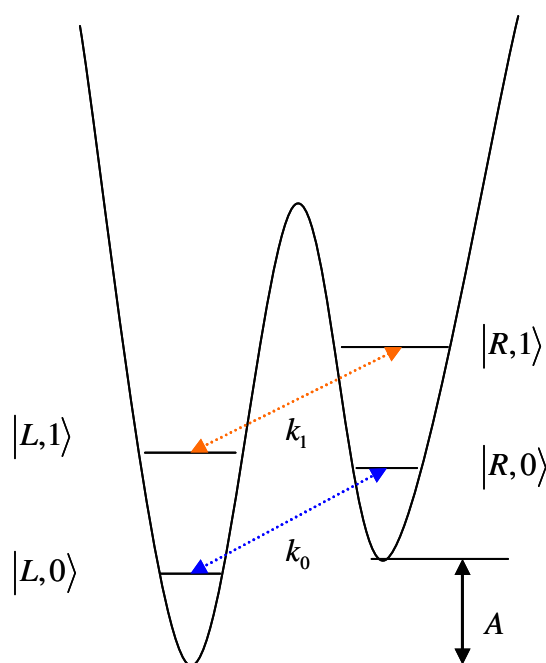
Fig 2.14 Tunnelling pathways (excited states) become available when the temperature rises.

At high temperatures, there is tunnelling via multiple states in the wells and the behaviour resembles classical barrier hopping. Therefore, the expression for the high temperature proton transfer rate is easily derived from the Arrhenius law:

$$\Gamma^{HT} = \tau_0^{-1}\left[\exp\left(-\frac{V}{k_B T}\right) + \exp\left(-\frac{V - A}{k_B T}\right)\right] \tag{2.32}$$

where V is high temperature activation energy, τ_0 is the correlation time at infinite temperature.

Consequently the expression for the correlation rate for the small energy asymmetry A is

$$\tau_c^{-1} = \Gamma^{LT} + \Gamma^{HT}$$

$$= \frac{k_0 + k_1 \exp(-V_{exc}/k_B T)}{1 + \exp(-V_{exc}/k_B T)} \coth\left(\frac{A}{2k_B T}\right) + \tau_0^{-1}\left[\exp\left(-\frac{V}{k_B T}\right) + \exp\left(-\frac{V-A}{k_B T}\right)\right] \quad (2.33)$$

The correlation rate τ_c^{-1} characterizes the molecular dynamics, next we establish how it can be measured directly from the spin-lattice relaxation time T_1. The expression for T_1 depends on the sample. For example, powder sample or single crystal, homonuclear or heteronuclear samples, will have different T_1 expressions. First, the homonuclear spin-lattice relaxation time T_1 expressions will be introduced.

2.3 Homonuclear spin-lattice relaxation

In NMR, spin-lattice relaxation is governed by random fluctuation in the magnetic interactions experienced by the nuclei. Random fluctuations in the proton-proton dipolar interaction dominate the relaxation processes in proton-rich molecules in the solid state. For a homonuclear $I = \frac{1}{2}$ spin system, there are only two spin states for single spin: $M_I = +\frac{1}{2}$ ($|\alpha>$) and $M_I = -\frac{1}{2}$ ($|\beta>$); there are four spin states for dipolar coupled spins: $|\alpha\alpha>$, $|\alpha\beta>$, $|\beta\alpha>$ and $|\beta\beta>$ as shown in Fig 2.15.

The four spin states are degenerate in the absence of a magnetic field. But when they are in the magnetic field, the degeneracy will be broken. The energy levels are shown in Fig 2.15. It is evident that the transitions between energy levels |1> and |3> or between |2> and |4> will introduce single spin flips while the transitions between |1> and |4> or between |2> and |3> will introduce two spin flips.
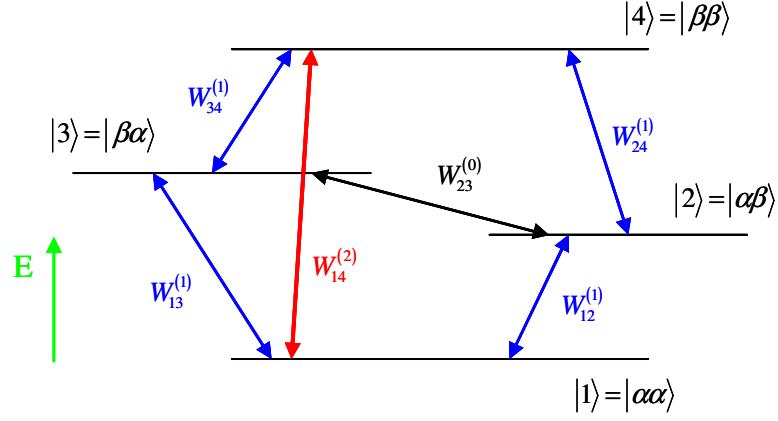
Fig 2.15 Energy levels and spin flipping in the dipolar interaction system.

The dipolar Hamiltonian can be written as

$$\hat{H}_{dd} = \sum_{m=-2}^{m=2} A^{(m)} \bullet F^{(m)} \tag{2.34}$$

where $A^{(m)}$ and $F^{(m)}$ are tensors representing the spin and spatial variables respectively.

This can be written in a well-known 'alphabet' form [24, 27]:

$$\hat{H}_{dd} = \eta(A + B + C + D + E + F) \tag{2.35}$$

The terms A to F are given explicitly as follows:

$$A = -\hat{I}_z^{(1)}\hat{I}_z^{(2)}\left(3\cos^2\theta - 1\right) \tag{2.36}$$

$$B = \frac{1}{4}\left[\hat{I}_+^{(1)}\hat{I}_-^{(1)} + \hat{I}_-^{(1)}\hat{I}_+^{(1)}\right]\left(3\cos^2\theta - 1\right) \tag{2.37}$$

$$C = -\frac{3}{2}\left[\hat{I}_z^{(1)}\hat{I}_+^{(2)} + \hat{I}_z^{(2)}\hat{I}_+^{(1)}\right]\sin\theta\cos\theta\exp(-i\phi) \tag{2.38}$$

$$D = -\frac{3}{2}\left[\hat{I}_z^{(1)}\hat{I}_-^{(2)} + \hat{I}_z^{(2)}\hat{I}_-^{(1)}\right]\sin\theta\cos\theta\exp(i\phi) \tag{2.39}$$

$$E = -\frac{3}{4}\hat{I}_+^{(1)}\hat{I}_+^{(2)}\sin^2\theta\exp(-2i\phi) \tag{2.40}$$

$$F = -\frac{3}{4}\hat{I}_-^{(1)}\hat{I}_-^{(2)}\sin^2\theta\exp(2i\phi) \tag{2.41}$$

where θ is the angle between the vector joining the two nuclei and the magnetic field. The common factor η is known as the dipolar coupling constant and is given by

$$\eta = \frac{\mu_0\gamma_1\gamma_2\hbar^2}{4\pi r^3} \tag{2.42}$$

where r is the internuclear distance.

In the dipolar Hamiltonian, the term A contains no spin flip operators; term B contains flip-flop operators which flip one spin up and simultaneously flip the other one down. Neither will change the population of spin states for homonuclear systems, they are secular, contributing only to the frequency of the lines in the NMR spectrum. The terms C and D contain spin operators, which can flip a single nuclear spin. The terms E and F contain spin operators, which can flip two nuclear spins.

Spin-lattice relaxation is driven by fluctuations in the dipolar interactions between nuclei labelled k and l,

$$T_1^{-1} = \frac{1}{8N} \sum_{k \neq l} \left[J_{kl}^{(1)}(\omega) + 4 J_{kl}^{(2)}(2\omega) \right] \tag{2.43}$$

The sum extends to over all proton pairs in the sample containing N protons.

The correlation function representing random fluctuations in the dipolar interactions arising from molecular motion is defined by

$$G(\tau) = \left< F^{(m)^*}(t+\tau) F^{(m)}(t) \right> \tag{2.44}$$

The Fourier transform of the correlation function $J^{(m)}(\omega)$ is known as the spectral density function:

$$J^{(m)}(\omega) = \int_{-\infty}^{+\infty} G(\tau) \exp(-\omega\tau) d\tau \tag{2.45}$$

Therefore it is evident that the terms C and D contribute to the spectral density term $J(\omega)$ and the terms E and F give rise to a spectral density term $J(2\omega)$.

In the weak collision regime, where $\tau_c \ll T_1$, evaluating the correlation functions, the spin-lattice relaxation rate in the applied magnetic field $\mathbf{B}$, where Larmor frequency $\omega = \gamma B$, is finally given as follows for a powder sample (the full derivation can be found in [52,53,54]):

$$T_1^{-1}(\omega,T) = C_D \operatorname{sech}^2 \left(\frac{A}{2k_B T} \right) \left[\frac{\tau_c}{1+\omega^2\tau_c^2} + \frac{4\tau_c}{1+4\omega^2\tau_c^2} \right] \tag{2.46}$$

Since we record the magnetic dependence of T_1^{-1}, it is more convenient for analysing experimental data to express the relaxation rate in terms of magnetic field $\boldsymbol{B}$. It is rewritten as

$$T_1^{-1}(B,T) = \frac{1}{\gamma} C_D \operatorname{sech}^2\left(\frac{A}{2k_B T}\right)\left[\frac{1}{1/\gamma\tau_c + \gamma\tau_c B^2} + \frac{4}{1/\gamma\tau_c + 4\gamma\tau_c B^2}\right] \tag{2.47}$$

In equations (2.46) and (2.47), C_D is the dipolar constant and is a function of geometry of the system, A is the energy asymmetry of the DMP and τ_c is the correlation time at the temperature T. The fit of the experimental data to the equation (2.47) gives rise to two crucial parameters which characterise the molecular quantum dynamics. One is $a = \frac{1}{\gamma} C_D \operatorname{sech}^2\left(\frac{A}{2k_B T}\right)$, may be applied to determine the dipolar constant C_D and energy asymmetry A; the other one is $b = 1/\gamma\tau_c$, directly leads to the measurement of correlation rate τ_c^{-1}. We will discuss these later in the experimental chapter.

With Equation (2.47), if we plot T_1^{-1} against magnetic field, we can map out the spectral density function directly as the black curve shown in Fig 2.16. The spin lattice relaxation rate is a sum of two Lorentzian lineshapes centered at zero frequency, $L(\omega)$ and $L(2\omega)$, which are the blue and red curve respectively. The linewidths are determined by the inverse correlation time. The two Lorentzians have amplitudes in the ratio 1:4 and linewidths in the ratio 2:1. To explore the magnetic field dependence of T_1^{-1}, we employ field-cycling techniques.
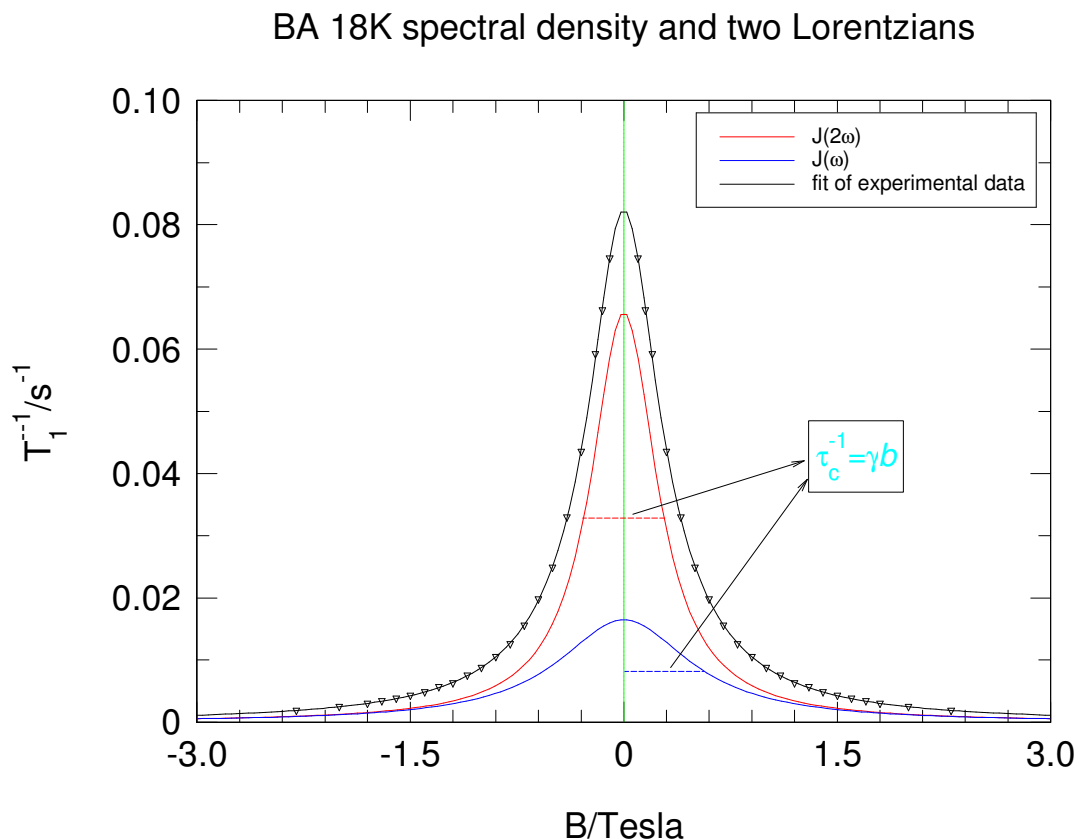
Fig 2.16 The spectral density curve measured in BA 18K to show that the two Lorentzians have amplitudes in the ratio 1:4 and linewidths in the ratio 2:1.

The half-width at half-maximum of $L(\omega)$ is τ_c^{-1} and the full width at half-maximum of $L(2\omega)$ is also τ_c^{-1}, so the spectral density provides a direct measurement of the proton transfer rate from a determination of the width of the spectrum. For the case in Fig 2.16, the correlation rate for sample BA (benzoic acid) at 18K is $\tau_c^{-1} = (1.507 \pm 0.004) \times 10^8 \, s^{-1}$. As we discussed above, the correlation rate τ_c^{-1} plays a vital role on studying the molecular quantum dynamics, in low temperature regime, τ_c^{-1} characterises the tunnelling process and determines the tunnelling rate, while in the high temperature regime, it characterises pseudo-classical 'Arrhenius' process. Therefore the field-cycling NMR becomes a reliable and effective technique in the study of molecular quantum dynamics. The most important feature of field-cycling NMR is its ability to map out the spectral density directly. In comparison with field-cycling NMR technique, it is more difficult or even impossible to directly measure the frequency dependence of the spin-lattice relaxation rate with many other NMR techniques due to their invariable magnetic field.

2.4 Heteronuclear dipolar interaction

We have discussed the role of homonuclear dipolar interactions in section *2.3*. However, not only do many samples naturally contain multiple magnetic nuclei, but also in the study of complex systems of biological interest, for example, isotopic labelling and deuteration may be used to discriminate different functional sites. Therefore dipolar interactions between different nuclear species can become important to the spin-lattice relaxation behaviour. The information related to the heteronuclear interaction is of significance to improve our understanding of the dynamics in the heteronuclear system in chemical and biological reactions.

The system chosen for introducing the theory of heteronuclear interaction is a two spin-½ heteronuclear species system. The heteronuclear spins are labelled as spin *I* and spin *S*. Due to the fact that the lightest atom, the proton, experiences the largest quantum effect and it is one of the most important atoms in biological and chemical reactions, the proton is one of the two spin species in the heteronuclear system we investigate and is labelled as spin *I*.

Each spin nucleus in the heteronuclear system possesses a thermal reservoir associated with its Zeeman energy (Fig 2.17). There are some different mechanisms for the interactions between the two spin species, such as dipole-dipole coupling, *J*-coupling, and spin-rotation interaction. Dipole-dipole coupling is the dominant interaction for the solid state samples studied in this thesis. Mutual interactions between the two spin species give rise to a coupling of the reservoirs and their spin-lattice relaxation behaviour is therefore interdependent. The typical structure for heteronuclear dipole-dipole coupling in context of proton transfer in hydrogen bonds is illustrated in Fig 2.18.
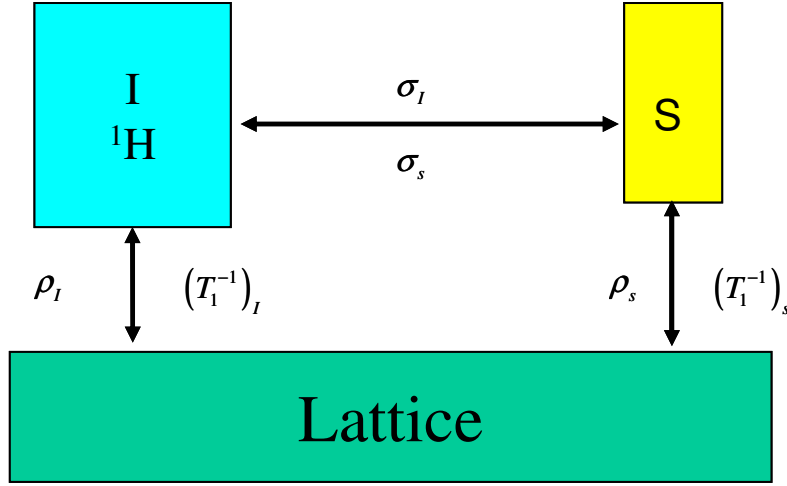
Figure 2.17 Spin I and spin S thermal reservoirs with their Zeeman energies and the coupling among the reservoirs (two spin thermal reservoirs and lattice reservoir).
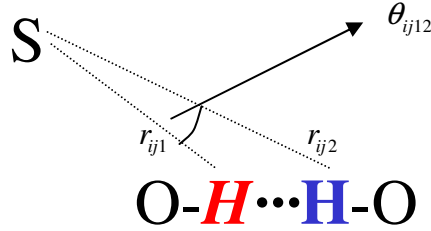
Fig 2.18 Geometry of two spin species interacting. The proton, labelled I, occupies a hydrogen bond. A second spin S acts as an observer of the proton transfer. The dash lines are distances between spin I and spin S**.**

The spin relaxation due to dipole-dipole coupling interaction has been established. The differential equations governing the longitudinal polarisations $\langle I_z \rangle$ and $\langle S_z \rangle$ are given by the Solomon equations [55]

$$
\begin{bmatrix} \dfrac{d}{dt}\langle I_z \rangle \\ \dfrac{d}{dt}\langle S_z \rangle \end{bmatrix} = - \begin{pmatrix} \rho_I & \sigma_I \\ \sigma_S & \rho_s \end{pmatrix} \begin{bmatrix} \langle I_z \rangle - I_0 \\ \langle S_z \rangle - S_0 \end{bmatrix}
\tag{2.48}
$$

where I_0 and S_0 are the magnetisations of spin I nuclei and spin S nuclei respectively at thermal equilibrium. The elements of the relaxation matrix, $\mathbb{R} = \begin{pmatrix} \rho_I & \sigma_I \\ \sigma_S & \rho_s \end{pmatrix}$, are inverse spin-lattice relaxation times defined in terms of spectral density contributions sampled at the Larmor frequencies of spin I and spin S (ω_I and ω_s respectively) , and

also the sums and differences of the two. Notice, whereas for a homonuclear system, there is only one characteristic relaxation rate, for a heteronuclear system there are four elements of a spin-relaxation matrix.

For heteronuclear interactions in a powder sample the elements of $\mathbb{R}$ have the form:

$$\rho_I^{IS} = C_{IS} \frac{4a}{(1+a)^2} \left(L(\omega_I - \omega_S, \tau_C) + 3L(\omega_I, \tau_C) + 6L(\omega_I + \omega_S, \tau_C) \right)$$

$$\sigma_I^{IS} = C_{IS} \frac{4a}{(1+a)^2} \left(-L(\omega_I - \omega_S, \tau_C) + 6L(\omega_I + \omega_S, \tau_C) \right)$$

$$\sigma_S^{IS} = C_{IS} \frac{4a}{(1+a)^2} \left(-L(\omega_I - \omega_S, \tau_C) + 6L(\omega_I + \omega_S, \tau_C) \right)$$

(2.49)

$$\rho_S^{IS} = C_{IS} \frac{4a}{(1+a)^2} \left(L(\omega_I - \omega_S, \tau_C) + 3L(\omega_S, \tau_C) + 6L(\omega_I + \omega_S, \tau_C) \right)$$

Here, $L(\omega, \tau_C) = \dfrac{\tau_C}{1 + \omega^2 \tau_C^2}$ is a Lorentzian with half-width at half-maximum amplitude equal to the inverse correlation rate τ_C^{-1}, and $a = \exp(A/k_B T)$ where A is the energy asymmetry of DMP. C_{IS} is the lattice sum of dipolar interactions,

$$C_{IS} = \frac{\gamma_I^2 \gamma_S^2 \hbar^2}{40} \left(\frac{\mu_0}{4\pi} \right)^2 \sum_{i,j} \left[r_{ij1}^{-6} + r_{ij2}^{-6} + r_{ij1}^{-3} r_{ij2}^{-3} \left(1 - 3\cos^2 \theta_{ij12} \right) \right]$$

(2.50)

γ_I and γ_S are the respective magnetogyric ratios and the sum involves spin S (labelled j) interacting with spin I atoms (labelled i) which undergo proton transfer. The geometrical parameters are defined in Fig 2.18.

Homonuclear spin I- spin I (^1H -- ^1H) interactions also contribute to ρ_I since proton-proton interactions will also modulated by the motion. For a powder sample,

$$\rho_I^{II} = C_{II} \frac{4a}{(1+a)^2} \left(L(\omega_I, \tau_C) + 4L(2\omega_I, \tau_C) \right)$$

(2.51)

where

$$C_{II} = \frac{3\gamma_I^4 \hbar^2}{40} \left(\frac{\mu_0}{4\pi} \right)^2 \sum_{k,j} \left[r_{kj1}^{-6} + r_{kj2}^{-6} + r_{kj1}^{-3} r_{kj2}^{-3} \left(1 - 3\cos^2 \theta_{kj12} \right) \right] \frac{1}{N}$$

(2.52)

which is a lattice sum involving the dipolar contacts of all protons (labelled k), with the hydrogen bond protons (labelled j) which undergo proton transfer. N is the number of protons contributing to the homonuclear dipole-dipole interactions.

Normally the relaxation in this kind of heteronuclear system is dominated by two symmetry related intra-dimer dipolar contacts with two dynamic protons. The homonuclear spin S interactions are insignificant and negligible.

Summing heteronuclear and homonuclear contributions, the overall relaxation may now be characterised by the matrix,

$$\mathbb{R} = \begin{pmatrix} \rho_I & \sigma_I \\ \sigma_S & \rho_s \end{pmatrix} = \begin{pmatrix} \rho_I^{IS} + \rho_I^{II} & \sigma_I^{IS} \\ \sigma_S^{IS} & \rho_S^{IS} \end{pmatrix} \tag{2.53}$$

The general solution of (2.48) describing the magnetisation recovery following a disturbance away from equilibrium is a weighted sum of two exponentials for each nuclear species [43, 48, 55],

$$\langle I_z \rangle = I_0 \left(c_1^I \exp(-R_1 t) + c_2^I \exp(-R_2 t) \right) + I_0$$

$$\langle S_z \rangle = S_0 \left(c_1^S \exp(-R_1 t) + c_2^S \exp(-R_2 t) \right) + S_0 \tag{2.54}$$

Where the weighting coefficients c are functions of R_1, R_2 and $\mathbb{R}$, determined by the magnetisation state of each reservoir at time $t = 0$, namely the spin temperatures of the two reservoirs associated with the two nuclear species. The spin-lattice relaxation rates R_1 and R_2 are eigenvalues of $\mathbb{R}$. These have the following functional form obtained by diagonalization of the relaxation matrix:

$$R_{1,2} = \frac{1}{2} \left[(\rho_I + \rho_s) \pm \sqrt{(\rho_I + \rho_s)^2 - 4(\rho_I \rho_s - \sigma_I \sigma_S)} \right] \tag{2.55}$$

The foregoing analysis highlights two consequences for the spin-lattice relaxation of both spin I and spin S species:

- The spectral density is sampled at multiple frequencies.
- In general, the magnetisation recovery curves will be biexponential.

Analytical expressions for the weighting coefficients can be determined under certain idealised initial conditions for the magnetisation states of the two spin species.

- Initial condition 1: when $t = 0$, $\langle I_z \rangle = I_0$ and $\langle S_z \rangle = 0$. (the spin S nuclei are saturated but the spin I nuclei are not).

$$\begin{cases} c_1^S = \dfrac{\rho_I - R_1}{R_1 - R_2} \\[3mm] c_2^S = \dfrac{R_2 - \rho_I}{R_1 - R_2} \end{cases} \qquad\qquad \begin{cases} c_1^I = -\dfrac{\sigma}{R_1 - R_2}\dfrac{S_0}{I_0} \\[3mm] c_2^I = \dfrac{\sigma}{R_1 - R_2}\dfrac{S_0}{I_0} \end{cases} \qquad (2.56)$$

- Initial condition 2: when $t = 0$, $\langle I_z \rangle = 0$ and $\langle S_z \rangle = 0$ (both the two kinds of nuclei are saturated at their resonance field).

$$c_1^S = \frac{\rho_I - R_1}{R_1 - R_2}\left[\frac{I_0}{\sigma S_0}(\rho_I - R_2) + 1\right] \quad c_2^S = -1 - \frac{\rho_I - R_1}{R_1 - R_2}\left[\frac{I_0}{\sigma S_0}(\rho_I - R_2) + 1\right]$$

$$c_1^I = \frac{\rho_S - R_1}{R_1 - R_2}\left[\frac{S_0}{\sigma I_0}(\rho_S - R_2) + 1\right] \quad c_2^I = -1 - \frac{\rho_S - R_1}{R_1 - R_2}\left[\frac{S_0}{\sigma I_0}(\rho_S - R_2) + 1\right]$$

$$(2.57)$$

Clearly the coefficients c_1^S, c_2^S, c_1^I and c_2^I depend on the initial conditions as shown in equations (2.56) and (2.57). However, according to equation (2.55), R_1 and R_2 depend on the temperature and magnetic field (or resonance frequency), but not on the initial conditions of the two nuclear species magnetisation. Significantly the spin-lattice relaxation is characterised by two relaxation rates R_1 and R_2. It means that traditional data analysing techniques must be modified for the heteronuclear spin systems; also there are significant consequences affecting the methodology of field-cycling relaxometry.

It is evident that the heteronuclear system has more information on the molecular dynamics. This can be advantageous since the spectral density function is sampled at multiple frequencies, but it is also more complicated than the homonuclear system and leads to more complex behaviour requiring a more complex interpretation and analysis of the experimental data. How to record and analyse the experimental data is a challenge. We will discuss this problem later in the experimental chapters.

2.5 Nuclear quadrupolar interaction in Solids

One of the systems studied in this thesis contained quadrulpoar nuclei. The quadrupolar nuclear energy level structure was probed by proton field-cycling NMR. Effectively, the quadrupolar system acted as a relaxation sink for ^{1}H Zeeman energy. Here the nuclear quadrupole interaction will be introduced [27, 56, 57].

The electric quadrupole moment Q is an intrinsic nuclear property. It can interact with the electric field gradient q governed by the surrounding electrostatic potential. The origin of this interaction is illustrated in Fig 2.19, where the electric field gradient is generated by point positive charges. It is clear that the orientation of Fig 2.19 (a) has a lower energy than that of Fig 2.19 (b) and will be energetically more favourable. Since each quadrupolar nucleus has a magnetic moment, this ordering produces a magnetic polarization in crystal, in a similar way to that produced by a magnetic field.

If $e\rho_n$ is the nuclear charge density, the quadrupole moment of such charge distributions may be defined by the equation

$$eQ = e\int \rho_n \left(3z^2 - r^2\right)dr \qquad (2.58)$$

(a)   (b)
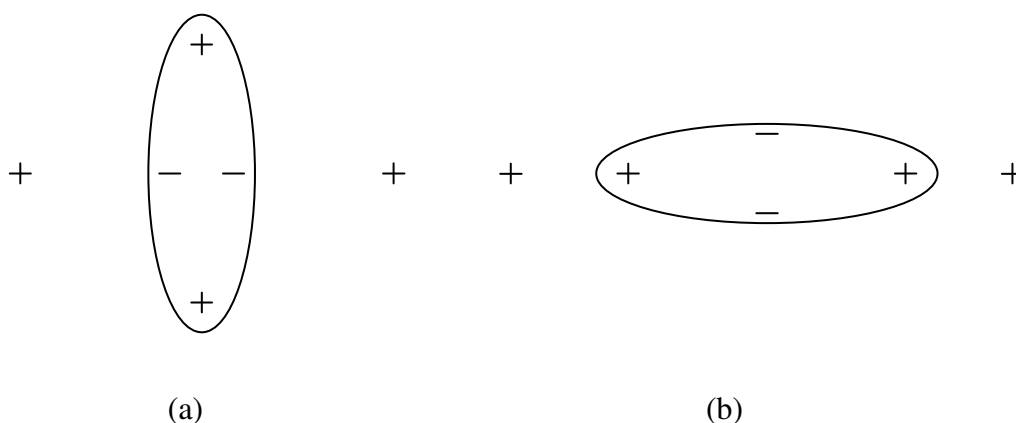
Fig 2.19 Two orientations for an electric quadrupole moment in the electric field gradient of a pair of point positive charges.

It is only non-zero if the nuclear spin quantum number $I \geq 1$, so ^{1}H is non-quadrupolar, but ^{14}N ($I = 1$) and ^{35}Cl ($I = 3/2$) are.

The electric field gradient, q, at a nuclear site arises from the electronic charge distribution in atoms, and from both electrons and neighbouring nuclei in molecules. q may be defined as a tensor,

$$q = \begin{pmatrix} q_{xx} & q_{xy} & q_{xz} \\ q_{yx} & q_{yy} & q_{yz} \\ q_{zx} & q_{zy} & q_{zz} \end{pmatrix} \tag{2.59}$$

It is always possible to find a set of axes, known as the principal axes, in which all non-diagonal matrix elements are zero and only q_{xx}, q_{yy} and q_{zz} finite. We use the common convention that

$$|q_{zz}| \geq |q_{yy}| \geq |q_{xx}| \tag{2.60}$$

and they can be described as below

$$q_{zz} = -\int\limits_{electrons} \psi^* \left(\frac{3\cos^2\theta - 1}{r^3} \right) \psi d\tau + \sum_{nuclei} Z_i \left(\frac{3\cos^2\theta_i - 1}{R_i^3} \right)$$

$$q_{yy} = -\int\limits_{electrons} \psi^* \left(\frac{3\cos^2\theta\sin^2\phi - 1}{r^3} \right) \psi d\tau + \sum_{nuclei} Z_i \left(\frac{3\cos^2\theta_i\sin^2\phi_i - 1}{R_i^3} \right) \tag{2.61}$$

$$q_{xx} = -\int\limits_{electrons} \psi^* \left(\frac{3\cos^2\theta\cos^2\phi - 1}{r^3} \right) \psi d\tau + \sum_{nuclei} Z_i \left(\frac{3\cos^2\theta_i\cos^2\phi_i - 1}{R_i^3} \right)$$

It is customary to set

$$q_{zz} = q \tag{2.62}$$

and it is usual to define an asymmetry parameter η by the equation

$$\eta = (q_{xx} - q_{yy})/q_{zz} \tag{2.63}$$

Now we can derive the energy of interaction of a nuclear electric quadrupole moment in the electric field gradient of an external charge distribution — the so-called quadrupolar Hamiltonian [24, 27, 56]. The energy operator $\hat{H}_Q$ is

$$\hat{H}_Q = \frac{e^2 qQ}{4I(2I-1)} \left\{ 3\hat{I}_z^2 - I(I+1) + \frac{\eta}{2}(\hat{I}_+^2 + \hat{I}_-^2) \right\} \tag{2.64}$$

in which $\hat{I}_z$, $\hat{I}_+$ and $\hat{I}_-$ are nuclear spin operators. $\hat{I}_\pm = \hat{I}_+ \pm i\hat{I}_y$. The solutions of equation (2.64) depend on the nuclear spin quantum number I.

For spin-1 nuclei, the actual eigenstates are linear combinations of the m_I sub-states |1>, |0>, |-1> and are given by

$$y = \frac{1}{\sqrt{2}}(|1> + |-1>) \qquad E_y = \frac{1}{4}(e^2qQ)(1+\eta)$$

$$x = \frac{1}{\sqrt{2}}(|1> - |-1>) \qquad E_x = \frac{1}{4}(e^2qQ)(1-\eta) \qquad (2.65)$$

$$z = |0> \qquad E_z = -\frac{1}{2}(e^2qQ)$$

There are three transitions allowed, Fig 2.20, with frequencies

$$\nu_x = \frac{3}{4}(e^2qQ/h)(1+\frac{\eta}{3})$$

$$\nu_y = \frac{3}{4}(e^2qQ/h)(1-\frac{\eta}{3}) \qquad (2.66)$$

$$\nu_z = \frac{1}{2}(e^2qQ/h)\eta$$

For $I = \frac{3}{2}$, the eigenstates also are suitable linear combinations of the m_I sub-states $|+\frac{3}{2}>, |+\frac{1}{2}>, |-\frac{1}{2}>, |-\frac{3}{2}>$; The energies are

$$E_{\pm\frac{3}{2}} = \frac{1}{4}(e^2qQ)\left(1+\frac{\eta^2}{3}\right)^{\frac{1}{2}}$$

$$\qquad (2.67)$$

$$E_{\pm\frac{1}{2}} = -\frac{1}{4}(e^2qQ)\left(1+\frac{\eta^2}{3}\right)^{\frac{1}{2}}$$

there are two transitions allowed, but only one frequency is observed, Fig 2.21,

$$\nu_Q = \frac{1}{2}(e^2qQ/h)\left(1+\frac{\eta^2}{3}\right)^{\frac{1}{2}} \qquad (2.68)$$

In both cases there is a zero-field splitting of the nuclear sub-states. In pure NQR (Nuclear Quadrupole Resonance) the transitions are driven directly in zero (or very small) magnetic field.
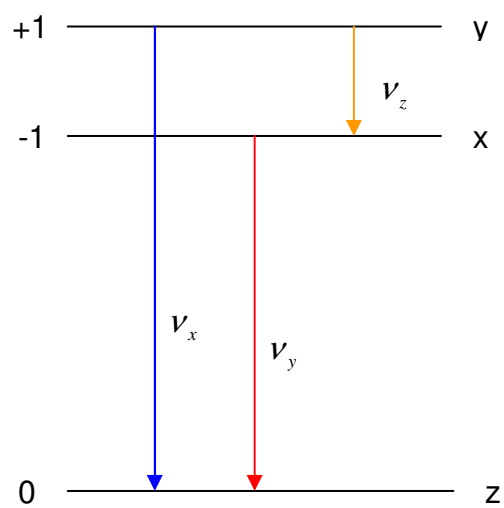
Fig 2.20 Energy level diagram for a spin-1 nucleus in zero field.
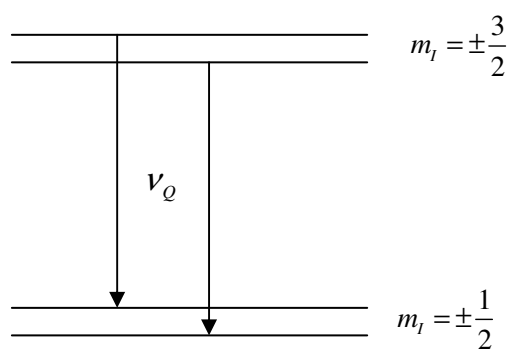
Fig 2.21 Energy level diagram for a spin-$\frac{3}{2}$ nucleus in zero field.

Chapter 3: Experimental

The majority of NMR spectrometers in the world are fixed field instruments. However there are significant advantages to study NMR phenomena as a function of magnetic field. To achieve this, we have adopted a magnetic field-cycling approach [17, 20, 21, 22, 58]. Field-cycling relaxometry is the only NMR technique that effectively enables one to investigate the frequency dependence of spin-lattice relaxation rate and cover several decades of frequency with the same instrument. This feature makes field-cycling relaxometry a most powerful tool for the study of molecular dynamics in complex systems.

In this chapter we will give a description of our field-cycling spectrometer and how it works. Here we give a brief description of the hardware and the software, which is indispensable to understand the whole system. In the description we will introduce the modifications we have made in hardware, software and experimental methods in carrying out the research in this thesis. The modifications include:

- modification of the probe and RF coils to improve the signal quality, to minimize the *dead time* and to choose an appropriate Q factor which is a compromise between the signal quality and frequency profile.

- modification of the magnetic field quenching detection program to protect the magnetic coil in case of a *quench*.

- modification and automation of a field offset to minimize the effect of magnetic field instability.

- modification of the time limit to tune or polarize the long T_1 sample easily and run a set of polarisation experiments automatically.

- modification of the measurement pulse amplitude to avoid the signal saturation at high field or low temperature.

- development of new pulse sequences to investigate spin-lattice relaxation in heteronuclear systems.

Finally in this chapter, we will discuss the experimental details of tuning the spectrometer, the T_1 experiment and low field experiment. The curve fitting of the experimental data will also be introduced as well as the simulation of experimental data.

3.1 Field-cycling NMR spectrometer
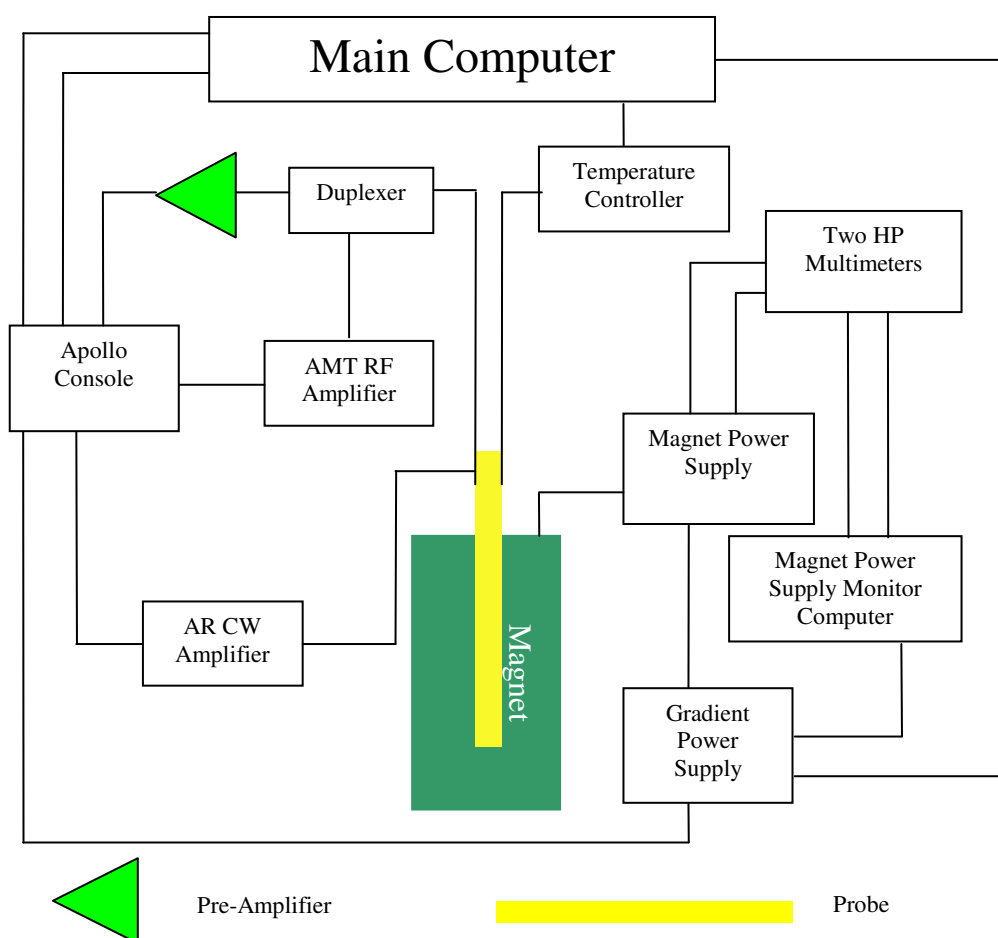
Fig 3.1 A schematic of the new state of art field-cycling system.

Our new state-of-art field-cycling NMR spectrometer has a field switching rate of 10T/s in the range of magnetic field 0-2.5T. A built-in cryostat provides a wide temperature range 4K-325K. Therefore, we can directly map out the field/frequency dependence of the spin-lattice relaxation rate, namely the spectral density as a

function of temperature. The fast test spin-lattice relaxation time that can be measured is in the order of 100ms. With the ability to map out the spectral density, the rate of molecular dynamics is directly determined. With the fast field switching, many faster T_1 experiments and other new experiments such as NQR which need fast field switching to minimize the magnetisation relaxation during the field switch become possible. A schematic diagram of the system is shown in Fig 3.1.

3.1.1 Magnet, cryostat and magnet power supply
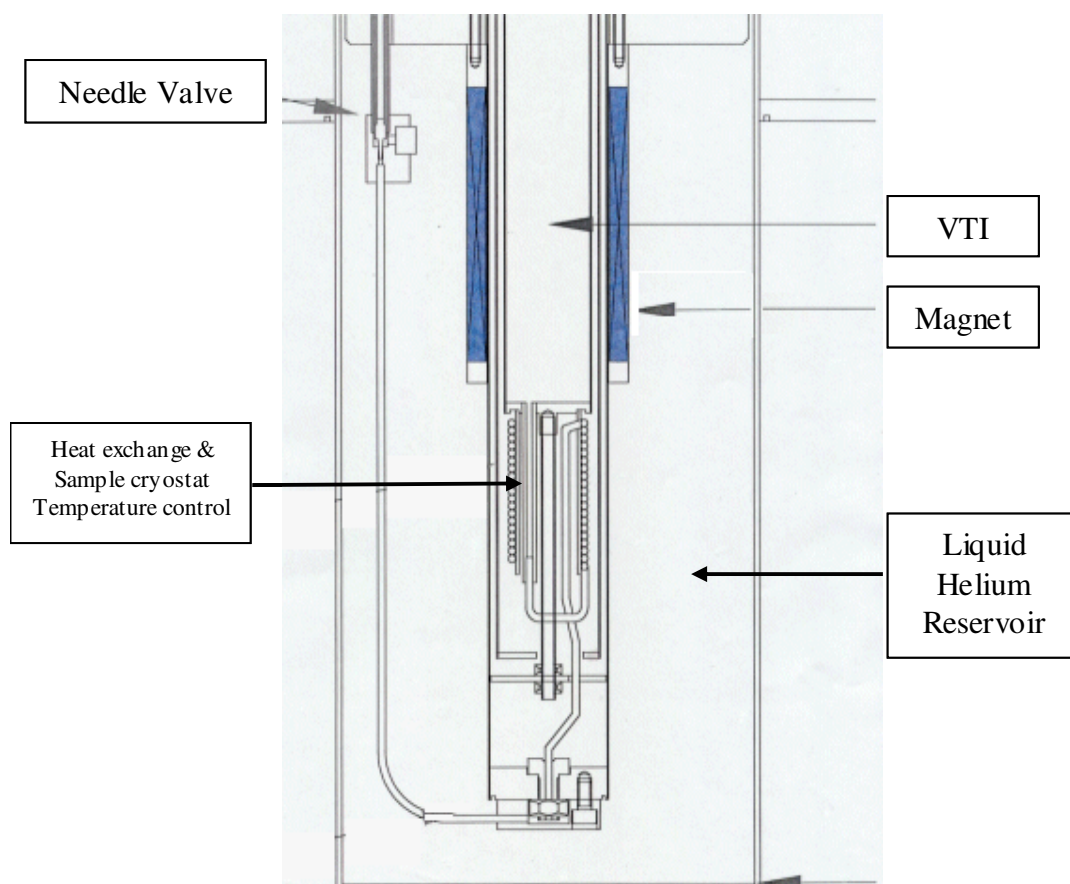
Fig 3.2 The structure of magnet and cryostat**.**

A diagram of the superconducting magnet and the low temperature cryostat is shown in Fig 3.2. The superconducting magnet is situated inside a helium bath cryostat (4.2K). The liquid helium bath is itself insulated by a large reservoir of liquid nitrogen (77K). The reservoirs are separated from each other, and from the outside environment, by evacuated barriers, in order to reduce thermal leakage. A variable temperature insert (VTI) is situated inside the cold bore of the magnet to provide a

variable temperature environment for the sample, $4.2 \leq T \leq 300\,\mathrm{K}$. The helium is drawn through a needle valve from the main helium bath to cool the sample. A heater and temperature controller are employed to stabilise the desired sample temperature (long term stability and accuracy is 0.05K for T < 100K and less than 1% for T > 100K).

The superconducting magnet is designed with a low inductance superconducting solenoid to allow fast field ramping and with high current operating mode to achieve high field. Unlike conventional NMR magnets, the solenoid in our system has no persistent mode switch and must be permanently connected to the magnet power supply by leads that carry not only the current but also heat from outside into the magnet; therefore the instantaneous magnetic field is proportional to the instantaneous current.

There always are some requirements for the NMR magnet, as follows:
- a good cooling efficiency permitting the high current densities needed for high fields
- a good field homogeneity (that is, the relative field variation in the sample volume should not exceed the stability and reproducibility of the detection field.)
- large room temperature bore diameters and large sample volumes (the signal sensitivity is proportional to the sample size).

The energy stored in the field of a gas-core magnet coil is given by

$$E = \frac{1}{2\mu_0} \int_{space} B^2 d\boldsymbol{r} \,, \tag{3.1}$$

where the integral covers the whole space over which the magnetic field is spread. This is the amount of energy that has to be cycled into and out of the magnet as fast as possible. Since a magnet with a smaller total field energy is easier to be cycled fast than a larger one, it is therefore important to minimize the total field energy while retaining large peak flux densities in the sample. So another requirement for the NMR magnet is that the magnet coil should be as compact as possible. It is in conflict with the three requirements listed above.

A compromise between the highest achievable ramp rate and the highest achievable field has to be made due to these conflicting requirements. In our case the superconducting solenoid was specified with an inductance of 0.023H which, with a ±15V power supply, is capable of being switched at the highest rate of 10 Tesla s^{-1}. The maximum operating current is 160 A, leading to a maximum magnetic field in excess of 2.5 Tesla. In our experiments, field switches have duration of order tens or hundreds of milliseconds, enabling us to measure the molecular dynamics of samples with short T_1. Important for our studies, there is no restriction on magnet *duty cycle*, allowing the magnet to be energised for very long periods of time, in particular for the study of very long T_1 samples.

The superconducting magnet is energised and fully protected against accidental *quench* by a magnet power supply (manufactured by CRYOGENIC). The power supply employs MOSFET transistors rather than power transistors to achieve a fast ramping rate. The MOSFET transistors are mounted on a water-cooled copper heat sink. There is automatic protection in case of a water supply failure. A thermo-switch is installed on the copper base to protect against overheating the MOSFET transistors.

The power supply incorporates a sophisticated microprocessor unit, with all operations controlled through the internal firmware. All operating functions are available either locally at the front panel or remotely via a standard digital interface. An important feature of the power supply is that it can work either with the internal mode or with the external mode. In the internal mode, the field is set as a constant by setting the current via front panel control. In the external mode, the magnet power supply is controlled by a custom interface to produce a variable current which will introduce a desired field profile in the superconducting magnet for field-cycling experiments. A 'gradient' power supply supplied with the Apollo spectrometer provides this signal. To avoid damaging the system under no circumstances should the internal mode be switched to the external mode while the superconducting magnet is energised, and vice versa.

The power supply possesses an internal protection unit which limits the voltage across the magnet in the event of a *quench* (loss of superconductivity of the current carrying

coil that may occur unexpectedly in a superconducting magnet). As the magnet becomes resistive, heat will be released that can result in rapid evaporation of liquid helium in the cryostat. However, the internal protection is only available in the internal mode; when the superconducting magnet is operated via the custom interface the normal over-voltage protection of the magnet is by-passed. In this case, suitable protection had to be designed to protect the superconducting magnet from quenching. This will be discussed later.

A gradient power supply, which has the maximum output 10V, is employed to drive the superconducting magnet power supply via the custom interface, hence to control the field since the instantaneous field is directly proportional to the instantaneous current. It is controlled by a gradient waveform generator with its own DSP (Digital Signal Processing) and an optically isolated 18-bit DAC (Digital to analog converter). The waveform shape is defined in the pulse sequence and this was used to ramp the field smoothly to the chosen value.

Concluding this section, the specifications of the superconducting magnet are summarized in Table 3.1:

Normal coil inductance	23mH
Maximum magnetic field	>2.5Tesla at 4.2K
Maximum operating current	160Amps
Homogeneity in 5mm DSV	+20ppm/-40ppm
Maximum ramping rate	10Tesla s^{-1}
Sample space bore	25mm
Sample temperature	4.2~300K
Duty cycles	Infinity
Field/current ratio	167Gauss/Amp

Table 3.1 Specifications of the superconducting magnet

3.1.2 Apollo console

The Apollo spectrometer is a digital NMR spectrometer console manufactured by Tecmag. It is equipped with two RF Channels and an integrated pulse programmer. A gradient waveform generator is employed to control the current supplied to the superconducting field-cycling magnet. The NTNMR controlling software is Windows NT based and an important feature is OLE control that enabled us to write Visual Basic control programs to provide a high level of automation and control.
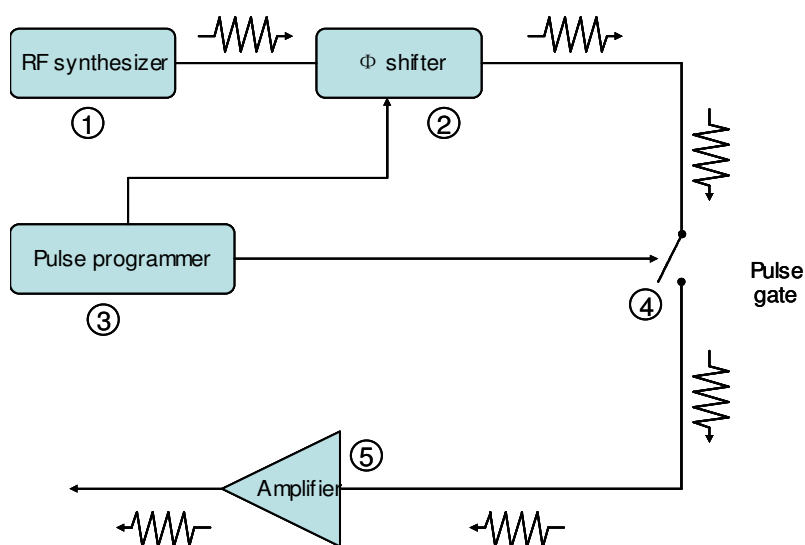
Fig 3.3 RF transmitter

A schematic diagram is shown above to illustrate the operation of RF transmitter. Here we briefly explain the function of each component marked in Fig 3.3. The RF synthesiser① produces an oscillating electrical signal with a well-defined frequency which is the spectrometer reference frequency, denoted ω_{ref}. The synthesiser output wave is given as

$$s_{synth} \sim \cos\left(\omega_{ref}t + \phi(t)\right) \tag{3.2}$$

where $\phi(t)$ is the r.f. phase controlled by the pulse programmer③. The pulse gate④ is a fast switch opened at defined moment (controlled by pulse programmer③) to allow the r.f. reference wave to pass through. The effect is to create an r.f. pulse with finite duration. The duration of the r.f. pulse is referred to as the pulse width,

determined by the pulse gate④ and the pulse programmer③. The r.f. amplifier⑤ is to scale up the gated wave to produce a large-amplitude r.f. pulse for transmission to the probe.

In our case, each RF transmitter channel comprises a DSP (Digital Signal Processing) driven DDS based (Direct Digital Synthesiser) frequency synthesiser① and a transmitter modulator board. The synthesiser board produces small angle phase shifts② and the transmitter board supplies amplitude modulation. The final output from the transmitter has a maximum nominal output of 1V pp into 50 ohms. We used one RF channel to generate the resonance NMR pulse. This was directed to the sample coil via the duplexer after amplification by the AMT RF amplifier⑤, which can amplify the signal in the range 10-150MHz up to 1kW. The other RF channel was used for secondary irradiation, which generates the CW signals with a quite wide range from 5kHz to 450MHz. The broadband AR CW amplifier with low frequency (2kHz) capability provides the irradiation with power levels up to 100W in the range 5kHz to 30MHz.

The DSP driven pulse programmer③ has 100ns timing resolution, 300ns minimum pulse width④, unlimited number of loop counters and 1024 events. The signal averager is controlled by an embedded PowerPC processor and is equipped with 4Mword complex (2048*2048) memory, dedicated real-time display memory, and ultra fast upload capability.

The Apollo spectrometer is controlled by the NTNMR software through two PCI cards, one is used to upload data to the main computer during and after data acquisition, the other one is responsible for all other communication between the main computer and the Apollo system, such as uploading pulse program data from the main computer to the system interface board.

The commercial NTNMR software offers a lot of functions to process the detected signal. The FID signal was acquired from the Apollo console. The signal processing is:
1) A baseline correction was performed to eliminate dc offset.
2) A *left shift* was applied to eliminate any remaining *dead time* signal.

3) An exponential multiplication was performed on the FID data set with a function

defined by $f(t) = \exp(-t \cdot value)$, where the '*value*' parameter is set to $1/2000\text{s}^{-1}$

in our processing. This simple low-pass filter improved the signal to noise ratio.

This process is called *apodization*.

4) Once the signal in the time domain had been optimised, a Fourier transform was

then applied to transform the signal from time domain to frequency domain, and

produced the NMR spectrum.

5) The crucial part of the signal processing, namely *phase correction* and integration,

was then performed. We compared the left and right wing of the dispersion

spectrum and adjusted the phase until the absorption spectrum was symmetrical.

The baseline correction was performed again to remove any dc offset. Finally, the

centre of the absorption spectrum was found by measuring the *moments* of the

line. The peak was then integrated to determine the magnetisation.

The *left shift*, *dead time*, *phase correction* and *moment* are often encountered terms in
the NMR technique and are used here in optimising the spectrometer set-up and the
data processing.
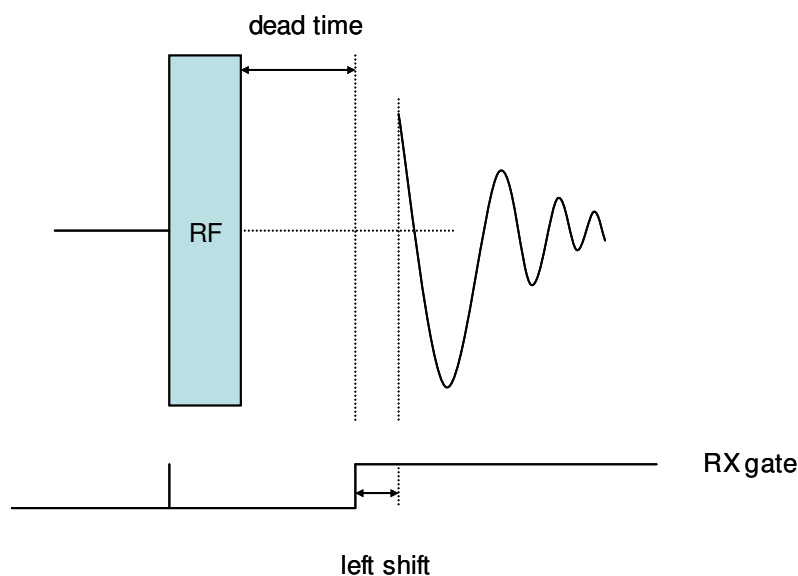
Fig 3.4 Dead time and left shift

Dead time: the time between the pulse and the switch on of the receiver to register the
FID, illustrated in Fig 3.4. To understand this effect, we must consider that the voltage
in the NMR coil during the pulse is generally of the order of 1kV, while the induced

signal is at most several hundred μV. Together with the receiver and the transmitter, the NMR coil is an RLC circuit, the oscillation of which does not stop suddenly, but follows the law $\exp(-t/RC)$. RC is known as the damping constant. For the voltage in the coil to fall to about $10\,\mu V$, when the measurement of the FID begins to be possible, we must wait for the time $t = \ln(1kV/10\mu V)RC \simeq 18RC$ known as the dead time. An additional factor which increases the dead time is the saturation-recovery of the receiver; this was minimized by using receiver blanking. The early part of the FID carries information about the highest frequencies, so that its loss during the dead time may lead to a distortion of the extremes of the spectrum.

Left shift: after the *dead time*, the receiver is switched on to record the FID, however there always some irregular *dead time* signal remaining during the first few points (the time between two neighbouring points is the *sampling interval*, τ_{sample}, $0.4\mu s$ in our spectrometer), *left shift* is applied to exclude these points and therefore eliminate the remaining *dead time* signal, Fig 3.4. It is also in time scale. Normally the *left shift* is recorded as the number of points excluded, and can be transferred as time,

$$\left(leftshift\right)_{timescale} = \left[\left(leftshift\right)_{points} - 1\right] \times \tau_{sample} \tag{3.3}$$

It is evident that the two parameters *dead time* and *left shift* depend on each other. If the *dead time* is defined longer, the *left shift* will become smaller, and vice versa. The sum of these two parameters is determined by the hardware (coil and receiver) and the sample being studied.

Phase correction: linear combination of the real and imaginary parts of the NMR spectrum to produce a peak with pure absorption mode shape. It can be performed automatically by software or interactively by the operator.

Moments: The nth moment M_n of a line shape function $G(\omega)$ with respect to the point ω_0 is given by,

$$M_n = \frac{\int_0^\infty (\omega - \omega_0)^n G(\omega)\, d\omega}{\int_0^\infty G(\omega)\, d\omega} \tag{3.4}$$

The zero moment is the integral of the line. The first moment determines the centre of the peak. The second moment M_2 characterises the line width.

The signal processing discussed above is only part of the whole signal processing. Some important processing is accomplished by the receiver section of NMR system, Fig 3.5. Some components (①,⑧ and ADCs) are built in the Apollo console.
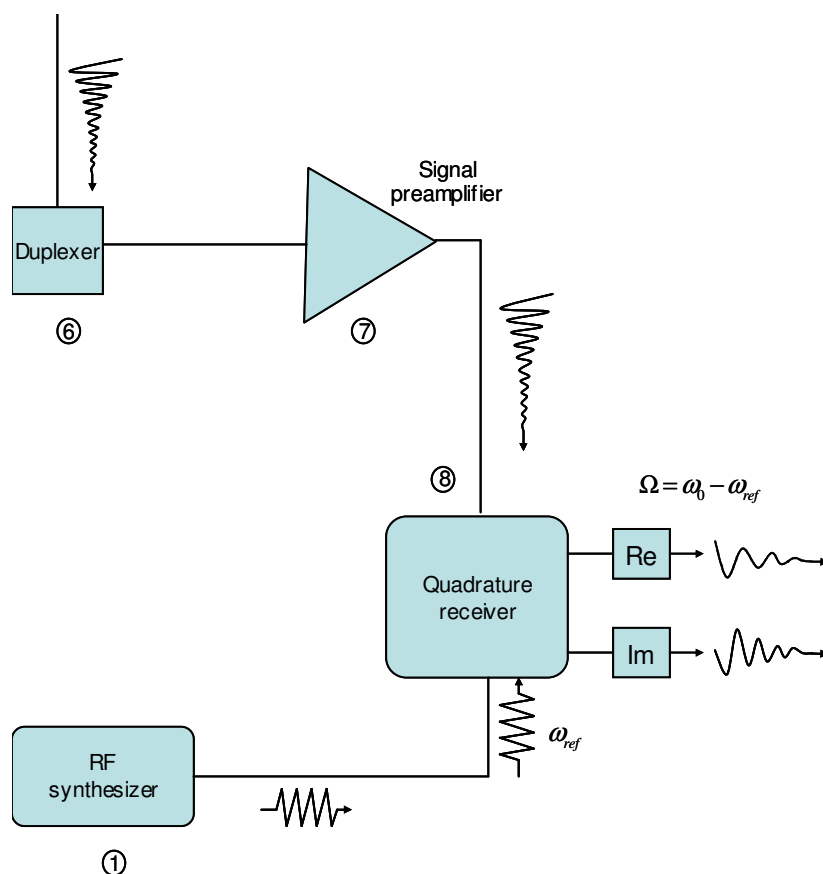
Fig 3.5 The receiver section

The NMR signal arrives at the duplexer ⑥ and is diverted towards the signal preamplifier ⑦ which is a low-noise r.f. amplifier which scales up the tiny signal to a more convenient voltage level. This signal is a continuous current or voltage which must be converted into digital form for further interpretation and presentation on a computer. But the original NMR signal oscillates at very high frequency, tens or hundreds of MHz, which is too fast for the ADCs (analogue-to-digital conversion). The quadrature receiver ⑧ is designed to generate a new frequency signal which is oscillating at the relative Larmor frequency (much slower than original signal) by

combining the NMR signal, which oscillates at the Larmor frequency ω_0, with the reference signal, oscillating at the frequency ω_{ref}. The relative Larmor frequency is

$$\Omega = \omega_0 - \omega_{ref} \tag{3.5}$$

The offset frequency $\Omega/2\pi$ is usually of the order of 1MHz or less, enabling the signal to be handled accurately by ADCs. Now the output of the receiver is

$$s(t) \sim \cos(\Omega t)\exp(-t/T_2) \tag{3.6}$$

It is similar to expression (2.20), with ω_0 substituted by Ω. The problem is that the equation (3.6) doesn't distinguish the difference between $\omega_0 > \omega_{ref}$ or $\omega_0 < \omega_{ref}$. That is why the absorption line and the dispersion line are needed in NMR experiments as discussed in Chapter 2. This two-output detection is called *quadrature detection*.

The two outputs of the quadrature receiver are connected to their own ADCs to convert the continuous analogue signal into digital form. The digitization is to sample at a set of points and record them as a set of values. The time separation between the sampling points of the ADCs is called the *sampling interval*, τ_{sample}. In our case, the sampling interval is 400ns, and the number of sampling points (usually an integer power of 2) is 1024.

The whole signal processing, comprising the signal processing by NTNMR software and the signal processing by receiver section, converts the original NMR signal to the visible NMR spectrum which is ready for rendering the dynamic information of the sample.

3.1.3 Duplexer

The duplexer is designed to achieve the following task: when a strong r.f. signal arrives from the amplifier ⑤, the duplexer diverts it down the cable leading to the probe; on the other hand, when the tiny NMR signal travels down the same cable in the opposite direction, the duplexer diverts it into the receiver section. The diagrams for the two modes are illustrated in Fig 3.6(a) and Fig 3.6(b).
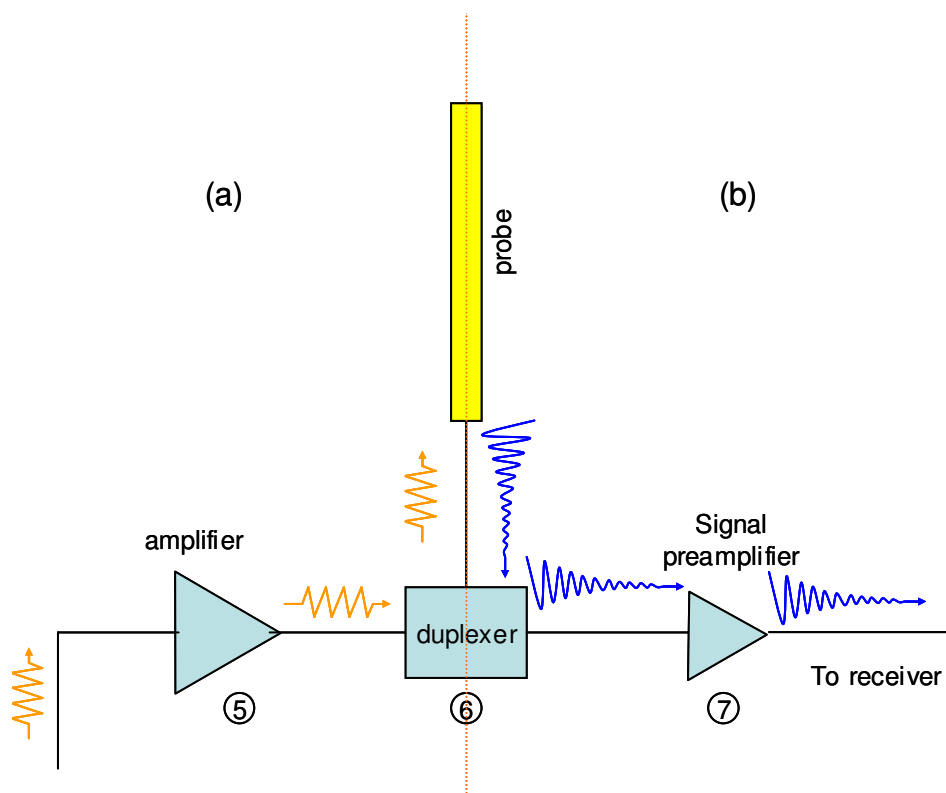
Fig 3.6 (a) the duplexer in transmit mode (b) the duplexer in receive mode.

3.2 Probe

The probe is located in the centre of the superconducting magnet and the sample cryostat to ensure the sample in the region of homogeneous magnetic field. The NMR probes, with primary and secondary r.f. irradiation coils, tank circuits and temperature control electronics, were designed and built in our laboratory, as shown in Fig 3.7.
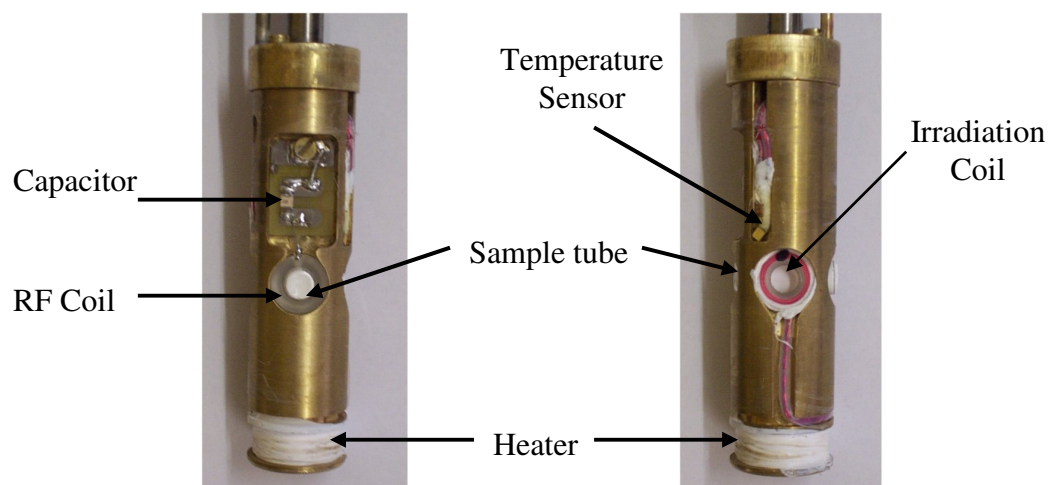
Fig 3.7 The probe structure

The sample was contained in a glass tube, which sits in cylindrical cavity inside the radiofrequency coil. The RF coil, core element, was made by winding wire tightly on a KEL-F former. It was connected to the top and outside of the cryostat by a 50Ω semi-rigid coaxial RF line approximate 1m long. The internal coil diameter was 5mm. The number of turns, the inductance, the resonance frequency of the coil and even the tank circuit depended on the types of experiment and sample. Because the experiments were run in field-cycling mode, the NMR detection/irradiation frequency could be chosen depending on a variety of constraints. Therefore it was possible to design the RF coil according to the requirements of sample, nucleus, matching, Q factor, signal quality, and dead time etc.

Two kinds of tank circuits, parallel and series, were designed for different experiments. They both comprised an RF coil and two capacitors, as illustrated in Fig 3.8(a) and Fig 3.8(b).
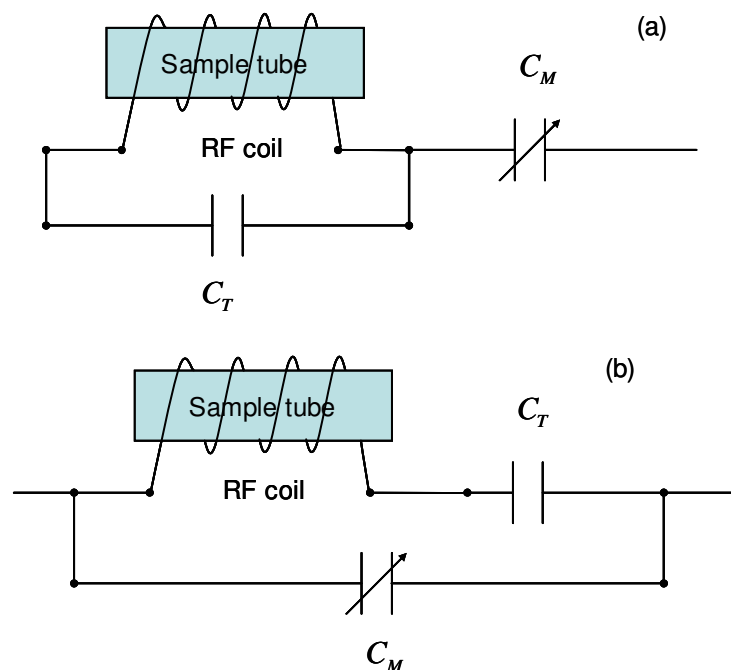
Fig 3.8 (a) parallel tank circuit (b) series tank circuit

The parallel tank circuit shown in Fig 3.8(a) is the typical tank circuit employed in many NMR probes. The two capacitors, C_T and C_M in the tank circuit have the following functions. The capacitor C_M is called the matching capacitor and the other

capacitor C_T is called the tuning capacitor. The matching capacitor matches the impedance of the loaded probe to that of the 50 Ohm cable coming from the spectrometer. The tuning capacitor changes the resonance frequency of the RF coil and enhances the current in the coil by electromagnetic resonance. The resonance frequency is determined by the inductance L of RF coil and the capacitance of the tuning capacitor C_T,

$$\omega = 1/\sqrt{LC_T} \tag{3.7}$$

In Fig 3.8(a), the RF coil is in parallel with the tuning capacitor C_T, so the tank circuit is called parallel tank circuit; and in Fig 3.8(b), the RF coil is in series with the tuning capacitor, the tank circuit is therefore called series tank circuit.

The electrical properties of the tuned circuit are affected by the nature of the nucleus. It is therefore necessary to adjust the values of capacitors C_T and C_M every time the nucleus is changed. Normally this is done by manual adjustments of the capacitors- a process called 'tuning the probe'. In practice, an oscilloscope is used to display the reflected power vs. frequency. The goal is to adjust the display so that the reflected power from the RF coil is zero at the resonance frequency of the nucleus, as shown in Fig 3.9.
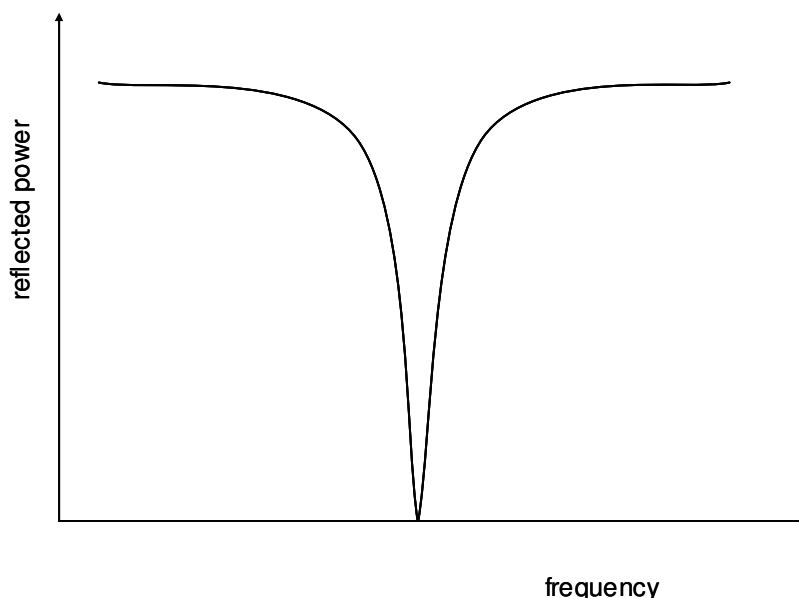
Fig 3.9 Reflected power close to zero at resonance frequency in well-tuned tank circuit.

The NMR spectrum achieves the maximum signal intensity when the measurement field matches the resonance field. The response function vs magnetic field of the tank circuit containing the NMR coil defined a 'calibration curve'; this was measured by determining the signal amplitude as a function of detection field.

It was evident, Fig 3.10, that different tank circuits, parallel and series, had a significant effect on the effective Q-factor for the resonance coil and hence the calibration curve. The parallel tank circuit had a narrow calibration curve which meant the effective Q factor was high and the signal was big. On the contrary, the series tank circuit had a broad calibration curve, low effective Q factor and small signal. If in our experiment the field shift was a problem to cause a critical error, we used the series tank circuit because the broad top of the calibration curve may minimize the effect of field shift. If the signal was tiny, the parallel tank circuit might be taken into account to improve the signal quality. Hence the choice was determined by the particular sample; for example, when measuring ^{13}C NMR, signal sensitivity was paramount and a parallel arrangement was chosen, whereas for ^{1}H NMR, signal stability as a function of field was more important and the series resonant circuit was used.

The irradiation coils were required for secondary irradiation in low field NMR and NQR experiments and were placed perpendicular to the RF coil on both sides. The irradiation coils were connected with the connector on the top of the probe using a 1m long twisted pair assembly. This arrangement minimized the self capacitance, enabling the circuit to possess low impedance and therefore provide broadband irradiation.

A relay was designed to minimize any noise introduced down the cable by limiting the connection to the AR CW amplifier. The relay was switched on only during the irradiation time in the low field NMR experiments, as illustrated in Fig 3.11.

The temperature sensor was mounted in a groove cut into the brass block of the probe tail adjacent to the NMR coil. This is a calibrated CERNOX resistance thermometer and the temperature range is from 4K to 325K. A heater consisting of copper wire

wound round a brass bobbin was fixed to the bottom of the probe tail. Temperature control with optimised settings of the proportional, integral and derivative parameters of the feedback circuit was carried out by a Lakeshore 331E temperature controller.
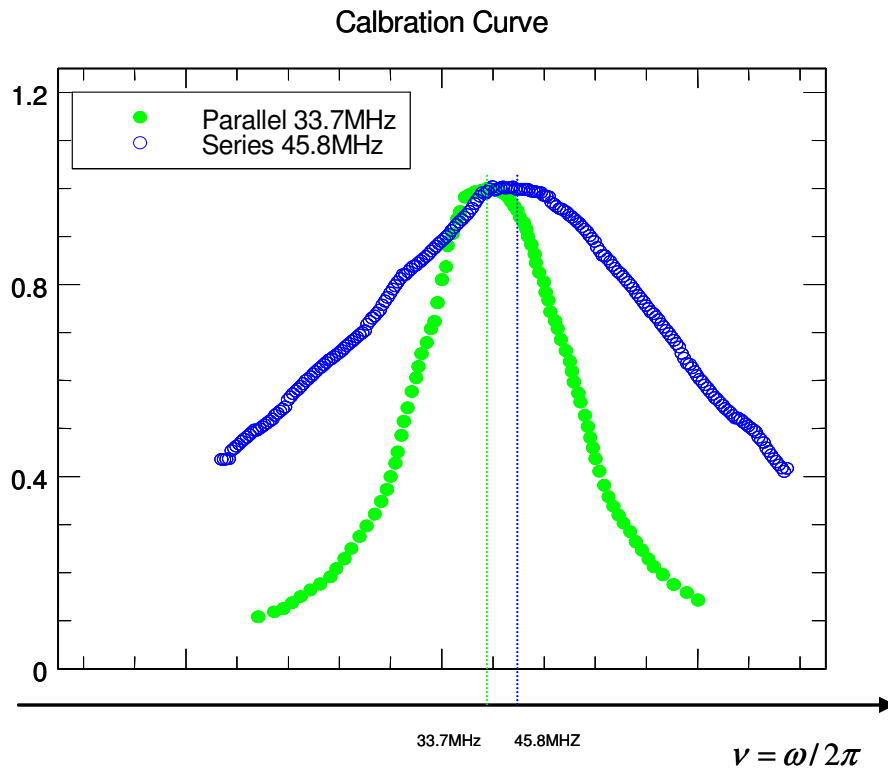
Fig 3.10 The normalized calibration curves of parallel and series tank circuits. The frequency axis is linear for each curve, but the blue curve was moved close to the green one for comparison.
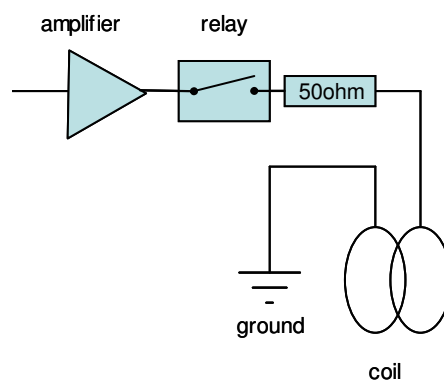
Fig 3.11 A relay was introduced between the AR CW amplifier and the probe to minimize the noise caused by other electrical circuits and increased by the amplifier.

3.3 Superconducting magnet protection

As reviewed in section *3.1.1*, the superconducting magnet has its internal protection against magnet quench. However, in our field-cycling experiments, the magnet was usually working in the external control mode, driven by the gradient power supply. In the external mode, the power supply provides no automatic protection for the magnet from 'quenching', which means it can't automatically detect an increasingly resistive load, and instantaneously switch the current to zero. To protect the magnet, we have a home-built interface connected with the gradient power supply to enable/disable its output. This interface is linked to both the main NMR control computer and a dedicated power supply monitor computer using digital I/O cards supplied by Amplicon Liveline Ltd. In the main computer we have built in a 4-bit 'Dongle' facility in the self-designed VB software; only when we send the 4-bit 'Dongle' correctly in the software and the 'quench detecting' program is enabled can the main NMR computer take over the control of the gradient power supply. The dedicated power supply monitor computer communicates with two HP 34401A multimeters at high speed, recording 1000 readings per second. One multimeter measures the voltage across the output terminal and the other measures the voltage across the shunt resistor, which is proportional to the current in the coil. A VB program operating on the dedicated power supply monitor computer was applied to detect the 'quench' condition, and send the signal through the Digital I/O card to trigger a relay, hence to disable the gradient power supply output in the event of 'quench'.

The dedicated power supply monitor computer directly reads the data from the two HP 34401A multimeters without any other communications or processes. It can detect a quench very effectively and protected the superconducting coil and power supply well. There were periodic problems with noise on the data line connecting the system, which led to a false quench condition at the start of a run before the magnet was energised. While not harmful, it was disruptive to the automated processes. To minimize the incidence of 'false quench' detection, some averaging was programmed into the procedure.

The Cryogenic Helium Level Gauge provided another protection for the magnet. The safety level was set to a value just above the level of top of the magnet; when the helium level was below this value, and the magnet power supply was working in the external mode, it triggered off the power supply.

3.4 Field switching

When the field-cycling experiment was running, the magnetic field switched on to higher field and switched off to lower field. In order to achieve the best performance of our field-cycling experiment, it was imperative to investigate the field switching profile.

Fig 3.12 is a typical magnetic field switching profile in a saturation-recovery pulse sequence. Each time when the field was switched externally, before the magnetic field reached the target field, there was always a small overshoot before settling down. This didn't matter much when the field was switched from resonance field to recovery field, as it was only around 20ms delay during the evolution of magnetisation which was normally much shorter than the evolution time. However, after the field was switched back to the NMR resonance field, the measurement pulse was triggered to measure the magnetisation. It was important that the hardware and software procedures were designed such that the actual field, at the moment the pulse was applied, was as consistent and repeatable as possible. Following a variety of trials and investigations, good results were obtained by introducing a delay (settle time) of 20ms between the end of the field ramp and the pulse trigger. Also, reducing the ramp rate to 5Ts for the field switch to the NMR detection field was also found to optimise performance.

In practice, the field switching time and the settle time will only have an effect on very short T_1 values (about 100ms). For the samples we studied, there was no predominant effect on the T_1 result, because T_1 is long enough.

Another effect that was observed was that drifts in the target field which were a function of recovery field and recovery time. These drifts were for the most part reproducible and predictable. Therefore a two-variable function was determined

experimentally to correct for the field drifts. A parameter 'offset' was programmed into the VB code to compensate. Using this, the field stability achieved was typically better than 20Gauss which was tolerated by the calibration curve.
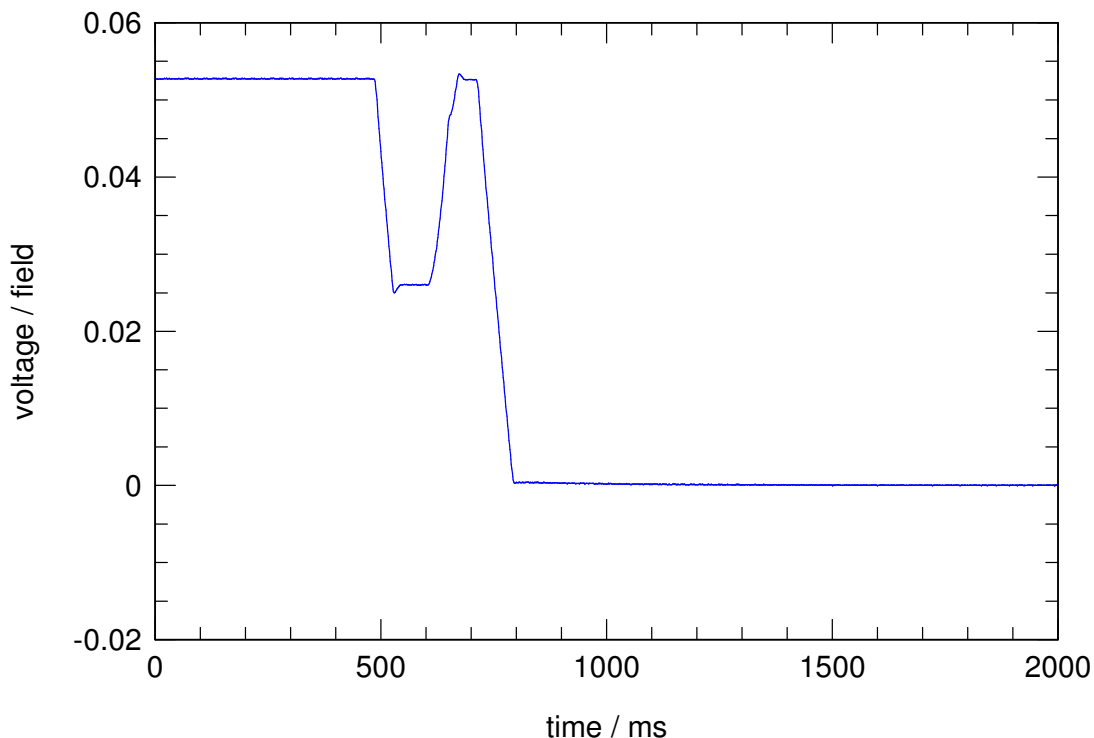
Fig 3.12 Magnetic field switching profile (saturation-recovery pulse sequence).

3.5 Magnetisation data calibration

Adding a parameter 'offset' into the VB program successfully minimized the field drifts, but could not completely eliminate them. This was a source of systematic error in the magnetisation measurement due to the response function of the NMR coil in its tank circuit. By measuring the response function, small corrections to the magnetisation were made by using the 'calibration curve'. The calibration curve is a convolution of the response function of the coil in its tank circuit with the Fourier transform of the pulse envelope.

Fig 3.13 is a figure of how the signal intensity changes with the field. There are two such calibration curves in the figure. The blue one was of 4-nitrobenzoic sample at 28MHz. It came from a Gaussian fit to the experimental data. But not all the experimental data could be fitted by Gaussian function within an acceptable error; for example the red curve was determined by numerical interpolation. The red curve was moved upward 0.5 to give a clear view of the whole figure. In each curve, the maximum appeared when the field was exactly at the resonance field. When the measurement field deviated from the resonance field, the signal amplitude decreased.
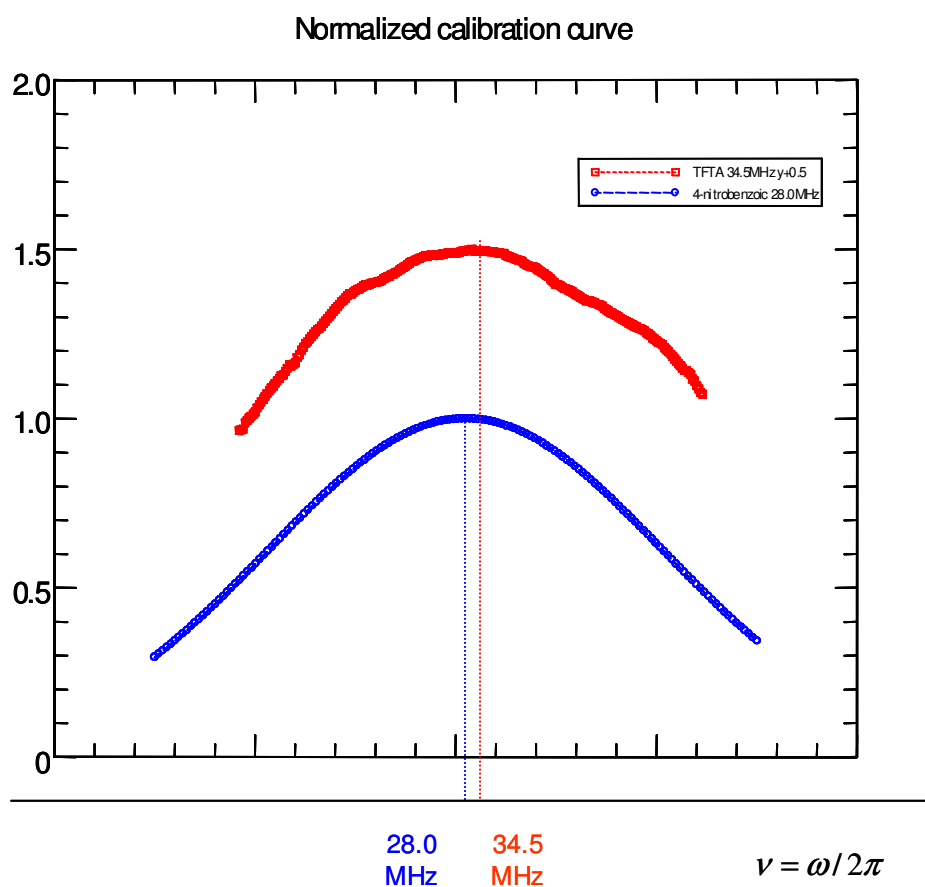
Fig 3.13 Two normalised calibration curves. The blue curve was a smooth Gaussian fit and centred at 28MHz ; the red curve was determined by numerical interpolation and centred at 34.5MHz. The frequency axis is linear for each. The red curve was moved close to the blue one for comparison and was moved upward 0.5 to give a clear view.
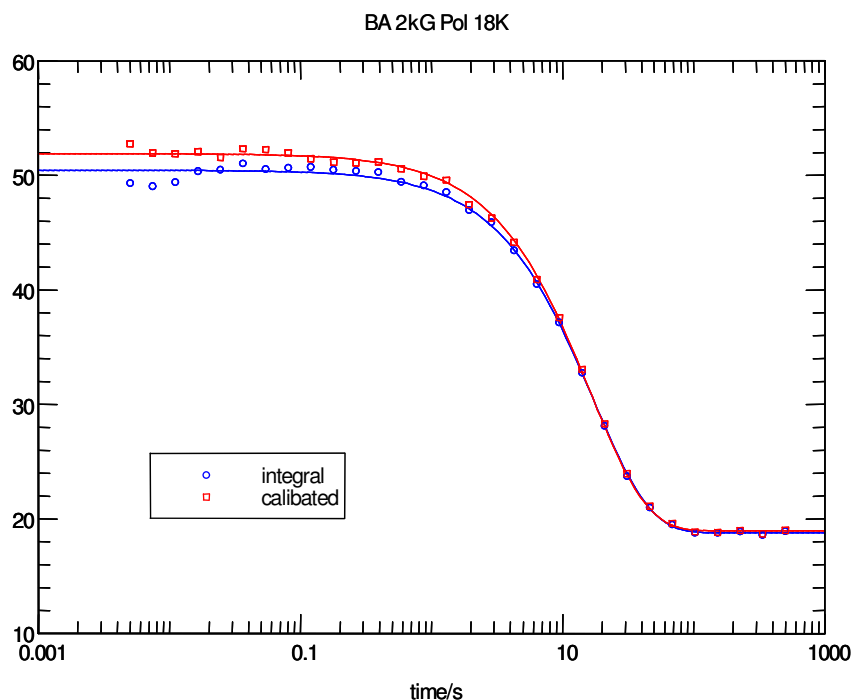
Fig 3.14 Comparison between raw data (integral) and calibrated data on the sample BA at 18K and 2kGauss with polarisation-recovery pulse sequence.

With the calibration curve, the measurement data can be properly corrected for small field drifts. All the data are calibrated to the central frequency/the resonance field to improve the data quality. The calibrating process was written in our VB program and was automatically done if the calibration curve was found in our system.

Fig 3.14 is a figure to illustrate the comparison between typical raw and calibrated data. The r^2 fit to red square calibrated data (0.9995) is better than that of blue circle raw data (0.9988). The T_1 values extracted from the red squares and blue circles, 16.28s and 17.16s respectively, are slightly different (5%). The relative error of T_1 is 1/3 smaller after data calibrating (from 0.4193/17.16 = 0.0244 to 0.2625/16.28 = 0.0161). It is clearly shown how the calibration works effectively on the first few points where the field drift is bigger.

That the measurement data can be calibrated doesn't imply that we can let the system work with significant field drifts. That is because, on one hand when the measured field deviated too much from the resonance field, the signal was small and the error of the signal was big. The uncertainty of the signal dominated the data quality even after

calibration; on the other hand, each point in the calibration curve has its own error. The farther away from the resonance field, the bigger the calibration error will be. So when we do field-cycling experiments, we normally try to set the measurement field in the range of 5% of the top of the calibration curve corresponding to a field drift in the range of ± 35 channels (1 channel equals to 0.57 Gauss in our system) or ±20 Gauss. That is why it is better to design a tank circuit with, a broad calibration curve which has more than 60 channels (or from -20 Gauss to 20 Gauss) in the top (95%-1) range.

As discussed above, many factors, such as RF coil turns probe tank circuit, Q factor, width of measurement pulse, temperature, etc., affect the shape of the calibration curve. When we design the probe, or do the field-cycling experiments, we need take the calibration curve into account. Here we summarize factors concerning the calibration:

- The higher the Q factor is, the narrower the calibration curve will be.
- The wider the measurement pulse is, the narrower the calibration curve will be since the spectrum is the Fourier transform of the pulse envelope.
- When the measurement pulse is too strong (the pulse amplitude is too big), there will be some fluctuations in the top of the calibration curve because at some fields the pulse is greater than 90-degree. For this reason we usually set measurement pulse to be less than 90-degree.
- The measurement field position should be in the top range (95%-1)
- If the calibration curve cannot be fitted by a Gaussian function, the interpolation method should be employed to generate a correct calibration curve.
- When the sample temperature is changed, we need check the calibration curve.
- When samples are changed especially if there are two or more spin species in the sample, the calibration curve needs to be checked, because different nucleus may have different field response.
- When the cooling system of the magnet power supply changes, for example the temperature of cooling water changes with environment temperature, the calibration curve also needs checking.

3.6 Software

There are two kinds of software employed in our NMR experiments. One is for improving the automation of the NMR spectrometer system and for designing different pulse sequences [61, 62]; the other one is for analysing the experimental data.

The former has been introduced separately or will be introduced in many applications such as the protection against quench, the 'offset' to stabilize the measurement field and different pulse sequences employed in the field-cycling NMR experiments which will be discussed later.

The latter is as important as the former. It directly led to the interpretation of the experimental data and publication of the research results. It was accomplished by the available software tools; for example, the graphic tool 'easyplot' was employed to plot the daily experimental data and extract the parameters such as spin-lattice relaxation time T_1 from best fits to model functions; Matlab or Visual Basic was employed to do the modelling and simulation of tunnelling and polarisation behaviour.

3.7 Pulse sequences and curve fit

Pulse sequences are programmed in the NTNMR software of the Apollo spectrometer. We can design them for different experiments by the OLE interface. Here we summarize the pulse sequences we employed in the experiments. Each kind of experiment has its own pulse sequence and its own experimental result. The data fits are introduced here as well as the simulation of our experimental data.

3.7.1 Tuning – Find 90º saturation and measurement pulse

Tuning in this context means that we optimise the width and amplitude of the r.f. pulse to match the 90º tipping angle. This is achieved by applying a two-pulse

sequence to the sample, Fig 3.15, with separation short compared with T_1 but long compared with T_2 to avoid echo generation. The separation time τ_p is normally set to $350\,\mu s$.
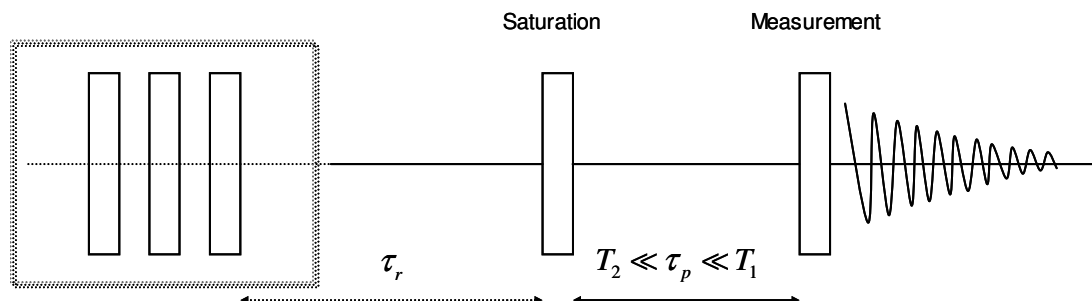
Fig 3.15 Two-pulse sequence to find the 90-degree pulse

In our tuning program, the first pulse (saturation) can be enable or disabled. Therefore there are two modes to find the 90-degree pulse. When the first pulse is enabled, and is a 90-degree pulse, the FID following the second pulse should be zero. Therefore by plotting this FID as a function of the amplitude of the first pulse, the curve follows a sine function and the pulse parameters defining a $90°$-pulse are obtained. When the first pulse is disabled, the FID following the measurement pulse can also be plotted as a function of the amplitude of the measurement pulse. The curve also follows a sine function but the $90°$ pulse appears in the first maximum of the sine function.

However the spin-polarisation before the saturation pulse (the first mode, saturation pulse enabled) or the spin-polarisation before the measurement pulse (the second mode, saturation pulse disabled) is an arbitrary value which may cause FID signal intensity fluctuations (with a significant random error). In view of this arbitrary spin-polarisation, the first mode is better than the second one, because the saturation pulse will reduce the random effect but one saturation pulse may not be enough to completely eliminate the random effect (due to the fact that the applied field cannot be perfectly homogeneous and the sample itself tends to distort the applied field). Therefore in practice, a saturation train of pulses are required, as shown in the shadow area in Fig 3.15. This saturation train of pulses, usually comprising 6 or more $90°$ pulses separated by approximately $350\,\mu s$ are employed to fully saturate the spin-polarisation. After the train of pulses, the spin-polarisation is built up during a fixed

recovery time τ_r and therefore a constant spin-polarisation is achieved before the first (single saturation) pulse. A simple diagram of the FID as a function of the measurement pulse is shown in Fig 3.16.
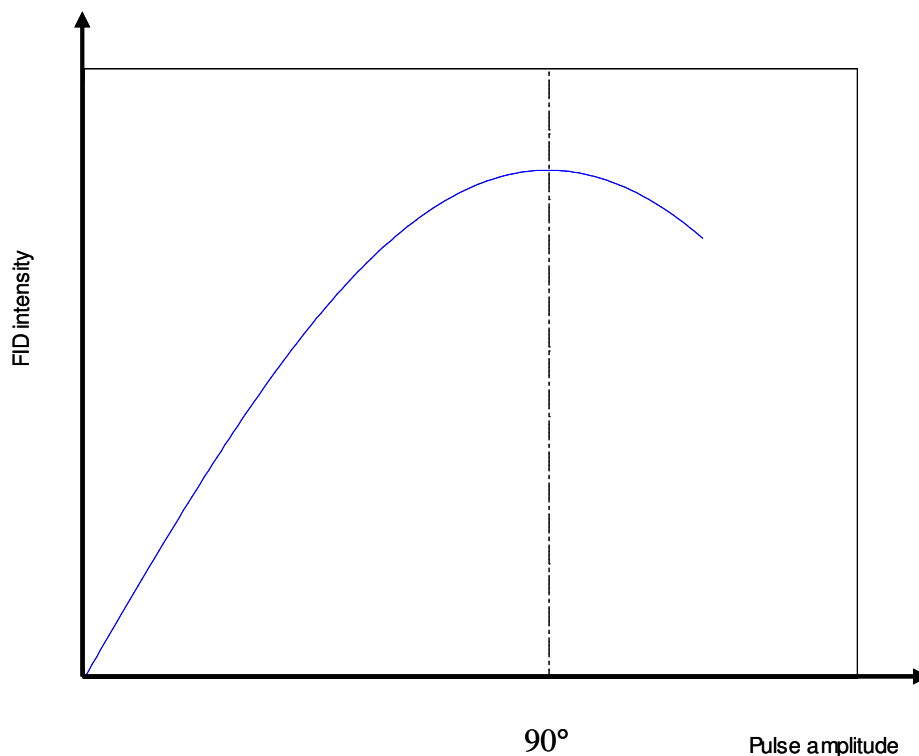
Fig 3.16 FID intensity as a function of pulse amplitude (sine function)

When the tipping angle of the measurement pulse is 90º, the emf voltage reaches the maximum value and we get the maximum amplitude of the NMR spectrum. If the spin-lattice relaxation time T_1 is not too long, that is to say, we don't have to employ spin-echo method to measure T_1, we will use a measurement pulse as strong as possible to get a big signal. A slightly less than 90º measurement pulse is recommended because the signal will be more stable (if the measurement pulse is stronger than 90º pulse, with field instability the signal might be over-saturated and the stability of it will be worse).

As discussed in the calibration curve section, the selection of measurement pulse width, pulse amplitude and pulse attenuation is not only on the basis of the 90º pulse and the signal amplitude, but also on the shape of the calibration curve to meet the

needs of the particular experiment. The selection is different from sample to sample, RF coil to RF coil. For example, the pulse width 2μs was normally used in ^{1}H experiments and 4μs was used in ^{13}C experiments.

According to the discussion above, we can conclude the procedure of tuning as follows:

1. run the tuning program.

2. set the correct field and estimated T_1 value.

3. change the measurement pulse amplitude (normally the pulse width and pulse attenuation could be set by experience) and record the signal amplitude without saturation pulse.

4. choose a value of measurement pulse amplitude where the signal amplitude is at maximum.

5. set the saturation pulse amplitude to be this value (if the saturation pulse width and pulse attenuation are same as measurement pulse's. The pulse attenuation is normally the same). Then run the tuning experiment with saturation to check how much signal is left. The interval between the saturation pulses is set to be 350μs to prevent echoes. Normally the signal remaining should be smaller than 10% of the original signal without saturation. If the saturation pulse width is different with measurement pulse, we have to sweep the saturation pulse amplitude to find where the minimum remaining signal is.

6. set the measurement pulse amplitude to be slightly less than the amplitude of 90° pulse.

7. analyse the FID signal to optimise the left shift and the dead time values. This is an essential step before data acquisition. In our ^{1}H experiments, left shift is typically around 6, dead time is about 5μs.

8. record the calibration curve and check that it is not too narrow and has a regular smooth shape.

3.7.2 Calibration curve pulse sequence

After the tuning procedure, a calibration curve experiment must be done before carrying out field-cycling experiments.

As discussed above, the calibration curve experiment is not only for field calibration, but also is to check the resonance field and to check the tuning quality. It plays a vital role in our field-cycling experiments.

The pulse sequence for the calibration curve experiment is similar to the pulse sequence of the saturation-recovery experiment, $\left(\dfrac{\pi}{2}\right)_x - \tau - \left(\dfrac{\pi}{2}\right)_x$. We send a train of 90° pulses to saturate the longitudinal magnetisation. Following a recovery delay τ, a 90° measurement pulse is employed to measure the recovered longitudinal magnetisation. There are two differences with the saturation-recovery pulse. One is that in the calibration curve pulse sequence the measurement field is not the resonance field. A variable field offset is applied which enables us to create a set of off-resonance fields and measure the field dependence of the signal intensity.

Because the signal intensity decreases rapidly when the offset is getting bigger, and our field shift can't be that big in our field-cycling experiments, the offset is normally set in the range of (-80Gauss-+70Gauss). The calibration curve in this range is adequate to calibrate all the experimental data points.

The other difference is that the recovery time is set to a fixed value which is about T_1. It is easy to understand because the calibration curve experiment is not for the study of relaxation but for the field dependence of signal intensity.

3.7.3 Field-cycling T_1 experiment

As reviewed in Chapter 2, the spin-lattice relaxation time is a two-variable function of temperature and magnetic field/frequency. Two kinds of experiments are therefore

employed to map out the profiles of spin-lattice relaxation time: T_1 vs temperature and T_1 vs field respectively. Finally we obtain the 2D (one dimension is temperature, the other one is field/frequency) profile of the spin-lattice relaxation time. The dynamics of the studied sample will be extracted from these data.

The T_1 versus temperature experiments could be run at the resonance field using the internal mode of the magnet power supply; there is no field-cycling and the field is stable at the NMR resonance field.

The spin-lattice relaxation time T_1 versus magnetic field experiments must be run with the field-cycling technique using the external mode of the magnet power supply. Different pulse sequences employed depend on the precise nature of the experiments. We will summarize the pulse sequences here and we also will discuss them in later chapters to explain them in the context of a specified experiment.

3.7.3.1 Saturation-recovery pulse sequence

The pulse sequence of saturation-recovery experiment is shown in Fig 3.17.
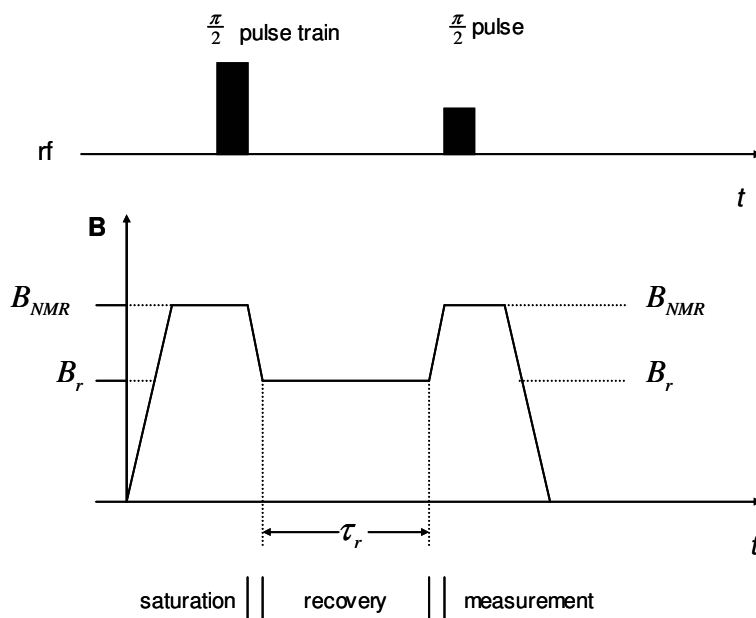
Fig 3.17 Saturation-recovery pulse sequence

1) Saturation of magnetisation with a comb of resonant 90° pulses at the resonance field B_{NMR}

2) Rapid magnetic field switch to recovery field B_r, which was selected for relaxation

3) Evolution of magnetisation in the field B_r for a period of time τ_r

4) Rapid magnetic field switch back to the resonance field B_{NMR}

5) Measurement of magnetisation with a 90° pulse

To measure the spin-lattice relaxation time at the fixed resonance field, we just need to simply disable the field switching. We normally repeat this sequence N times with different recovery time delays τ_r to obtain a magnetisation recovery curve with N points. The value N depends on the sample. Normally if it is homonuclear system and the relaxation curve is single exponential, N is set to 20; if the relaxation curve is bi-exponential which is a normal phenomenon in heteronuclear system, N is set to 30 or even more to make sure that there are enough points in the relaxation curve to show both the fast and slow components clearly. The recovery time is determined by two parameters set before the experiment, initial delay time $t_{initial}$ and estimated spin-lattice relaxation time $T_{1estimate}$. The minimum recovery time is given by $t_{min} = t_{initial}$ and maximum recovery time is given by $t_{max} = 10 \times T_{1estimate}$. The recovery times are incremented with steps that are linear in the logarithm of time; some example data is shown in Fig 3.18.

As reviewed in equation (2.19) of Chapter 2, the longitudinal magnetisation recovery equation is:

$$\frac{dM_z}{dt} = -\frac{M_z - M_0}{T_1} \tag{3.8}$$

Given the conditions $t \rightarrow \infty$, $M_z = M_0$ and $t = 0$, $M_z = 0$, the solution is:

$$M_z(t) = M_0\left(1 - \exp\left(-t/T_1\right)\right) \tag{3.9}$$

BA 18K 7kGauss
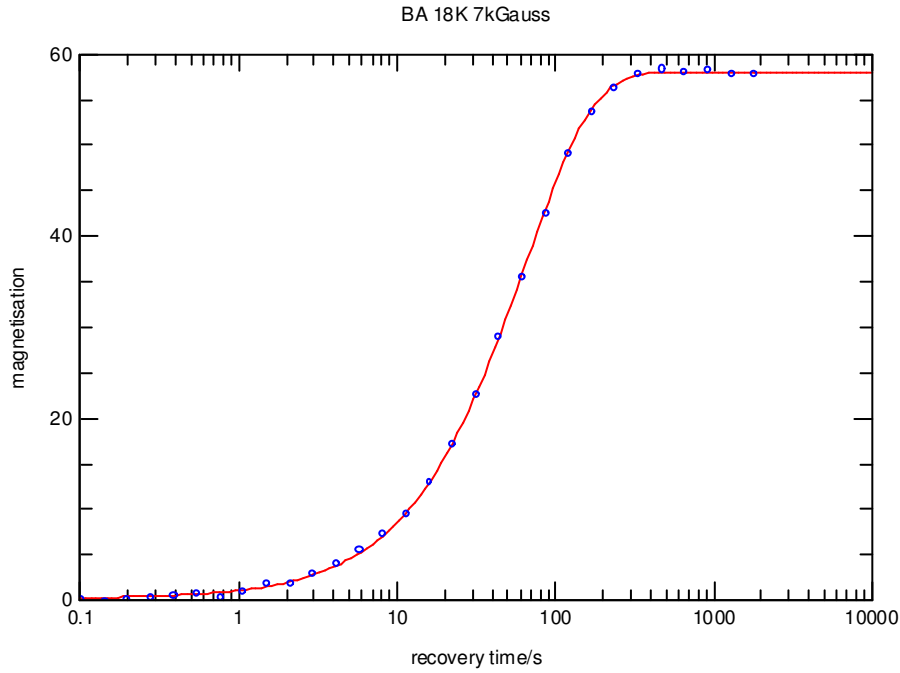
Fig 3.18 The spin-lattice relaxation curve of sample BA recorded at 18K and 7kG. The data points are equally separated along time axis in log scale. Best fit to equation (3.10) is shown with a red solid line. The spin-lattice relaxation time for this case is $T_1 = (64.2 \pm 0.4)\, s$.

Due to the fact that there is often some recovered magnetisation during the field switch to recovery field after the saturation pulses, there may be some magnetisation offset at short times ($t = 0$). Also, there may be baseline corrections, so the spin-lattice relaxation curve fitting equation is therefore as follows:

$$M_z(t) = M_0 \left(1 - \exp\left(-t/T_1\right)\right) + c \tag{3.10}$$

where c is the magnetisation offset. As an example, this equation was employed to fit the curve (red solid line) in Fig 3.18.

It was important to check the signal intensity in low temperature and/or in high field. That was because in these two conditions the signal intensity might be so strong that the amplifiers became saturated and operated in a non-linear region. The signal saturation problem could be checked by plotting the curve of the equilibrium magnetisation versus inverse temperature. It should be a linear curve as shown in Fig 3.19.
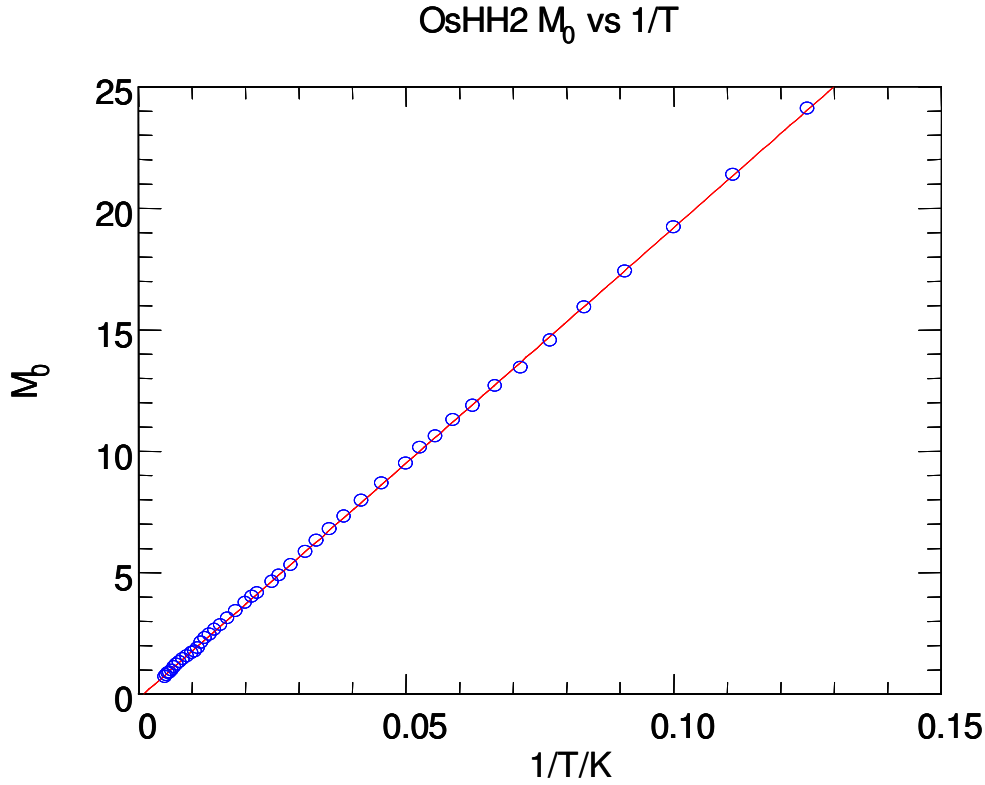
Fig 3.19 Curve of the equilibrium magnetisation vs inverse temperature. Sample is OsHH2.

The time range of the relaxation curve is determined by the parameters $t_{initial}$ and $T_{1estimate}$. To get an accurate T_1 from the relaxation curve, two base lines are crucial; one base line is the base line of the magnetisation offset c, which is close to 0; the other one is the base line of the equilibrium magnetisation M_0. According to the equation (3.9), when the recovery time τ_r is longer than $5T_1$, the magnetisation is about 99.3% of the equilibrium magnetisation, consequently t_{max} was set to $10T_{1estimate}$. Normally 5 points on the relaxation curve were measured to get a rough estimation of T_1 before running the experiments in an automated sequence.

3.7.3.2 Polarisation-recovery pulse sequence

To measure the spin-lattice relaxation time, a non-equilibrium state is created and the return to equilibrium is obtained. Conventionally the non-equilibrium state can be either saturated ($M_z(0)=0$) or inverted ($M_z(0)=-M_0$). With field-cycling, an alterative sequence is available, namely the polarisation-recovery pulse sequence, as

shown in Fig 3.20.
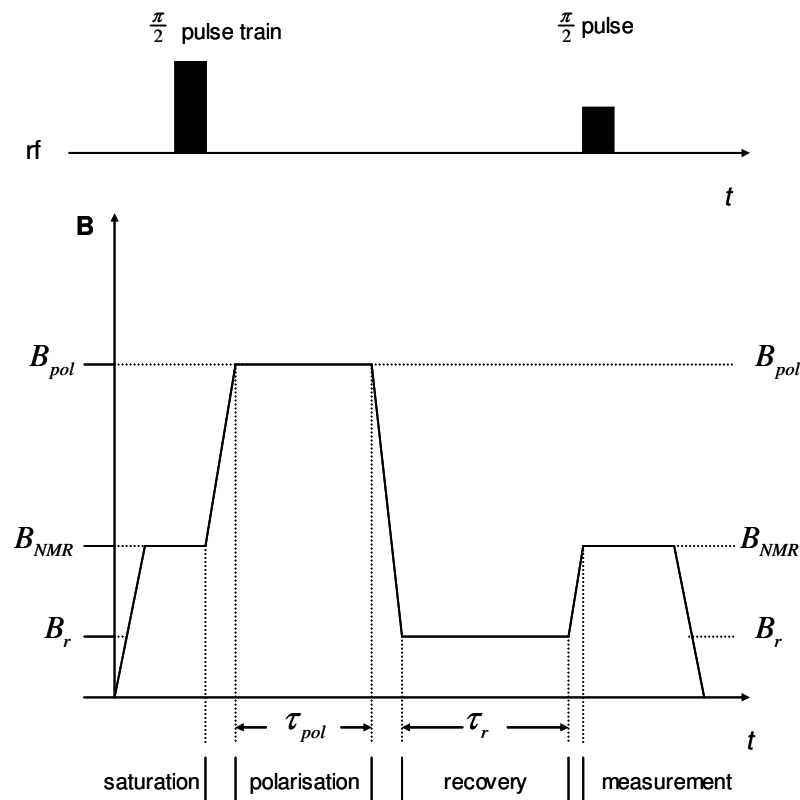
Fig 3.20 Polarisation-recovery pulse sequence.

1) Saturation of magnetisation with a comb of resonant 90° pulses at the resonance field B_{NMR}

2) Rapid magnetic field switch to high polarising field B_{pol} for a period of time τ_{pol} to allow growth of spin polarisation

3) Rapid magnetic field switch to B_r, which was selected for relaxation

4) Evolution of magnetisation in the field B_r for a period of time τ_r

5) Rapid magnetic field switch back to the resonance field B_{NMR}

6) Measurement of magnetisation with a 90° pulse

As the magnetisation is proportional to the magnetic field, the NMR signal intensity we detect in low measurement field is weak. It is at low field that the polarisation-recovery pulse sequence is an advantage. To gain the better signal noise ratio, and hence improve the accuracy of spin-lattice relaxation time measurement, we introduced the polarisation-recovery pulse sequence.
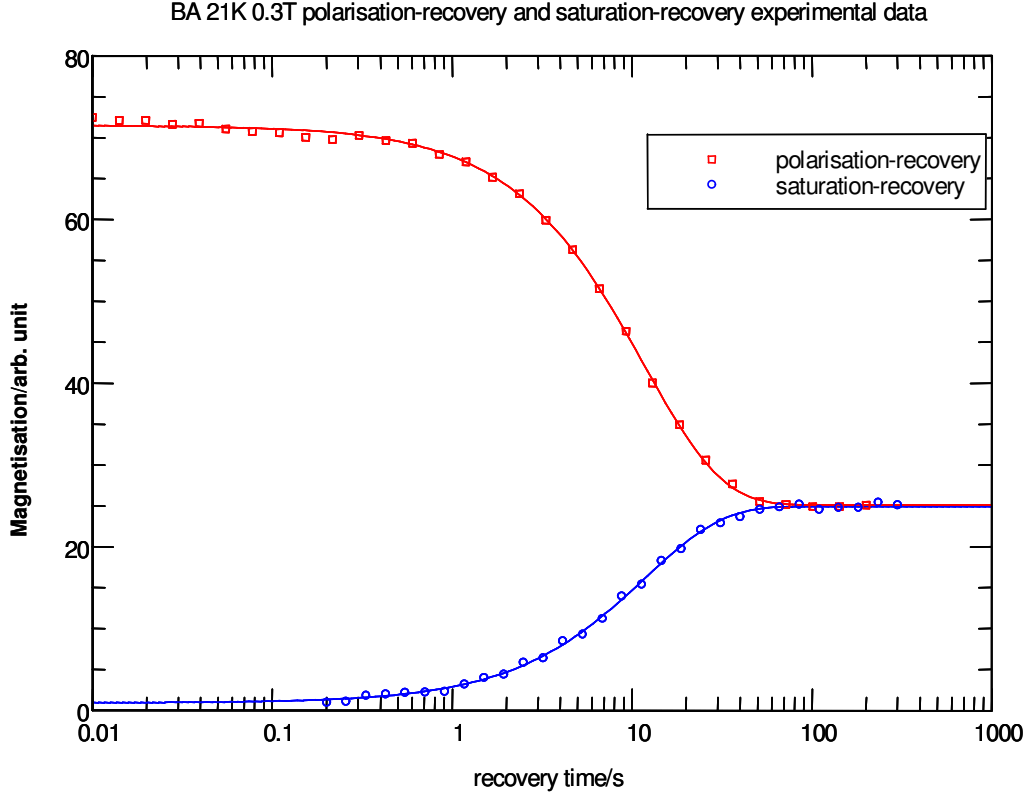
Fig 3.21 A comparison of polarisation-recovery and saturation-recovery experimental data and curve fit on the BA sample at 21K and 0.3T. The spin-lattice relaxation times extracted from these two curves are consistent with each other. One is $(11.77 \pm 0.22)\,s$ on the saturation-recovery curve, the other one is $(11.73 \pm 0.17)\,s$ on the polarisation-recovery curve. The equilibrium magnetisation in the recovery field is same in the two curves.

Similar to the saturation-recovery field-cycling experiment, this sequence is repeated N times with different evolution time to obtain the spin-lattice relaxation curve as shown in Fig 3.21.

The longitudinal magnetisation recovery equation is the same as equation (3.8), but the initial condition is different to that of saturation-recovery experiment. In the polarisation-recovery experiment, the initial condition is when $t = 0$, $M_z = M_{Pol}$; $t \rightarrow \infty$, $M_z = M_0$; M_{Pol} is the magnetisation built up at high polarising field. The solution of the equation (3.8) is:

$$M_z(t) = M_0 + (M_{Pol} - M_0)\exp\left(-\frac{t}{T_1}\right) \qquad\qquad (3.11)$$

In Fig 3.21, the polarisation-recovery field cycling pulse sequence was applied to measure the spin-lattice relaxation time of BA at 21K and the measurement field was 0.3T; the polarisation field was 1T and polarisation time was 120s; the result is plotted as red squares. The result from saturation-recovery pulse sequence is plotted as blue circles as well. The results from the two different pulse sequences are in good agreement each other.

To improve the signal to noise ratio, the polarisation field is chosen to be much bigger than the recovery field. To build up the magnetisation, the polarisation time is about the T_1 or twice the T_1 in the polarisation field at that temperature. If the polarisation time is too short, the obtained magnetisation will not be big enough to improve the signal quality.

This polarisation-recovery pulse sequence is also employed in the low field experiments, such as NQR, which will be discussed in Chapter 5.

3.7.3.3 Pulse sequences designed for heteronuclear systems

The saturation-recovery and the polarisation-recovery pulse sequences discussed above are the basic pulse sequences employed to study spin-lattice relaxation and therefore the dynamics of the sample, irrespective of whether it is a homonuclear system or a heteronuclear system.

In homonuclear system, these two pulse sequences work very well and give good data. But when they are applied in heteronuclear system, due to the cross relaxation between the two different spin species, spin I and spin S, they are not powerful enough to express the more complex information on cross relaxation. Hence two pulse sequences were designed to investigate the heteronuclear interaction [65, 66]. These pulse sequences are called the heteronuclear preparation-recovery pulse sequence and the heteronuclear cross relaxation pulse sequence.

3.7.3.3a Heteronuclear preparation-recovery pulse sequence

Inspection of the Solomon equations reveals that the effects of cross relaxation can be minimized when the second spin species is at thermal equilibrium at the beginning of the experiment. The pulse sequence that achieves this is shown in Fig 3.22, which was applied on the ^{13}C-BA sample.
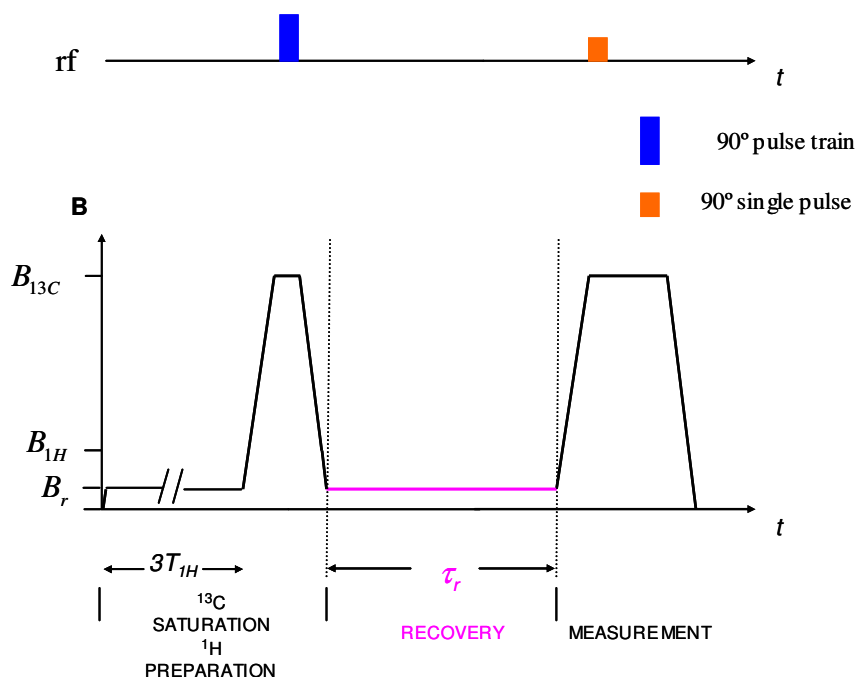
Fig 3.22 Heteronuclear preparation-recovery pulse sequence applied on the ^{13}C-BA sample. B_{13C} and B_{1H} are the resonance fields of ^{13}C (spin S) and ^{1}H (spin I) respectively. B_r is the recovery field for the ^{13}C spin to recover its magnetisation after saturation pulses. The measurement field is on the spin S resonance field to measure the relaxation process of spin S.

1) Preparation of spin I at the recovery field of spin S for at least three times the T_1 of spin I at this field.

2) Saturation of spin S magnetisation with a comb of resonant 90° pulses at the spin S resonance field driving a rapid field excursion.

3) Rapid magnetic field switch to B_r, which was selected for relaxation.

4) Evolution of magnetisation in the recovery field B_r for a period of time.

5) Rapid magnetic field switch back to the spin S resonance field.

6) Measurement of spin S magnetisation with a 90° pulse.

This pulse sequence was employed to satisfy the initial condition which can minimize the cross relaxation effect and measure the relaxation of spin S consistently and accurately according to our simulation based on the theory in chapter 2. The expected initial condition is: when $t = 0$, $I_z = I_0$ and $S_z = 0$. The time zero point is chosen to be just after the saturation pulses.

The experimental data will be discussed in the chapter of ^{13}C-BA experiment.

3.7.3.3b Heteronuclear cross-relaxation pulse sequence

Field-cycling can be used to monitor cross relaxation between the two spin species: as part of this thesis, we have developed a new pulse sequence for this purpose. The pulse sequence is shown in Fig 3.23, which was applied on the sample of TFTA.

As reviewed in the theory chapter 2, when the initial condition at $t = 0$, is $I_z = I_0$ and $S_z = 0$, the expression for the time dependence of the spin I magnetisation is

$$\langle I_z(t) \rangle = -\frac{\sigma S_0}{R_1 - R_2}\left(\exp(-R_1 t) - \exp(-R_2 t)\right) + I_0 \tag{3.12}$$

It is a combination of equation (2.54)

$$\begin{cases} \langle I_z \rangle = I_0\left(c_1^I \exp(-R_1 t) + c_2^I \exp(-R_2 t)\right) + I_0 \\ \langle S_z \rangle = S_0\left(c_1^S \exp(-R_1 t) + c_2^S \exp(-R_2 t)\right) + S_0 \end{cases}$$

and equation (2.56)

$$\begin{cases} c_1^I = -\frac{\sigma}{R_1 - R_2}\frac{S_0}{I_0} \\ c_2^I = \frac{\sigma}{R_1 - R_2}\frac{S_0}{I_0} \end{cases}$$
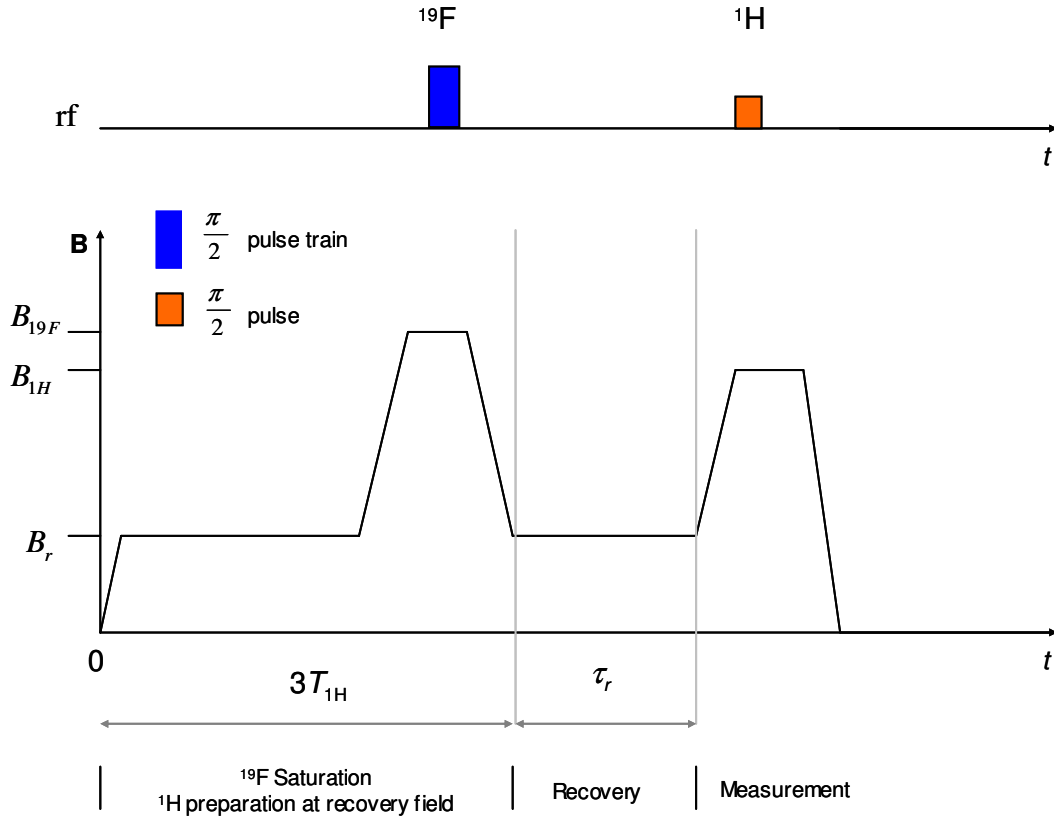
Fig 3.23 Heteronuclear cross-relaxation pulse sequence applied on the sample of TFTA. The only difference with the pulse sequence in Fig 3.22 is the measurement field. In this pulse sequence, we measure the magnetisation of spin I instead of spin S.

The magnetisation recovery curve of spin I in this pulse sequence is shown in Fig 3.24. By fitting the curve in the Fig 3.24 to the equation (3.12), we extracted four parameters from the experimental data, recorded as $c_1^I = -\dfrac{\sigma S_0}{R_1 - R_2}$, R_1, R_2 and I_0.

Therefore the off-diagonal element σ was calculated directly from the four parameters which were extracted from the magnetisation recovery curve,

$$\sigma = -\frac{c_1^I}{I_0}(R_1 - R_2)\frac{I_0}{S_0} = -\frac{c_1^I}{I_0}(R_1 - R_2)\frac{\gamma_I}{\gamma_s} \tag{3.13}$$

By measuring the field dependence curve of the off-diagonal element, we can extract the correlation rate τ_c^{-1} accurately. We will discuss this pulse sequence later in the chapter of TFTA.

TFTA 20K 3T1 3500Gauss
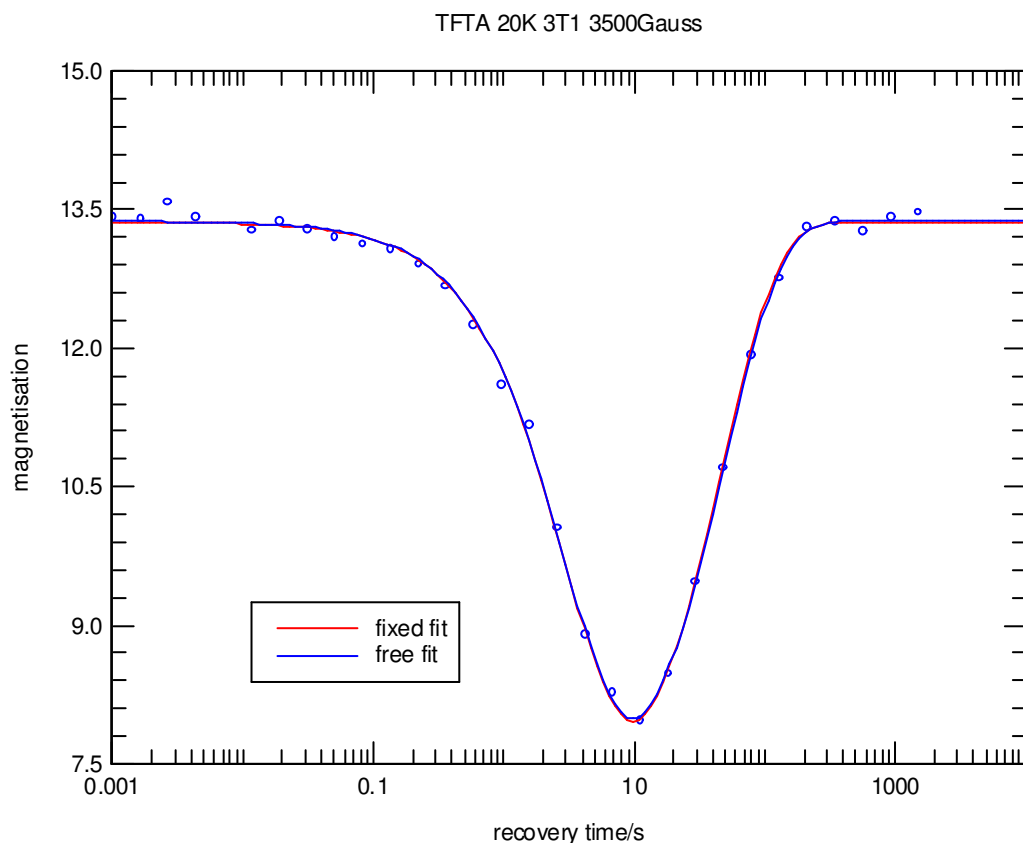
Fig 3.24 Magnetisation recovery curve of spin I by the heteronuclear cross relaxation pulse sequence recorded on the sample TFTA at 20K and at the recovery field 3500Gauss. Due to the fact the R_1 and R_2 can be measured by other method, we can get a more accurate R_1 and R_2, and fix them in the fitting equation to get the other two parameters c_1^I and I_0. These four parameters were employed to calculate the off-diagonal element σ. For the data recorded in this figure, the off-diagonal element $\sigma = (0.135\pm0.003)\, s^{-1}$.

3.7.4 Curve fit and simulation of our experimental data

We have introduced how to extract the spin-lattice relaxation time constants by the fit to the magnetisation recovery curves. Hence we can have two kinds of curves to investigate the dynamics of the sample. One is the temperature dependence of the spin-lattice relaxation time at a fixed field; the other is the field/frequency dependence of the spin-lattice relaxation time at a fixed temperature.

As reviewed in Chapter 2, the parameters such as the energy asymmetry A, dipolar interaction constant C_{HH} (homonuclear), C_{CH}, C_{FH} (heteronuclear), incoherent

tunnelling rate constant k_0, high temperature activation energy V, and correlation time τ_c, etc, are needed to depict the dynamics of the sample. Some parameters can be extracted directly from the temperature dependence curve of the spin-lattice relaxation time and the field dependence curve of the spin-lattice relaxation time while other parameters need to be calculated or to be simulated from the two curves.

The temperature dependence curve of the proton spin-lattice relaxation time in ^{13}C-BA sample measured at 37.8MHz is illustrated in Fig 3.25.

We know, in low temperature regime, $\Gamma^{LT} = k_0 \coth\left(\dfrac{A}{2k_B T}\right)$, the correlation rate is close to the incoherent tunnelling rate constant k_0, which means in the expression of the spin-lattice relaxation time $T_1^{-1}(\omega, T) = C_D \operatorname{sech}^2\left(\dfrac{A}{2k_B T}\right)\left[\dfrac{\tau_c}{1+\omega^2\tau_c^2} + \dfrac{4\tau_c}{1+4\omega^2\tau_c^2}\right]$, the correlation time τ_c is a constant, and

$$T_1^{-1}(\omega, T) \propto \operatorname{sech}^2\left(\frac{A}{2k_B T}\right) \propto \frac{\exp(A/k_B T)}{\left(1+\exp(A/k_B T)\right)^2} \cong \frac{1}{\exp(A/k_B T)}. \tag{3.14}$$

Therefore we get the fit equation, as shown in equation (3.15), of the temperature dependence curve in low temperature regime.

$$T_1(\omega, T) \propto \exp\left(\frac{A}{k_B T}\right) \tag{3.15}$$

Thus the energy asymmetry A can be extracted directly from the low temperature region on the temperature dependence curve of the spin-lattice relaxation time. In the case investigated in Fig 3.25, the energy asymmetry is $A/k_B = 80.7 \pm 0.9 K$. When we perform a computer simulation to fit both the temperature dependence and the field dependence of the spin-lattice relaxation time to get a more accurate dynamics expression for the sample, this energy asymmetry from the fit of low temperature regime will be a reference value to make a first step estimation.

In high temperature regime, the correlation rate is

$$\Gamma^{HT} = \tau_0^{-1}\left[\exp\left(-\frac{V}{K_B T}\right) + \exp\left(-\frac{V-A}{K_B T}\right)\right]$$ and in the expression of the spin-lattice

relaxation time $T_1^{-1}(\omega,T) = C_D \operatorname{sech}^2\left(\frac{A}{2k_B T}\right)\left[\frac{\tau_c}{1+\omega^2\tau_c^2} + \frac{4\tau_c}{1+4\omega^2\tau_c^2}\right]$,

$\operatorname{sech}^2\left(\frac{A}{2k_B T}\right) \to 1$. Therefore leading to the approximate fit equation for which we

can make an estimation of the parameter V,

$$T_1^{-1}(\omega,T) \propto \tau_c = \left(\Gamma^{HT}\right)^{-1} \text{ or } T_1\ (\omega,T) \propto \Gamma^{HT} \tag{3.16}$$
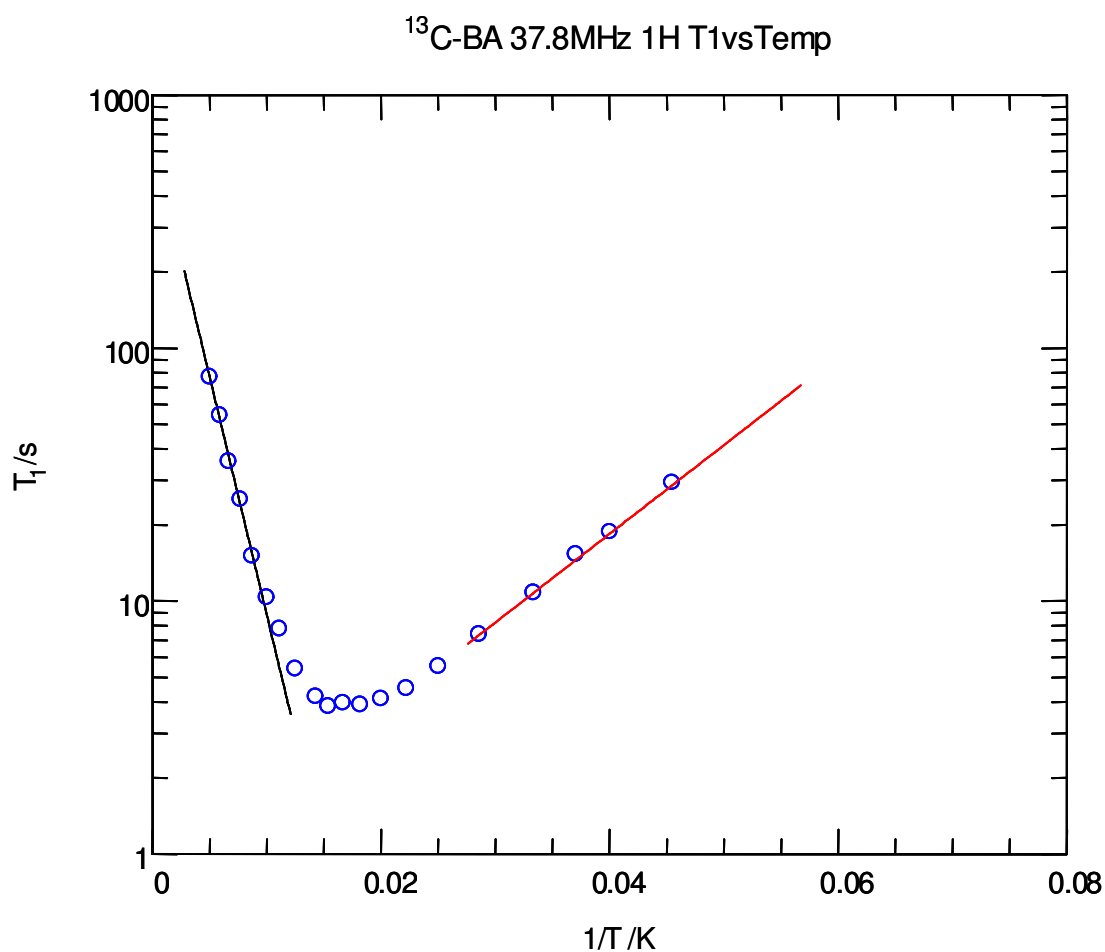
Fig 3.25 The temperature dependence of the spin-lattice relaxation time in ^{13}C-BA. The red fit at low temperature is to find the value of energy asymmetry. The black fit at high temperature is to investigate the barrier when the dynamics is the Arrhenius law.

In the expression of high temperature correlation rate, $\exp\left(-\dfrac{V-A}{K_B T}\right)$ will be

dominant. So when we fit the data in high temperature regime, the value $\dfrac{V-A}{K_B}$ is the

gradient. In the case investigated in Fig 3.25, $\dfrac{V-A}{K_B} \cong 433K$, therefore

$V/k_B \cong 433 + 80 = 513\,K$, is a good first estimate.

These estimations from the T_1 versus 1/T curve provide preliminary estimations which will help us to find the best values of A and V from a full computer simulation.

In the expression of $T_1^{-1}(\omega,T) = C_D \, \mathrm{sech}^2\left(\dfrac{A}{2k_B T}\right)\left[\dfrac{\tau_c}{1+\omega^2 \tau_c^2} + \dfrac{4\tau_c}{1+4\omega^2 \tau_c^2}\right]$, we know

the frequency ω, the energy asymmetry A, and the dipolar constant C_D which can be calculated from the structure or extracted from the spectral density curves (will be discussed next). The only unknown at a given temperature, the correlation time τ_c could be obtained by solving the equation. Thus the correlation rate τ_c^{-1} versus 1/T curve can be transferred directly from the T_1 versus 1/T curve. This transferred curve is employed to check our theory, to help us find the best parameters especially for the intermediate temperature regime and to compare with the correlation rate extracted directly from the spectral density curves. This kind of method was applied to analyse the data before the fast field-cycling technique was available. The result is shown in Fig 4.13, Chapter 4. The results from this method and from the spectral density curves are in perfect agreement with each other.

Here we have discussed the information we could obtain from $T_1^{-1}(\omega,T)$ curve when ω is a constant. To get whole profile of $T_1^{-1}(\omega,T)$ and the dynamics of the sample, the $T_1^{-1}(\omega,T)$ results need to be discussed when temperature T is a constant.

The expression of $T_1^{-1}(\omega,T)$ can be rewritten as follows when temperature T is a constant (referred to equation (2.47)),

$$T_1^{-1}(\omega) = c\left[\frac{\tau_c}{1+\omega^2\tau_c^2} + \frac{4\tau_c}{1+4\omega^2\tau_c^2}\right] = c\left[\frac{\tau_c}{1+\gamma^2 B^2\tau_c^2} + \frac{4\tau_c}{1+4\gamma^2 B^2\tau_c^2}\right]$$

$$= \frac{c}{\gamma}\left[\frac{1}{1/\gamma\tau_c + \gamma\tau_c B^2} + \frac{4}{1/\gamma\tau_c + 4\gamma\tau_c B^2}\right]$$

(3.17)

where

$$c = C_D \operatorname{sech}^2\left(\frac{A}{2k_B T}\right)$$

(3.18)

c is a constant when temperature is a constant. The two parameters in this equation, c and τ_c, can be directly determined by fitting the spectral density curve to this equation.

The spectral density measured at 18K on BA sample by field-cycling experiments is shown in Fig 3.26. Equation (3.17) was fitted to the data, the correlation rate was $\tau_c^{-1} = (1.507 \pm 0.006) \times 10^8 s^{-1}$ and the amplitude was $c = (2.484 \pm 0.006) \times 10^6 s^{-2}$ in this case.

BA 18K spectral density
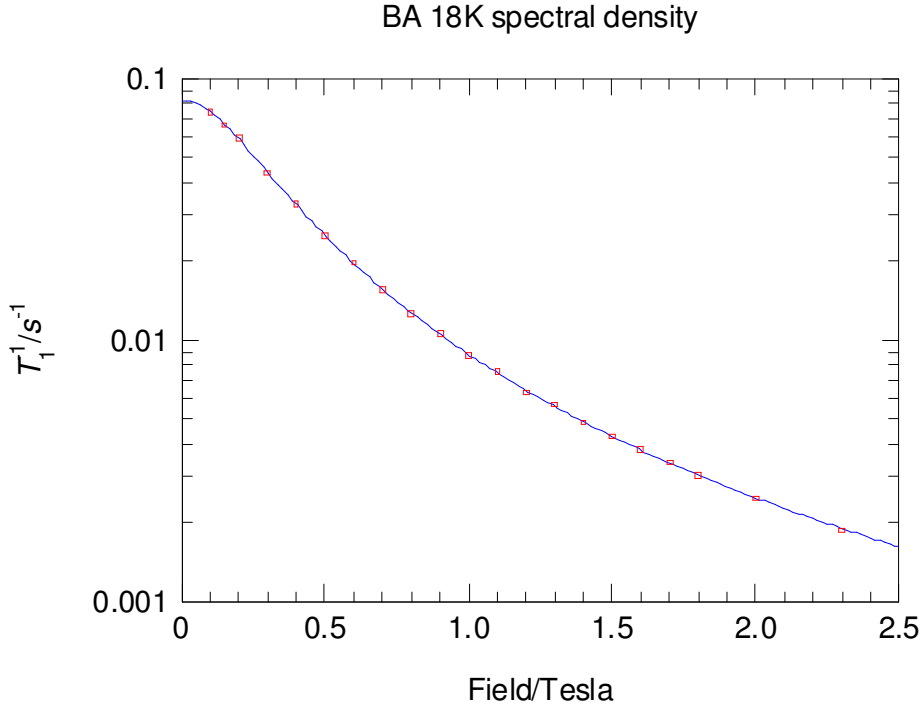
Fig 3.26 The field dependence of the spin-lattice relaxation time measured at 18K on BA sample.

If the spectral density curves were measured at a set of temperatures (as for the BA sample which will be discussed in Chapter 4), by fitting the spectral density curves with expression (3.17), the τ_c^{-1} vs 1/T (the correlation rate versus inverse temperature)

curve and the c vs 1/T curve were therefore obtained. The former curve (τ_c^{-1} vs 1/T) can be employed to investigate the theoretical model of the correlation rate, while the latter one (c vs 1/T) can be used to extract the parameters C_D and A by fitting with the equation (3.18). The results will be shown in Fig 4.12 and Fig 4.13, Chapter 4.

In conclusion, we now have two methods for evaluating C_D, A and τ_c^{-1} vs 1/T curve, (the second method for C_D is to calculate it directly according to equation (2.52)). A large parameter space encompassing frequency and temperature is available for our experiments, so we are able to obtain good estimates of the dynamical parameters that we can use to confront theories for tunnelling dynamics.

However all discussed above is based on homonuclear system where a single spin-lattice relaxation time characterises the relaxation process. The data analysis and curve fit will be more complex in heteronuclear systems. The details will be discussed later in the chapters on heteronuclear samples.

Chapter 4: The dynamics of proton transfer in the hydrogen bonds of benzoic acid [67]

4.1 Introduction

The dynamics of proton transfer in the hydrogen bonds has been of topical interest in recent years. The system represents one of the most fundamental chemical reactions and plays a crucial role in a variety of important chemical and biological processes.

A full theoretical description of the proton transfer process requires knowledge of the potential energy surface (PES) characteristic of the molecule. The proton displacement is always accompanied by readjustments in the molecule so the PES is multi-dimensional. To a first approximation the potential energy along the trajectory of the particle through the multi-dimensional PES may be described as a double minimum potential (DMP) (Fig 4.1a and Fig 4.1b). For an isolated molecule, this DMP is symmetrical, however in the solid state, asymmetry in the environment introduces an asymmetry into the depth of the wells. Therefore, when a particle moves between the two wells, energy must be exchanged with its environment; the process is dissipative and consequently the dynamics of the proton may be modelled as that of a particle in a DMP which is coupled to a bath of phonons.

The light mass of the proton means that its de Broglie wavelength can achieve a value which is of similar order to the distance the proton moves. The classically forbidden barrier region of the potential exhibits transmissibility arising from the partial delocalization of the particle wavefunction, so tunnelling matrix elements which connect the potential minima provide pathways for the proton dynamics. Consequently quantum effects dominate the low temperature dynamics and make an important contribution to the motional spectrum at all temperatures.

Indeed, for carboxylic acid dimers in the solid state at low temperature, the proton dynamics are dominated by phonon assisted tunnelling. This system, exhibiting a concerted double proton transfer motion in the pair of hydrogen bonds bridging the dimer, is established as a model system for translational atomic tunnelling.

Classical 'Hopping'

$$\tau_c^{-1} = \tau_0^{-1} \exp\left(-\Delta E \middle/ k_B T \right)$$
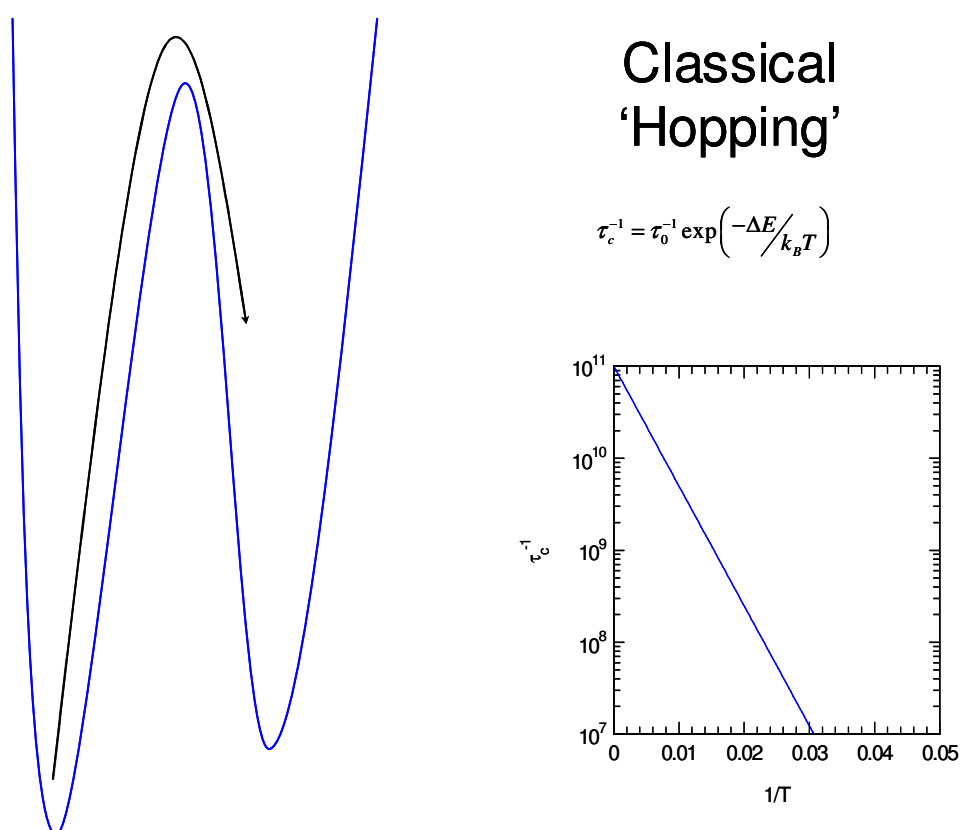
Fig 4.1a Classical hopping over the barrier in DMP

An interesting perspective arises in the description of these proton transfer dynamics; at low temperature (typically T<50K) tunnelling dominates and the proton transfer rate is independent of temperature as shown in Fig 4.1b. However, when the temperature is increased, the dynamics acquires more classical characteristics and more closely to Arrhenius behaviour. Therefore the system provides the opportunity to investigate the so-called quantum-to-classical transition, a topic which is becoming increasingly important as issues of coherence and decoherence are raised in the context of, for example, small scale devices, quantum computing and tunnelling on a

multi-dimensional potential energy surface.
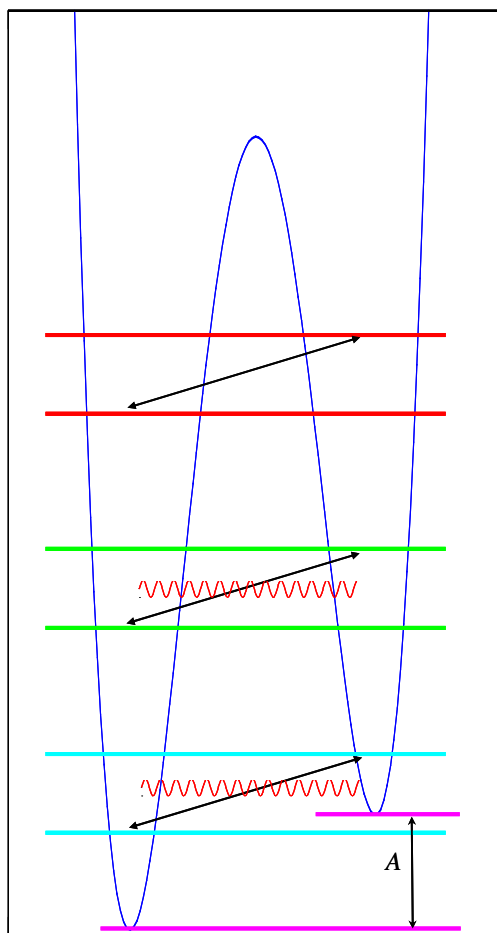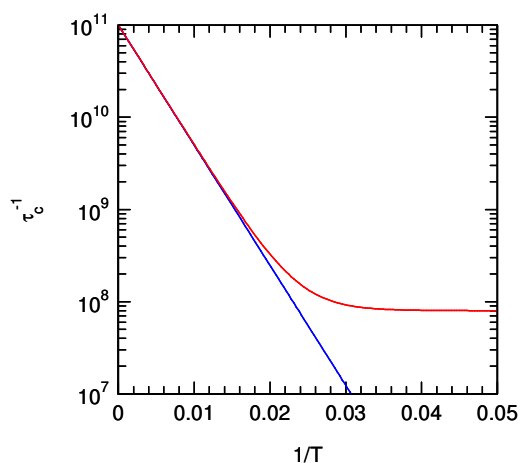
Fig 4.1b Phonon assisted quantum tunnelling in an asymmetric DMP

4.2 Benzoic Acid (BA): the model system

The structure of the benzoic acid dimers is illustrated in Fig 4.2. There are two tautomeric forms (L and R) and the interchange between the two is mediated by double proton transfer within the bridging hydrogen bonds. In the isolated dimer the energies of the two tautomers are equal, however, in the solid state the crystal field breaks the symmetry and one tautomer is energetically favoured. We characterise the energy asymmetry by the symbol A as shown in Fig 4.1b.
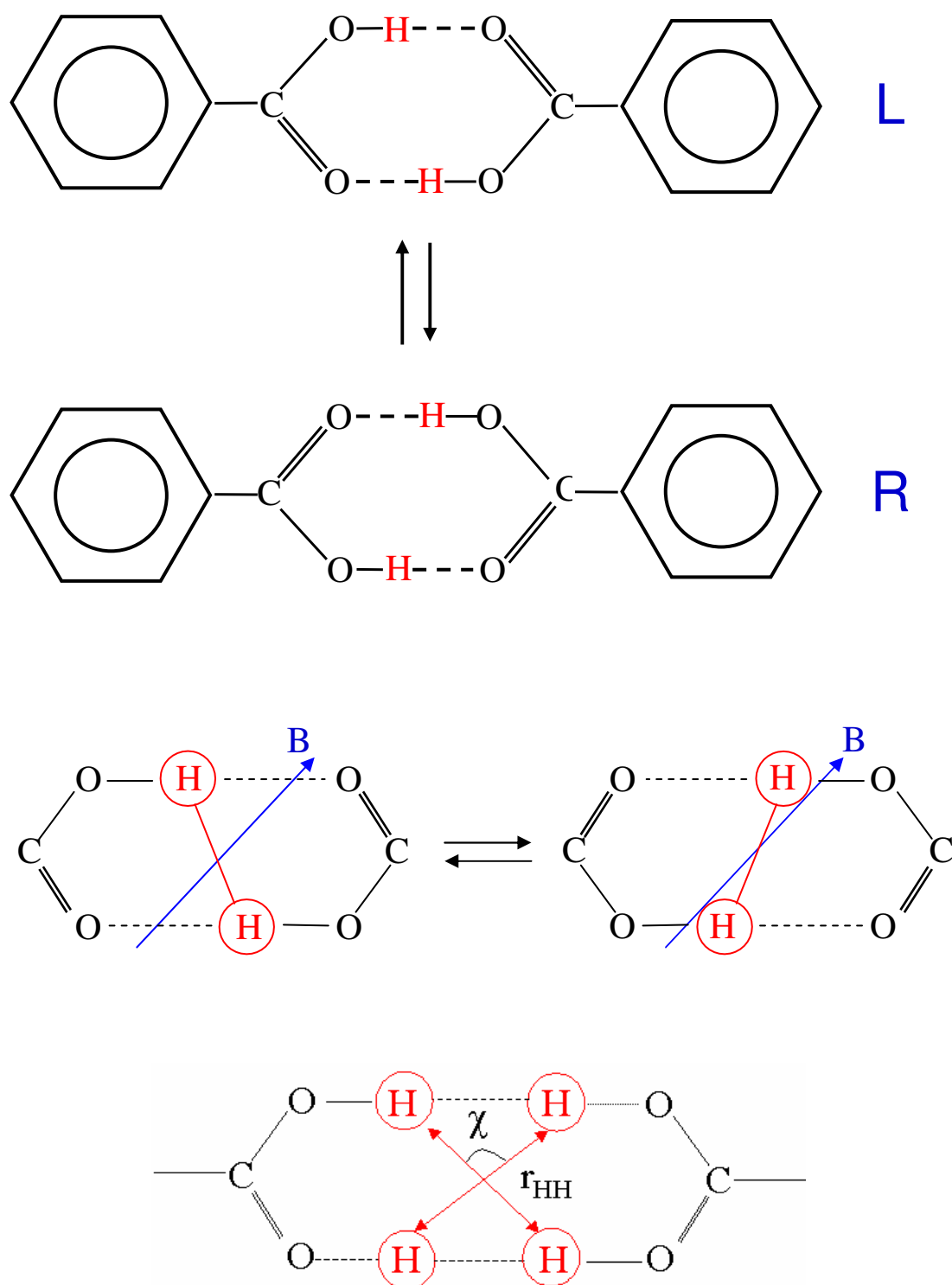
Fig 4.2 The two tautomers of BA dimer showing the double proton transfer process in the bridging hydrogen bonds which mediates the conversion between the two tautomers. χ is the angle subtended by the inter-nuclear vectors and r_{HH} is the intra-dimer proton-proton distance.

It is the dipole-dipole interaction that is modulated by the molecular dynamics and which gives rise to transitions that reveal the tunnelling dynamics. The spin-lattice relaxation time dominated by the proton-proton dipolar was discussed in the theory section (Chapter 2). In our experiment, the influence of proton tunnelling is investigated by making direct measurement of the spectral density function from the dispersion of the spin-lattice relaxation time using field-cycling relaxometry, which enables us to analyse the correlation rate τ_c^{-1} (as shown in Fig 4.1a and Fig 4.1b) directly.

4.3 Comparison of two theories

Before discussing the experiments, we need to compare two theoretical descriptions of the dynamics of the proton transfer in the hydrogen bonds. One is the theory of Skinner and Trommsdorff (ST) [5], which has been discussed in the theory section (Chapter 2) and will be summarised here; the other one is proposed by Latanowicz and Reynhardt (LR) [23], which will be described here.

For a homonuclear system the spin-lattice relaxation time T_1 can be written as follows:

$$T_1^{-1} = C\left[J^{(1)}(\omega) + J^{(2)}(\omega) \right],$$
(4.1)

where C is a constant and $J^{(m)}(\omega)$ is the spectral density function which is the Fourier transform of the correlation function for the spatial part $F^{(m)}$ of the dipolar interaction between nuclei,

$$J^{(m)}(\omega) = \int_{-\infty}^{+\infty} \left\langle F^{(m)^*}(t+\tau) \cdot F^{(m)}(t) \right\rangle \exp(-i\omega\tau)d\tau .$$
(4.2)

ST theory and LR theory differ in the evaluation of the spectral density functions, equation (4.2). In both approaches stochastic jumps are invoked between the two wells and a variety of pathways are identified. The height and width of the interceding

barrier determines the magnitude of the tunnelling matrix elements which characterise through barrier pathways. The asymmetry of the wells means that interaction with a phonon heat bath is necessary to mediate the proton transfer. Therefore coherent tunnelling is quenched and all barrier crossing processes are necessarily incoherent.

At low temperature, through barrier tunnelling pathways involving deep-lying vibrational states of the DWP dominate the dynamics. This is the regime of phonon-assisted tunnelling and at the lowest temperatures these connect only the ground state of each well and involve only single phonons. With increasing temperature so higher vibrational states become populated and these also provide conduits for through barrier tunnelling, albeit with greater barrier transparency since the barrier region is narrower in these excited states. With sufficient thermal energy then barrier crossing can emulate classical Arrhenius behaviour.

In LR theory the concept of over barrier hopping in the classical sense appears to be invoked more literally, whereas in ST theory this regime is considered more as a limiting sum of barrier crossing processes via states with elevated energies. These could conceivably include states above the barrier but for BA it is known that the actual barrier is approximately one order of magnitude larger than the measured Arrhenius activation energy at room temperature.

4.3.1 ST theory

The proton transfer rate is an algebraic sum of the rates of various barrier crossing processes since the probabilities of interchange between the two sites are additive. In the simplest approximation just two processes are considered, ground state tunnelling and pseudo-classical barrier hopping. The latter has Arrhenius form and is classified as pseudo-classical because it is well established that even at room temperature when the dynamics appear Arrhenius, the dynamics are in fact mediated by through barrier tunnelling pathways. The proton transfer rate is then characterised by the inverse correlation time:

$$\tau_c^{-1} = \Gamma_{tu}^{(0)} + \Gamma_{Arrh},\tag{4.3}$$

where $\Gamma_{tu}^{(0)}$ is the ground state tunnelling rate and Γ_{Arrh} is the pseudo-classical barrier hopping rate. They are given by

$$\begin{cases} \Gamma_{tu}^{(0)} = k_0 \coth\left(\dfrac{A}{2k_B T}\right) \\[4mm] \Gamma_{Arrh} = \tau_0^{-1}\left[\exp\left(-\dfrac{V}{k_B T}\right) + \exp\left(-\dfrac{V-A}{k_B T}\right)\right] \end{cases}\tag{4.4}$$

where k_0 is the incoherent tunnelling rate constant which is proportional to the square of the tunnelling matrix element, V is the activation energy for thermally activated hopping from the lowest well.

More refined approximations can be obtained by adding terms to allow for through barrier tunnelling in low lying excited states [11] and multiple phonon processes [69]. However, at whatever level of approximation, what characterises this theory is the fact that the dynamics are defined by a single correlation time. This being the case, for powder samples, assuming stochastic interchange between two tautomers, the spectral density functions are evaluated as follows [53, 54]:

$$J^{(m)}(\omega) = J^{(m)}(\omega,\tau_c) = S^m K_D(T)\left[\frac{2\tau_c}{1+(\omega\tau_c)^2}\right],\tag{4.5}$$

where $K_D(T)$ is a temperature dependent constant determined by the spatial parts of the dipolar interaction, $S^1 = 2/15$ and $S^2 = 8/15$. So the expression for the spin-lattice relaxation rate is:

$$T_1^{-1}(\omega) = C_D \operatorname{sech}^2\left(\frac{A}{2k_B T}\right)\left(\frac{\tau_c}{1+\omega^2\tau_c^2} + \frac{4\tau_c}{1+(2\omega)^2\tau_c^2}\right),\tag{4.6}$$

where A is the energy asymmetry of the two wells and C_D is a dipolar constant. The angular frequency can be probed via the Larmor frequency, $\omega_L = \gamma B$, associated with spin precession in the magnetic field B (γ is the proton magnetogyric ratio). In field-cycling NMR relaxometry, the technique is to record T_1^{-1} as a function of magnetic field thereby directly plotting out the spectral density functions [21, 46]. $T_1^{-1}(B)$ (equation (4.6)) represents a superposition of two Lorentzians with half widths at half

maximum equal to the inverse correlation time τ_c^{-1} and $\tau_c^{-1}/2$. the respective amplitudes have the ratio of 1:4 and diminish with decreasing temperature according to $\mathrm{sech}^2\left(\dfrac{A}{2k_BT}\right)$.

4.3.2 LR theory

In LR theory, tunnelling and classical barrier hopping retain their separate identities. The pathway undertaken by the particles when the system interchanges between the two sites remains knowable to the observer. Distinguishable spectral features appear corresponding to each pathway.
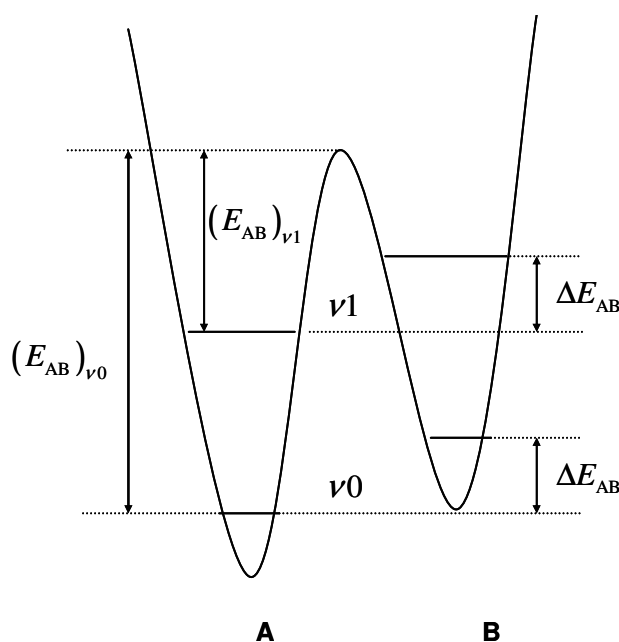
Fig 4.3 The potential energy diagram for the proton transfer in asymmetric DMP. $\nu 0$ and $\nu 1$ are the local vibrational states.

The spin-lattice relaxation rates due to the dipole-dipole interaction of a homonuclear pair (i, s) are given by

$$\frac{1}{T_1^{is}} = \frac{9}{8}\left[J_{is}^{(1)}(\omega) + J_{is}^{(2)}(2\omega) \right],$$
(4.7)

If the population of molecules and the Boltzmann distribution law are taken into account, the relaxation rate is given by

$$T_1^{-1} = n_{v0}\left\{\frac{1}{i}\sum_{i,s}\frac{1}{\left(T_1^{is}\right)_{v0}}\right\} + n_{v1}\left\{\frac{1}{i}\sum_{i,s}\frac{1}{\left(T_1^{is}\right)_{v1}}\right\} + \cdots, \qquad (4.8)$$

where n_{v0}, n_{v1},......, are the fractions of molecules in the separate vibrational levels associated with the average energies E_{v0}, E_{v1},......, of the ground, first and other excited vibrational levels. Because the population of molecules in the second excited vibrational level is very low, it is reasonable to take into account only two vibrational levels: ground level and first excited level. Therefore,

$$\begin{cases} n_{v0} + n_{v1} = 1 \\ n_{v1}/n_{v0} = \exp\left(-\left(E_{v1} - E_{v0}\right)/RT\right) \end{cases} \qquad (4.9)$$

where $R = N_A k_B$, N_A is Avogadro constant and k_B is Boltzmann constant. So

$$\begin{cases} n_{v1} = \dfrac{1}{\exp\left[\left(E_{v1} - E_{v0}\right)/RT\right] + 1} \\[4mm] n_{v0} = \dfrac{\exp\left[\left(E_{v1} - E_{v0}\right)/RT\right]}{\exp\left[\left(E_{v1} - E_{v0}\right)/RT\right] + 1} \end{cases} \qquad (4.10)$$

The spectral density in LR theory is characterised by three correlation rates, which is a significant difference with the spectral density in ST theory, for the dynamics consisting of thermally activated jumps between two sites **A** and **B** and incoherent tunnelling, as follows:

$$J^{(m)}(\omega) = J^{(m)}\left(\omega, \tau_{vx}^{ov}, \tau_{vx}^{tu}\right)$$

$$= \frac{S^m}{C_0}\left[C_1 C_2 \frac{2\tau_{vx}^{ov}}{1+\left(\omega\tau_{vx}^{ov}\right)^2} + C_1 C_2 \frac{2\tau_{vx}^{tu}}{1+\left(\omega\tau_{vx}^{tu}\right)^2} + C_2^2 \frac{2\tau_{vx}}{1+\left(\omega\tau_{vx}\right)^2}\right] \qquad (4.11)$$

where

$$C_0 = \frac{1}{K_{AB}+1}d_{cc}^2(A) + \frac{K_{AB}}{K_{AB}+1}d_{cc}^2(B) \qquad (4.12)$$

$$C_1 = \frac{K_{AB}}{\left(K_{AB}+1\right)^2}\left[K_{AB}^{-1}d_{cc}^2(A) + K_{AB}d_{cc}^2(B) + d_{cc}(A)d_{cc}(B)\left(3\cos^2\theta_{AB}^{is}-1\right)\right] \qquad (4.13)$$

$$C_2 = \frac{K_{AB}}{\left(K_{AB}+1\right)^2}\left[d_{cc}^2(A) + d_{cc}^2(B) - d_{cc}(A)d_{cc}(B)\left(3\cos^2\theta_{AB}^{is}-1\right)\right] \qquad (4.14)$$

$$K_{AB} = \exp\left(\frac{\Delta E_{AB}}{RT}\right) \tag{4.15}$$

$$d_{cc} = \gamma_i \gamma_s \hbar R_{is}^{-3} \tag{4.16}$$

correlation rates for thermally activated jumps:

$$\frac{1}{\tau_{vx}^{ov}} = k_0^{ov}\left\{\exp\left[-\frac{(E_{AB})_{vx}}{RT}\right] + \exp\left[\frac{-(E_{AB})_{vx} + \Delta E_{AB}}{RT}\right]\right\} \tag{4.17}$$

correlation rates for incoherent tunnelling:

$$\begin{cases} \dfrac{1}{\tau_{v0}^{tu}} = k_{v0}^{tu} \dfrac{\exp(\Delta E_{AB}/RT)+1}{\exp(\Delta E_{AB}/RT)-1} = k_{v0}^{tu} \coth\left(\dfrac{\Delta E_{AB}}{2RT}\right) \\ \dfrac{1}{\tau_{v1}^{tu}} = k^{'} \dfrac{1}{\tau_{v0}^{tu}} \end{cases} \tag{4.18}$$

Additionally a complex motion is invoked, involving both tunnelling and over barrier hopping. For this motion the correlation rate is:

$$\frac{1}{\tau_{vx}} = \frac{1}{\tau_{vx}^{ov}} + \frac{1}{\tau_{vx}^{tu}} \tag{4.19}$$

vx indicates $v0$ or $v1$, θ_{AB}^{is} is the angle between $R_{is}(A)$ and $R_{is}(B)$, ΔE_{AB} is the energy asymmetry of the two wells, $(E_{AB})_{vx}$ is the thermally activated energy as shown in Fig 4.3, $S^m = 2/15$, $8/15$ for $m = 1, 2$, respectively, k_0^{ov}, k_{v0}^{tu} and $k^{'}$ are the activation parameters, $k^{'} \gg 1$.

LR theory introduces some restrictions as follows:

- If $J^{(1)}(\omega, \tau_{vx}^{ov}) > J^{(1)}(\omega, \tau_{vx}^{tu})$ and if $\tau_{vx}^{ov} < \tau_{vx}^{tu}$ then $J^{(1)}(\omega, \tau_{vx}^{ov}, \tau_{vx}^{tu}) = J^{(1)}(\omega, \tau_{vx}^{ov})$

- If $J^{(2)}(2\omega, \tau_{vx}^{ov}) > J^{(2)}(2\omega, \tau_{vx}^{tu})$ and if $\tau_{vx}^{ov} < \tau_{vx}^{tu}$ then

    $J^{(2)}(2\omega, \tau_{vx}^{ov}, \tau_{vx}^{tu}) = J^{(2)}(2\omega, \tau_{vx}^{ov})$

These restrictions actually mean the tunnelling spectral densities are eliminated from the spin-lattice relaxation process when the value of this spectral density is comparable with that of classical jumping, and they are based on the assumption that

in the higher temperature range there is no tunnelling process. This assumption is contrary to the ST theory where the classical hopping is associated with incoherent tunnelling even in room temperature and named pseudo-classical hopping, and is in conflict with quantum theory in which quantum phenomenon can happen at any temperature. The lower the temperature is, the more evident the quantum effect will be.

The spectral density will have two typical features according to the LR theory:

- If the LR theory is employed to fit the experimental data, there must be three or more components which are characterised by the three correlation rates: $1/\tau_{\nu x}^{ov}$, $1/\tau_{\nu x}^{tu}$ and $1/\tau_{\nu x}$; there will be multiple spectral density components.

- The restrictions will lead to the discontinuities in the spectral density curve especially in the intermediate and high temperature regimes.

4.4 Experimental results and discussion

4.4.1 Experimental

We have made measurements of the proton spin-lattice relaxation time in the magnetic field range 0.1 to 2.3T at a variety of temperatures from 18K to 80K.

- Benzoic acid (BA), in its natural abundance isotopic form (C_6H_5COOH) was purified and studied as a powder.

- The NMR spectrometer operated at the fixed frequency 50.7MHz, with very short dead time 1.5µs and typical Gaussian calibration curve.

- From 0.4T to 2.3T, the saturation recovery pulse sequence was employed to record the spin relaxation process. When the field was lower than 0.4T, the signal was getting smaller and the signal to noise ratio was getting worse, the polarisation recovery pulse sequence was employed to record the spin relaxation curve.

- In low temperature or high field, when the signal is so big that the amplifiers might be saturated, a measurement pulse factor was introduced into the Visual Basic program to control the amplitude of the measurement pulse. If the polarisation recovery pulse sequence was employed, the polarisation field was also selected to prevent the signal from being saturated.

- The field offsets were selected to make sure that the spectra were always centred within a narrow range of frequency which should be in the top 5% region of the calibration curve.

4.4.2 Experimental results and simulation

According to the comparison of the ST theory and the LR theory, the principal characteristic which distinguishes the ST theory from LR theory is the number of correlation times: in ST theory there is just one, in LR theory tunnelling and classical pathways retain their separate identities to the observer and there are at least three, more as the temperature is increased.

The other characteristic which also distinguishes the ST theory from the LR theory is the discontinuities in the spectral density curve: in ST theory there is no discontinuity, while in LR theory the restrictions prohibiting tunnelling at intermediate temperature lead to the discontinuities especially as the temperature is increased.

Field-cycling NMR has been employed to record the spectral densities and to establish whether the experimental data is consistent with single or multiple correlation times. The data are presented in Fig 4.4.
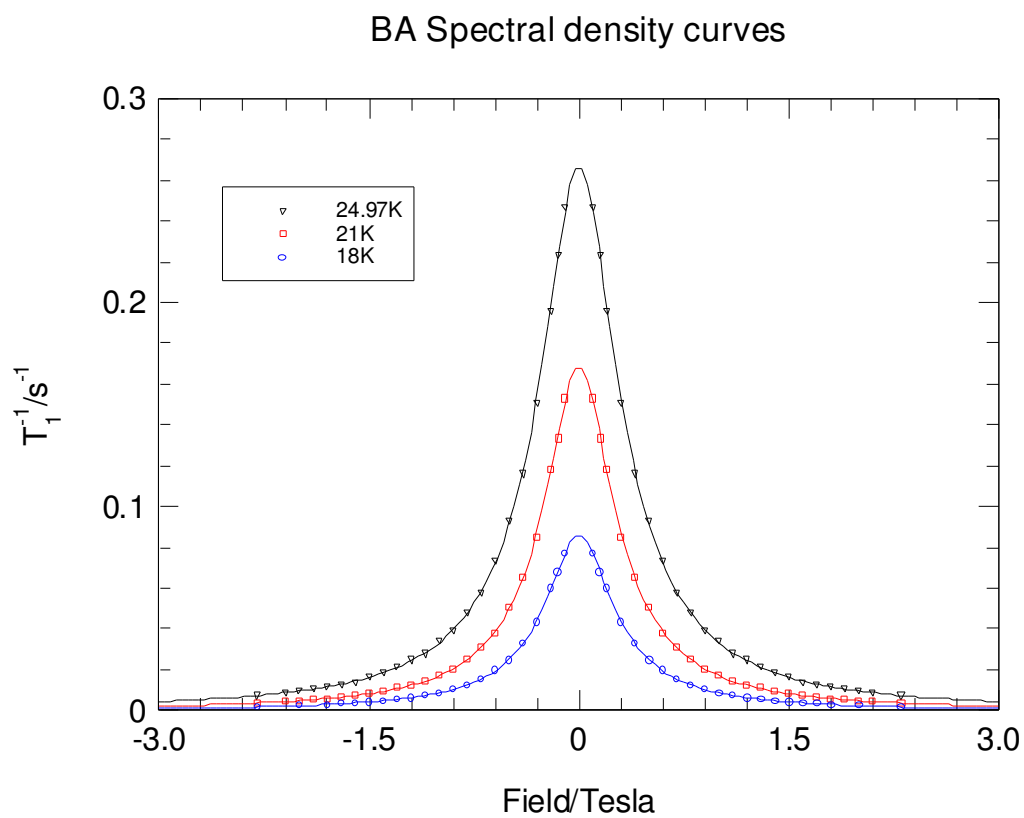
Fig 4.4a The magnetic field dependence of the relaxation rate for benzoic acid recorded at 18K, 21K and 24.97K.

BA Spectral density curves
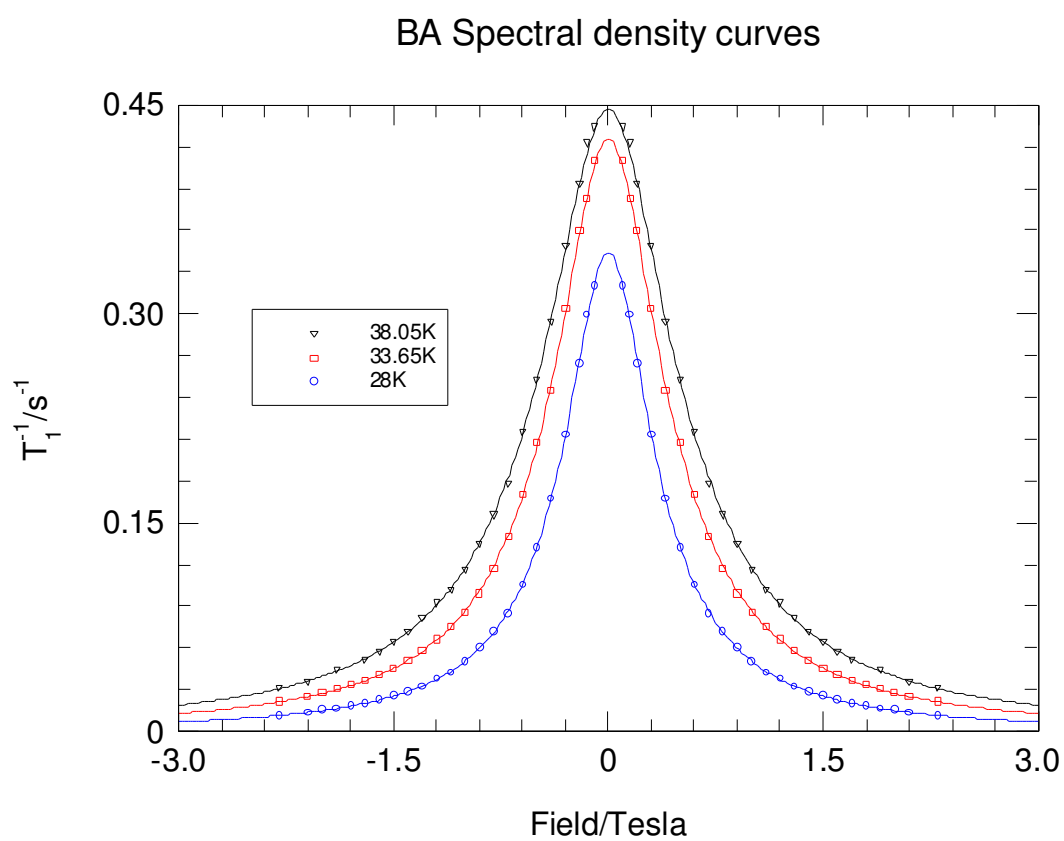
Fig 4.4b The magnetic field dependence of the relaxation rate for benzoic acid recorded at 28K, 33.65K and 38.05K.
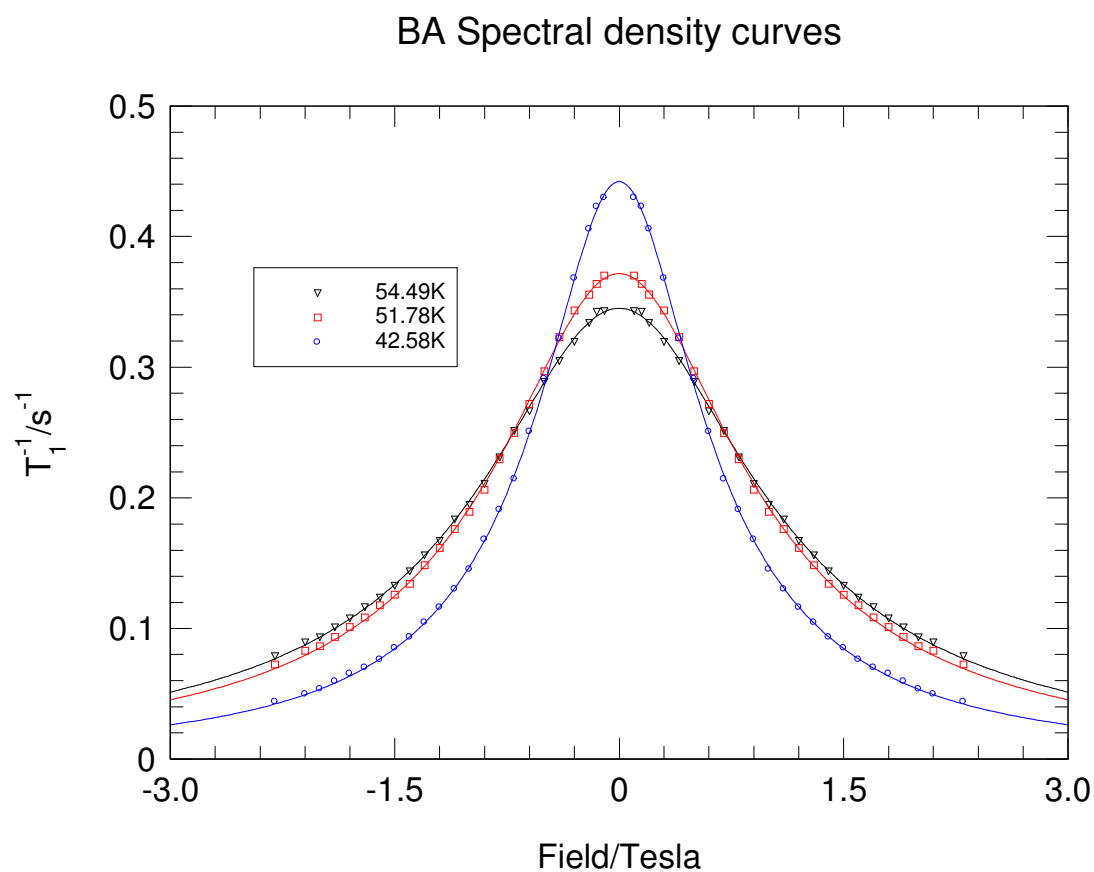
Fig 4.4c The magnetic field dependence of the relaxation rate for benzoic acid recorded at 42.58K, 51.78K and 54.49K.

BA Spectral density curves
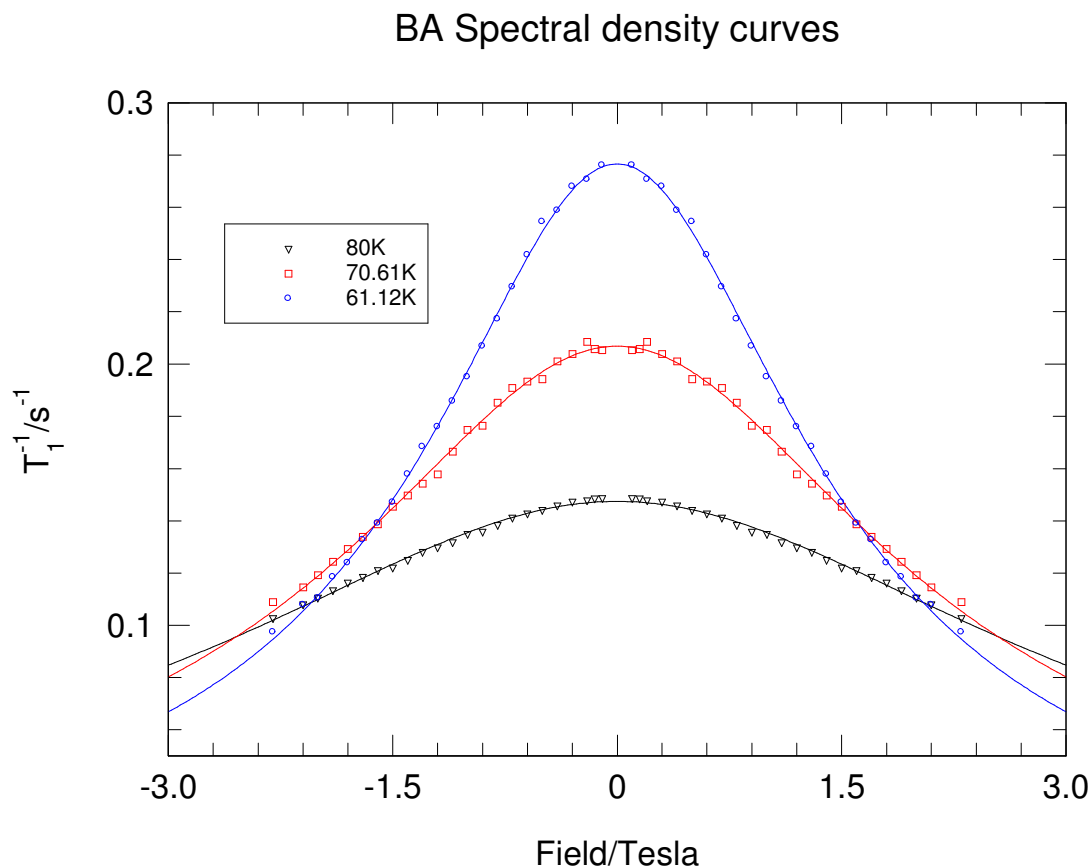
Fig 4.4d The magnetic field dependence of the relaxation rate for benzoic acid recorded at 61.12K, 70.61K and 80K.

The data in all these four figures (Fig 4.4a, Fig 4.4b, Fig 4.4c and Fig 4.4d) record the spectral densities for proton transfer in the intermediate temperature range where proton dynamics interchanges between quantum tunnelling and Arrhenius behaviour. The solid lines are fit to equation (4.6) assuming a single correlation time. The data have been reflected in the B-axis to accentuate the Lorentzian character of the lineshapes.

The equation $T_1^{-1}(\omega, T) = C_D \operatorname{sech}^2\left(\dfrac{A}{2k_B T}\right)\left[\dfrac{\tau_c}{1+\omega^2\tau_c^2} + \dfrac{4\tau_c}{1+4\omega^2\tau_c^2}\right]$ is employed to fit the curve. It is evident that, when temperature is increased, both the amplitude c ($c = C_D \operatorname{sech}^2\left(\dfrac{A}{2k_B T}\right)$(3.18)) and the correlation rate τ_c^{-1} will increase. It is confirmed by the experimental data illustrated in the four figures. The curves are broadening

with increasing temperature: 'the half-width at half-maximum of $L(\omega)$ is τ_c^{-1} and the full width at half-maximum of $L(2\omega)$ is also τ_c^{-1}, so the spectral density provides a direct measurement of the proton transfer rate from a determination of the width of the spectrum' as discussed in Chapter 2. Also the amplitude is increasing when temperature increases. Two parameters extracted from the curves are listed in Table 4.1 for comparison.

Temperature (K)	Amplitude c (s^{-2})	Correlation rate τ_c^{-1} (s^{-1})
18	2.50×10^6	1.460×10^8
21	4.94×10^6	1.465×10^8
24.97	8.81×10^6	1.655×10^8
28	1.26×10^7	1.826×10^8
33.65	1.92×10^7	2.248×10^8
38.05	2.41×10^7	2.675×10^8
42.58	2.87×10^7	3.242×10^8
51.78	3.64×10^7	4.880×10^8
54.49	3.81×10^7	5.514×10^8
61.12	4.21×10^7	7.716×10^8
70.61	4.57×10^7	1.105×10^9
80	4.89×10^7	1.657×10^9

Table 4.1 The amplitude and the correlation rate extracted from the spectral density curves at a set of temperatures.

At each temperature an excellent fit to the experimental data is obtained with just one correlation time. In no spectrum is there any evidence of multiple spectral density components and multiple correlation times.

Simulations to fit the experimental data with the LR theory and the parameters they published in the paper [23] show that only in low temperature range (<20K) the LR theory can fit the experimental data with small error. This is inevitable because the

theories converge at low temperature where there is only ground state incoherent tunnelling with a single correlation time. In their paper, only T_1 vs temperature data at fixed frequency were considered.

As the temperature is increased, the error between the simulation with LR theory and the experimental data gets bigger and bigger and becomes unacceptable when the temperature is higher than 50K (intermediate temperature region).

As the temperature is increased, the discontinuities appear in the spectral density curve of the simulation with LR theory, which are never found in the experimental data and also unreasonable even only in view of the mathematics.

The simulation results and the comparison with ST fit are shown in Fig 4.5 to Fig 4.11, where we can find easily which one is acceptable.
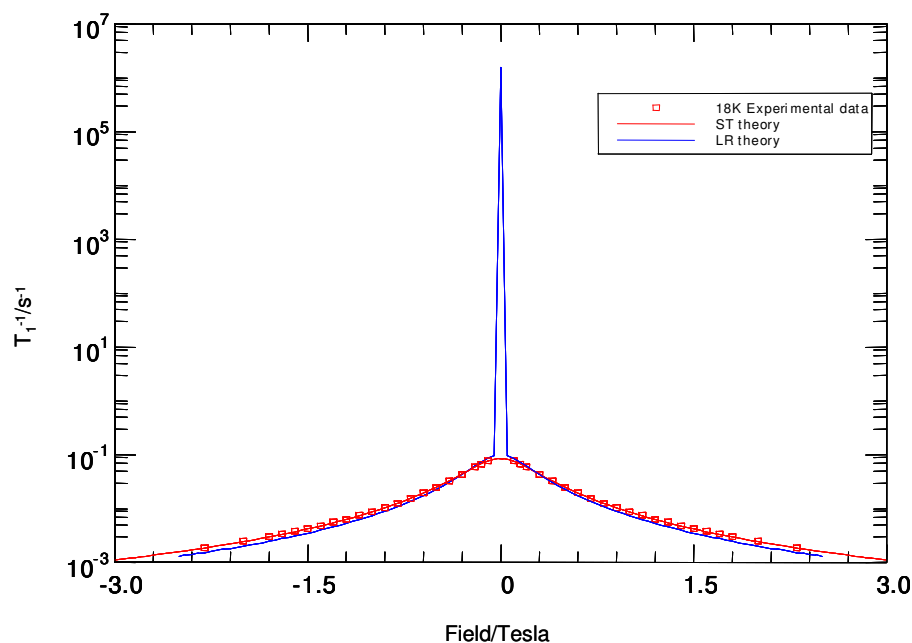
Fig 4.5 Fit the experimental data to ST and LR theories at 18K
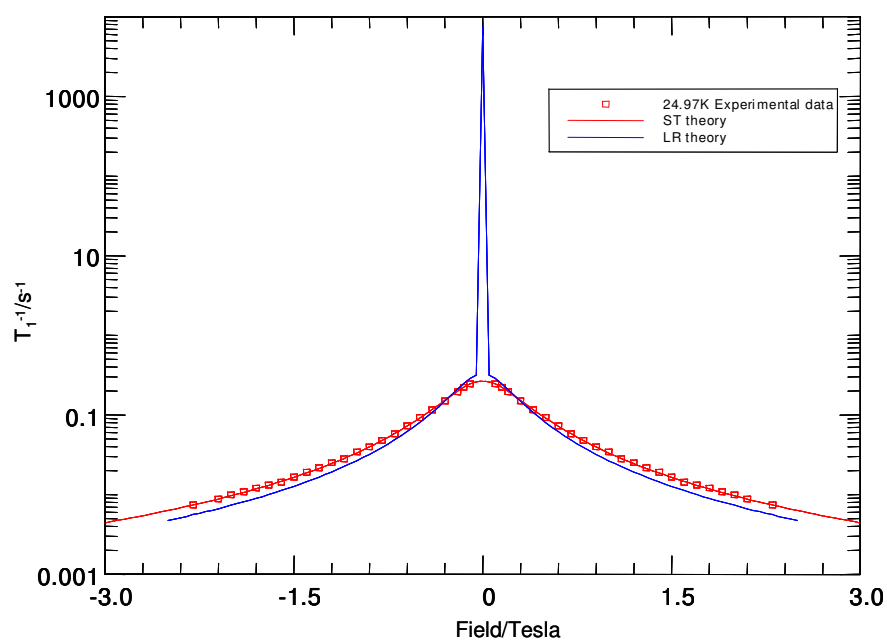
Fig 4.6 Fit the experimental data to ST and LR theories at 24.97K
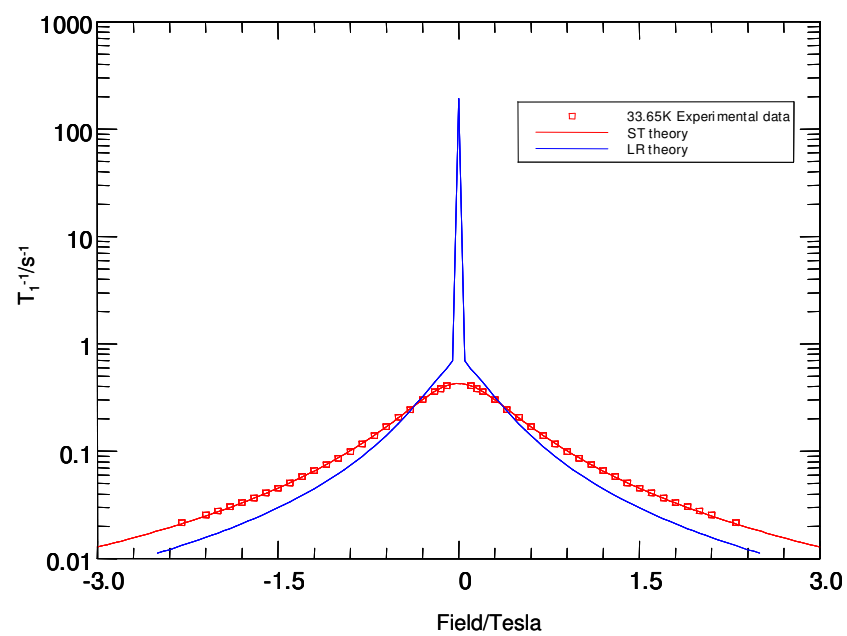
Fig 4.7 Fit the experimental data to ST and LR theories at 33.65K
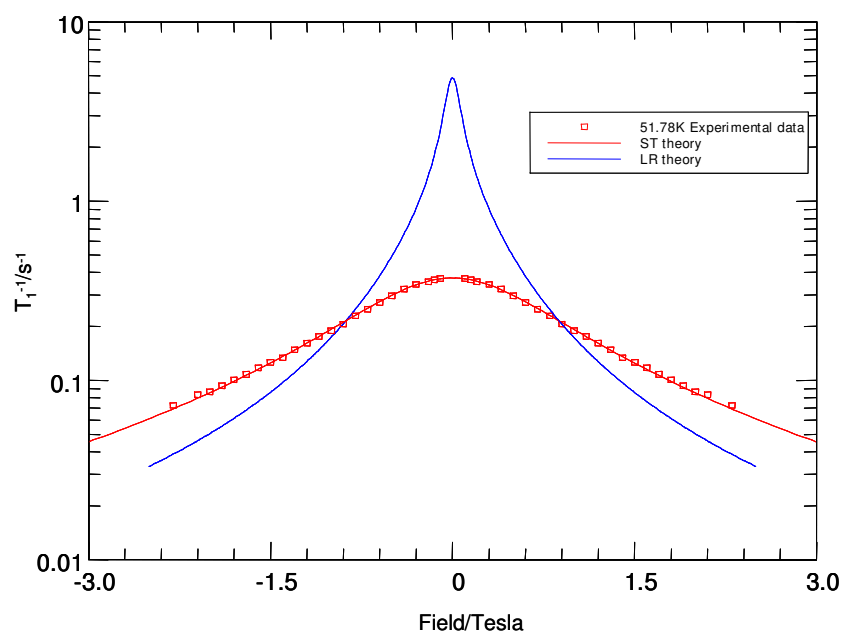
Fig 4.8 Fit the experimental data to ST and LR theories at 51.78K
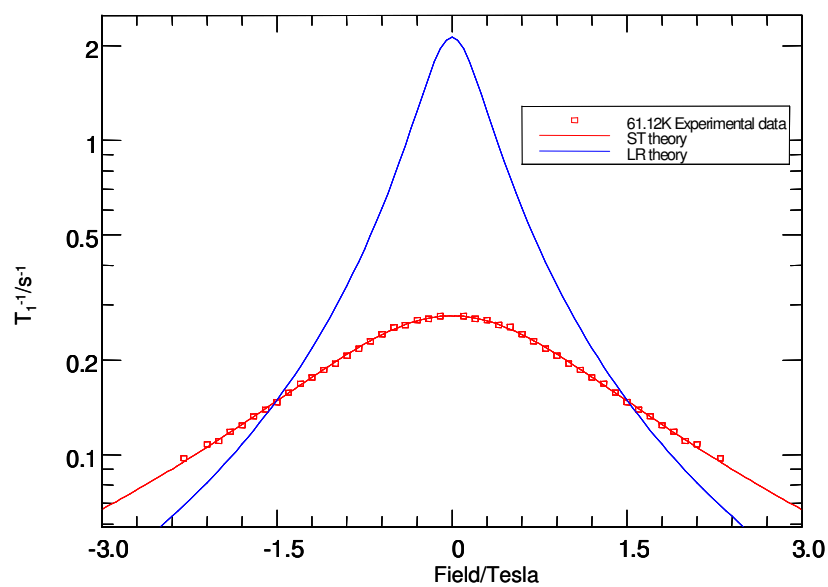
Fig 4.9 Fit the experimental data to ST and LR theories at 61.12K
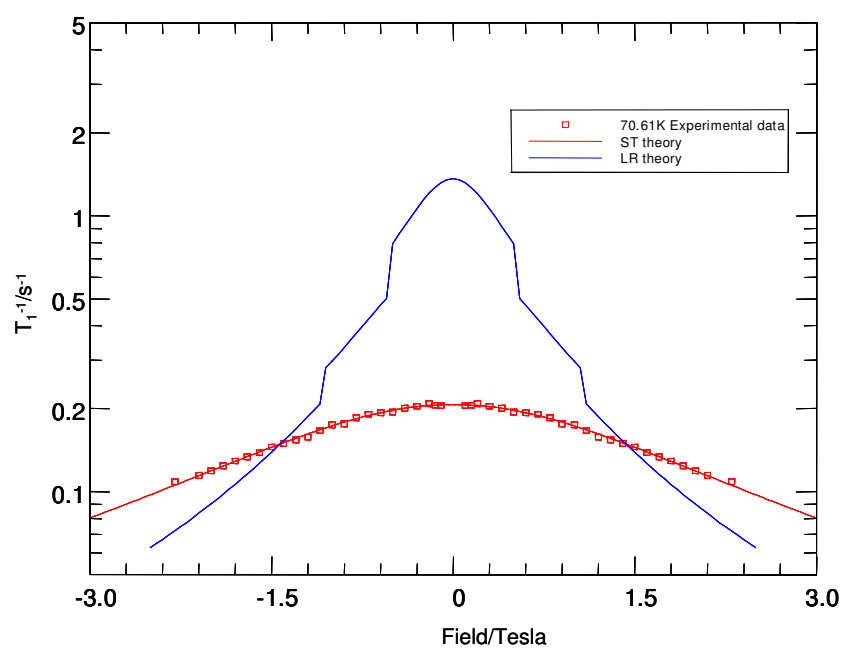
Fig 4.10 Fit the experimental data to ST and LR theories at 70.61K
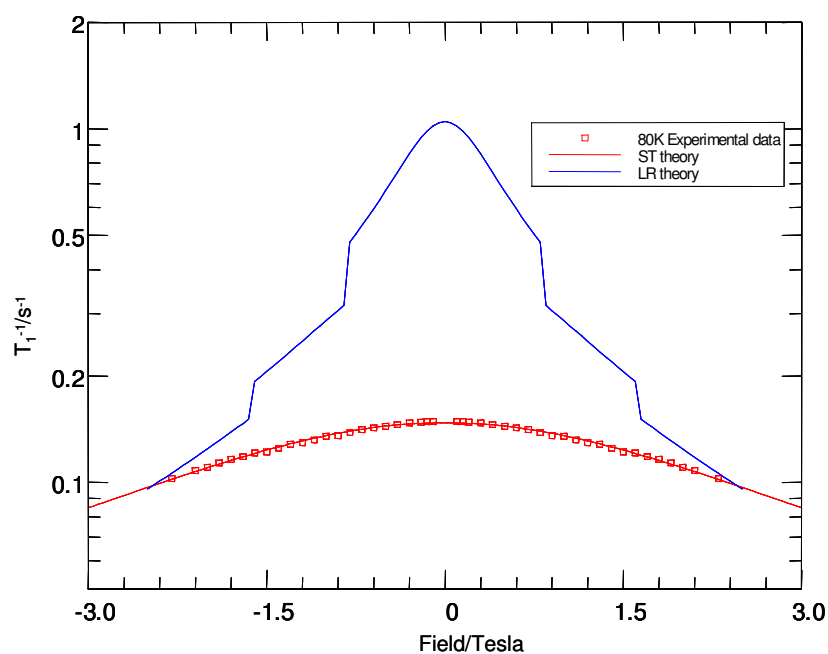
Fig 4.11 Fit the experimental data to ST and LR theories at 80K

The figures from **Fig 4.5** to **Fig 4.11** are the comparisons between two theories in a variety of temperatures to show the evolutions of the spectral densities fitted to the two theories and show to what extent they agree with the experimental data.

It is evident that the features of the LR theory are unphysical and in complete disagreement with the experiment data. On the contrary, the ST theory works very well across the whole temperature range. This demonstrates the inaccurate conclusions that can arise from analysing only T_1 data at fixed frequency and the advantage of recording the relaxation as a function of field/frequency.

In Fig 4.12 the Lorentzian amplitudes are plotted as a function of inverse temperature and fitted to the function $C_D \operatorname{sech}^2(A/2k_BT)$, equation (4.6). Excellent agreement is obtained with $A/k_B = (80 \pm 1)\,\mathrm{K}$ and $C_D = (6.30 \pm 0.05) \times 10^7\,\mathrm{s}^{-2}$. This also shows that the ST theory gives a correct molecular dynamics description.
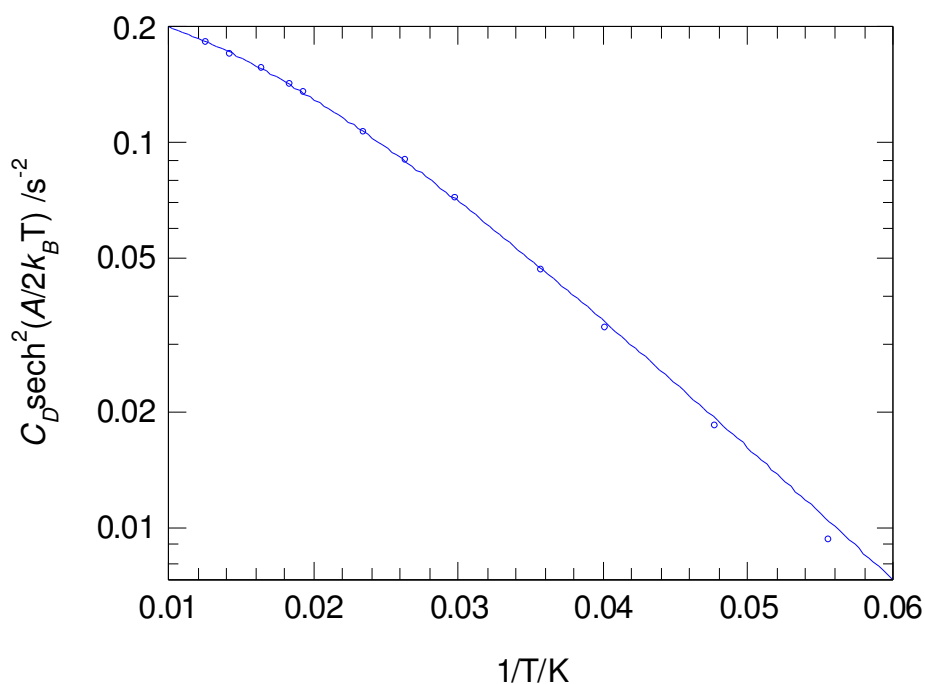
Fig 4.12 The inverse temperature dependence of the amplitudes of the spectral density lineshapes in Fig 4.4a, b, c and d. The solid line is a fit to the function $C_D \operatorname{sech}^2(A/2k_BT)$.

The proton transfer rates, τ_c^{-1}, determined from the data in Fig 4.4a, Fig 4.4b, Fig 4.4c and Fig 4.4d are plotted as a function of inverse temperature in Fig 4.13. At low temperature the proton transfer rate is independent of temperature, characteristic of phonon-assisted tunnelling. With increasing temperature the proton transfer rate gradually increases, approaching Arrhenius behaviour at ambient temperature. The data spans the intermediate temperature region corresponding to the changeover between quantum and Arrhenius regimes. It is a typical smooth transition without any distortion as expected in the LR theory. If multiple correlation times were present as mentioned in the LR theory, it is here that we would expect them to be most evident. No such multiple component character is observed in any of the data in Fig 4.13.

BA τ_c^{-1} vs 1/T

Fig 4.13 The inverse temperature dependence of the inverse correlation times, τ_c^{-1}, for proton transfer in BA. At low temperature the proton transfer rate is independent of temperature but smoothly evolves towards Arrhenius behaviour at higher temperatures. The blue filled circles are the data transferred directly from T_1 vs 1/T curve, the red filled rectangles were extracted from the fits shown in Fig 4.4a and Fig 4.4b, the black triangles were earlier field-cycling data from [11]. It is evident that all these data are in good agreement with each other and with the ST model. The solid line has been calculated from the ST model and parameters reported in [11] and listed in Table 4.2, determined before field-cycling data was available at temperatures above 17K.

Table 4.2 parameters employed to calculate the τ_c^{-1} vs inverse temperature from the ST model:

Energy asymmetry A/k_B	78.2K
Dipolar constant C_D	$6.25 \times 10^7 s^{-2}$
Incoherent tunnelling rate constant k_0	$1.22 \times 10^8 s^{-1}$

These parameters are in good agreement with our field-cycling experimental result. The energy asymmetry listed in Table 4.2, 78.2K, is slightly smaller than the result of field-cycling experiments, 80K; this is because it was directly extracted from the gradient of T_1 vs inverse temperature curve in low temperature region, but the fit equation (3.15) is based on the assumption: $\exp(A/k_B T) \gg 1$ which is not entirely correct when the temperature is higher than 30K; the extracted value is normally slightly smaller than actual value or the value we employ in our simulation to provide a perfect fit. It also turns out that the energy asymmetry extracted from the Lorentzian amplitude vs inverse temperature curve is more accurate than the result extracted from the gradient in T_1 vs inverse temperature curve.

4.5 Discussion and concluding remarks

Here we have demonstrated how the field-cycling NMR technique may be applied to the direct measurements of incoherent molecular dynamics and the evolution of the temperature dependence of the correlation rate.

In both ST and LR theories, different barrier crossing pathways are identified, involving tunnelling in the ground state, tunnelling in excited states and related processes which imitate classical hopping. What distinguishes the two theories is the manner in which these different pathways are combined to determine the overall dynamics. In ST theory, the probabilities for interchange are additive leading to a summation of the rates of the individual pathways and a single correlation rate. In LR theory, the different pathways retain their separate identities and it is the spectral densities which are additive. The experimental evidence supports the ST approach and the concept of a smooth transition between quantum and classical regimes. Quantum

and classical descriptions are consistent with each other. The fundamental foundations of molecular dynamics are quantum mechanical; it is issues of coherence allied to the de Broglie wavelength which determine in what temperature range the behaviour resembles classical dynamics.

Only with field-cycling are the inadequacies of the LR theory completely evident-their theory was developed for T_1 at fixed field.

Chapter 5 Heteronuclear experiments I – NQR detection of heroin hydrochloride monohydrate [68]

Beginning with this chapter, we present our investigation of heteronuclear systems with field-cycling NMR. It is a significant part of the research in this thesis. Many samples contain multiple nuclei, and therefore the heteronuclear interaction becomes a relevant and crucial topic to the study of complex systems and those of biological interest.

An example of the heteronuclear interaction between spin I (½) and spin S (≥ 1) is discussed in this chapter. As reviewed in Chapter 2, when spin≥ 1, the nucleus is quadrupolar. The NQR of quadrupolar nuclei is detected by a heteronuclear transfer of polarisation with ^{1}H nuclei. Therefore the NQR is detected through measurements of the ^{1}H NMR signal. Generally such inverse peaks characterising the detected spectrum are called *quadrupole dips* [21]. However, here the NQR transitions are driven externally by irradiating with r.f. rather than via natural relaxation pathways.

NQR (Nuclear Quadrupole Resonance) is related to NMR. We know when a nucleus with spin is placed into a magnetic field, this results in some sub-states and the Zeeman splitting. When an irradiation r.f. frequency matches the transition frequency among the Zeeman sub-states, a resonance we call NMR occurs. NQR concerns nuclear quadrupole resonance that arises due to the splitting in the quadrupolar nuclear sub-states; the levels acquire a zero-field splitting due to the quadrupolar interaction. The quadrupolar nuclear sub-states and the allowed transitions have been introduced in Fig 2.19, Fig 2.20 and equations (2.66), (2.68) in Chapter 2.

5.1 Introduction

Heroin (diacetylmorphine), Fig 5.1, is a class 'A' drug, closely related to morphine and codeine, and derived from the opium poppy.

It was produced by acetylation of morphine extracted from poppy latex, followed by treatment with HCl to give the hydrochloride, which was recrystallised from ethanol and diethyl ether to give heroin hydrochloride monohydrate. The monohydrate could be dried to give an anhydrous form. While simple colorimetric tests exist to detect the presence of drugs such as heroin hydrochloride, a simple quantitative, portable and non-destructive method for selectively identifying heroin in the presence of closely related compounds such as acetylcodeine is highly desirable. The ratio of acetylcodeine to heroin is, for example, often used as an indication of the origin of illicit drugs. This was part of a wider study to assess whether NQR could be used as diagnostic tool.
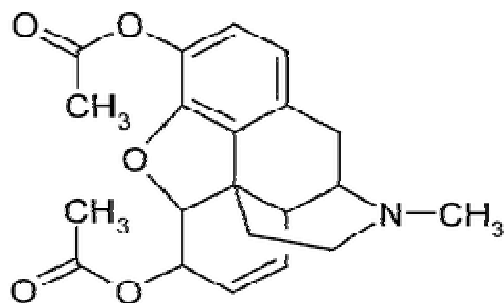
Fig 5.1 structure of heroin (diacetylmorphine)

A sample of heroin hydrochloride was supplied by Professor John A. S. Smith of King's College London and used in our NQR low field experiments. We were in collaboration with him to determine the unusual crystal structure of heroin hydrochloride monohydrate and experimentally confirm the calculated ^{14}N and ^{35}Cl nuclear quadrupole resonance (NQR) frequencies using Gaussian (method: HF/6-31+G*).

5.2 Experimental

As reviewed in Chapter 2, due to the quadrupolar interaction, there is a zero-field splitting of the nuclear sub-states. To investigate the quadrupolar transitions arising from the splitting, the low field NMR technique [22] is applied for measuring the transition frequencies in the range 6kHz to 3MHz. The low field NMR technique

employs a polarisation-recovery pulse sequence, with r.f. irradiation applied via secondary coils during the recovery period where the magnetic field is low; in fact for the NQR experiment, the magnetic field is chosen close to zero field. The F1 Channel of the Apollo spectrometer was used to provide the secondary low field r.f. irradiation, and the irradiation times were typically 400ms for the sample we studied. The low field experiment pulse sequence is illustrated in Fig 5.2.
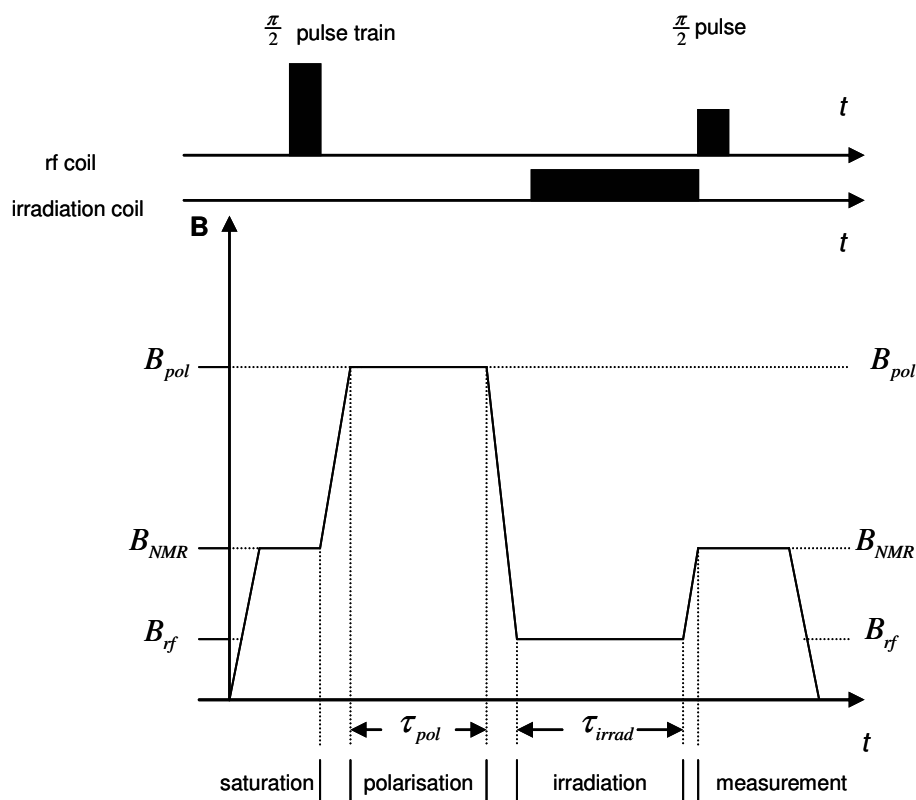
Fig 5.2 low field experiment pulse sequence

1) Saturation of the ^{1}H magnetisation with a comb of 90° pulses at the resonance field B_{NMR}

2) Rapid magnetic field switch to the polarisation field B_{pol}, evolution for a period of time to polarise the nuclear spins

3) Rapid magnetic field switch to the low field B_{rf}, simultaneously apply the r.f. irradiation at frequency ν_{rf} for a period of time

4) Rapid magnetic field switch to the resonance field

5) Measurement of magnetisation with a 90° pulse

The sequence is repeated many times so the magnetisation spectrum can be recorded in one of two modes,

1) Frequency swept mode, in which B_{rf} is constant and ν_{rf} is systematically incremented in each cycle

2) Field switch mode, in which ν_{rf} is constant and B_{rf} is systematically incremented in each cycle

In our experiments, at constant low magnetic field, B_{rf}, the spectrum is recorded point by point as a function of irradiation frequency. When the irradiation frequency matches a magnetic transition, in NQR experiments the transition is a quadrupolar transition, then ^{1}H magnetisation will be destroyed. The heteronuclear quadrupole interaction between ^{1}H and the studied quadrupolar nuclei will introduce a significant relaxation mechanism due to quadrupolar coupling which is not present in a spin ½ system. The relaxation rate due to quadrupolar coupling is recorded as T_{1q}^{-1}. Thus the relaxation rate of ^{1}H magnetisation becomes,

$$\frac{1}{T_1} = \frac{1}{T_{1dd}} + \frac{1}{T_{1q}}$$ (5.1)

where T_{1dd}^{-1} is the relaxation rate due to dipole-dipole interaction which is dominant for the spin ½ sample in solid state. Thus the relaxation of ^{1}H magnetisation is speeded up, leading to quadrupole dips appearing in the curve of the ^{1}H magnetisation vs irradiation frequency when quadrupolar transition occurs. This curve is applied for searching the Nuclear Quadrupolar Resonance frequency.

Due to the fact the quadrupolar interaction is much weaker than the interaction between the nucleus and the magnetic field, the magnetisation of the proton only undergoes a small change when the NQR transition was irradiated, which means the quadrupole dips in the spectrum are tiny and the signal to noise ratio becomes the dominant problem in this kind of experiment.

To get the maximum inverted peak, the NQR experiment was run at the lowest practical temperature 4.2K (liquid helium temperature).

The polarisation field B_{pol} was typically set between 0.8 to 1T with a polarisation time of 30 to 60s. This polarisation field was set as high as possible to improve the signal quality, however during the field switching time, the relaxation of ^{1}H magnetisation was inevitable and became significant, therefore the polarisation field was chosen as a compromise between high preparation field and short field switching time.

The NMR observation field B_{nmr} was 0.627T (^{1}H frequency of 26.7MHz). The low field B_{rf} was between 0 and 20Gauss as required to investigate the quadrupolar nuclear splitting at zero field. Higher fields would lead to broadening of the NQR peaks which was not desirable.

The field switching rate was set to 8T/s in preference to the maximum value 10T/s. This was a compromise since if the field switching rate was set too high, a long settle time had to be chosen to allow field to stabilize. We found that the magnet power supply did not perform so well at low field, with a long 'tail', as shown in Fig 5.3b. So that we only irradiated when the field was less than 20G, a 'settle time' was introduced into the sequence. This was typically 200ms in our experiments. It was unfortunate that it was required, since the protons relax during this period, reducing the signal to noise in our data. However, we were still able to record satisfactory NQR data.

Field switch profile
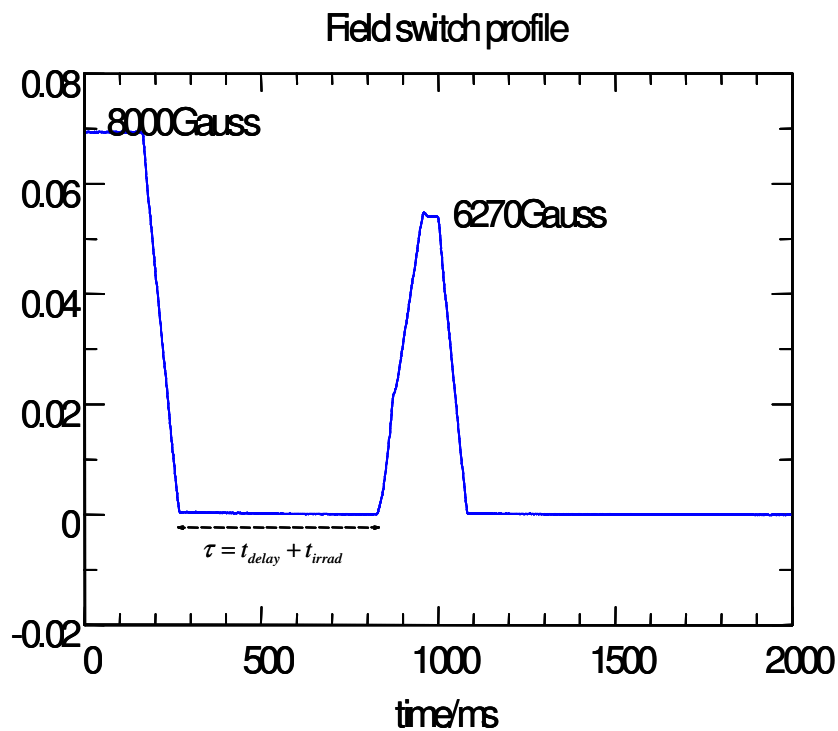
Fig 5.3a The field switch profile for low field experiment. After switching down from 8000Gauss to zero irradiation field at 8T/s, the start field in the irradiation period τ is about 35Gauss instead of zero as we expected, so the delay t_{delay} was introduced.
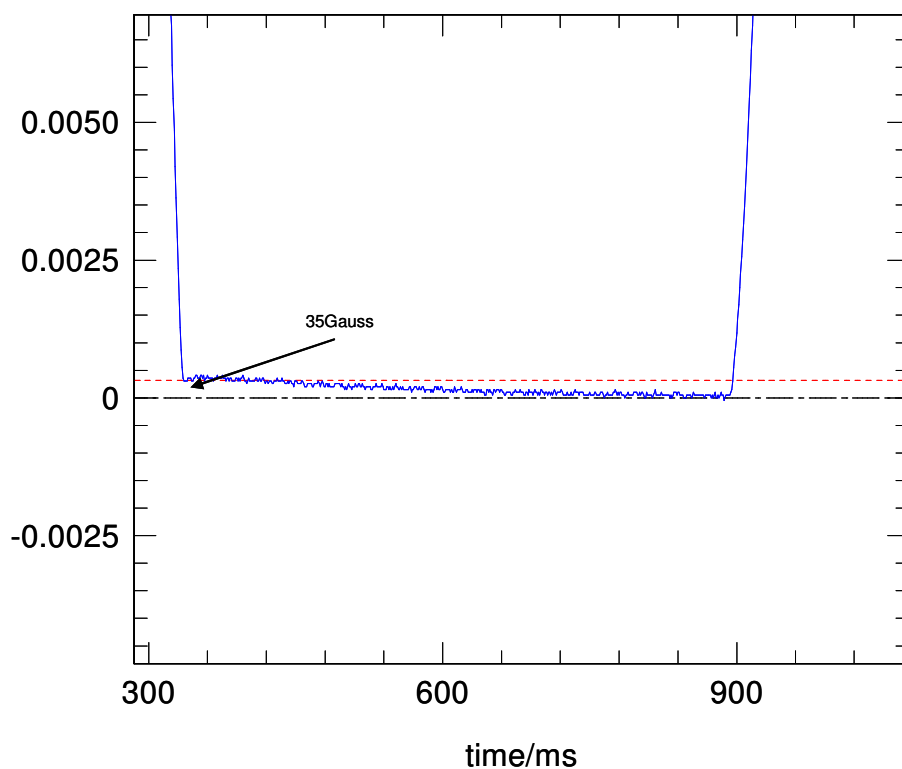
Fig 5.3b Zoom in of Fig 5.3a to illustrate the long 'tail'

5.3 Results and discussion

At the outset, we didn't know the NQR peak positions, but Prof. Smith indicated the broad frequency range in which they might be found. By making repeated scans, small dips were obtained that might be candidates as 'quadrupole dips', but by optimising the experimental parameters and averaging a series of scans, good NQR spectra were finally obtained, as shown in Fig 5.4.

Inspection of the experimental spectrum suggested a zero field NQR frequency of around 2000kHz (for ^{35}Cl) and two zero field NQR frequencies around 1000kHz (for ^{14}N). No separately identifiable dip for ^{37}Cl was observed.
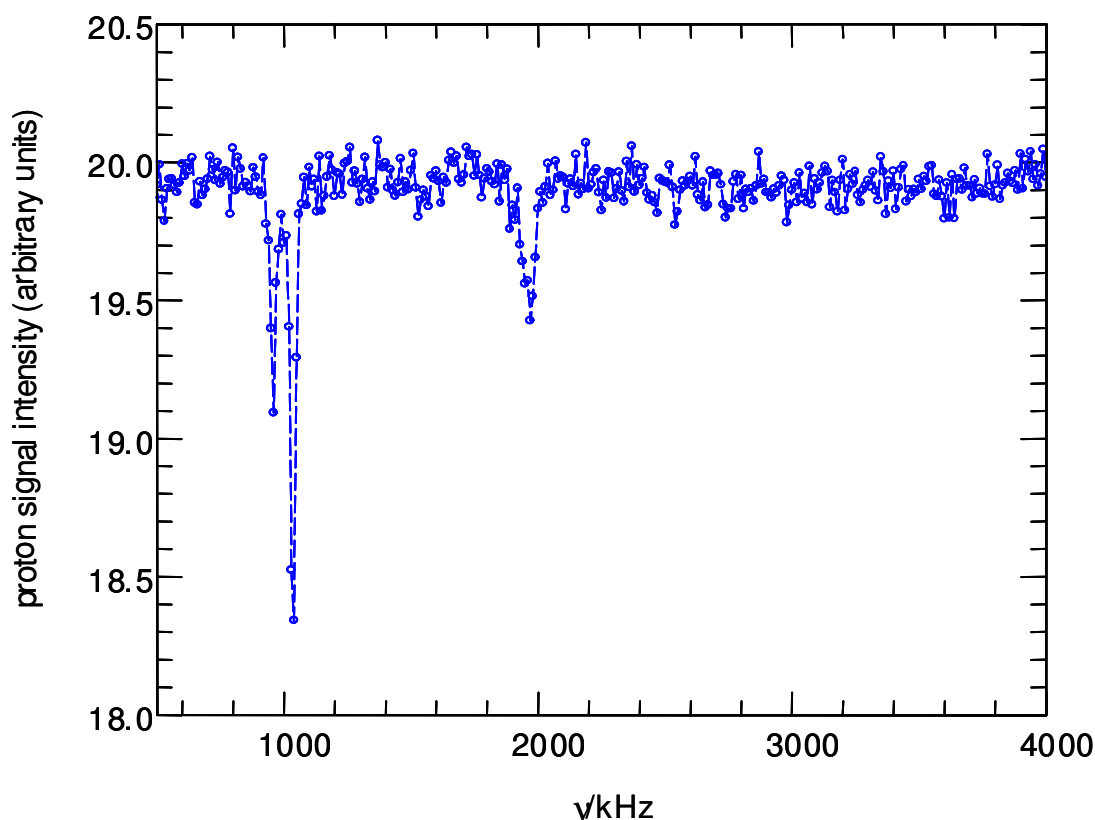
Fig 5.4 The best NQR data for heroin hydrochloride monohydrate sample supplied by Professor John A. S. Smith. Experimental conditions have been introduced in the text. Step frequency was 2kHz and the irradiation frequency was searched from 700kHz to 4000kHz. Two dips around 1000kHz for ^{14}N and one smaller dip for ^{35}Cl close to 2000kHz were found.

Refinement of these values were achieved by repeating the frequency search in narrow frequency ranges, as shown in Fig 5.5, 1800kHz to 2200kHz for ^{35}Cl, and in Fig 5.7, 700kHz to 1200kHz for ^{14}N.

5.3.1 Results for ^{35}Cl

The upper three curves in Fig 5.5 were three scans in the frequency range from 1800kHz to 2200kHz with the same experimental conditions. The lower spectrum was the average of these three curves. The baseline of the latter was adjusted for clarity. Two ^{35}Cl NQR frequencies at 1950kHz and 1965kHz were found in the averaged spectrum.
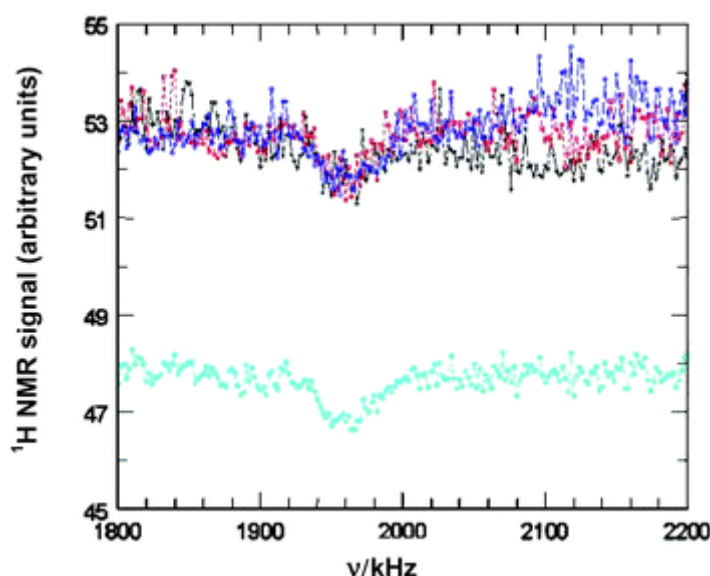
Fig 5.5 The ^{35}Cl NQR frequency search at 4.2K with frequency step 2kHz. The upper curves were three experimental data from same experimental conditions. The lower spectrum was the average of these three.

According to the theory of quadrupolar interaction discussed in Chapter 2, ^{35}Cl is a spin-$\frac{3}{2}$ nucleus, and there should be one NQR frequency observed as expressed in equation (2.68) and Fig 2.20. The frequency is

$$\nu_Q = \frac{1}{2}(e^2qQ/h)\left(1+\frac{\eta^2}{3}\right)^{\frac{1}{2}} \tag{5.1}$$

The crystal structure need to be introduced which has been determined by the group in King's College London. The result is shown in Fig 5.6 and Table 5.1.The asymmetric hydrogen bonding around each chlorine ion in the crystal structure leads to a non-zero quadrupolar interaction at this nucleus and a finite NQR frequency. It is evident, both in Fig 5.6 and Table 5.1, that there are two kinds of ^{35}Cl ions, Cl(1) and Cl(2), crystallographically non-equivalent, being hydrogen bonded to one N-H group and two water molecules. The slightly different positions of the hydrogen-bonded hydrogen atoms make a small difference between the electric field gradients at these two chlorine ions. Therefore two ^{35}Cl NQR frequencies are expected. The observed peak is broad and any site splitting must be within this linewidth. There is some evidence in the averaged data that a doublet is just resolved.
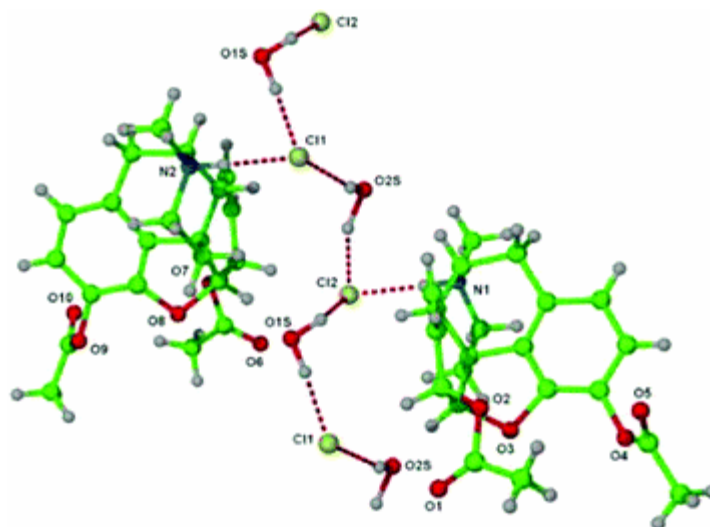
Fig 5.6 Projection of two independent molecules on the *ab* plane, showing the N–H•••Cl⁻ and Cl⁻••• OH₂ hydrogen bonding.

It is impossible to deduce the quadrupole coupling constants e^2qQ/h and the asymmetry parameter η for these two ^{35}Cl ions separately from equation (5.1). Other experiments are needed for obtaining these two parameters in combination with the NQR results.

Table 5.1 Hydrogen bonds in heroin hydrochloride monohydrate

D–H•••A	d(D–H)/Å	d(H•••A)/Å	D(D•••A)/Å	∠DHA/°
O(1S)–H(1S1)•••Cl(1)	0.98	2.15	3.119(11)	167.5
N(1)–H(1)•••Cl(2)	0.93	2.17	3.095(14)	172.1
N(2)–H(2)•••Cl(1)	0.93	2.14	3.056(15)	169.0
O(2S)–H(2S1)•••Cl(2)	1.16	2.01	3.103(11)	154.9
O(2S)–H(2S2)•••Cl(1)	0.94	2.29	3.174(11)	158.1
O(1S)–H(1S2)•••Cl(2)	0.96	2.46	3.153(11)	128.9

5.3.2 Results for ^{14}N

Higher resolution results for ^{14}N using a frequency step of 2kHz are illustrated in Fig 5.7. Two dips were found at 0.957 and 1.035MHz, assigned to ν_- and ν_+ respectively. Each peak had its own doublets. For spin-1 nucleus, ^{14}N, the peaks are related to the quadrupole coupling constant and asymmetry parameter as

$$\nu_\pm = \frac{3}{4}\left(\frac{e^2qQ}{h}\right)\left(1\pm\frac{\eta}{3}\right)$$

(5.2)

which has been expressed in equation (2.66) in Chapter 2.

The x-ray crystal structure analysis completed by the group of KCL (King's College London) showed that the doublet structure was clearly resolved with splittings of 6.5kHz for ν_+ and 5.7kHz for ν_-. Therefore the frequencies (four possible values: $957\pm5.7/2\,\mathrm{kHz}$ and $1035\pm6.5/2\,\mathrm{kHz}$) for ^{14}N peaks are paired off as shown in Table 5.2 as well as the quadrupole coupling constants and the asymmetry parameters calculated from equation (5.2).
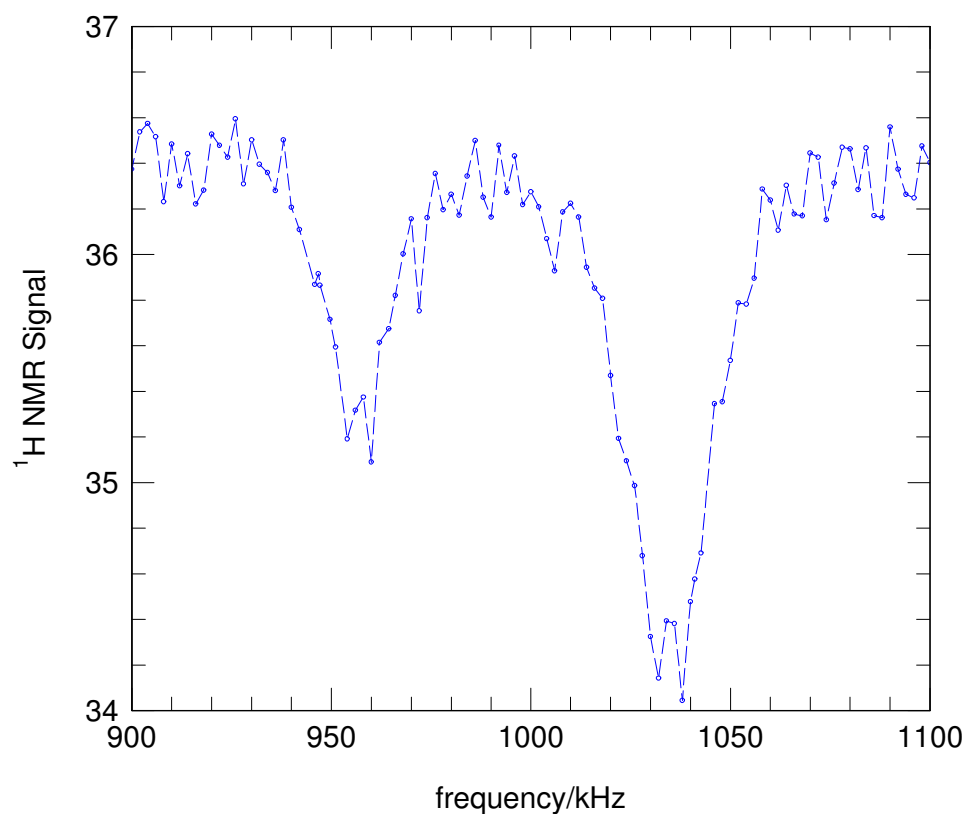
Fig 5.7 NQR spectrum of ^{14}N searched by frequency swept mode with frequency step 2kHz from 700kHz to 1200kHz. Two dips assigned to ν_- and ν_+ were found at 0.957 and 1.035MHz respectively. Each dip had its own doublet.

Table 5.2 Frequency pairs and the related quadrupole coupling constants, asymmetry parameters.

(ν_-,ν_+)	$(e^2qQ/h(\mathrm{MHz}),\eta)$
$(0.960,1.039)$ MHz	$(1.333,0.119)$
$(0.954,1.032)$ MHz	$(1.324,0.118)$
$(0.960,1.032)$ MHz	$(1.328,0.108)$
$(0.954,1.039)$ MHz	$(1.329,0.128)$

The first two frequency pairs for the observed doublets was made to optimise the agreement between the asymmetry parameters (0.119 and 0.118 in Table 5.2), while the last two frequency pairs was made to optimise the agreement between the quadrupole coupling constants (1.328 and 1.329MHz in Table 5.2).

The predicted NQR frequencies (v_- at 1.142 and 1.000MHz, v_+ at 1.220 and 1.099MHz) by theoretical calculation were close to the NQR experimental results (doublets close to 0.957 and 1.035MHz), bearing in mind the neglect of temperature effects.

5.4 Conclusions

NQR technique has been successfully implemented on our field-cycling spectrometer to detect ^{14}N and ^{35}Cl quadrupole nuclei in the sample and furthermore confirm the structure of the sample by the detailed NQR spectrum. For example, the ^{35}Cl NQR doublets and the related quadrupole parameters in this sample can be applied to determine the electric field gradients governed by the positions of hydrogen-bonded hydrogen atoms at this ion, therefore to confirm the structure of the studied sample. The unique structure of heroin hydrochloride hydrate was reflected in the NQR data and hence suggested that NQR technique could form the basis for a sensitive method for the selective detection of this material in the presence of other closely related compounds.

Chapter 6 Heteronuclear experiments II-^{13}C-BA [65]

6.1 Introduction

^{13}C -BA was the first sample chosen to investigate the spin½-spin ½ heteronuclear interaction system. In conducting the investigation of ^{13}C -BA there is a strong motivation to develop the techniques of field-cycling relaxometry and the methodology of data analysis for cases where heteronuclear dipolar interactions are present. Compared with the model system benzoic acid (BA), ^{13}C -BA sample has 99% ^{13}C substitution of the carboxy carbon, Fig 6.1. There is another motivation to study isotope effects of the skeletal framework atoms on the proton transfer dynamics. This is a long term motivation. Some research on isotope effects due to deuterium substitution in the hydrogen bonds has been completed by another PhD student in our group [62]. However, when the hydrogen atoms move, the heavy skeletal framework atoms also move and the quasi-particle involved in the motion is 'dressed' with the displacements of the skeletal framework atoms. Theoretical techniques for calculating such effects are only just becoming available; we sought experimentally for such effect.
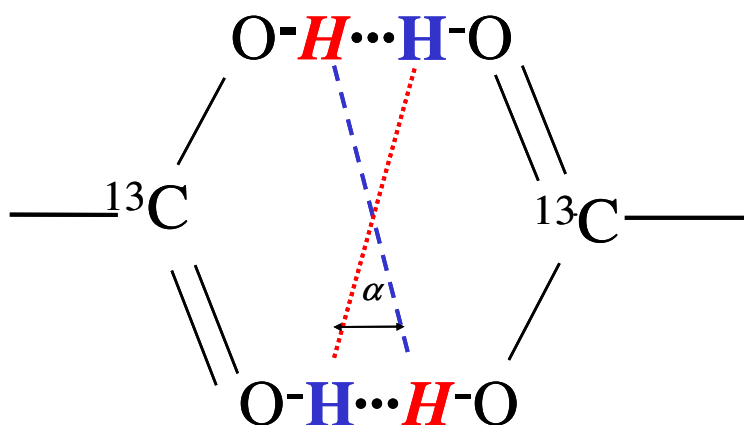
Fig6.1 Double proton transfer in ^{13}C-BA. ^{13}C acts as a 'spy' nucleus to monitor the concerted motion of the two hydrogen atoms in the hydrogen bonds.

The ^{13}C -BA sample chosen for the investigation is based on the following

motivations,

- BA is the established model system for translational molecular tunnelling. Experimental and theoretical aspects are very well characterised and understood both in structure and in dynamics.

- The ^{13}C substitution of the carboxy carbon will not change the structure significantly. We can still use the same structure geometry parameters such as the coordinate of each atom in the molecule in our simulations. With the geometry parameters, the lattice sum of heteronuclear dipolar interaction C_{CH} can be derived according to equation (2.50).

- The dynamic parameters A, k_0, k_1, V, V_{exc} and τ_0^{-1} will not change much when the carboxy carbon is substituted by ^{13}C. Then when we analyse the ^{13}C-BA experimental data and simulate them, we will have a good initial estimate of these dynamic parameters

- ^{13}C acts as a 'spy nucleus' monitoring the concerted motion of the two hydrogen atoms in the hydrogen bonds that bridge the BA dimer. The 99% ^{13}C substitution of the carboxy carbon represents an additional advantage of studying heteronuclear relaxation because the system is 'clean'. Relaxation of the ^{13}C is dominated by just two symmetry related intra-dimer dipolar contacts with the two labile protons. There are no homonuclear ^{13}C - ^{13}C interactions contributing to the relaxation.

This is the first ever ^{13}C NMR investigation by field-cycling system; this led to a number of experimental challenges,

- The natural abundance of ^{13}C is only 1.108%. Even 99% enriched in our sample, the ^{13}C NMR spectra is still a tiny signal due to the small magnetogyric ratio. Only the carboxy carbon is enriched, so the ^{13}C abundance in the molecule is also small.

- NMR is intrinsically an insensitive technique; it is desirable to use all possible means to improve the signal-to-noise ratio. One of them is to increase the magnetic field B_0. But it is restricted by our field-cycling system. The maximum field we can have in our system is only 2.5T.

- As reviewed in Chapter 3, high-Q tank circuit is desirable for getting high quality signal both in amplitude and in signal to noise ratio. However this leads to a long dead time and a narrow calibration curve which makes it difficult to control the field drifts. Fortunately the field drifts are very small at high field (the ^{13}C resonance field was chosen more than 2T) and the lineshapes of ^{13}C are narrow, so we could afford a long dead time.

- With field-cycling NMR, we can record the magnetic field dependence of the spin-lattice relaxation time. However at low field the NMR signal is very weak. In a homonuclear experiment, we usually employ saturation-recovery pulse sequence when the field is higher than 4000Gauss, and to overcome S/N problems, we employ the polarisation- recovery pulse sequence when the field is low. The pulse sequences are shown in Fig 3.17 and Fig 3.20. However in a heteronuclear experiment, the initial conditions of the second spin reservoir restrict the use of a particular recovery technique. This will be discussed later.

Implications for field-cycling relaxometry

The spin-lattice relaxation rate constants are weighted sums of various Lorentzian lineshapes, equations (2.49) and (2.51). There are two outlooks on an experiment to study molecular dynamics by NMR relaxometry. In the first, plotting T_1^{-1} as a function of frequency, Fig 6.2a, the width of the spectral density curve is determined by τ_c^{-1} and the experiment samples this function at the specified frequencies. In the second, relevant to a field-cycling study of spin-lattice relaxation, plotting T_1^{-1} as a function of magnetic field, Fig 6.2b, the observed relaxation is a sum of Lorentzians with different width. The Lorentzians widths are scaled by the magnetogyric ratios when plotted as a function of magnetic field. Therefore, it is to be expected that, in interpreting such experimental data, information on the amplitudes of the various Lorentzian components would be required to unambiguously determine an accurate value for the correlation rate.
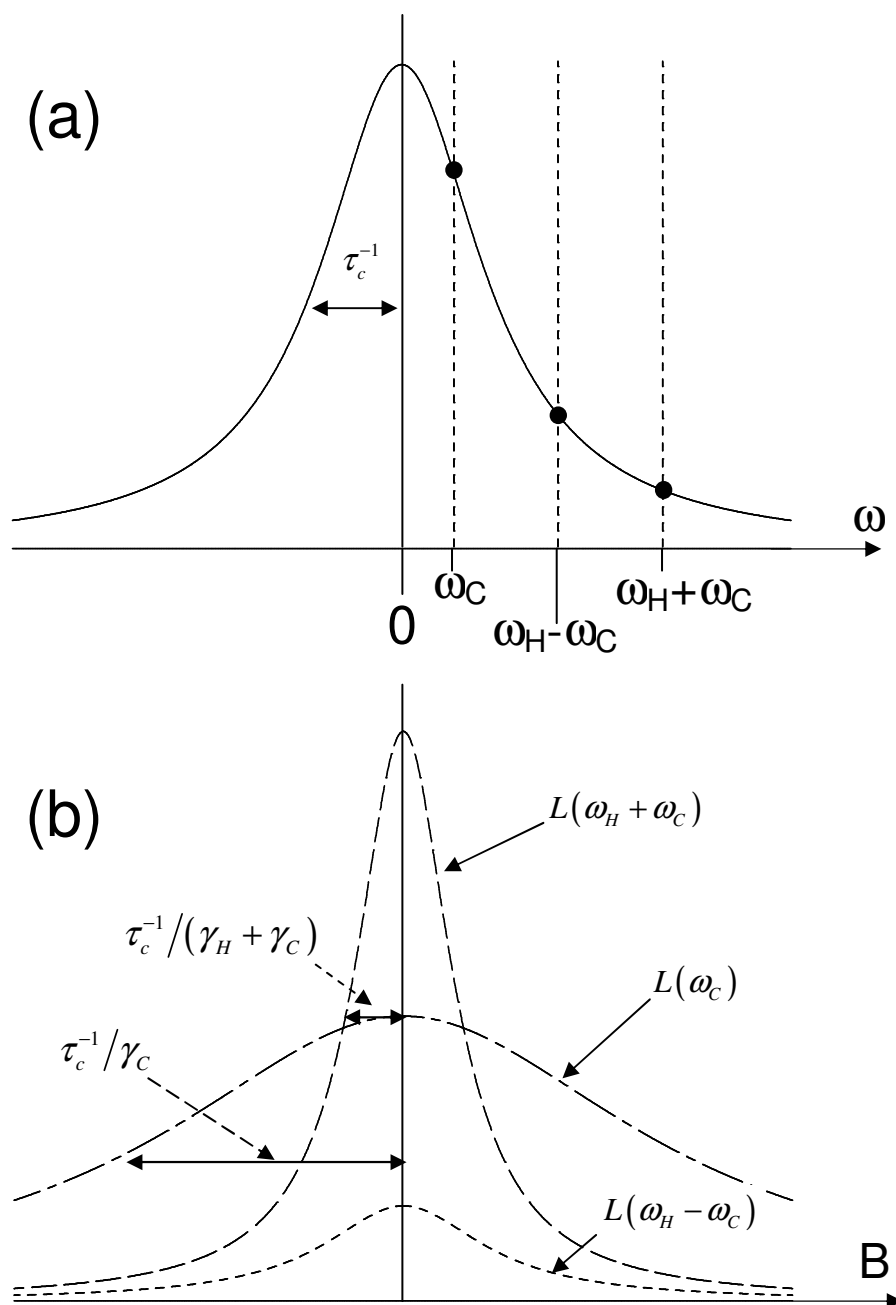
Fig 6.2 Two outlooks on the spectral density function: (a) plotted as a function of frequency, ω, where the half-width at half-maximum is equal to the correlation rate, τ_c^{-1}. In a spin-lattice relaxation experiment this curve is sampled at the three frequencies ω_C, $\left(\omega_H + \omega_C\right)$ and $\left(\omega_H - \omega_C\right)$ (b) plotted as a function of B-field, as applicable to field-cycling NMR. The proton transfer dynamics are determined by τ_c^{-1} but the observed spin-lattice relaxation is determined by the sum of three Lorentzian components with widths $\tau_c^{-1}\big/\gamma_C$, $\tau_c^{-1}\big/\left(\gamma_H + \gamma_C\right)$ and $\tau_c^{-1}\big/\left(\gamma_H - \gamma_C\right)$.

Additionally, the spin-lattice relaxation rate constants R_1 and R_2 are molecular properties independent of the experimental procedures but the weighting coefficients,

c, depend on the initial polarisation states of both Zeeman reservoirs. Therefore, to obtain spin-polarisation recovery curves from which molecular parameters can be reliably recovered, the preparation of the initial states need to be rigorously systematic. This requires special procedures in the case of field-cycling relaxometry. We shall return to a discussion of these issues in the light of experimental data.

6.2 Experimental

A variety of pulse sequences were employed to study the spin-lattice relaxation. They will be described in the next section 6.3. In all cases saturation was achieved using a comb of six $\pi/2$ pulses and the longitudinal polarisation of the nucleus of interest was measured with a single pulse. Using logarithmic increments in τ, magnetisation recovery curves were recorded from which the spin-lattice relaxation parameters were obtained.

The enriched (99 atom %) *carboxy*-^{13}C benzoic acid ($C_6H_5{}^{13}COOH$) was obtained commercially and used without further purification. The sample temperature was controlled by a variable flow helium cryostat that was incorporated into the cryostat of the superconducting magnet (supplied by Cryogenic Ltd). Sample temperatures in the range 4 – 300K were measured with a calibrated Cernox resistance thermometer; the long term stability and accuracy of the temperature in the region 20K was better than 0.01K.

The resonance frequency of ^{13}C for the field-cycling experiment was chosen to be 21.9MHz, and the resonance field was about 2.03T, which was a compromise in consideration of 2.5T field limitation and the signal quality.

The dead time is $20\,\mu s$ for the ^{13}C probe, which is much longer than the value of $4\,\mu s$ which typified a ^{1}H probe. The chosen saturation and measurement pulse widths were $4\,\mu s$, double the value of typical ^{1}H experiments. Fortunately the observed ^{13}C linewidths, shown in Fig 6.3, were very much narrower than for ^{1}H in the same sample, due to scaling of the dipolar interaction, by the smaller ^{13}C

magnetogyric ratio. In fact the narrow line was a further advantage because it improved the effective S/N. However as discussed in Chapter 3, the measurement pulse width was bigger than normally used, so that the calibration curve was much narrower than that of ^{1}H experiments, making the field stability more important than in ^{1}H experiments. Although the field drifts are smaller in high field than in low field (the ^{13}C resonance field is more than 2T), the spectrometer's set up and field offset parameters still had to be very carefully determined before a set of experiments were run automatically over night or over weekends.
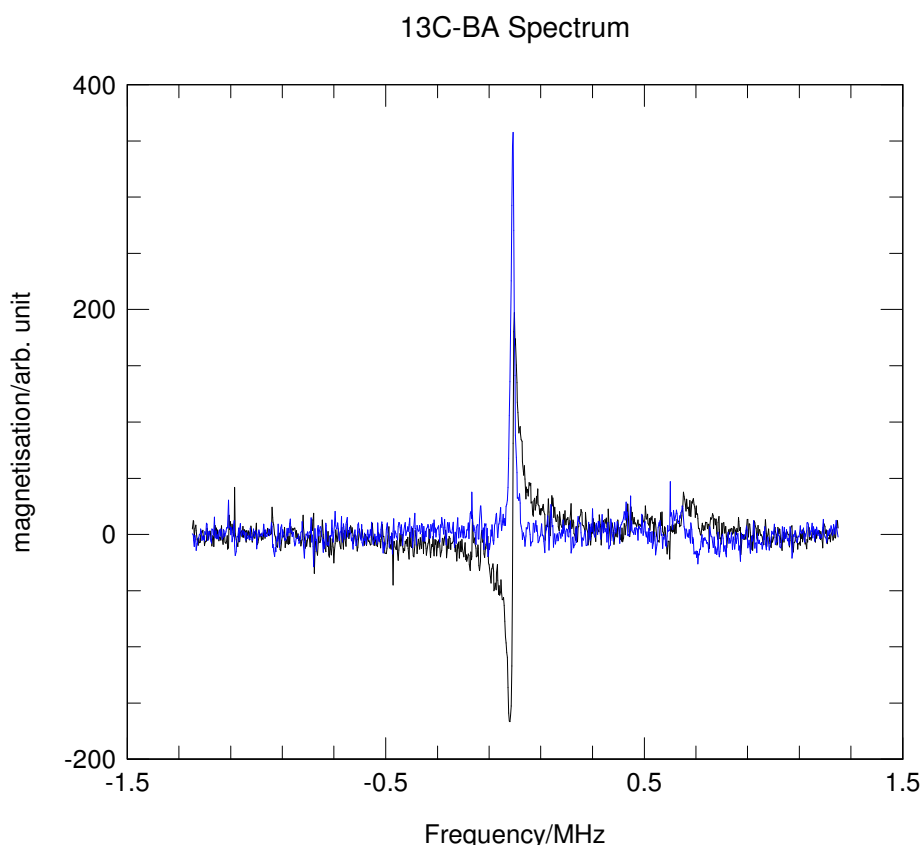
Fig 6.3 A spectrum of ^{13}C in 13C-BA illustrating the narrow lineshape.

6.3 Experimental and Simulation Results

Two kinds of experiments have been carried out to investigate the heteronuclear interactions and dynamics on ^{13}C-BA. One is for measuring the temperature dependence of spin-lattice relaxation time; the other is for measuring the field/frequency dependence of spin-lattice relaxation time.

6.3.1 ^{13}C and ^1H spin-lattice relaxation at constant field

The temperature dependence of ^{13}C spin-lattice relaxation time T_{13C} measurements were made on the Oxford NMR 270 magnet system operating in persistent mode using a saturation-recovery pulse sequence as shown in Fig 3.17. The magnetic field operated at 24280Guass and for ^{13}C the resonant Larmor frequency was 26MHz in this field. Field shimming was carried out at room temperature by noting the shape of the off-resonance free induction decay (FID) envelope following a single pulse of RF. An Oxford instrument continuous-flow cryostat was used to cool the sample, good temperature control was achieved by adjusting the liquid helium flow rate and the PID settings of the temperature controller.

The ^1H spin-polarisation recovery curve was recorded as a function of temperature using a conventional saturation-recovery pulse sequence at fixed magnetic field (0.883T/37.8MHz) as shown in Fig 3.17. The measurements were made on the custom built field-cycling NMR spectrometer which has been described in Chapter 3.

In these experiments, both for ^{13}C (Oxford magnet in persistent mode) and for ^{1}H (field-cycling spectrometer in internal mode), the magnet was always on; therefore at time $t = 0$, the spin-polarisation of the nuclear species under investigation was saturated while the spin-polarisation of the second nuclear species was established close to its thermal equilibrium (i.e. for ^{13}C, $\langle S_z \rangle_{t=0} = 0, \langle I_z \rangle_{t=0} = I_0$).

The polarisation state of the second nuclear species is important to the spin-polarisation recovery of the nuclear spin being studied. According to the Solomon equations (2.48) the effect of cross relaxation will be minimized when the second spin is at thermal equilibrium. In any case, the polarisation state must be same for all measurements in a sequence. Unfortunately this is not the case when the magnet is working in external mode for field-cycling experiments. In field-cycling experiments, if no special control procedures are in place, the initial spin-polarisation can be any value which means different recovery curves may be obtained for different initial conditions at same temperature and same field. We will discuss it later when

analysing the field dependence experimental data.

13C-BA 30K
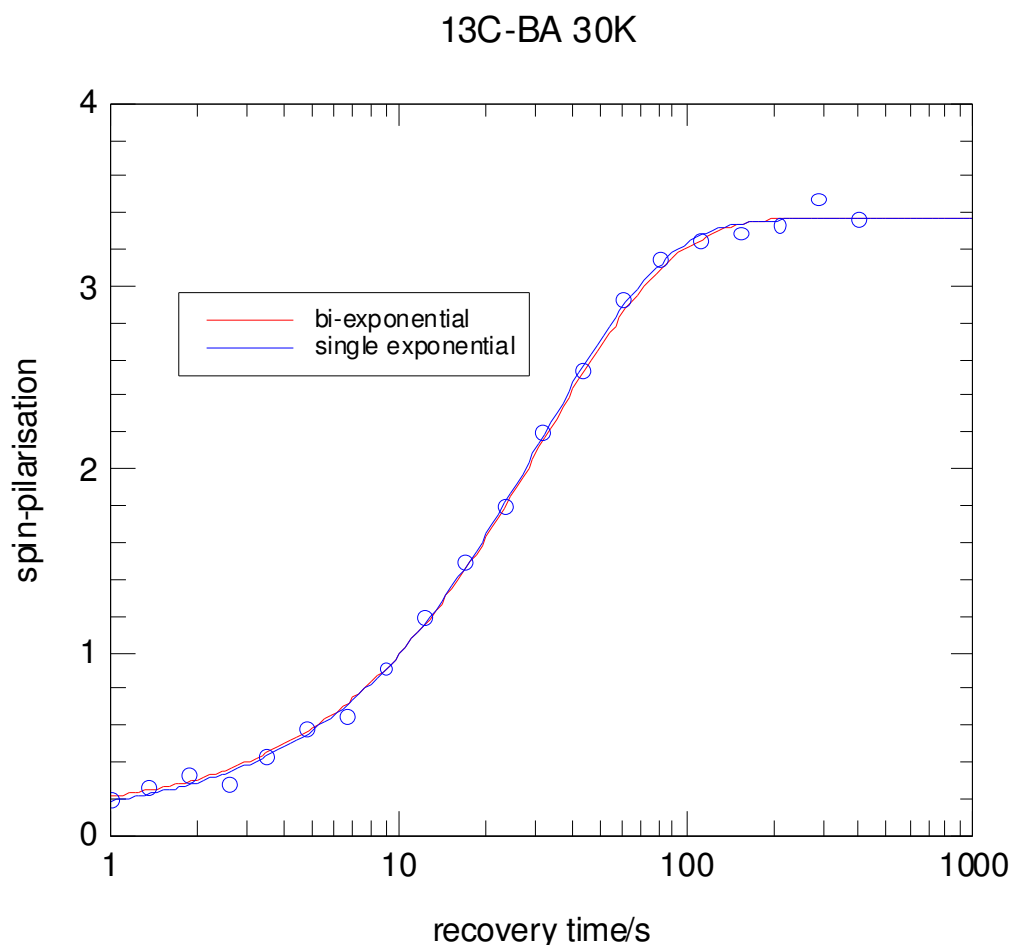
Fig 6.4 The spin-polarisation recovery curve characterised by a single exponential function, blue solid curve. The red solid curve was a fit to bi-exponential function, which was nearly same as the blue solid curve. The fit to bi-exponential function had an unacceptable error.

According to the theory described in Chapter 2, the spin-polarisation recovery curves for the nuclei in ^{13}C-BA should be bi-exponential. However, the spin-polarisation recovery curves for both nuclei were well represented by a single exponential with a single time constant, $T_1^{(eff)}$, within experimental error, as shown in Fig 6.4. Fitting to bi-exponential function did not improve the fit quality; furthermore although the spin-polarisation recovery curve was a bi-exponential function characterised by two time constants as discussed in the theory chapter (Chapter 2), it was difficult or even impossible to extract these two time constants with any accuracy in this sample (the accuracy for the bi-exponential fit in another heteronuclear sample which will be discussed in next chapter was so good that the two time constants were accurately extracted). Therefore special experimental techniques and data analysis method were

required for investigating the dynamics of this sample.

That the spin-polarisation recovery for both nuclei is single exponential is a significant observation. This suggests that the off diagonal elements in the relaxation matrix, σ_I and σ_S, are small by comparison with the diagonal terms ρ_I and ρ_S. Simulations also show that the effects of the off diagonal terms are further minimised by preparing the polarisation of the 'second' nucleus close to its thermal equilibrium value. This being the case, the two observed relaxation times $T_{1I}^{(eff)}$ and $T_{1S}^{(eff)}$ should closely approximate ρ_I^{-1} and ρ_S^{-1} respectively under the measured conditions of magnetic field and temperature. To assess the validity of this assertion, the values of the relaxation matrix have been calculated using the following procedure:

i. **Determination of the dipolar relaxation constants**: the value of C_{CH} was calculated from equation (2.50) given the atomic coordinates determined at low temperature by single crystal neutron diffraction. For this purpose it was sufficient to include only intra-dimer contributions since, for ^{13}C-^{1}H interactions, these dominate over inter-dimer contributions. In performing this calculation, as in reference [13], the atomic coordinates of the energetically less favourable dimer were determined by rotating the dimer about its central axis [60, 71]. The calculated value is $C_{CH}^{(calc)} = 1.36 \times 10^7$ s^{-2}. The value $C_{HH} = 6.3 \times 10^7$ s^{-2} was obtained from the field-cycling ^{1}H NMR relaxometry study of BA in natural isotopic abundance [67].

ii. **Simulation of proton transfer rate**: for the purposes of analysing the temperature dependence data, the correlation rate, τ_c^{-1}, was modelled using the dynamical parameters determined in earlier investigations of proton transfer in benzoic acid,

$$\tau_c^{-1} = 1.22 \times 10^8 \coth\left(\frac{A}{2k_BT}\right) + 1 \times 10^{10} \exp\left(\frac{-180}{T}\right) + 5 \times 10^{11} \exp\left(\frac{-600}{T}\right) \qquad (6.1)$$

The first term on the right hand side is a contribution from proton tunnelling in the ground state, the second term is due to tunnelling in an intermediate state and the final term is an Arrhenius law to accommodate the Boltzmann weighted average of through barrier processes via states higher up the barrier (pseudo-classical dynamics).

In Fig 6.5a, Fig 6.5b and Fig 6.5c, Fig 6.5d the calculated values of the relaxation rates R_1^{-1} and R_2^{-1} (solid lines), the weighting coefficients $c_2^{I,S}$ and $c_1^{I,S}$, and the inverse of the diagonal elements ρ_I^{-1} and ρ_S^{-1} (dashed lines) are presented as a function of temperature for two values of magnetic field:

   a) B=2.428 T, appropriate to the ^{13}C saturation-recovery experiments
   b) B =0.8878 T, appropriate to the ^{1}H saturation-recovery experiments.
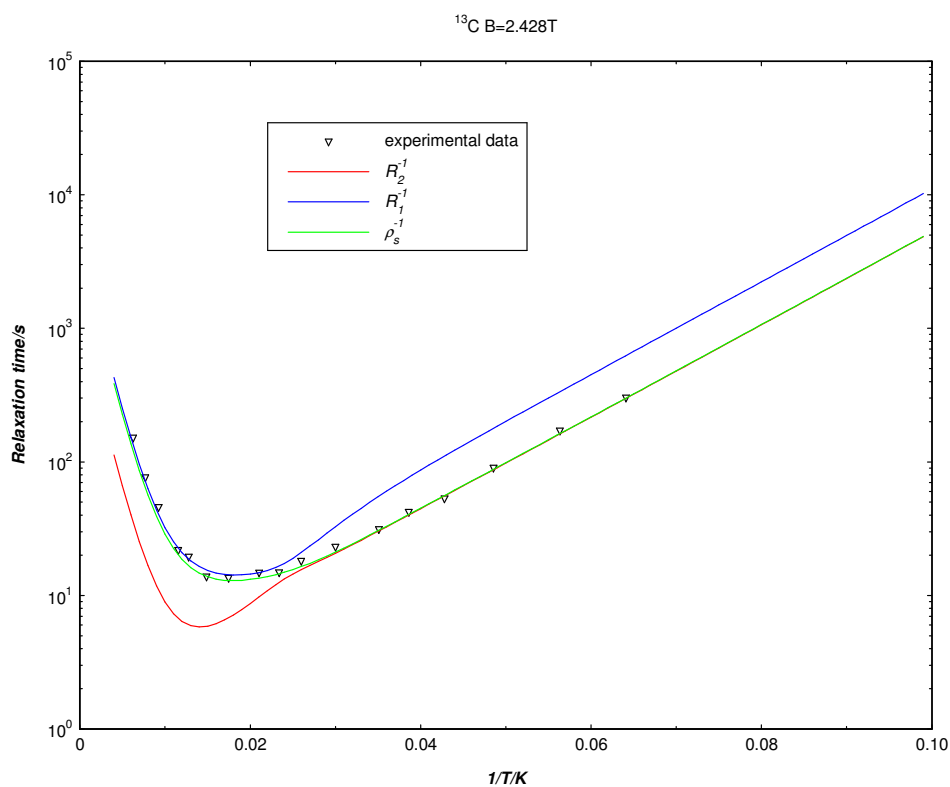
Fig 6.5a Calculation as a function of inverse temperature of relaxation rates (blue and red solid lines) and the inverse of the diagonal elements (green dashed line) for ^{13}C at B = 2.428T.
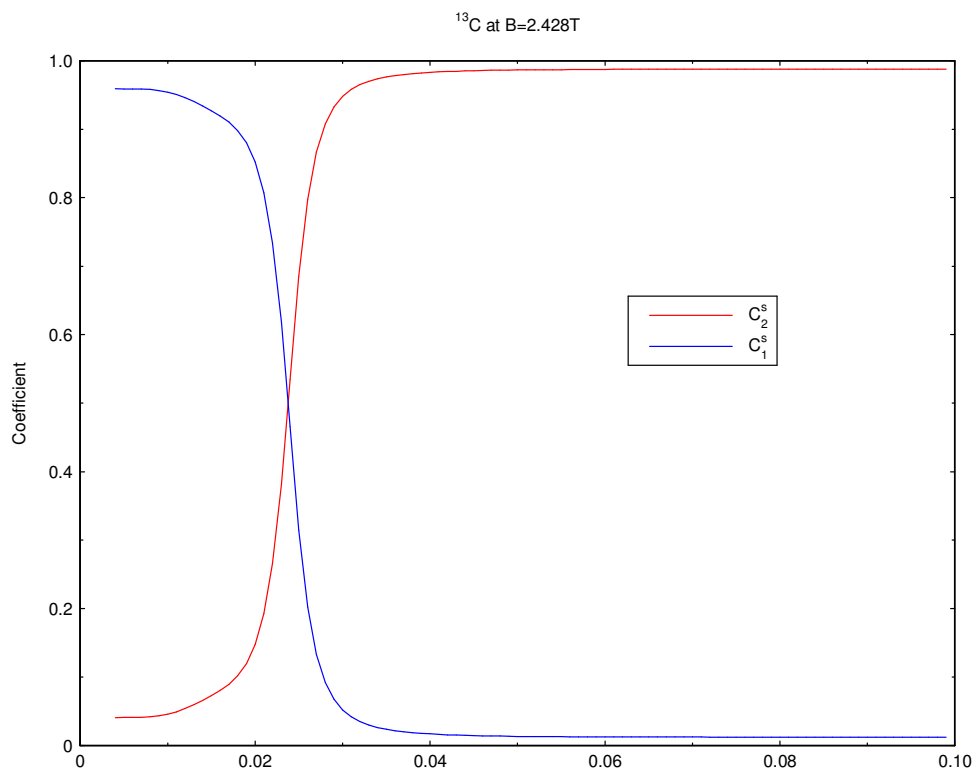
^{13}C at B=2.428T

Fig 6.5b Calculation as a function of inverse temperature of the weighting coefficients for ^{13}C at B = 2.428T.
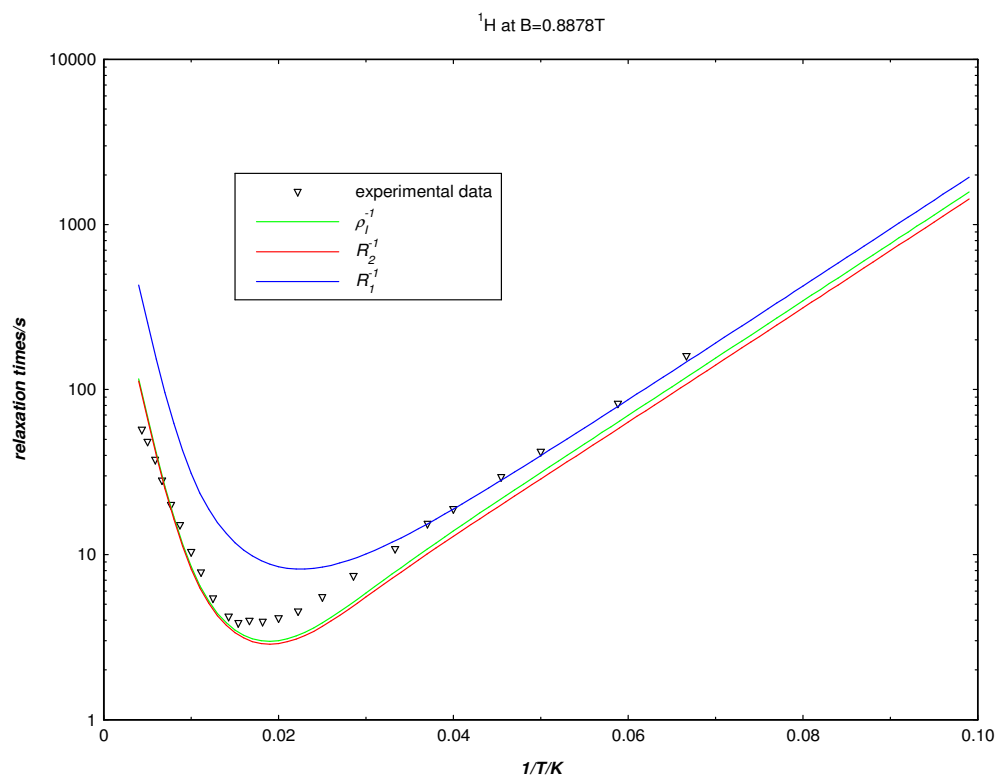
^{1}H at B=0.8878T

Fig 6.5c Calculation as a function of inverse temperature of the relaxation rates (blue and red solid lines) and the inverse of the diagonal elements (green solid line) for ^{1}H at B = 0.8878T.
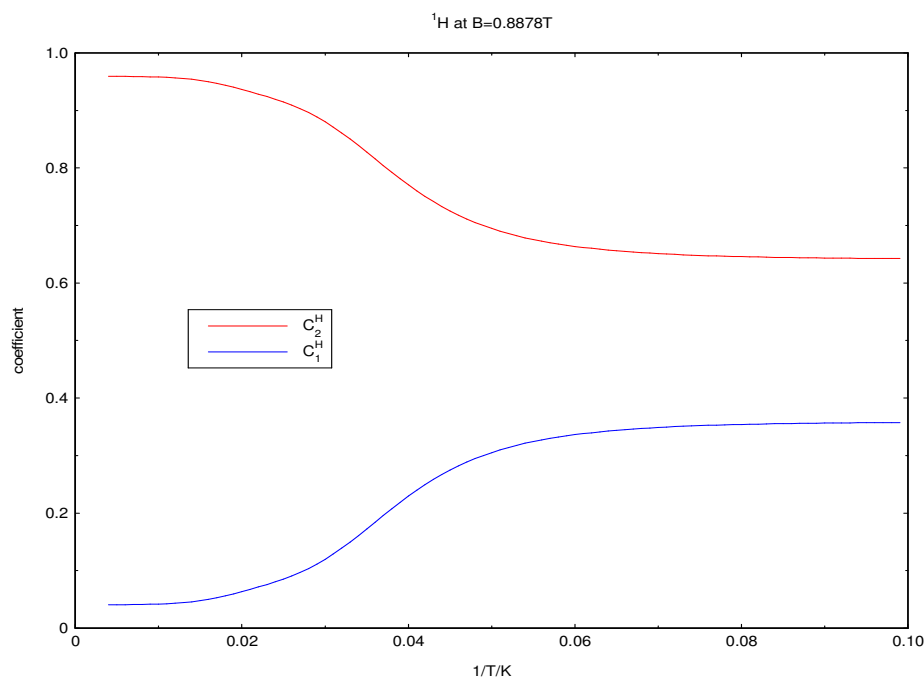
Fig 6.5d Calculation as a function of inverse temperature of the weighting coefficients for ^{1}H at B = 0.8878T.

Inspection of the calculated weighting coefficients shows that across a wide temperature range, the ^{13}C relaxation, Fig 6.5b, is indeed dominated by one exponential component. Only in a narrow temperature region do the weighting coefficients adopt values significantly different from 0 and 1, however, in this region R_1 and R_2 have similar values, Fig 6.5a, so it is doubtful that the observed spin-polarisation recovery will deviate significantly from a single exponential function. Therefore, the calculated behaviour shows that in practice the ^{13}C spin-polarisation recovery over the whole temperature range will be characterised by a single relaxation time constant, in agreement with observation. Similarly for the ^{1}H relaxation represented in Fig 6.5d; there is bi-exponential character revealed in the values of the weighting coefficients at low temperature, but the values of R_1 and R_2, Fig 6.5c, are insufficiently different for the ^{1}H relaxation to be distinguished from a single exponential.

To compare the calculated behaviour with the ^{13}C experiment we equate the effective T_1 at B=2.428 T with the weighted mean of the two spin-lattice relaxation time constants,

$$T_{1S}^{(eff)} = \frac{c_1^S/R_1 + c_2^S/R_2}{c_1^S + c_2^S} \qquad (6.2)$$

Similarly, using the same parameter set but at $B = 0.8878$ T we have evaluated the effective T_1 for the ^{1}H NMR constant field spin-lattice relaxation experiments,

$$T_{1I}^{(eff)} = \frac{c_1^I/R_1 + c_2^I/R_2}{c_1^I + c_2^I} \qquad (6.3)$$
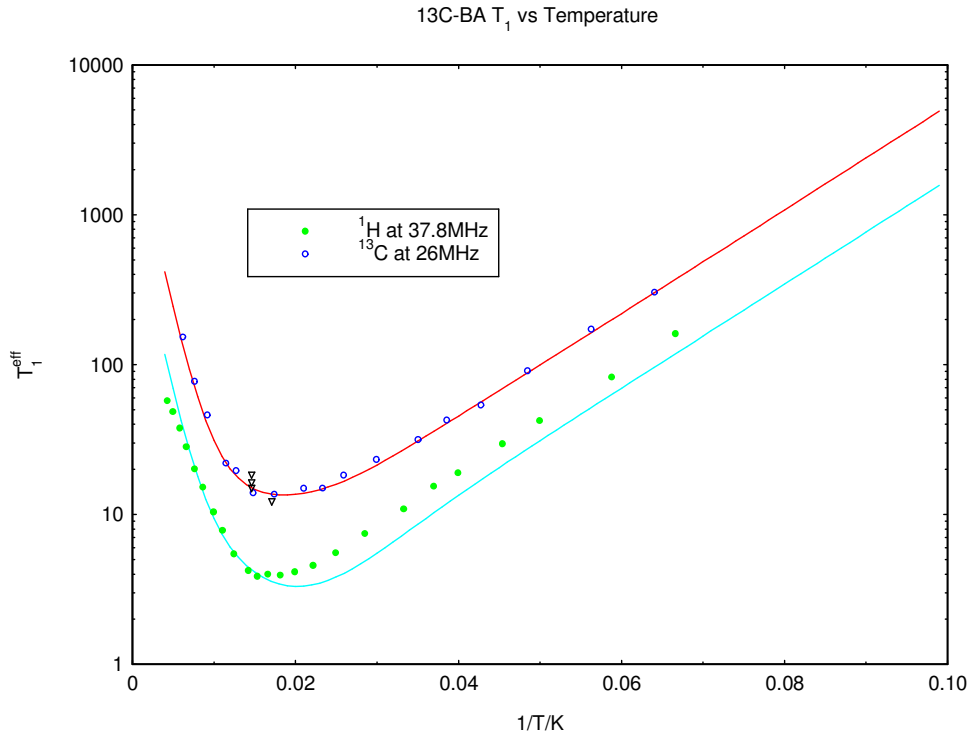
Fig 6.6 the inverse temperature dependence of the effective ^{13}C and ^{1}H spin-lattice relaxation time parameters recorded at constant field in each case. (^{13}C: 26MHz, 2.428T; ^{1}H: 37.8MHz, 0.8878T). The solid lines were calculated with dipolar constants $C_{CH} = 1.36 \times 10^7\ s^{-2}$ and $C_{HH} = 6.3 \times 10^7\ s^{-2}$.

The experimental (blue circles and green filled circles) and calculated spin-lattice relaxation times (solid lines) for both nuclei are plotted in Fig 6.6 as a function of inverse temperature. The parameters in equation (6.2) and (6.3) have been calculated and plotted in Fig 6.5a, Fig 6.5b, Fig 6.5c and Fig 6.5d. Neither C_{CH} or C_{HH} reported in (i) above was adjusted in calculating these curves. The best fit value of the energy asymmetry, $A/k_B = 80 \pm 2$ K, is consistent with the value reported in Chapter 4 for the sample with natural isotopic abundance.

As illustrated in Fig 6.6 that the calculation result for ^{13}C at 2.428T/26 MHz is in perfect agreement with the experimental data suggests that the dipolar constant C_{CH} calculated from the structure of BA without ^{13}C substitution is a good approximation. There is a small difference between the calculation result of ^{1}H and the experimental data in low temperature regime (< 50K) and high temperature regime (>150K), which may have arisen from a small error in allowing for the effect of spin-diffusion and related uncertainties in the effect of other protons from impurities such as water; however the bi-exponential behaviour in low temperature regime (as illustrated in Fig 6.5d) for ^{1}H also makes the effective relaxation time less valid for presenting the relaxation. To fully present the bi-exponential relaxation, the relaxation rates are the only choice and need to be extracted accurately from the spin-polarisation recovery curves, as will be discussed in next chapter; however it was difficult to extract these relaxation rates accurately for this case as discussed above, fortunately no significant error was introduced to the analysis of ^{13}C and ^{1}H data.

It is notable and significant that the calculated values of $T_{1I}^{(eff)}$ and $T_{1S}^{(eff)}$ correspond very closely with the respective inverse diagonal elements ρ_I^{-1} and ρ_S^{-1} of the relaxation matrix; the latter are plotted in Fig 6.5a, Fig 6.5c (green lines). This confirms the assertion made earlier and will facilitate the interpretation of the field-dependent T_1 data in later sections, including the extraction of accurate values of the correlation rate for proton transfer.

Concluding this section on the constant field experiments: Using an estimate for the proton transfer correlation rate based on the behaviour of BA in natural isotopic abundance, equation (6.1), good agreement between the relaxation model and the experimental spin-lattice relaxation data is obtained. Clearly the heteronuclear interactions play an important role in the relaxation processes. Indeed it is the modulation of the ^{13}C-^{1}H interactions arising from the proton motion that drives the spin-lattice relaxation of the ^{13}C nuclei. However, for both nuclei the spin-polarisation recovery appears single exponential to within experimental error. This characteristic will be further explored in the context of variable field measurements in the next section.

6.3.2 Field cycling: ^{13}C and ^{1}H spin-lattice relaxation as a function of B-field

In a constant field experiment it is relatively straightforward to prepare the system in a systematic state where, for example, one nuclear spin system is saturated while the second has its equilibrium polarisation. In a field-cycling experiment, where the nature of the experiment is such that the magnetic field is switched rapidly across a wide range of values this is less easy and it is evident that particular care must be taken to establish consistent polarisation states before each measurement.

Firstly we consider the results of a series of saturation-recovery experiments on ^{13}C. Three field-cycling sequences were employed as illustrated in Figure 6.7a, Fig 6.7b and Fig 6.7c, each designed to prepare the ^{1}H magnetisation differently. Some have been discussed in Chapter 3. For comparison and illustrating the purpose of designing them, we plotted them here again.
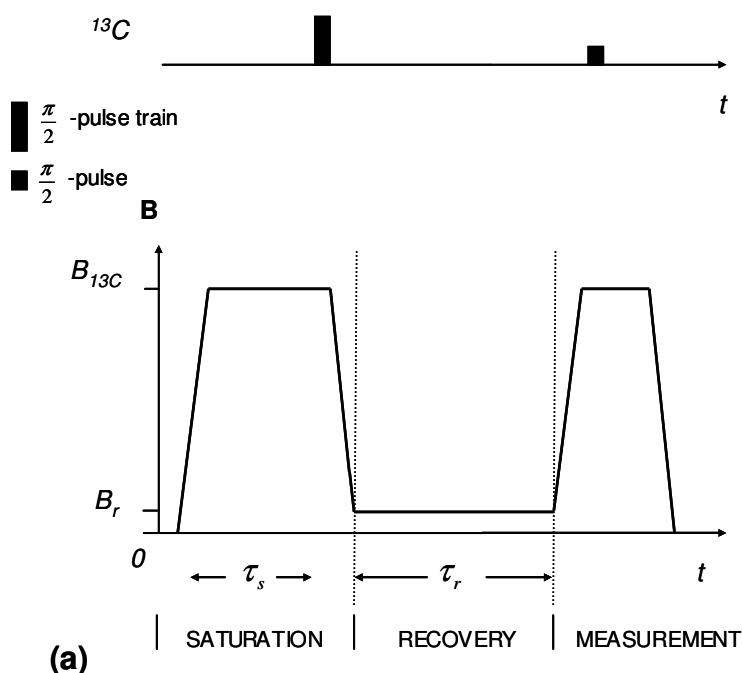
Fig 6.7a Traditional saturation-recovery pulse sequence same as the sequence in Fig 3.17. A settle time 10s was normally employed to stabilize the field before saturation pulse train applied and it also create a pre-determined polarisation of the second spin ^{1}H.

Seq. a.   Beginning from zero, the field was switched rapidly to the resonance

condition for ^{13}C ($B_{13C} = 2.026$ T , $\nu_{13C} = 21.7$ MHz) where it remained for

a period τ_s to create a pre-determined polarisation of the ^{1}H nuclei. The ^{13}C

nuclei were then saturated with a burst of $\pi/2$ pulses before the field was

rapidly switched to the field of interest, B_r, where the nuclei were allowed to

relax for a time interval τ_r. A rapid field switch then took the field back to

resonance with the ^{13}C nuclei and the ^{13}C spin-polarisation was measured

with a $\pi/2$ pulse before the field reverted to zero.

(b)
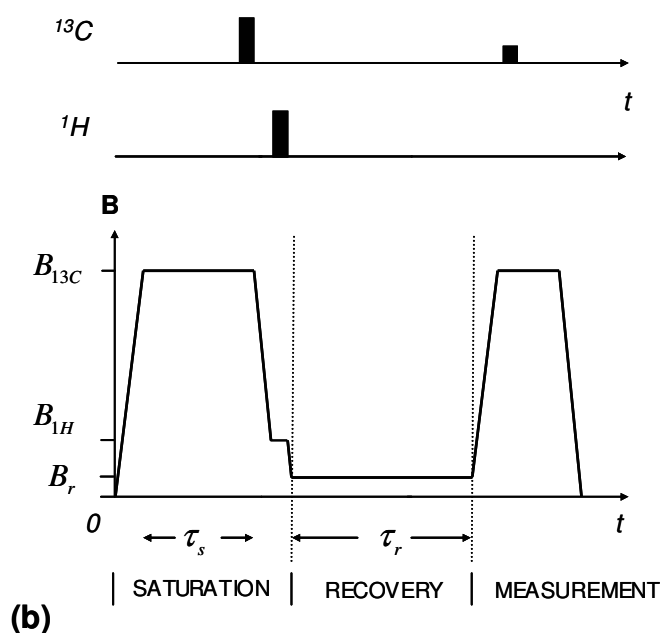
Fig 6.7b A variant to the sequence in Fig 6.7a, designed for saturating both the ^{13}C and ^{1}H spin-polarisation before relaxation at recovery field.

Seq. b.   In a variant to sequence a, a short pause at the resonance field of the ^{1}H

nuclei ($B_{1H} = 0.5092$ T , $\nu_{1H} = 21.7$ MHz) was introduced into the field

switch immediately following ^{13}C saturation; here the ^{1}H nuclei were

saturated with a burst of $\pi/2$ pulses. The original purpose of designing this

pulse sequence was to eliminate the effect of ^{1}H. However the experimental

results were not as we expected, but the importance of initial conditions was

elicited.
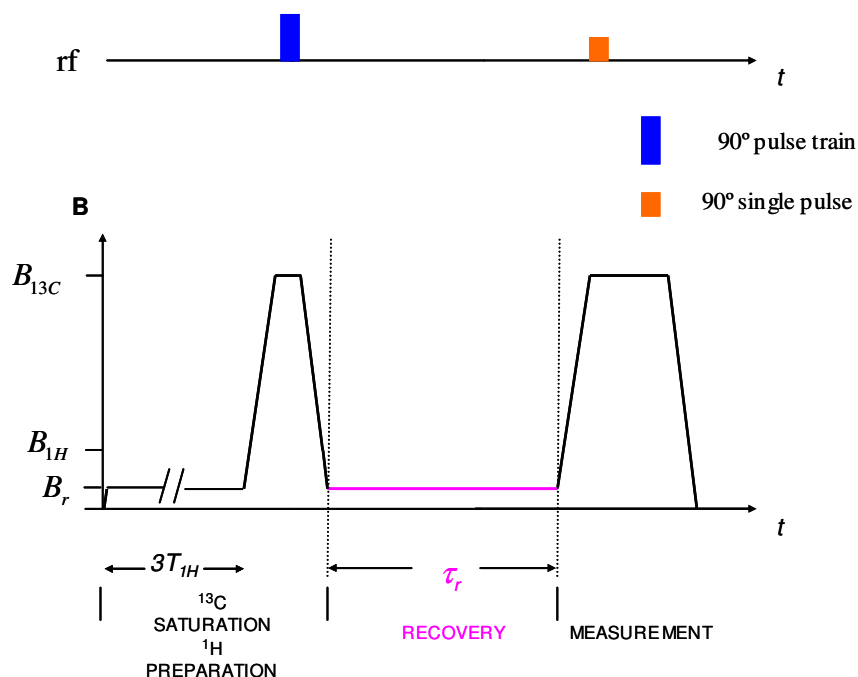
Fig 6.7c Heteronuclear preparation-recovery pulse sequence applied on the ^{13}C-BA sample. B_{13C} and B_{1H} are the resonance fields of ^{13}C (spin S) and ^{1}H (spin I) respectively. B_r is the recovery field for the ^{13}C spin to recover its magnetisation after saturation pulses. The measurement field is on the spin S resonance field to measure the relaxation process of spin S. This figure is same as Fig 3.22

Seq. c. In a third sequence, the sample was prepared at B_r for at least three times the proton T_1 before the ^{13}C spin-polarisation was saturated. This prepared the ^{1}H polarisation close to its thermal equilibrium value at the field the ^{13}C relaxation was to be recorded. It was expected that this experiment would minimise the effects of cross relaxation between the two nuclear species.

One polarisation pulse sequence designed to measure the relaxation time at low field is also plotted here, which will be discussed later.

Seq. d. In this sequence, a polarisation field was employed to enhance the signal quality at low field. Two variants were employed; in one experiment the initial conditions of both ^{13}C and ^{1}H spins were polarised, whereas in the other experiment the ^{1}H polarisation was destroyed.
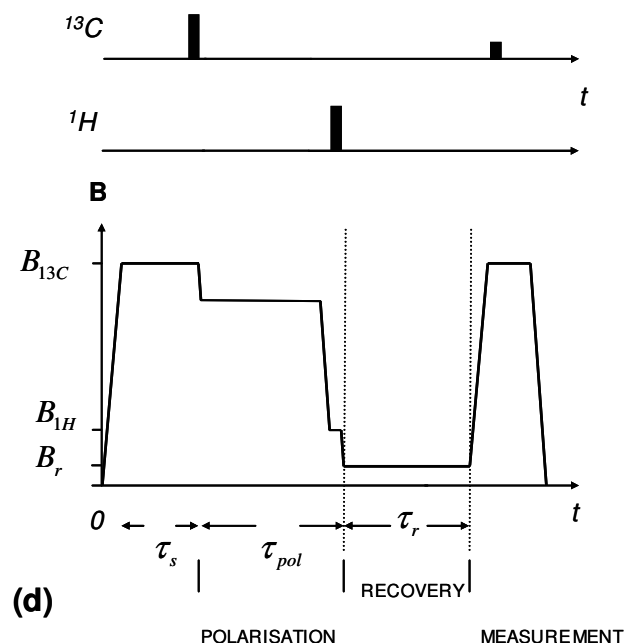
Fig 6.7d Polarisation-recovery pulse sequence designed to measure the relaxation time at low field.

Magnetisation Recovery Curves

Magnetisation recovery curves were recorded using the three field-cycling sequences. In Fig 6.8 the magnetisation recovery of ^{13}C arising from pulse sequences (a) and (c) is plotted; B_r=1.2 T, τ_S=10 s, T=20 K. Each set of data fitted well to a single exponential recovery law from which a relaxation time constant, $T_{1S}^{(eff)}$, was extracted. Within experimental uncertainties, no significant improvement was gained by fitting to a bi-exponential function. Significantly we observe a systematic difference between the two recovery curves leading to different $T_{1S}^{(eff)}$ values. As with constant field experiments, in no field-cycling experiment was it possible to definitively resolve two exponential components in any magnetisation recovery curve. The systematic differences arise from the preparation of the initial polarisation states and the resulting effects on the weighting coefficients, $c_{1,2}^S$.
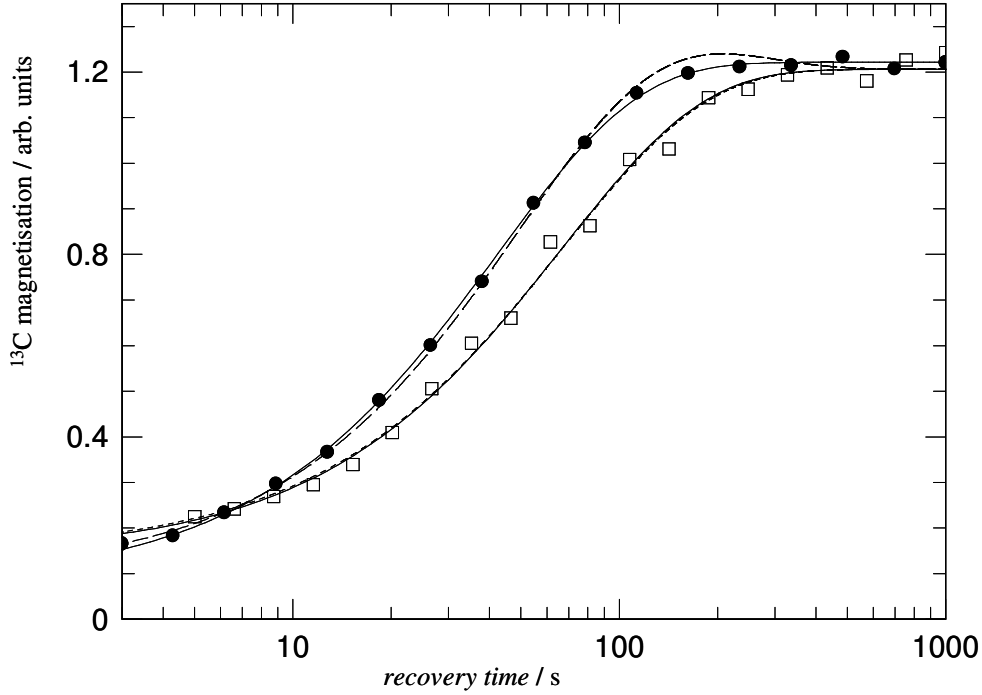
Fig 6.8 ^{13}C magnetisation recovery curves recorded using saturation-recovery pulse sequences (a) (filled circles) and (c) (open squares): $B = 1.2$ T, $T = 20$K. The simulations, representing the solutions of the coupled equation (2.48), are shown with dashed lines. The differences arise from the different initial polarisation states of the ^{1}H reservoir.

We have simulated the solutions to equation (2.48) using the calculated relaxation matrix defined by the parameters $C_{CH} = 1.36 \times 10^7$ s^{-2} and $C_{HH} = 6.3 \times 10^7$ s^{-2} employed in the previous section. The Solomon equations are rewritten as follows,

$$\begin{cases} \Delta I_z(t) = \left[-\rho_I \left(I_z(t) - I_0 \right) - \sigma_I \left(S_z(t) - S_0 \right) \right] \Delta t \\ \Delta S_z(t) = \left[-\sigma_s \left(I_z(t) - I_0 \right) - \rho_s \left(S_z(t) - S_0 \right) \right] \Delta t \end{cases} \tag{6.4}$$

Given initial conditions, with small time increment Δt (0.01s is enough for this sample), the time dependence of polarisation can be calculated and plotted as a recovery curve. It is noticeable that in Solomon equations I_z and S_z are spin polarisations of the two nuclei respectively. They are not magnetisations as often encountered in the homonuclear systems. Magnetisation is proportional to $\gamma^2 B$, whereas spin polarisation is proportional to γB, as discussed in Chapter2. In homonuclear system, only one magnetogyric ratio is present, there is no confusion between the two terms: magnetisation and polarisation; but in heteronuclear system,

149

the difference between these two terms becomes so important that the term polarisation, rather than the term magnetisation, must be used to investigate the relaxation process.

Computed ^{13}C polarisation recoveries, subject to the initial conditions defined for sequences (a) and (c), are superimposed on the experimental curves in Fig 6.8 (dashed lines). In these calculations we estimate that the initial proton polarisation for field cycling sequence (a) is approximately 10% of I_0 at 1 T. The model successfully simulates the apparent shortening of the effective T_1 when the initial proton polarisation differs from equilibrium. Close inspection of the simulation curve for sequence (a) reveals some bi-exponential character culminating in a very small Nuclear Overhauser Effect (NOE) [24-27], [70] enhancement of the ^{13}C polarisation during the approach to equilibrium. An NOE enhancement is not evident in this particular set of experimental data, but the predicted effect is not large compared with experimental uncertainties. Small NOE enhancements were observed in some experimental data sets. The agreement between the experimental and computed recovery curves is generally very good given,

   i)   the manner in which spin-diffusion is accommodated in the model,

   ii) effects arising from relaxation during the field switches

   iii) systematic uncertainties in our knowledge of the actual initial polarisation
        states.

The third might be a relevant issue, particularly for sequence (a), since polarisation can be preserved for extended periods via the dipolar order, even if the field is switched to zero.

Therefore to conclude the result of these calculations, the initial preparation of the second spin (^{1}H) reservoir affects the effective spin-lattice relaxation time that is observed. However, the magnitude of the cross-relaxation effect is not large enough to enable us to resolve any bi-exponential curve experimentally.

Magnetic Field Dependence: Mapping the Spectral Density

Using the three saturation-recovery field-cycling sequences, the magnetic field dependence of the ^{13}C spin-lattice relaxation time, $T_{1S}^{(eff)}$, was measured at 20K in the field range $0.4 \leq B_r \leq 2.3 \, \text{T}$. Measurements at fields lower than 0.4 T were impractical due to the small ^{13}C signal amplitude. The results are plotted in Fig 6.9 as $\left(T_{1S}^{(eff)}\right)^{-1}$ vs. B_r on log-log axes. Systematic differences in the measured values of $T_{1S}^{(eff)}$ of the kind illustrated in Fig 6.8 are reflected in this graph. The band encompassing the three sets of data has a range of order 40%. However, significantly, the three curves are parallel to each other meaning that the information content regarding the proton transfer correlation rate is identical for the three sequences. Free fits to the three relaxation curves separately provide correlation rates that agree to within 5%.

For sequences (a) and (b), since the proton polarisation is far removed from equilibrium, the effects of cross relaxation and the off-diagonal elements of the relaxation matrix influence the measured relaxation rates. Only for sequence (c) is cross-relaxation minimised. The disadvantage of this sequence, however, is the preparation time required. Since each data point on the magnetisation curve requires establishment of thermal equilibrium within the proton Zeeman reservoir, given the very long T_1 values, the measurement of a ^{13}C T_1 can become excessively time consuming, especially if full field dependence is required. Fortunately, as is evident from the fits to the experimental data in Fig 6.9 and the simulations, where the off-diagonal elements of $\mathbb{R}$ are small then to a good approximation only the amplitude and not the shape of the $T_{1S}^{(eff)}$ vs. B curve is affected by the preparation of the ^{1}H Zeeman reservoir.
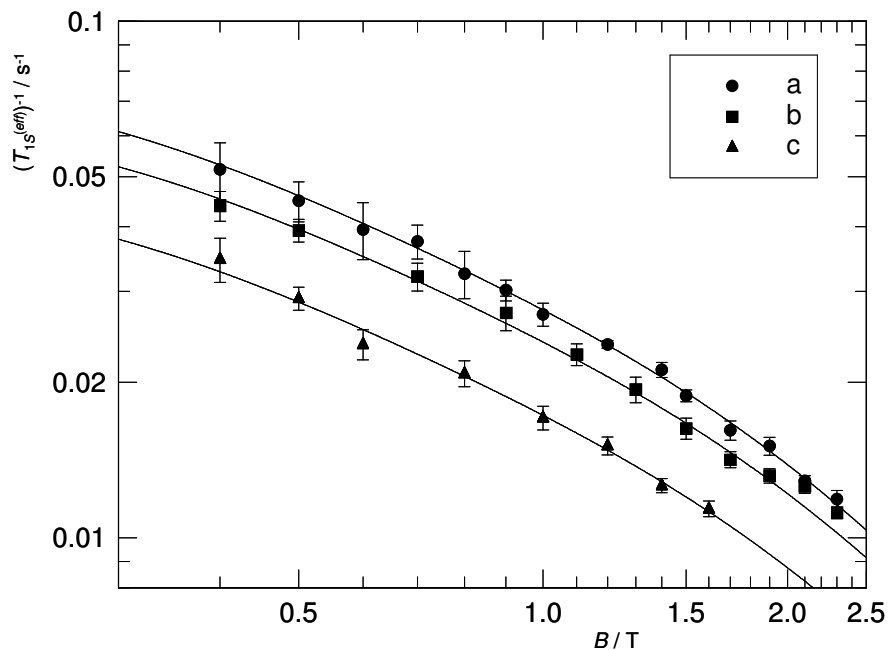
Fig 6.9 The magnetic field dependence of the ^{13}C inverse spin-lattice relaxation time, $\left(T_{1S}^{(eff)}\right)^{-1}$,

recorded at $T = 20$K using pulse sequences (a), (b) and (c). The solid lines represent free-fits to

equation (6.5). The initial ^{1}H polarisation states are different for the three sets of data but the curves

are parallel indicating that the information content regarding the correlation rate, τ_c^{-1}, is same for all

three.

(a) ^{1}H

(b) ^{13}C: 20K
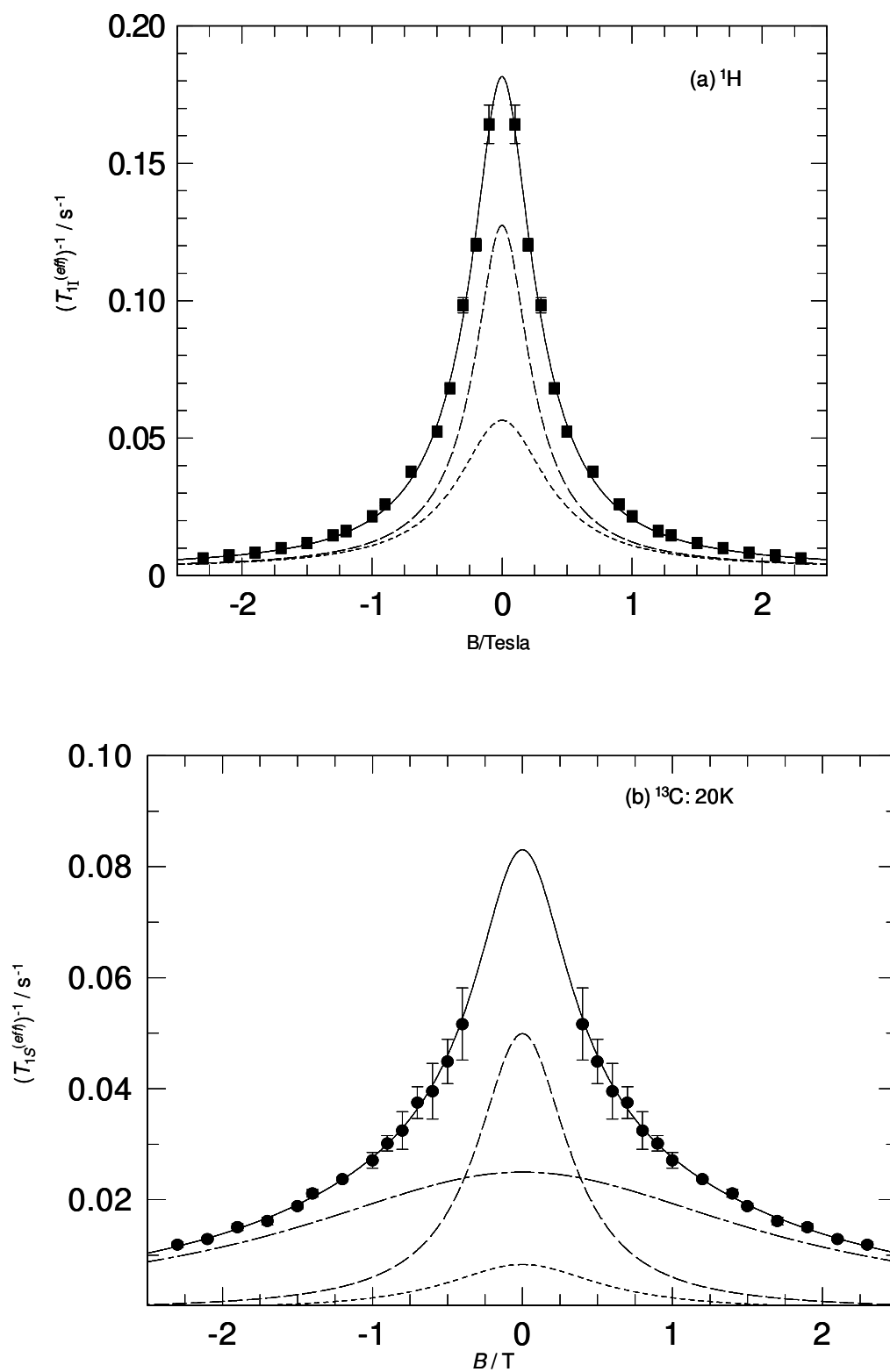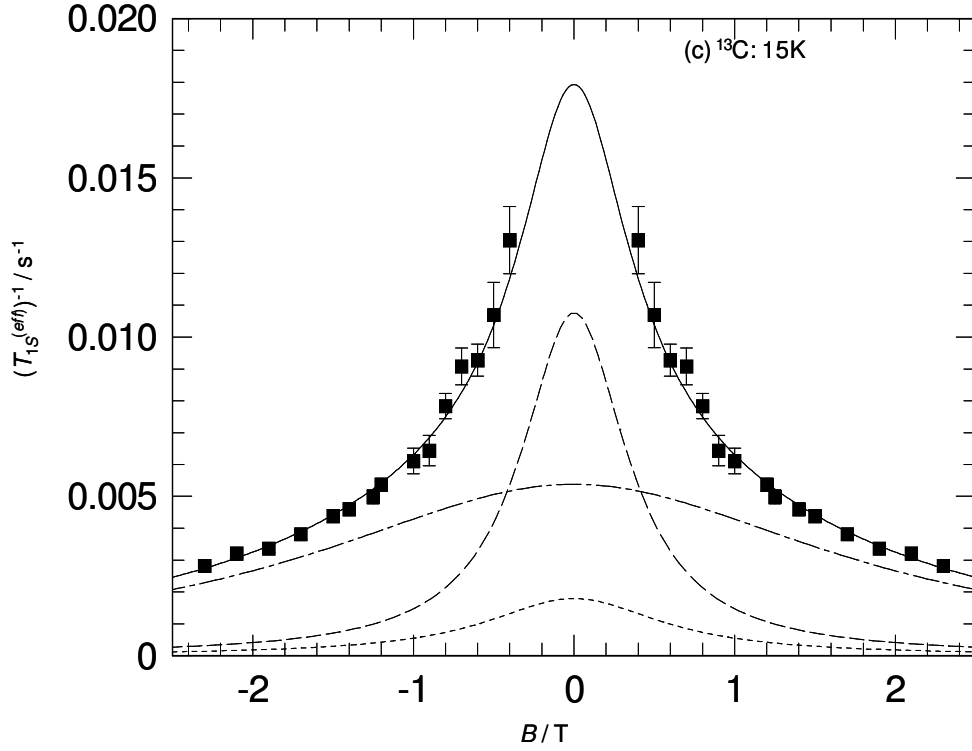
Fig 6.10 The magnetic field dependence of the inverse spin-lattice relaxation times (a) ^{1}H: $T_{1I}^{(eff)}$ ($T =$ 20K), (b) ^{13}C: $T_{1s}^{(eff)}$ ($T = 20$K) and (c) ^{13}C: $T_{1s}^{(eff)}$ ($T = 15$K) where the proton transfer dynamics are dominated by phonon-assisted tunnelling. The data have been reflected in the B-axis to emphasise the Lorentzian character. Solid lines are fits to equation (6.4) and (6.5) respectively. The dashed lines in (a) represent the heteronuclear (ρ_I^{CH}; long dash) and homonuclear (ρ_I^{HH}; short dash) components of equation (6.4). The dashed lines in (b) and (c) represent the three Lorentzian components of equation (6.5) ($L(\omega_H + \omega_C)$; long dash, $L(\omega_C)$; dash-dot, $L(\omega_H - \omega_C)$; short dash).

The field dependence of the effective ^{1}H spin-lattice relaxation rate $\left(T_{1I}^{(eff)}\right)^{-1}$ was also measured using field-cycling sequence (a). These measurements were found to be independent of the initial polarisation state of the ^{13}C spins, consistent with the small heat capacity of the ^{13}C Zeeman reservoir. The ^{1}H data is plotted in Fig 6.10a. The field dependence of the effective ^{13}C spin-lattice relaxation rate $\left(T_{1S}^{(eff)}\right)^{-1}$ was also measured at two temperatures, Fig 10b, 20K and Fig 10c, 15K. The data are plotted with linear axes and are reflected about the $B = 0$ axis to emphasize the Lorentzian lineshapes. It is noticeable that the width of the relaxation peak appears broader for the ^{13}C data than the ^{1}H data; this reflects not a difference in correlation

rate but a difference in the frequencies at which the spectral density is sampled.

6.4 Discussion

6.4.1 Interpretation of the spectral densities

The experimental data in Fig 6.10 represents a weighted mean of the spin-lattice relaxation rates R_1 and R_2. Our objective is to interpret this data in terms of the various Lorentzian components that constitute the relaxation matrix and to extract the correlation time for proton transfer. Our approach will be necessarily pragmatic. Independent experimental information on the elements of $\mathbb{R}$ are unavailable to us, although the agreement with the temperature dependence data, the simulations of spin-polarisation recovery and our knowledge of the proton transfer behaviour in samples with natural isotopic abundance, gives us confidence that these can be calculated reliably in this particular material. Calculations confirm that at low temperature the values of $\left(T_{1I}^{(eff)}\right)^{-1}$ and $\left(T_{1S}^{(eff)}\right)^{-1}$ closely match the diagonal elements of $\mathbb{R}$, ρ_I and ρ_S, consistent with the off-diagonal elements being small. This being the case we are able to write;

$$
\begin{aligned}
\left(T_{1I}^{(eff)}(B)\right)^{-1} &= \rho_I^{CH} + \rho_I^{HH} \\
&= K_{CH}\left(L\left((\gamma_H - \gamma_C)B, \tau_c\right) + 3L(\gamma_H B, \tau_c) + 6L\left((\gamma_H + \gamma_C)B, \tau_c\right)\right) \\
&+ K_{HH}\left(L(\gamma_H B, \tau_c) + 4L(2\gamma_H B, \tau_c)\right)
\end{aligned}
\tag{6.5}
$$

and

$$
\begin{aligned}
\left(T_{1S}^{(eff)}(B)\right)^{-1} &= \rho_S^{CH} \\
&= K_{CH}\left(L\left((\gamma_C - \gamma_H)B, \tau_c\right) + 3L(\gamma_C B, \tau_c) + 6L\left((\gamma_C + \gamma_H)B, \tau_c\right)\right)
\end{aligned}
\tag{6.6}
$$

where the functions are expressed in terms of the magnetic field B. The Ks are the dipolar constants incorporating the temperature dependence factor associated with the energy asymmetry (See equations (2.49) and (2.51)).

We have independently fitted the ^{1}H and ^{13}C T_1 data in Fig 6.10 to the functions (6.5) and (6.6) above and the best fits are shown as solid lines; good agreement is

observed. The dashed curves depict the different Lorentzian components comprising the net spectral density. The proton transfer correlation rate values determined from the ^{13}C and ^{1}H data sets, $\tau_c^{-1} = (1.24 \pm 0.04) \times 10^8$ s^{-1} (^{13}C: 20K), $\tau_c^{-1} = (1.33 \pm 0.08) \times 10^8$ s^{-1} (^{13}C: 15K) and $\tau_c^{-1} = (1.25 \pm 0.05) \times 10^8$ s^{-1} (^{1}H:20K), agree within experimental uncertainties.

6.4.2 Polarisation-recovery experiments

At low field, in this case defined as $B_r < 0.4$ T, the ^{13}C NMR signal is too small to make possible saturation-recovery experiments to measure the ^{13}C relaxation. In such cases in homonuclear field-cycling relaxometry it is customary practice to employ polarisation-recovery pulse sequences to record the relaxation properties. We have investigated the ^{13}C magnetisation recovery in such experiments on this heteronuclear material. Here the spin systems are first polarised at high field before the field is switched to the low relaxation field, B_r, where the return to thermal equilibrium of the spins is monitored. The polarisation-recovery pulse sequence is illustrated in Fig 6.7d and two variants were employed: in a first experiment the initial states of both ^{1}H and ^{13}C spins were polarised, whereas in a second experiment the ^{1}H polarisation was destroyed with a resonant pulse during the switch from the polarisation field to the low relaxation field. The spin-polarisation recovery curves for these two experiments are depicted in Fig 6.11 where the relaxation field was $B_r = 0.3$ T and the polarisation field was $B_{pol} = 1.5$T. There is a considerable systematic difference in the recovery curves, reflecting the different initial polarisation states. Both recovery curves can be fitted satisfactorily with a single exponential function (solid lines) but clearly in both there is underlying a significant bi-exponential character. As earlier with the saturation-recovery experiments, we have simulated the solutions of the coupled relaxation equations (2.48) with $C_{CH} = 1.36 \times 10^7$ s^{-2} and $C_{HH} = 6.3 \times 10^7$ s^{-2}. Simulated curves are superimposed on the experimental data in Fig 6.11 (dashed lines) and there is good agreement.
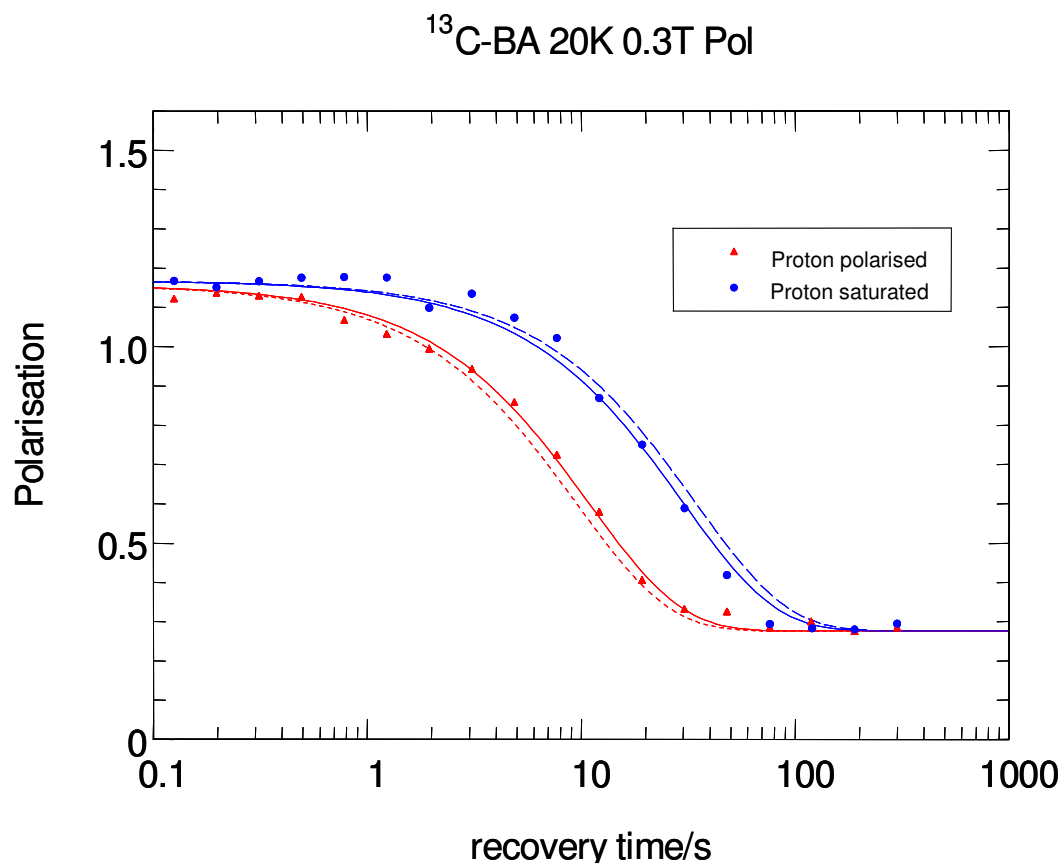
Fig 6.11 ^{13}C magnetisation recovery curves recorded using polarisation-recovery pulse sequence (d) with and without initial polarisation of the ^{1}H reservoir. Filled red triangles; protons polarised. Filled blue circles; protons saturated. The simulations, representing the solutions of the coupled equation (2.48), are shown with dashed lines. Solid lines are free single exponential fit.

Clearly the relaxation model is corroborated but where does this leave our experiment to measure the low field relaxation behaviour? Unfortunately, it is difficult to see how such a polarisation-recovery experiment can independently lead to a measurement of a relaxation rate that can be plotted as a function of field to map out the spectral density. We are no longer in a regime where the effects of the off-diagonal elements of the relaxation matrix are negligible and where the observed relaxation rate corresponds closely with a diagonal element. Unless the ^{13}C signal to noise ratio is sufficiently good to facilitate an accurate bi-exponential analysis, no independent reduction of the polarisation-recovery data can lead to a relaxation rate that can be assimilated into the magnetic field dependent data of Figs 6.9 and 6.10. Only if additional information from a model is input into the analysis can the polarisation-recovery curves be interpreted. Therefore, this polarisation-recovery

data, together with the simulations, provides corroboration of the dynamical model for proton transfer and the relaxation model but it does not unfortunately provide independent information on the correlation rate.

6.4.3 Effects of ^{13}C substitution on the proton transfer rate

At temperatures of 20K and below the proton transfer dynamics are dominated by ground state phonon assisted tunnelling and the correlation rate is in the temperature independent 'plateau' region. We designate this as the 'tunnelling rate' and our experiments show that this value is the same within experimental error for ^{13}C-BA and BA in natural isotopic abundance. Given the multi-dimensional character of the PES and the significant changes in bonding which occur as the protons move this result might be viewed as somewhat disappointing, especially as the tunnelling matrix element is an exponential function of the particle mass and the barrier properties. However, it is demonstrated how field-cycling experiments provide impressive accuracy (approximately 2% for homonuclear systems and 5% for heteronuclear) in the determination of correlation rates and now that *ab-initio* calculations of multi-dimensional tunnelling are becoming tractable on systems of the size of BA it will provide a useful result against which to evaluate the theoretical framework and the efficacy of contemporary quantum chemistry computations.

6.5 Concluding Remarks

Even though the ^{13}C abundance was enriched at the carboxyl site, the measurement of the ^{13}C relaxation properties was still a challenging one due to the small NMR signal amplitude arising from its small magnetogyric ratio and small mole fraction. Additionally, the very long relaxation times often precluded the possibility of extensive signal averaging. Nonetheless, a very satisfactory account of the relaxation properties of a heteronuclear system has emerged from this investigation.

There is a sense in which the study of the ^{13}C relaxation in this material provides a very well-defined system with the ^{13}C nucleus acting as a 'spy' on the proton transfer dynamics; just two ^{13}C-^{1}H dipolar contacts dominate. The advantages are familiar in the guise of isotopic labelling but no spin system can act in isolation and the disadvantage is the additional complexity in the spectral density components. The study benefited from prior knowledge and experience of the BA system and the relaxation theory has been validated to a highly satisfactory degree of precision. The relaxation theory for heteronuclear, coupled systems is long established but relatively few experimental investigations have been undertaken as a function of magnetic field. Here we have separately identified the different Lorentzian components for the first time. This study has confronted some interesting practical issues regarding the methodology of field-cycling relaxometry in heteronuclear spin systems. Clearly the initial polarisation of the spin systems is an important factor and must not be overlooked as experiments on isotopically labelled samples become more prevalent; neither must spectral density components that characterise the heteronuclear interactions be ignored if accurate values of the correlation times are to emerge. Systematic effects influencing the interpretation of single-spin relaxation data are readily observable and must be accommodated in any model used to interpret the data. Furthermore, as strategies to enhance NMR signals from traditionally unreceptive systems via polarisation transfer become more prevalent, investigations such as this to quantify the coupling between spin reservoirs are likely to become more important.

The use of polarisation-recovery pulse sequences, often used in field-cycling, presents its own challenges for heteronuclear systems. Usually such schemes are necessary to obtain an adequate signal amplitude at low field but it is difficult to envisage a methodology that provides a systematic idealised polarisation state where the second spin system, in this case ^{1}H, is close to its equilibrium value for the relaxation field B_r. It should be possible with carefully manicured ^{1}H pulses and preparation periods but it would present a significant experimental challenge.

A field-cycling investigation is confronted with difficulties in multi-spin systems, however, as this example shows, if the preparation of the initial polarisations is systematic then all of the advantages of the field-cycling technique can be realised in providing accurate values for the correlation times and information on the mechanism driving the dynamics. This particular system benefited from relaxation processes that were dominated by the diagonal elements of the relaxation matrix, facilitating the analysis of the spectral density components and widths; the ^{13}C relaxation was often mono-exponential and the bi-exponential character was usually only revealed when the ^{1}H spin reservoir was far from equilibrium. In systems where the off-diagonal elements play a more significant role and bi-exponential behaviour is more apparent, as for example in ^{1}H-^{19}F heteronuclear systems, then alternative field-cycling methodologies must be adopted to determine all elements of the relaxation matrix individually. Only then can the relaxation data be reduced in such a way as to permit the spectral density components to be resolved with sufficient accuracy; such an investigation has been conducted on proton transfer in tetrafluoroterephthalic acid (TFTA) in our laboratory and will be discussed in the next chapter.

Chapter 7 Heteronuclear experiments III-TFTA [66]

As discussed in Chapter 6, the magnetisation recovery curve of the spin ½ -spin ½ heteronuclear system should be characterised by two spin-lattice relaxation rates R_1 and R_2 , and therefore present itself as bi-exponential behaviour. But for the ^{13}C-BA sample, the bi-exponential behaviour is suppressed and two relaxation rates cannot be extracted from the magnetisation recovery curve since the off-diagonal element of the relaxation matrix is too small. Therefore the two relaxation rates are too close to each other making it difficult to resolve them from the magnetisation recovery curve.

We have discussed how to deal with the special case of heteronuclear systems like ^{13}C-BA in the last chapter. Here we would like to develop a methodology for how to extract useful information from the bi-exponential magnetisation recovery curve and express the dynamics of the heteronuclear interaction for samples where the off diagonal element is significant.

A field-cycling NMR pulse sequence was designed for studying cross-relaxation between unlike nuclear spins in the solid state. This technique gave us an opportunity to directly measure the off-diagonal element which characterises the cross-relaxation. It has been applied to study proton tunnelling in the hydrogen bonds of a carboxylic acid containing ^{19}F and ^{1}H spins. The field-cycling technique has enabled us to map out for the first time the field dependence of the off-diagonal element that characterises the cross-relaxation process. Therefore an accurate measure of the proton transfer rate is obtained, not from the diagonal elements of the relaxation matrix, but from the off-diagonal elements; this is novel to this work and is reported for the first time here. To understand these results, they must be discussed in the context of polarisation transfer in magnetic resonance.

In this chapter the context of polarization transfer in magnetic resonance will be briefly introduced. Some simulations will be discussed as well as the experimental results. These simulations will be in comparison with the results of ^{13}C-BA to illustrate the difference between these two heteronuclear samples.

7.1 Cross relaxation and polarisation transfer

Consider an ensemble of coupled heteronuclear spin systems, each consisting of a spin I (½) coupled to a spin S (½). There are four energy eigenstates, and hence 12 different transition probabilities. There are eight single-quantum transitions, each with different probabilities, illustrated in Fig 7.1.
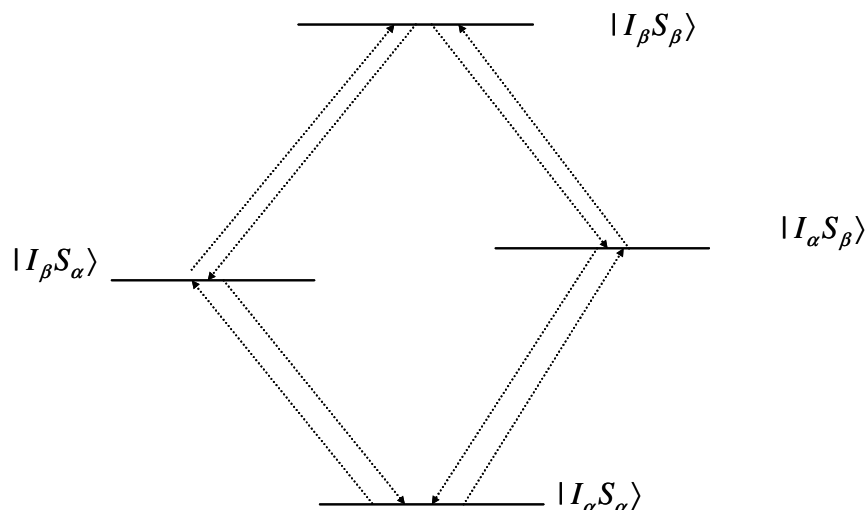
Fig 7.1 Eight single-quantum transition probabilities within a two-½ coupled heteronuclear spin system.

Taking the transition from $|I_\alpha S_\alpha\rangle$ to $|I_\beta S_\alpha\rangle$ for example, we can find only the spin state of spin I has changed. It means this transition is due to auto-relaxation and it contributes to the diagonal element in the relaxation matrix $\mathbb{R}$. While we can write down the expression for the diagonal elements of the relaxation matrix, its precise form is determined by homonuclear and heteronuclear dipolar constants C_{HH} and C_{HF}; these are not known a priori, so we do not know the precise form of the equation when fitting experimental data for our field-cycling experiments on the TFTA sample.

There are another four transition probabilities (double- and zero-quantum) illustrated in Fig 7.2 corresponding to the cross relaxation. It is evident that during each transition, both spins change the spin states. It means that application of a weak r.f. field at the Larmor frequency of one of the spins, for a sufficiently long time, has a strong effect on the longitudinal magnetisation of the non-irradiated spins, and in some cases, even enhances the magnetisation of those spins. This is called the *steady-*

state nuclear overhauser effect, or steady-state NOE.
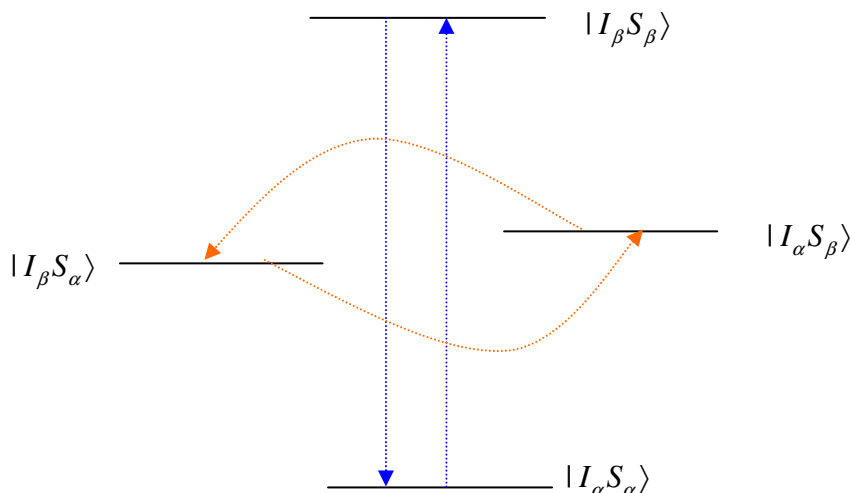
Fig 7.2 Four transition probabilities related to cross relaxation.

The polarisation transfer can only take place in a cross relaxation process where the spin states of both spins change at the same time. This phenomenon indicates the magnetisation transfer from one spin to the other spin, and it is called cross-polarization or polarization transfer.

With the advent of techniques in magnetic resonance for enhancing the spin polarisation of nuclei [73, 74, 75], there is increasing interest in measuring and understanding cross-polarisation and cross-relaxation processes connecting different spin-species in the same material. By facilitating the transfer of spin polarisation from highly polarized spin systems, such techniques have the potential to substantially increase the sensitivity of NMR and to facilitate the observation of NMR spectra and images from nuclei in low abundance.

Cross-polarisation processes are mediated by magnetic interactions which connect the two spin-species. In particular, the magnetic interactions must be rendered time dependent in order to provide an effective mechanism for transferring spin polarisation. The time-dependence can be introduced experimentally, for example by using the rotating-frames as with Hartmann-Hahn cross-polarisation, or as in our investigation, by utilizing inherent molecular motion in the material. Since spin

polarisation is proportional to inverse temperature, substantial gains can be made by operating at low temperature. However the spectral density characterizing the molecular motion must be strong enough to drive the relaxation processes in order that such gains can be realized. Since classical barrier hopping will invariably be too slow at low temperature, in practice it will be necessary to choose or design a molecular system in which quantum tunnelling dominates the motion; only then will the motion be sufficiently fast.

Our research is to measure the cross-relaxation between ^{1}H and ^{19}F nuclei in a carboxylic acid in the solid state with a new magnetic field-cycling NMR technique instead of studying how to enhance the cross-polarisation. The cross-relaxation process is driven by proton tunnelling in the hydrogen bonds of the material and the magnetic field dependence of cross-relaxation provides a direct measure of the proton tunnelling rate.

7.2 Experimental

Experiments have been conducted in the solid state at low temperature on tetrafluoroterephthalic acid (TFTA: $C_6F_4(COOH)_2$) where we assign spins I to be ^{1}H and spins S to be ^{19}F; Fig. 7.3. This di-carboxylic acid molecule forms infinite chains linked by pairs of bridging hydrogen bonds. Within each pair of hydrogen bonds there are two possible tautomeric configurations which can interchange by double proton transfer within the hydrogen bonds. In such infinite chains, experimental evidence to date is able to identify motion within a single pair of hydrogen bonds, however, coordinated motion along the chain involving many such hydrogen bond pairs has not yet been separately identified in experiments. Therefore, for the purposes of discussion we identify a dimer as a single pair of TFTA molecules. The concerted double proton transfer process leads to a modulation of both homonuclear ^{1}H-^{1}H dipolar interactions and heteronuclear ^{19}F-^{1}H dipolar interactions. Changes in both internuclear distances and in the angle made by the internuclear vector with respect to the applied B-field are responsible for this modulation. ^{1}H-^{1}H interactions are dominated by the intra-dimer internuclear vector connecting the two acid protons in

the bridging hydrogen bonds. Of more importance to this study are the numerous [19]F-^{1}H dipolar contacts, both intra- and inter-dimer, involving ^{19}F nuclei on the phenyl ring and the hydrogen bond protons.
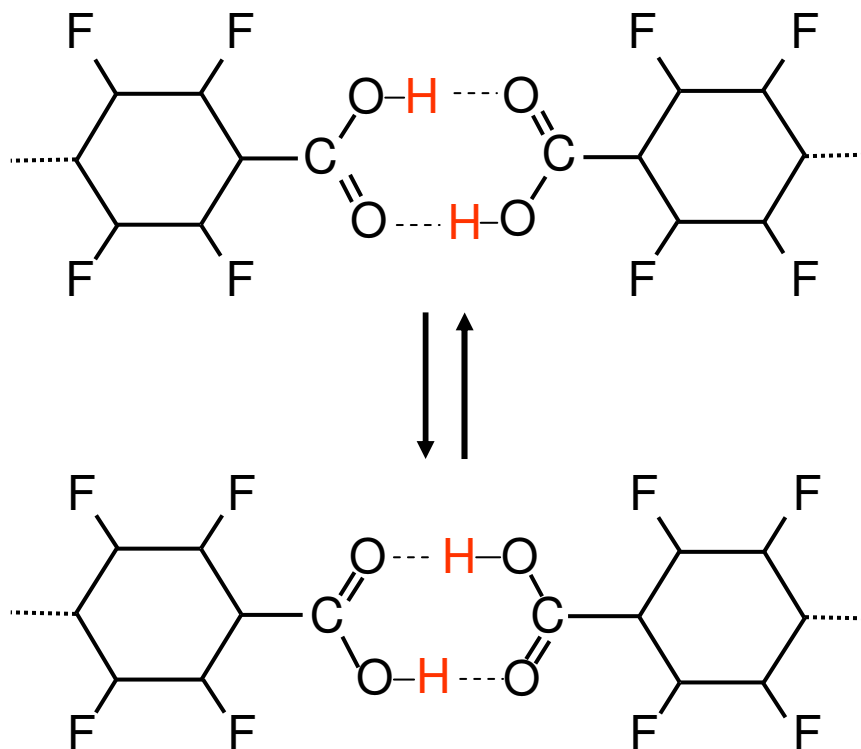
Fig 7.3 Concerted double proton transfer in the di-carboxylic acid, TFTA

Measurements were made using field-cycling NMR techniques. The temperature dependence of the spin-lattice relaxation time has been investigated at fixed field by former researchers in our group [43]. The state-of-art field-cycling spectrometer enabled us to investigate the field/frequency dependence of spin-lattice relaxation time and therefore to obtain the 2D profile (one is temperature, the other one is frequency) for analysing the dynamics of the sample and understanding the cross-relaxation process which is crucial in heteronuclear spin systems.

The frequency dependence of spin-lattice relaxation time experiments were conducted at a set of magnetic fields from 0.01T to 1T. Saturation-recovery pulse sequence was employed to record the data when the magnetic field was higher than 0.2T. When the magnetic field was below 0.2T, a polarisation-recovery pulse sequence was employed

to improve the signal and record the spin-lattice magnetisation recovery curve. The experiment at higher fields than 1T became difficult due to the very long relaxation time.

A new sequence called the heteronuclear cross-relaxation pulse sequence was designed to measure the off-diagonal element σ directly, as reviewed in Chapter 2. This kind of experiments was conducted at a set of fields from 0.02T to 1T, slightly different from the fields we mentioned above, since the signal to noise ratio was too poor to obtain reasonable data when the magnetic field was lower than 0.02T while the high field polarisation method cannot be applied in this pulse sequence.

7.3 Results and Discussion

7.3.1 Spectral density experiments

The spin-lattice relaxation behaviour was observed to be bi-exponential at all B-fields studied and temperatures below 50K; the ratio of the two rates, R_1/R_2 was typically 10 to 15 depending on field and temperature (in this thesis, R_1 is chosen bigger than R_2). R_1 and R_2 could be extracted from the magnetisation recovery curve by fitting the curve with a bi-exponential equation. Fig 7.4 shows a typical set of data recorded using the saturation-recovery sequence; Fig 7.5 shows some data recorded using the polarisation-recovery sequence. The initial conditions for the experiments to measure the relaxation rates were not as important as for the spin-lattice relaxation time measurements on ^{13}C-BA sample. This was because, changes in initial conditions affected only the weighting coefficients but not R_1 and R_2. In TFTA we can resolve R_1 and R_2 separately, but in ^{13}C-BA we could only determine a single time constant which was weighted average. Without the limitation of initial conditions, our experiments to measure the relaxation rates on TFTA sample could go to very low fields and we could employ both saturation-recovery pulse sequence and polarisation-recovery pulse sequence to record the field dependence of relaxation rates.

The equations for fitting the experimental data are

1. saturation-recovery pulse sequence,

$$\langle I_z \rangle = c_1 \left(1 - \exp\left(-R_1 t\right)\right) + c_2 \left(1 - \exp\left(-R_2 t\right)\right) + c \tag{7.1}$$

where $c_1 + c_2 = I_0$, I_0 is the spin-polarisation at thermal equilibrium, c is the magnetisation offset caused by the relaxation during the field switch time.

2. polarisation-recovery pulse sequence,

$$\langle I_z \rangle = I_0 + c_1 \exp\left(-R_1 t\right) + c_2 \exp\left(-R_2 t\right) \tag{7.2}$$

where $c_1 + c_2 = I_{pol} - I_0$, I_{pol} is the magnetisation built up at the polarisation field.
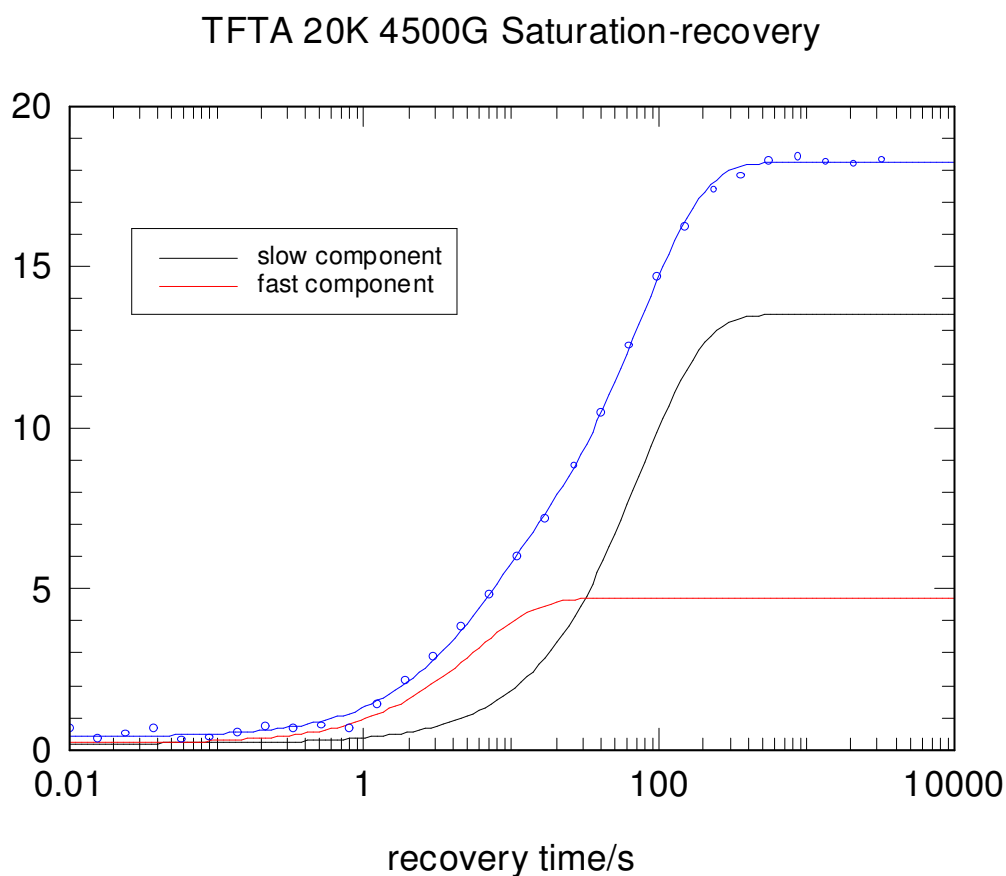
Fig 7.4 The magnetization recovery curve recorded at 4500Gauss, 20K with the saturation-recovery pulse sequence on sample TFTA. Blue solid curve is a fit with bi-exponential equation. Red curve and black curve are the two components characterized by R_1 and R_2 respectively. For the case in this figure, $R_1 = 0.179 s^{-1}$, $R_2 = 0.0133 s^{-1}$.

TFTA 20K 1200Gauss Pol

recovery time/s
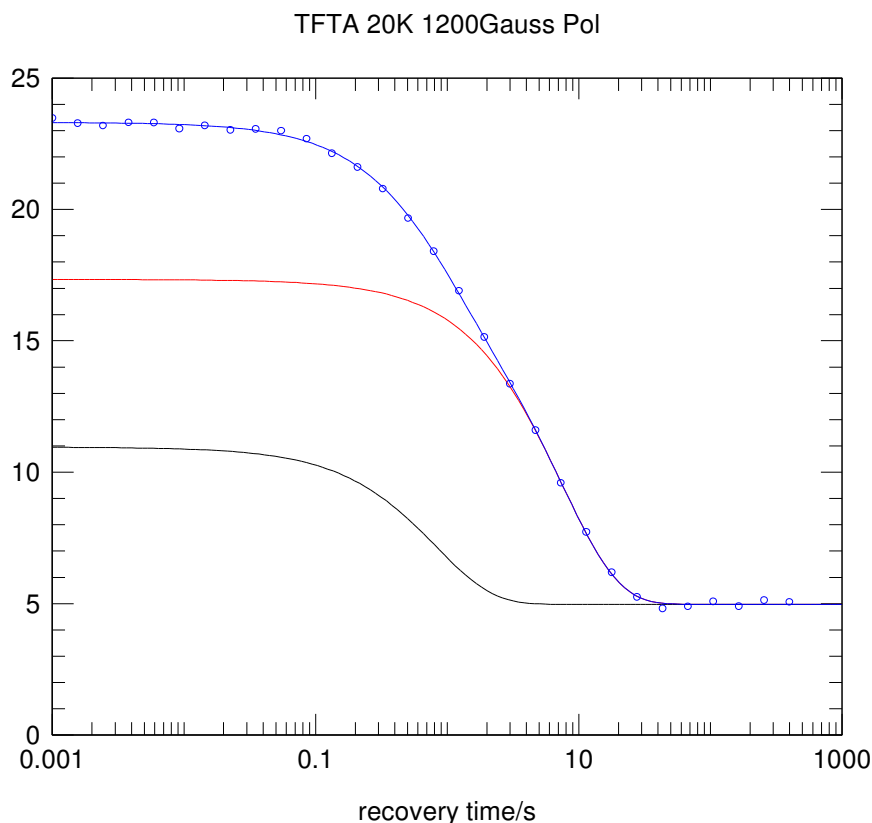
Fig 7.5 The magnetization recovery curve recorded at 1200G, 20K with polarization-recovery pulse sequence on sample TFTA. Blue solid curve is a fit with bi-exponential equation. Red curve and black curve are the two components characterized by R_1 and R_2 respectively. For this case, $R_1 = 1.216 s^{-1}$, $R_2 = 0.133 s^{-1}$.

It is evident that in both Fig 7.4 and Fig 7.5, the blue solid curves fitted with bi-exponential equation are in perfect agreement with the experimental data. All the magnetization recovery experimental data were fitted with bi-exponential equations (7.1) and (7.2) and two sets of relaxation rates extracted from experimental data, plotted in Fig 7.6 as a function of magnetic field. Data were collected using two preparation schemes, (a) the polarization of the second nucleus was prepared by polarizing for 10s at the ^{1}H NMR field; (b) the polarization of the second nucleus was prepared by polarizing for more than $3 \times T_1$ at the ^{1}H NMR field. The values of R_1 and R_2 were not affected by the preparation, as expected.

Since there are five variables in the fitting equations (7.1) and (7.2), the values of R_1 and R_2 could not be as accurate as that obtained for a single relaxation rate in a single

exponential fit for a homonuclear system. Nevertheless, a good account emerges in Fig 7.6 of the field dependence of the two relaxation rates. The error bars of R_1 and R_2 are also plotted. In the figure, the relative errors in R_1 are slightly bigger than the relative errors in R_2. This was because the weighting coefficient for R_1 was generally smaller. This is also confirmed by the heteronuclear cross relaxation experimental data which are also plotted in Fig 7.6, where the error between red squares and green filled circles is much bigger than the error between blue circles and black triangles. These relaxation rates were employed to calculate the off-diagonal element σ, as expressed in equation (3.13). We will discuss them later.

TFTA 20K Spectral Density

Legend:
- 20K R_1 (red open squares)
- 20K R_2 (blue open circles)
- cross-relaxation R_1 (green filled circles)
- cross-relaxation R_2 (black open triangles)

x-axis: Field/Tesla
y-axis: relaxation rates/s^{-1}
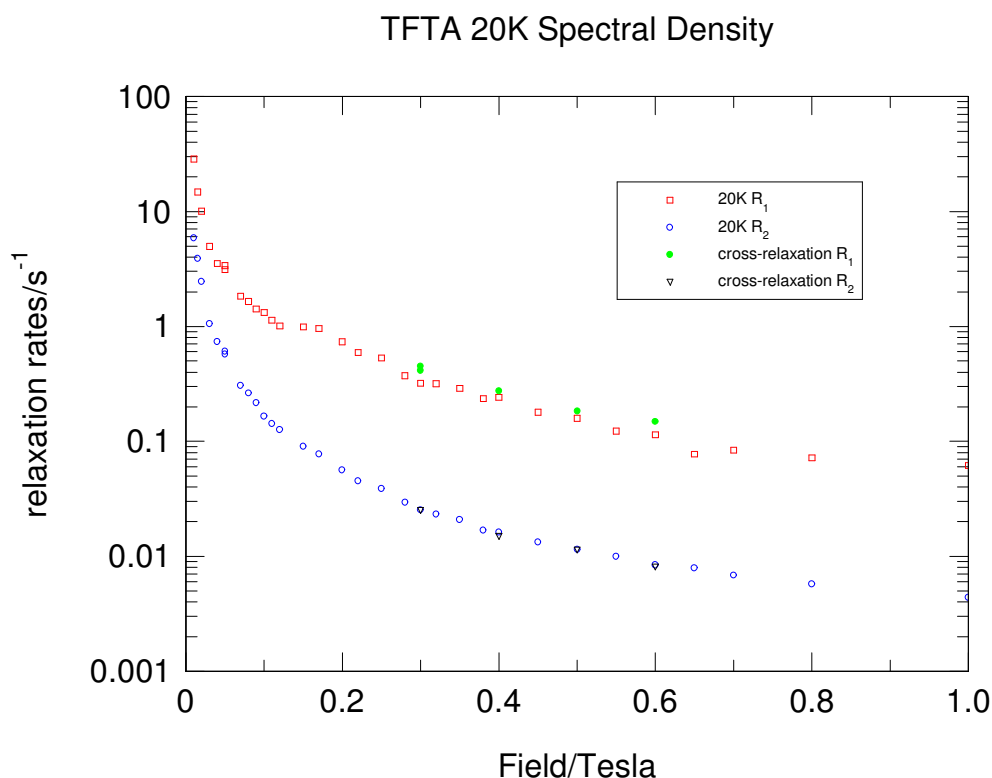
Fig 7.6 The field dependence curves of relaxation rates recorded at 20K on sample TFTA. The blue circles and red squares are the results extracted from the polarisation recovery curves. The black triangles and green filled circles are the results from cross-relaxation experimental data, will be discussed later. The data of blue circles and black triangles are in good agreement with each other, while there is a noticeable error between the data of red squares and green filled circles.

In comparison with the spectral density curve in a homonuclear system, for example, BA sample discussed in Chapter 4, the spectral density curves in Fig 7.6 are the field dependence of the relaxation rates R_1 and R_2 rather than T_1^{-1}. The expressions for R_1

and R_2, equation (2.55),

$$R_{1,2} = \frac{1}{2}\left[(\rho_I + \rho_s) \pm \sqrt{(\rho_I + \rho_s)^2 - 4(\rho_I \rho_s - \sigma_I \sigma_S)}\right] \qquad (7.3)$$

indicate that it is too complicated to extract the correlation rate directly from the spectral density curves illustrated in Fig 7.6 as we did in the spectral density curve of homonuclear system. R_1 and R_2 can be calculated, but the complexity means that fitting functions is not knowable a priori and an accurate value of the correlation rate cannot be extracted from these data alone.

An alternative approach was devised to extract the correlation rate from the off-diagonal elements instead of diagonal elements or the relaxation rates. This was not only because the off-diagonal elements had the simplest expression as expressed in equation (2.49), but also because the off-diagonal elements could be measured if the initial conditions were well controlled.

7.3.2 Cross relaxation experiments

For obtaining the value of the correlation rate, cross-relaxation experiments were designed to measure the off-diagonal element and therefore extract the correlation rate directly from the field dependence of off-diagonal element. The pulse sequence for cross-relaxation experiments has been discussed in Chapter 3. Here we summarize it before we discuss the experimental results.
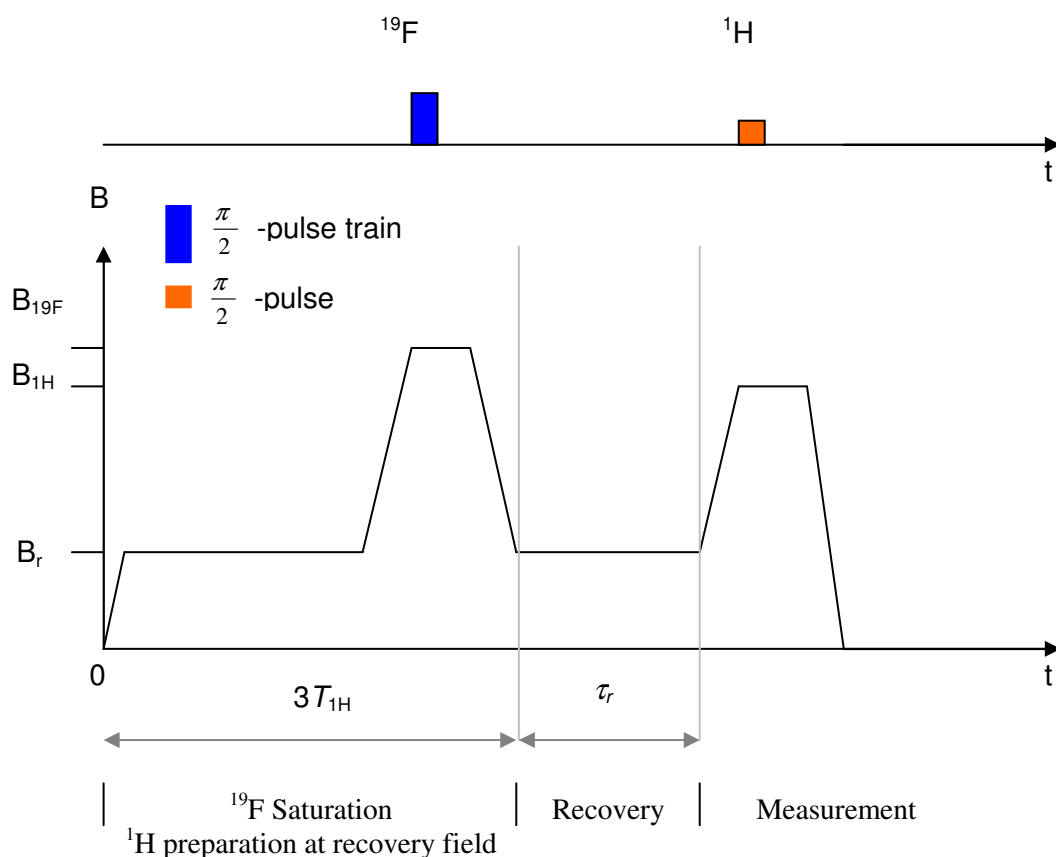
Fig 7.7 Cross-relaxation pulse sequence for measuring the off-diagonal element on sample TFTA.

1) Preparation of spin I at the recovery field of spin S for at least three times the spin I T_1 at this field to gain polarisation close to equilibrium.

2) Saturation of spin S magnetisation with a comb of resonant 90° pulses at spin S resonance field.

3) Rapid magnetic field switch to recovery field B_r, which was selected for relaxation.

4) Evolution of magnetisation in the field B_r for a period of time.

5) Rapid magnetic field switch back to spin I resonance field.

6) Measurement of spin I magnetisation with a 90° pulse.

The first step is to build up the equilibrium polarisation for spin I. The second step is to saturate the magnetisation of spin S. Hence the initial condition we created is that $I_z = I_0$ and $S_z = 0$ at $t = 0$. I_0 is the polarisation at thermal equilibrium of spin I at recovery field. That is why the preparation field illustrated in Fig 7.7 is chosen to be same as the recovery field. Given this condition, the measured magnetisation of spin I

after relaxing at the recovery field is

$$\langle I_z(t) \rangle = \frac{\sigma I_0}{R_2 - R_1} \frac{\gamma_S}{\gamma_I} \left(\exp(-R_1 t) - \exp(-R_2 t) \right) + I_0 \qquad (7.4)$$

The experimental data can be plotted as a cross-relaxation magnetisation recovery curve which can be fitted with this equation. The fitting results provide a direct measurement of the off-diagonal element σ.

In Fig 7.8 the polarization-recovery curve, $\langle I_z(\tau_r) \rangle$, for a cross-relaxation field-cycling NMR experiment is presented; the temperature was 20K and B_r=0.35T. In order that equation (7.4) applies, it was necessary for the initial polarization of spins I to match the thermal equilibrium polarization, I_0, at the field B_r. This condition was tailored experimentally by selecting appropriate values of τ_{pol} and B_{pol}. In Fig 7.8, following the saturation of spins S, the polarization $\langle I_z \rangle$ initially decreases with rate R_1 as polarization is transferred to spins S via the cross relaxation pathway; thereafter $\langle I_z \rangle$ recovers towards its thermal equilibrium value at the field B_r with rate R_2. Fitting equation (7.4) to the data enables the value of σ to be determined. In this case, the off-diagonal element is $\sigma = -0.1353 s^{-1}$ at 3500G, 20K.

It is illustrated in Fig 7.8 that the off-diagonal element can be calculated after the parameters are extracted from the polarization recovery curve. The two relaxation rates R_1 and R_2 are in excellent agreement with the values from traditional field-cycling experiments with saturation-recovery or polarization-recovery pulse sequence when the field is higher than 1500G, as illustrated by the comparison of free fit and fixed fit shown in Fig 7.8.

In low field, the quality of the experimental data is not good enough to independently extract an accurate value R_1, due to the fact that in low field the relaxation time R_1^{-1} (fast component) is comparable with the field switching time and therefore the relaxation during the field switch becomes a dominant systematic error factor. Furthermore in low field the low signal to noise ratio leads to significant random error as well.

TFTA 20K 3T1 3500Gauss
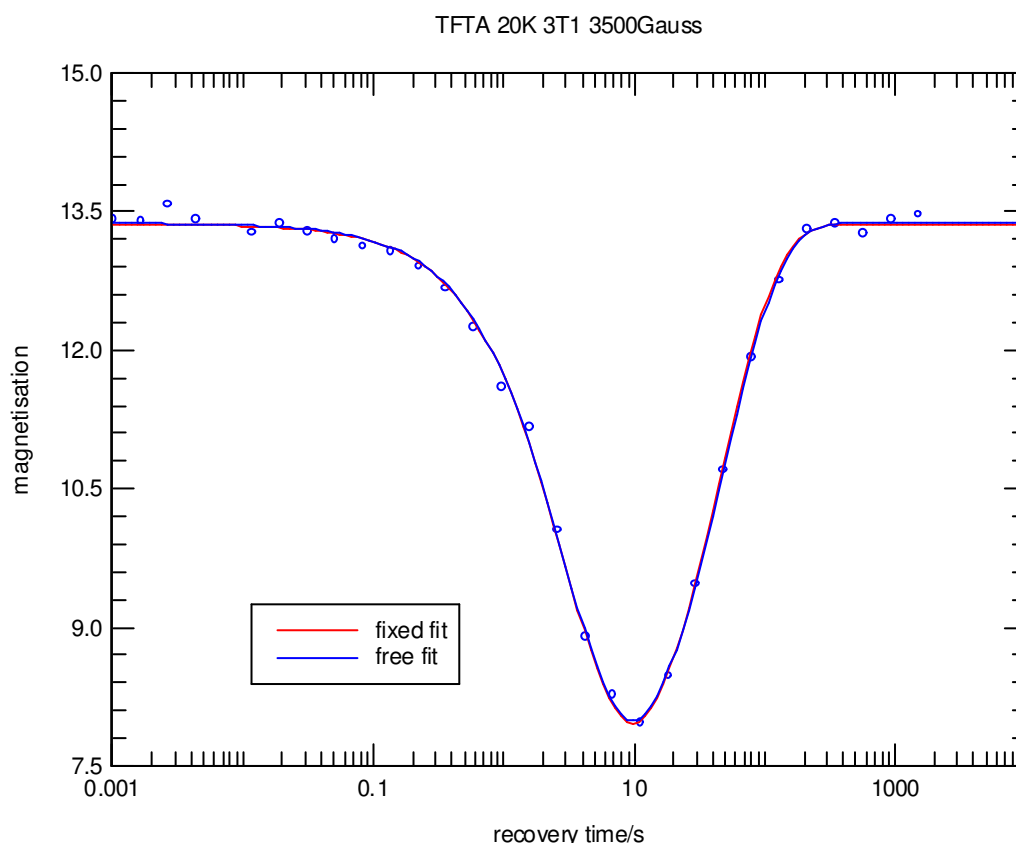
Fig 7.8 Polarisation recovery curve recorded at 3500G, 20K with cross-relaxation pulse sequence on sample TFTA. The relaxation rates derived from the free fit (R_1=0.2946s^{-1}, R_2=0.0198s^{-1}) are consistent with the relaxation rates from the traditional field-cycling experiments (R_1=0.2895s^{-1}, R_2=0.0207s^{-1}) shown in the spectral density curves in Fig 7.6.

The random error could be minimized by doing many averages. It was time-consuming, but the average result was satisfactory, as shown in Fig 7.9 for the recovery field at 500Gauss.

The systematic error caused by the field switching time is not directly illustrated in the cross-relaxation recovery curve. It can be found by carefully analyzing the experimental data. Taking the cross-relaxation experiment at 500G, 20K for example, the average experimental result illustrated in Fig 7.9, we find the relaxation time R_1^{-1} extracted from the cross-relaxation recovery curve is about 0.14s shorter than the value from the traditional field-cycling experiments shown in Fig 7.6. This value 0.14s is close to the field switch time (0.17s switch to ^{19}F resonance field 8950G/36.35MHz at 5T/s, 0.11s switch to recovery field at 8T/s). It is evident that the

polarization relaxation during the field switching time has a strong impact on the shape of the cross-relaxation recovery curve and therefore on the determination of relaxation time R_1^{-1}. The data on left half of the cross-relaxation recovery curve, not shown in Fig 7.9, have large systematic error, are not reliable and have to be abandoned. The data on right half of the cross-relaxation recovery curves do not suffer from this problem and were fitted to equation (7.4) with fixed R_1 and R_2 (from the spectral density curve and our simulation). It was only for the lowest three field values, $B_r \leq 500 Gauss$, that it was necessary to choose the relaxation rates from the spectral density curves we measured and to constrain the values of R_1 and R_2 in the fits.

As σ is proportional to $(R_1 - R_2)$ (the difference of these two relaxation rates), it is the absolute errors in R_1 and R_2 instead of relative errors that determine the error in σ. Therefore the error in R_1 becomes the most important factor in determining the accuracy of the cross-relaxation experiments.

If the errors are taken into account only mathematically, the relative error of σ will be well determined by the relative errors of the relaxation rates which are 2-5% when field is higher than 0.15T and 5-8% when field is lower than 0.15T. However this is not entirely correct, because the R_1 and R_2 are employed to fit the cross relaxation experimental data; the uncertainty of R_1 will cause an increased uncertainty of σ, especially in low field where the signal quality is very poor and the relaxation is faster than the field switch.

TFTA 20K 500G Ave
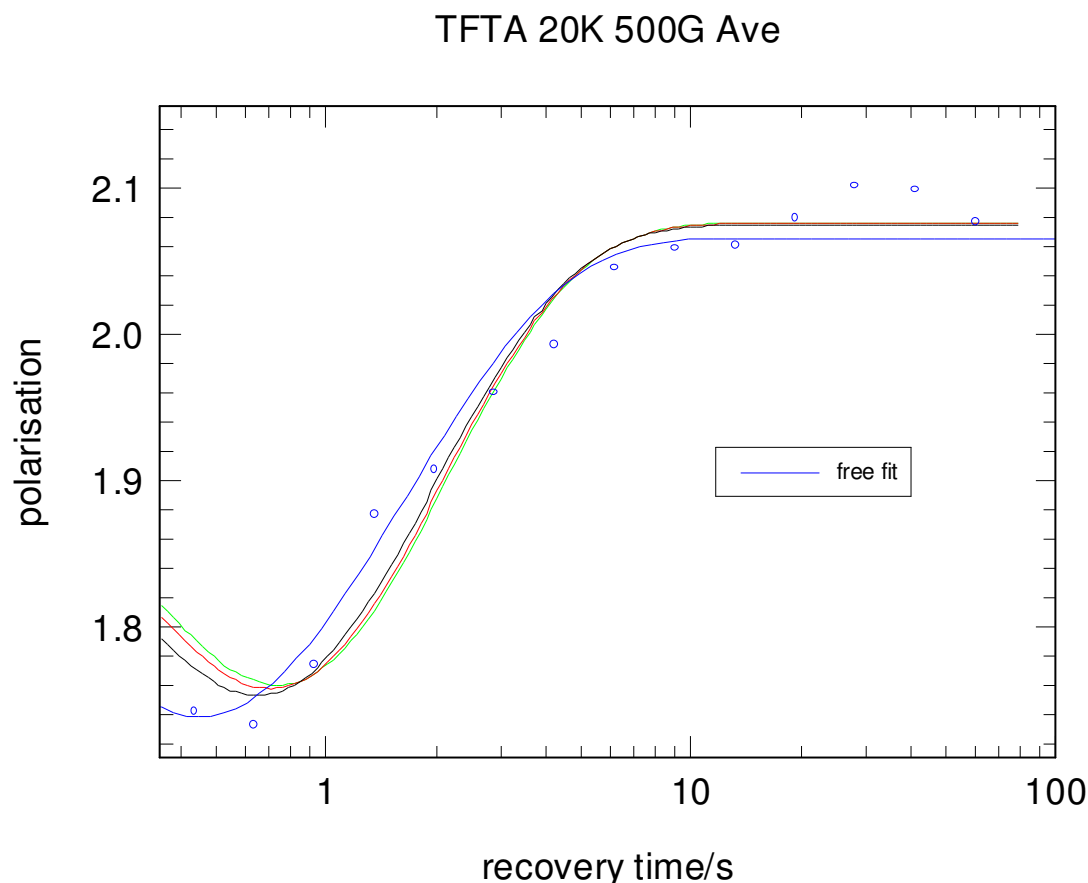
Fig 7.9 Average of cross relaxation recovery curves recorded at 20K, 500G. Blue solid line was free fit all the data points to equation (7.4). The other three solid lines (black, red and green) were fixed fit to the right half data points to equation (7.4) with different sets of relaxation rates R_1, R_2. These fixed fit led to the extraction of off-diagonal element σ. There is a significant difference between the results of free fit and fixed fits.

At the temperature T=20K, the cross-relaxation experiment was repeated for different values B_r permitting the magnetic field dependence of σ to be mapped out, as presented in Fig 7.10 and Fig 7.11. For fields $B \geq 800G$, a free fit was made to the polarization curves to extract R_1, R_2 and σ: the values of the relaxation rates agreed within experimental error with those determined in a separate series of measurements using a conventional single-nucleus pulse sequence. In this field regime the uncertainties were of order 2-5% and dominated by random scatter. For fields $B \leq 500G$ the relaxation rates were increasing and the NMR signal, proportional to field, was becoming very small; both trends made the measurements more challenging. To minimize uncertainties for the lowest three field values, the fits to the polarization-recovery data were constrained with values of R_1 and R_2 determined in separate

measurements using conventional single-nucleus pulse sequences. As illustrated in Fig 7.9, three sets of R_1 and R_2 were chosen to fit the curve, the difference among the three extracted off-diagonal elements was dominated by the R_1 value, but it was much smaller than the difference between the extracted off-diagonal elements of free fit and fixed fits. In this field regime, $B \leq 500G$, the errors in σ were dominated by systematic uncertainties in R_1 leading to the larger error bars are illustrated in Fig 7.10, Fig 7.11.
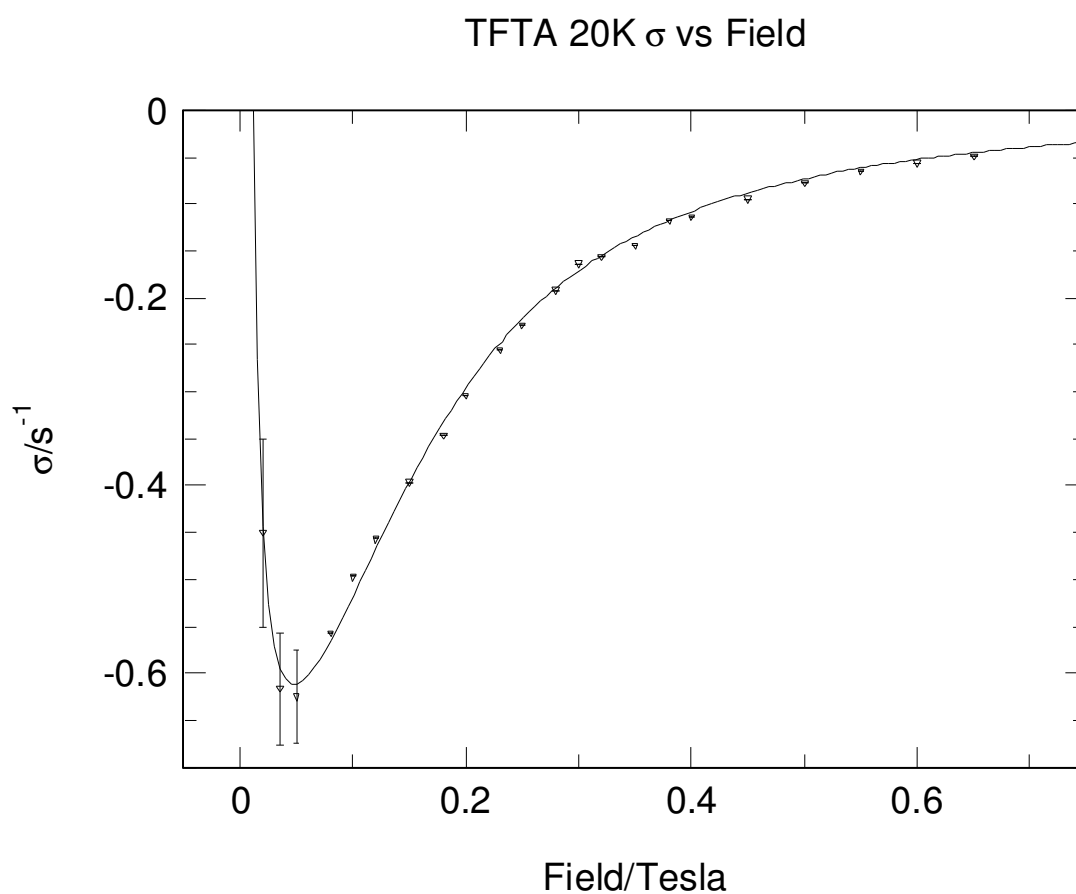
TFTA 20K σ vs Field

Fig 7.10 The field dependence of the cross-relaxation time constant, σ, recorded at $T = 20K$. The minimum is around 500G.

TFTA 20K σ vs Field
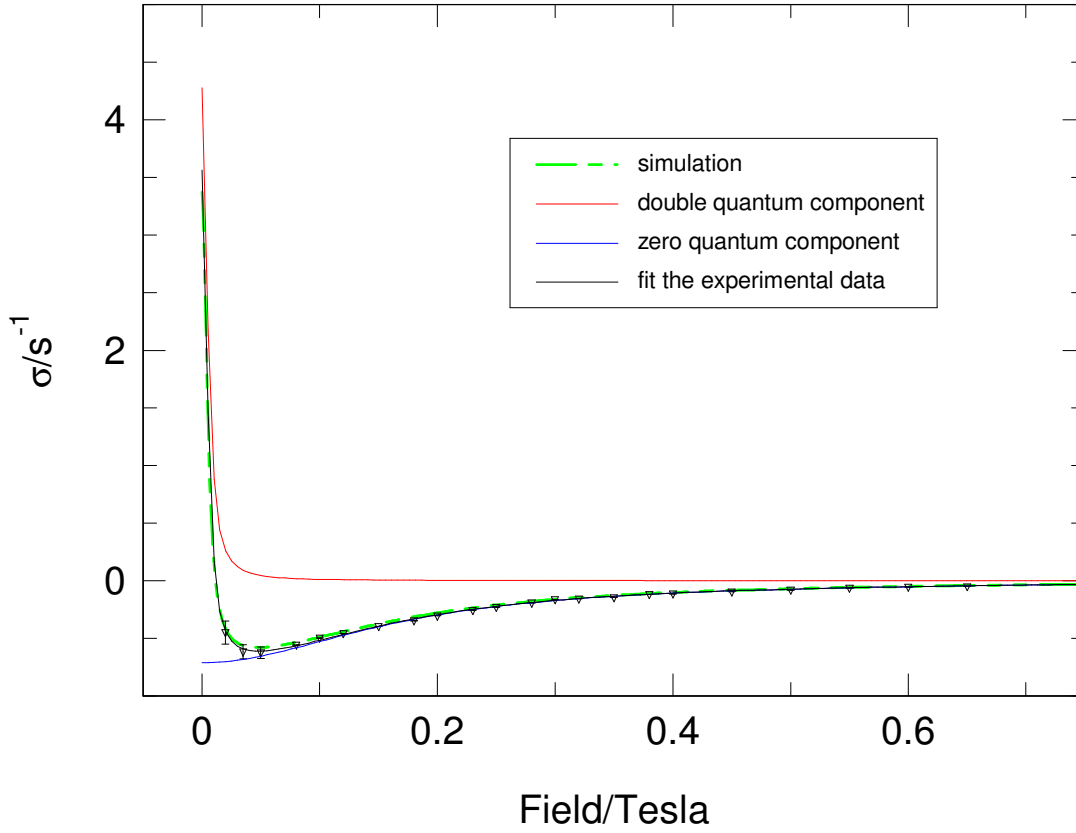
Fig 7.11 the field dependence of the cross-relaxation time constant, σ, recorded at $T = 20\text{K}$. The black triangles are experimental data; the black solid line is the fit with equation (2.49) from which the correlation rate for proton transfer, $\tau_c^{-1} = (2.66 \pm 0.08) \times 10^6 \, s^{-1}$, is determined; the blue solid line and the red solid line are the spectral density components, $L(\omega_I - \omega_s, \tau_c)$ and $L(\omega_I + \omega_s, \tau_c)$, respectively. The blue line and the red line have opposite signs and significantly different widths when plotted as a function of field, as discussed in Fig 6.2b, Chapter 6. The minimum of σ is around 500G. The green dashed line is the simulation result.

In this particular system, for the range of *B*-field studied, Fig 7.11 reveals that σ is a negative quantity. According to equation (2.49),

$$\sigma_I^{IS} = C_{IS} \frac{4a}{(1+a)^2} \left(-L(\omega_I - \omega_s, \tau_C) + 6L(\omega_I + \omega_s, \tau_C) \right) \tag{7.5}$$

we can conclude that the spectral density component $L(\omega_I - \omega_s, \tau_c)$ arising from zero-quantum transitions and characterized by the difference Larmor frequency, dominates the cross-relaxation process. Equation (7.5) was fitted to the σ data in Fig 7.11, resulting in the solid black line. For ^{1}H and ^{19}F, ω_I and ω_s differ by only 5.9%,

consequently in a plot versus B-field, since Larmor frequency is proportional to B, the Lorentzians $L(\omega_I - \omega_S, \tau_c)$ and $L(\omega_I + \omega_S, \tau_c)$ have very different widths. As the fit shows, in the field range studied for this heteronuclear system, the data is indeed dominated by the Lorentzian arising from the difference in Larmor frequencies. The Lorentzian $L(\omega_I + \omega_S, \tau_c)$ would only become observable at very low B-field, beyond the range of the current experiment; but we still can find the turning point is around 500G. When the field is lower than 500G, the Lorentzian $L(\omega_I + \omega_S, \tau_c)$ starts to play its important role in the cross relaxation. From the fit we determine the inverse correlation time for concerted double proton transfer in the hydrogen bonds of TFTA at 20K to be $\tau_c^{-1} = (2.66 \pm 0.08) \times 10^6 s^{-1}$. Unlike many conventional studies of molecular dynamics by spin-lattice relaxation, this measurement has been determined wholly from an investigation of the cross-relaxation process. At the temperature recorded, the proton transfer dynamics are dominated by incoherent tunneling in the ground state of the double minimum potential. It is noteworthy that the proton transfer rate is nearly fifty times slower than similar processes in the model compound, benzoic acid. That this much slower motion is accessible to the B-field range studied in these cross-relaxation field-cycling NMR experiments is due to the fact that the spectral density is sampled at the difference Larmor frequency which for ^{1}H-^{19}F is relatively small.

From the expression of the off-diagonal element σ, the minimum position can be found mathematically, in equation (7.5) $\omega_I = \gamma_I B$, $\omega_S = \gamma_S B$.

At the turning point

$$\frac{\partial \sigma}{\partial B} = 0 \tag{7.6}$$

then we get the equation for B^2,

$$c_1 c_2 (c_2 - 6c_1) B^4 - 10 c_1 c_2 B^2 - (6c_2 - c_1) = 0 \tag{7.7}$$

where $c_1 = (\gamma_I - \gamma_S)^2 \tau_c^2$, $c_2 = (\gamma_I + \gamma_S)^2 \tau_c^2$

the solution is

$$B^2 = \frac{5 c_1 c_2 \pm \sqrt{6 c_1 c_2} (c_2 - c_1)}{c_1 c_2 (c_2 - 6c_1)} \tag{7.8}$$

1) if $c_2 - 6c_1 > 0$, and due to $6c_2 - c_1 > 0$, then the equation (7.7) has two solutions,

one is positive, the other one is negative. So $B^2 = \dfrac{5c_1c_2 + \sqrt{6c_1c_2}\,(c_2 - c_1)}{c_1c_2\,(c_2 - 6c_1)}$

2) if $c_2 - 6c_1 < 0$, but $6c_2 - c_1 > 0$, then the equation (7.7) becomes $ax^2 + bx + c = 0$,

where $a, b, c > 0$. This kind of equation has two negative solutions. No solution

for this kind of nucleus.

So the condition $c_2 - 6c_1 > 0$ is the premise enabling us to find the turning point in the

σ curve, which means $\gamma_S > \dfrac{7 - 2\sqrt{6}}{5}\gamma_I = 0.4202\gamma_I$. If spin I is proton, γ_S must be

bigger than $1.1242 \times 10^8 \ T^{-1}s^{-1}$. It is really not easy to find this kind of spin $\dfrac{1}{2}$ nucleus.

^{19}F nucleus is one of the nuclei which can satisfy the condition, if we substitute the

correlation time τ_c from the experimental data at 20K into equation (7.8),

$\tau_c = 3.76 \times 10^{-7} s$, $\gamma_H = 2.67522 \times 10^8 T^{-1}s^{-1}$ and $\gamma_{19F} = 2.518147 \times 10^8 T^{-1}s^{-1}$, the

turning point will appear at the field:

$$B = 0.0476T = 476 Gauss \tag{7.9}$$

This theoretical result is in good agreement with our experimental result illustrated in

Fig 7.10, where the minimum is around 500Gauss. This is a good confirmation of our

new method of directly measuring the off-diagonal element by the cross-relaxation

field-cycling technique.

Further simulation of the experimental data reveals more characteristics of this

particular sample. We employ the parameters listed below to obtain the best fit of

spectral density curves R_1 & R_2 and the field dependence curve of σ.

$$\begin{cases} C_{HH} = 9.5 \times 10^8 \, s^{-2} \\ C_{HF} = 2.8 \times 10^7 \, s^{-2} \\ A/k_B = 82K \\ \tau_c^{-1} = 2.575 \times 10^6 \coth\left(\dfrac{A}{2T}\right) + 1.18 \times 10^{11} \exp\left(-\dfrac{820}{T}\right) \end{cases} \tag{7.10}$$

The simulation fits are illustrated in Fig 7.11 with green dashed line and Fig 7.12 with solid line. These fits are in good agreement with the experimental data. The off-diagonal element is only related to the dipolar constant C_{HF}, therefore the curve in Fig 7.11 can be used to obtain an accurate value of C_{HF}. Fitting the curve in Fig 7.11 to equation (7.5) leads to the determination of the amplitude $C_{HF} \operatorname{sech}^2\left(\dfrac{A}{2k_B T}\right)$, which is $1.72 \times 10^6 \, s^{-2}$ at 20K; the energy asymmetry has been determined to be $A/k_B = (82 \pm 5)\,\mathrm{K}$ [43]; therefore the dipolar constant measured by cross-relaxation experiments is $C_{HF} = (2.69 \pm 0.15) \times 10^7 \, s^{-2}$, which is in good agreement with the value employed in our simulation as shown in (7.10). It is also in relatively good agreement with the result, $C_{HF} = (1.8 \pm 0.6) \times 10^7 \, s^{-2}$, determined before field-cycling data was available [43].

The two relaxation rates have the contribution of C_{HH}, which is from ρ_{HH} or ρ_{II}. However in our fit, when we change the value of C_{HH}, the fast component, R_1, only has a slight change in comparison with the slow component, R_2. Mathematical analysis will be complicated. Here we just give a qualitative explanation: R_1 is about 10-15 times bigger as R_2; the change of C_{HH} only has a small relative change in R_1 while it has a significant relative change in R_2.
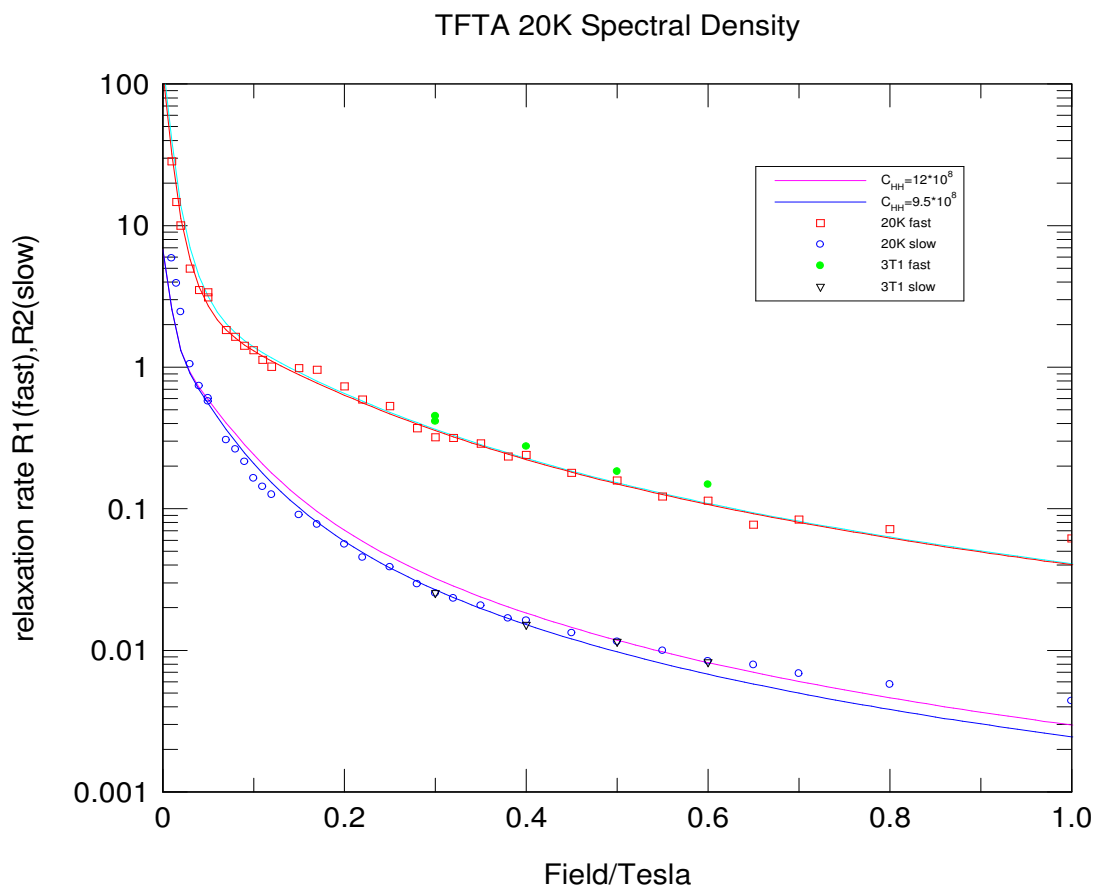
Fig 7.12 Simulation fit (solid line) of relaxation rates. The change of C_{HH} has a more significant effect on R_2 than on R_1.

The simulation illustrated in Fig 7.11 also confirms our theoretical analysis of the minimum position on the field dependence curve of σ and the experimental results.

Given the parameters in (7.10), the field dependence of the ratio of $\sigma^2 / \rho_I \rho_s$ can be mapped out as illustrated in Fig 7.13.
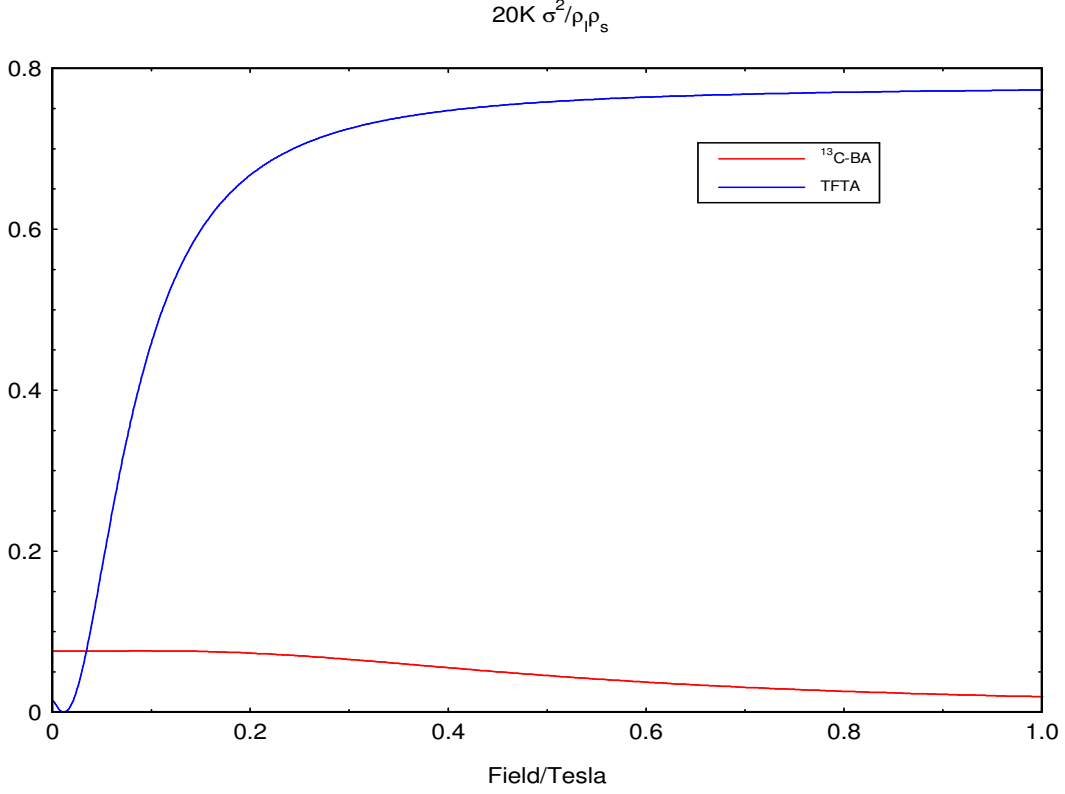
Fig 7.13 Field dependence of the ratio $\sigma^2 / \rho_I \rho_s$ on sample TFTA and ^{13}C-BA at 20K.

The ratio $\sigma^2 / \rho_I \rho_s$ in TFTA is about 0.75 when the field is higher than 0.3T, while the ratio $\sigma^2 / \rho_I \rho_s$ in ^{13}C-BA is smaller than 0.08 (0.02 at high field). The huge difference between the ratios on these two samples leads to the significant difference between the relaxation behaviours of these two samples. It will be easily understood if these ratios are substituted into the expression of relaxation rates,

$$R_{1,2} = \frac{1}{2}\left[(\rho_I + \rho_s) \pm \sqrt{(\rho_I + \rho_s)^2 - 4(\rho_I \rho_s - \sigma^2)} \right] \tag{7.11}$$

for sample ^{13}C-BA, $R_1 \approx \rho_I$, $R_2 \approx \rho_s$, as illustrated in Fig 6.5a and Fig 6.5c, at 20K; for sample TFTA, the R_1 and R_2 can not be calculated directly, but since σ^2 is close to $\rho_I \rho_s$, it is easily deduced that R_1 is much bigger than R_2, as presented in our experimental data where R_1 is about 10-15 times bigger than R_2. Therefore in ^{13}C-BA, the polarisation recovery curve is characterised by single relaxation time constant, which is recorded as T_1^{eff}, while in TFTA, the magnetisation recovery curve must be analysed by two relaxation time constants, the weighted average of these two

relaxation time constants has no physical meaning. Furthermore, the correlation time τ_c can be derived directly from the field dependence of T_1^{eff} on sample ^{13}C-BA, but it cannot be extracted from the field dependence of R_1 or R_2 in TFTA.

So the technique we employed to investigate the dynamics of sample TFTA is a technique which can be applied in the study of general heteronuclear interaction. The study of ^{13}C-BA is only a special case, but it does improve our understanding of the heteronuclear interaction.

Back to Fig 7.13, an interesting feature is illustrated when the field is lower than 0.1T: the ratio $\sigma^2/\rho_I\rho_s$ is getting smaller when field is getting lower; it goes to 0 at about 0.01T; then it increases again. The minimum to 0 implicates that the off-diagonal element is changing in sign around 0.01T, which is also illustrated in Fig 7.11. At the minimum position, the zero-quantum transition is in balance with the double-quantum transition. When field is higher than 0.01T, the zero-quantum transition dominates the cross-relaxation, but when field is lower than 0.01T, the double-quantum transition starts to dominate the cross-relaxation, and it increases rapidly when field is getting smaller.

This is quite interesting, not only in mathematical terms. In order to understand this, the mechanism of double-quantum transition needs to be investigated. Simply speaking, the double-quantum transition is due to the dipolar local magnetic field rotation which is modulated by the molecular rotation. When the field is high, the fluctuation of the local magnetic field is not enough to introduce a lot of double-quantum transitions, therefore in the spectral density the double-quantum transition term $L(\omega_I + \omega_s)$ is very small and is negligible in comparison with zero-quantum transition term $L(\omega_I - \omega_s)$. However when field is very low, comparable with the local fluctuating magnetic field, not only is the fluctuation of local magnetic field dominant, but also the coupling between the applied field (or the Larmor spin precession) and local magnetic field is strong, hence the double-quantum transition becomes dominant in the cross-relaxation processes.

7.4 Conclusions

The field-cycling NMR techniques described in this chapter provide an experimental procedure for directly studying cross-relaxation processes in magnetic resonance. As a wider range of polarization transfer experiments are developed to improve the sensitivity of NMR and MRI, the methodology described in this chapter, including importantly the study of the magnetic field dependence, may be applied to provide insight into the mechanisms responsible for mediating the coupling between the two spin systems. It is note-worthy that quantum tunneling plays a vital role in the cross-relaxation process in this case since in its absence, if the dynamics had been dominated by classical barrier hopping, the coupling between the two spin-reservoirs would have been vanishingly small at these temperatures. Furthermore, we have shown how the techniques have the potential to be applied in new ways to study molecular dynamics in systems where heteronuclear spins are coupled, as with the direct measurement of spectral density components that characterize the off-diagonal element of the relaxation matrix; in this case the study enabled the measurement of proton tunnelling in the hydrogen bonds of TFTA.

Chapter 8 Conclusions

Field-cycling NMR (FCNMR) relaxometry has been successfully employed to investigate the nuclear spin relaxation and proton tunnelling both in homonuclear and heteronuclear systems.

Using a model system that displays quantum tunnelling, the proton transfer is shown to be characterised by a single correlation time at all temperatures by directly measuring the field dependence of the spin-lattice relaxation rate. A smooth quantum-to-classical transition is therefore obtained. The consistency between quantum and classical descriptions is of fundamental importance in investigating the proton transfer in hydrogen bonding which is the basic process in chemical and biological reactions.

For homonuclear systems, there is just one spin-lattice relaxation time, but for heteronuclear systems, there are four elements of a relaxation matrix. By designing new pulse sequences, we have been able to measure the field-dependence of the off-diagonal element and cross relaxation process.

First ^{13}C FCNMR has given us a good start in investigating the heteronuclear interaction, although it turned out to be a special case since the off-diagonal element is small and the two relaxation rates cannot be resolved accurately from the recovery curve which has to be fitted to a single exponential function and characterised by an effective relaxation time. It enables us to have insight on the importance of the initial condition for the second nucleus and on the method of data analysis. Different spectral density components that appear in relaxation theory have been resolved and the correlation rate has been accurately measured from the field dependence of the inverse effective relaxation time recorded by ^{13}C FCNMR. It is ^{13}C FCNMR that illuminates a possible approach to obtain the correlation rate both from diagonal and off-diagonal elements by setting up an appropriate initial condition.

This possible approach has been achieved in TFTA which is chosen to be a general sample with significant off-diagonal elements and typical bi-exponential relaxation behaviour. A new FCNMR pulse sequence was designed for investigating the cross

relaxation by evolving the second spin polarisation to thermal equilibrium before saturating the first spin polarisation. The off-diagonal element is measured from the cross-relaxation recovery curve as a function of field. Therefore the field dependence of the off-diagonal element has been obtained with high accuracy. This is the first case to extract the correlation rate from the field dependence of the off-diagonal element. This method can be utilised in any heteronuclear system with typical bi-exponential recovery curve which means the two relaxation rates can be accurately resolved.

Quadrupolar dips in the proton magnetisation curve in heroin hydrochloride have been found as evidence for an enhanced proton relaxation process introduced by the quadrupolar interaction. It turns out that FCNMR can become a sensitive method for searching the quadrupolar transition frequencies and has potential applications in drug detection.

Chapter 9 Bibliography

[1]. Oppenländer, C. Rambaud, H.P. Trommsdorff and J.-C. Vial, <u>Phys. Rev. Lett.</u> **63**(1989):1432.

[2]. A. Heuer and U. Haeberlen, <u>J. Chem. Phys.</u> **95**(1991):4201.

[3]. O. Klein, F. Aguilar-Parrilla, J.M. Lopez, N. Jagerovic, J. Elguero and H.H. Limbach, <u>J. Am. Chem. Soc.</u> **126**(2004):11718.

[4]. A. Stöckli, B.H. Meier, R. Kreis, R. Meyer and R.R. Ernst, <u>J. Chem. Phys.</u> **93**(1990):1502.

[5]. J. L. Skinner and H.P. Trommsdorff, <u>J. Chem. Phys.</u> **89**(1988):897.

[6]. G. Robinson, <u>J. Phys. Chem.</u> **90**(1986) :4224.

[7]. V.A. Benderskii, D.E. Makarov and A.A. Wight. Wiley Intersci, N.Y. 1994.

[8]. A. Kohen, R. Cannio, S. Bartolucci and J.P. Klinman, <u>Nature</u> **399**(1999):496.

[9]. N. S. Scrutton, J. Basran and M.J. Sutcliffe, <u>Eur. J. Biochem.</u> **264**(1999):666

[10]. R. Meyer and R.R. Ernst, <u>J. Chem. Phys.</u> **93**(1990):5529.

[11]. D.F. Brougham, A.J. Horsewill and R.I. Jenkinson, <u>Chem. Phys. Lett.</u> **272**(1997):69.

[12]. A.J. Horsewill, C.J. McGloin, H.P. Trommsdorff and M.R. Johnson, <u>Chem. Phys.</u> **291**(2003):41.

[13]. Q. Xue, A.J. Horsewill, M.R. Johnson and H.P. Trommsdorff, <u>J. Chem. Phys.</u> **120**(2004):11107.

[14]. M. Plazanet, N. Fukushima, M.R. Johnson, A.J. Horsewill and H.P. Trommsdorff, <u>J. Chem. Phys.</u> **115**(2001):3241.

[15]. U. Langer, L. Latanowicz, C. Hoelger, G. Buntkowsky, H.M. Vieth and H.H. Limbach, <u>Phys. Chem. Chem. Phys.</u> **3**(2001):1446.

[16]. R.I. Jenkinson, A. Ikram, A.J. Horsewill and H.P. Trommsdorff, <u>Chem. Phys.</u> **294**(2003):95.

[17]. F. Noack, <u>Prog. Nucl. Magn. Reson Spectrosc.</u> **18**(1986):171.

[18]. K.H. Schweikert and F. Noack, <u>Mol. Crys. Liq. Crys.</u> **212**(1992):33.

[19]. F. Noack, M. Notter and W. Weiss, <u>Liquid Crystals.</u> **3**(1988):907.

[20]. R. Kimmich, <u>Bull. Magn. Reson.</u> **1**(1980):195.

[21]. R. Kimmich and E. Anoardo, <u>Prog. Nucl. Magn. Reson. Spectrosc.</u> **44**(2004):257.

[22]. A.J. Horsewill, <u>Prog. Nucl. Magn. Reson. Spectrosc.</u> **35**(1999):359.

[23]. L. Latanowicz and E. Reynhardt, <u>Chem. Phys. Lett.</u> **341**(2001):561.

[24]. A. Abragam. The Principles of Nuclear Magnetism, Clarendon Press, Oxford, 1961.

[25]. M.H. Levitt. Spin dynamics, John Wiley & Sons, Ltd., 2000.

[26]. J.W. Hennel and J. Klinowski. Fundamentals of Nuclear Magnetic Resonance, Longman Scientific & Technical, 1993.

[27]. C.P. Slichter. Principles of Magnetic Resonance, Third Edition, Springer-Verlag, 1990.

[28]. E. Fukushima and S.B.W. Roeder. Experimental Pulse NMR. A Nuts and Bolts Approach, Addision-Wesley, Reading, Massachusetts, 1981.

[29]. F. Bloch, <u>Phys. Rev.</u> **70**(1946):460.

[30]. R.M. Green and A.J. Horsewill, <u>Mol. Phys.</u> **57**(1986):887.

[31]. A.J. Horsewill, R.M. Green and A.M. Alsanoosi, <u>Springer Proc. Phys.</u> **17**(1987):28.

[32]. K.J. Abed, S. Clough, A.J. Horsewill and M.A. Mohammed, <u>Chem. Phys. Lett.</u> **147**(1988):624.

[33]. S. Clough, A. Heidemann, A.J. Horsewill, J.D. Lewis and M.N.J. Paley, <u>J. Phys. C</u> **14**(1981):L525.

[34]. S. Clough, A. Heidemann, A.J. Horsewill, J.D. Lewis and M.N.J. Paley, <u>J. Phys. C</u> **15**(1982):2495.

[35]. A.J. Horsewill, R.M. Green and A.M. Alsanoosi, <u>Chem. Phys.</u> **138**(1989):179.

[36]. M.A. Neumann, S. Craciun, A. Corval, M.R. Johnson, A.J. Horsewill, V.A. Benderskii and H.P. Trommsdorff, <u>Ber. Bunsenges. Phys. Chem.</u> **102**(1998):325.

[37]. A.J. Horsewill, D.F. Brougham, R.I. Jenkinson, C.J. McGloin, H.P. Trommsdorff and M.R. Johnson, <u>Ber. Bunsenges. Phys. Chem.</u> **102**(1998):317.

[38]. R.M. Hochstrasser and H.P. Trommsdorff, <u>Chem. Phys.</u> **115**(1987):1.

[39]. A.J. Horsewill, P.J. McDonald and D. Vijayaraghavan, <u>J. Chem. Phys.</u> **100**(1994):1889.

[40]. A.J. Horsewill, N.H. Jones and R. Caciuffo, <u>Science</u> **291**(2001):100.

[41]. D.F. Brougham, R. Caciuffo and A.J. Horsewill, <u>Nature</u> **397**(1999):241.

[42]. A.J. Horsewill and A. Ikram, Physica B **226**(1996):202.

[43]. A.J. Horsewill, A. Ikram and I.B.I. Tomsah, Mol. Phys. **84**(1995):1257.

[44]. M. Neumann, D.F. Brougham, C.J. McGloin, M.R. Johnson, A.J. Horsewill and H.P. Trommsdorff, J. Chem. Phys. **109**(1998):7300.

[45]. D.F. Brougham, A.J. Horsewill, A. Ikram, R.M. Ibberson, P.J. McDonald and M. Pintar-Krainer, J. Chem. Phys. **105**(1996):979.

[46]. A.J. Horsewill and Q. Xue, Phys. Chem. Chem. Phys. **4**(2002):5475.

[47]. M. A. Neumann, S. Craciun, A. Corval, M.R. Johnson, A.J. Horsewill, V.A. Benderskii and H.P. Trommsdorff, J. Luminescence. **76-77**(1998):56.

[48]. A.J. Horsewill and I.B.I. Tomash, Solid State Nucl. Magn. Reson. **2**(1993):61.

[49]. A.J. Horsewill, A. Heidemann and S. Hayashi, Z. Phys. B **90**(1993):319.

[50]. A.J. Horsewill and A. Aibout, J. Phys.:Condens. Matter **1**(1989):9609.

[51]. S. Clough, A. Horsewill, P.J. McDonald and F.O. Zelaya, Phys. Rev. Lett. **55**(1985):1794.

[52]. B.H. Meier, F. Graf and R.R. Ernst, J. Chem. Phys. **76**(1982):767.

[53]. E.R. Andrew and L. Latanowicz, J. Magn. Reson. **68**(1986):232.

[54]. D.C. Look, I.J. Lowe, J. Chem. Phys. **44**(1966):3437.

[55]. Solomon Lefschetz, Phys. Rev. **99**(1955):559.

[56]. J.A.S. Smith, Chem. Soc. Rev. **15**(1986):225.

[57]. H.B.G. Casimir. On the Interaction between Atomic Nuclei and Electrons, W.H. Freeman, San Francisco and London, 1963.

[58]. S.H. Koenig and R.D. Brown III, Prog. Nucl. Magn. Reson. Spectrosc. **22**(1990) 487.

[59]. C.J. McGloin, PhD Thesis, Nottingham, 1997.

[60]. R.I. Jenkinson, PhD Thesis, Nottingham, 1998.

[61]. N.H. Jones, PhD Thesis, Nottingham, 2002.

[62]. Q. Xue, PhD Thesis, Nottingham, 2003.

[63]. P.J. McDonald, PhD Thesis, Nottingham, 1984.

[64]. M.R. Johnson, PhD Thesis, Nottingham, 1992.

[65]. W. Wu, D.L. Noble, J.R. Owers-Bradley and A.J. Horsewill, J. Magn. Reson. **175**(2005):210.

[66]. A.J. Horsewill and W. Wu, JMR-05-252, received and on publication.

[67]. W. Wu, D.L. Noble and A.J. Horsewill, Chem. Phys. Lett. **402**(2005):519.

[68].   E. Balchin, D.J. Malcolme-Lawes, M.D. Rowe, J.A.S. Smith, M.J. Bearpark, J.W. Steed, W. Wu, A.J. Horsewill and D. Stephenson, <u>New J. Chem.</u> **28**(2004):1309.

[69].   R. Silbey and H.P. Trommsdorff, <u>Chem. Phys. Lett.</u> 165(1990):540.

[70].   J. Keeler. Understanding NMR spectroscopy (2002). http://www-keeler.ch.cam.uk.

[71].   C.C. Wilson, N. Shankland and A.J. Florence, <u>Chem. Phys. Lett.</u> **253**(1996):103.

[72].   D. Neuhaus and M.P. Williamson. The Nuclear Overhauser Effect in Structural and Conformational Analysis, 2nd Edition, Wiley, 2000.

[73].   G. Navon, Y.Q. Song, T. Room, S. Appelt, R.E. Taylor and A. Pines, <u>Science</u> **271**(1996):1848.

[74].   C.R. Bowers and D. Weitekamp, <u>J. Am. Chem. Soc.</u> **109**(1987):5541.

[75].   D.A. Hall, D.C. Maus, G.J. Gerfen, S.J. Inati, L.R. Becerra, F.W. Dahlquist and R.G. Griffin, Science 276(1997):930.